Towards Engineering Living Functional Materials

Tzu-Chieh Tang

B.Sc. in Life Science, National Taiwan University, 2009
M.Sc. in Materials Science and Engineering, Masdar Institute of Science and Technology, 2014

Submitted to the Department of Biological Engineering in partial fulfillment of the requirements
for the degree of
Doctor of Philosophy in Biological Engineering
at the

MASSACHUSETTS INSTITUTE OF TECHNOLOGY

February 2021

Signature of Author: ____________________
Department of Biological Engineering
January 8, 2021

Certified by: ____________________
Timothy K. Lu
Associate Professor of Biological Engineering and Electrical Engineering and Computer Science
Thesis Supervisor

Certified by: ____________________
Neri Oxman
Associate Professor of Media Arts and Sciences
Thesis Supervisor

Accepted by: ____________________
Katharina Ribbeck
Professor of Biological Engineering
Graduate Program Chair, Department of Biological Engineering

The following committee has evaluated this doctoral thesis:

James J. Collins, Ph.D.
Chair, Thesis Committee
Professor of Biological Engineering, MIT

Timothy K. Lu, M.D., Ph.D.
Thesis Supervisor
Associate Professor of Biological Engineering and Electrical Engineering and Computer Science, MIT

Neri Oxman, Ph.D.
Thesis Supervisor
Associate Professor of Media Arts and Sciences, MIT

Benedetto Marelli, Ph.D.
Member, Thesis Committee
Assistant Professor of Civil and Environmental Engineering, MIT

Towards Engineering Living Functional Materials

Tzu-Chieh Tang

Submitted to the Department of Biological Engineering on January 8, 2021
in partial fulfillment of the requirements for the degree of
Doctor of Philosophy in Biological Engineering

Abstract

Synthetic biology has become one of the most rapidly evolving research fields, with impacts on all aspects of our daily life. Through applying engineering principles to programming biological systems, synthetic biology provides advanced techniques to program organisms to perform desired tasks, similar to machines created by humans. Today, it has enabled the development of alternative meat substitutes, biosensors for water contamination, and living fertilizers that promote plant growth. The grand challenge to bridge the concept-to-product gap is twofold: scalability and safe deployment. First, most model microorganisms cannot produce a macroscale matrix to sustain themselves as standalone devices. The field of engineered living materials (ELMs) aims to recapitulate the remarkable properties of natural biology to create novel, growable, multifunctional materials using genetically engineered organisms. Nevertheless, most relevant pioneering work was created using nano- to microscale biofilm, which has rather small yields and usually requires costly modification. Second, releasing genetically modified microorganisms (GMMs) into the field for food, water, or agricultural applications is often considered risky due to the uncertainty of wild-type organisms acquiring undesirable traits, such as antibiotic resistance, from the GMMs. A significant effort in addressing these unmet needs is called for. This Thesis starts with an introduction of genetic circuits and an in-depth review of the current trends in materials synthetic biology, which includes two major categories of ELMs: self-organizing functional materials and hybrid living materials. The following chapters describe the technologies developed to achieve high scalability and safe deployment of ELMs in these two categories and living devices suitable for real-world applications. Finally, a detailed outlook summarizes the challenges and prospects for materials synthetic biology and engineering living functional materials.

Thesis Supervisor: Timothy K. Lu
Title: Associate Professor of Biological Engineering and Electrical Engineering and Computer Science

Thesis Supervisor: Neri Oxman
Title: Associate Professor of Media Arts and Sciences

Acknowledgment

I am truly grateful for all the mentors and colleagues who participated in this amazing journey I had in the past six years. To my advisor: Tim, thank you for providing this nurturing environment, resources, and freedom for me to learn and explore the beauty of synthetic biology. To my co-advisor: Neri, thank you for being an inspiration and showing me the boundless possibilities of life and materials. To Jim and Benedetto: I could not have asked for a more supportive committee that helped me grow and build confidence along the way. To my long-term research partners: Eleonore, Charlie, and Xinyue, thank you for being such reliable coworkers and good friends. I could not have finished these projects without your significant contribution. To my mentors: Tom, Matteo, Chao, and Mark, thank you for helping me lay a solid foundation during my career development. To the great teachers: George, Ed, Katharina, James, and Jing-Ke, thank you for the chats and insightful guidance. To Ky, our lab hero, thank you for making our life so much easier and being our trustworthy source of wisdom. To the J-WAFS family, thank you for providing funding and support in many different ways.

I feel extremely lucky to have collaborated with or worked alongside many bright minds. To the folks in the Lu lab: Fahim, Rob, Kevin, Nate, Isaak, Giyoung, Jicong, Cheng, Bryan, Eugenia, Naoki, Yong, Bolin, Heechul, Cesar, Ming-Ru, Sam, Logan, Cheryl, Lior, Dou, Charles, Tristan, William, Tim, Shota, Allen, Bijan, Seb, Jasper, Juliane, Ying-Chou, Dacheng, Qing, Barbara, Hyunjun, Jake, Rashmi, Roger, and Karen, thank you for always being generous in helping me and teaching me many useful things that could never be found in textbooks. To the people from the Mediated Matter group: Steve, Sunanda, Christoph, Rachel, Dominik, Jorge, Laia, Nassia, Will, Andrea, VV, Josh, Tim, and Jean, thanks for your friendship and for showing me your limitless creativity. To the brilliant mates in the Ellis lab: Wolfgang, Will, Glen, Marcus, Vivianne, Jelle, and Olivier, thank you for making my exchange days splendid and teaching me everything about yeast and *K. rhae*. To the hydrogel experts in the Zhao lab: Hyunwoo, Shaoting, and German, thank you for lending me your knowledge and skills when I was in need. To the ELM team: Chris, Chelsea, and Dan, thank you for having me on this wild project that truly broadened my horizon. To the food microbiome experts at Tufts: Ben and Liz, thank you for introducing me to the colorful world of kombucha. To the GRO masters from Yale: Farren and Lexi, thank you for offering me your magical technology that brought my project to a new height. To George: my classmate and collaborator, thank you for being a great role model of perseverance and creativity.

Finally, I would like to express my appreciation to my friends, who made my life enjoyable as a Ph.D. student. To the BE 2014 classmates and the extended BE family: thank you all for sharing all those memorable moments with me and showing me how to achieve excellence while having fun. To the people in the Weiss and Voigt labs: thank you for your constant presence and warm greetings even during the worst snowstorms. To the MIT Microbiome Club board: thank you for giving me the opportunity to be part of your inspiring outreach events. To my Taiwanese friends in Boston: thank you for being so caring and making me feel like being home. To my Masdar comrades here in town: thanks for your rock-solid support and always reminding me how we should all contribute to making this world a better place. To my old friends back in Taipei: thank you for your friendship and for providing a roof over my head when I visited. Finally, thank you, Kertu, for being my only family and my home. Life is more interesting when shared.

Contents

Preface

The following chapters use texts and figures from previously published articles I co-first authored. I want to note that these materials were a joint effort with my colleagues during my tenure at MIT, and I owe them my most sincere appreciation. Specifically, the contents from the following publications were used directly or modified with permission from the publishers.

Chapter 1 and 5 are based on a Review Article I wrote together with Bolin An:
Tang, T. C.*, An, B.*, Huang, Y., Vasikaran, S., Wang, Y., Jiang, X., Lu, T. K., & Zhong, C. (2020) Material design by synthetic biology. *Nature Reviews Materials*. https://doi.org/10.1038/s41578-020-00265-w

Chapter 2 is adapted from an Article I authored together with Dr. Charlie Gilbert:
Gilbert, C.*, Tang, T. C.*, Ott, W., Shaw, W., Dorr, B. A., Sun, G. L., Lu, T. K., & Ellis, T. (2021) Living materials with programmable functionalities grown from engineered microbial co-cultures. *Nature Materials*. https://doi.org/10.1038/s41563-020-00857-5

Chapter 3 is adapted from an Article I authored together with Dr. Eleonore Tham and Xinyue Liu:
Tang, T. C.*, Tham, E.*, Liu, X*, Yehl, K., Rovner, A. J., Yuk, H., de la Fuente-Nunez, C., Isaacs, F. J., Zhao, X., & Lu, T. K. (2021). Tough hydrogel-based biocontainment of engineered organisms for continuous sensing and computation. *Nature Chemical Biology* (Accepted).

Chapter 4 is adapted from an Article I authored together with Xinyue Liu, Dr. Eleonore Tham, and Dr. Hyunwoo Yuk:
Liu, X.*, Tang, T. C.*, Tham, E.*, Yuk, H.*, Lin, S., Lu, T. K., & Zhao, X. (2017). Stretchable living materials and devices with hydrogel–elastomer hybrids hosting programmed cells. *Proceedings of the National Academy of Sciences*, 114(9), 2200-2205.

*Co-first authors

Chapter 1

Materials Design by Synthetic Biology

Synthetic biology applies genetic tools to engineer living cells and organisms analogous to the programming of machines. In materials synthetic biology and living materials, engineering principles from synthetic biology and materials science are integrated to redesign living systems as dynamic and responsive materials with emerging and programmable functionalities. As an introduction, in this Chapter, we discuss synthetic biology tools, including genetic circuits, model organisms, and design parameters, which can be applied to construct smart living materials. We investigate non-living and living self-organizing multifunctional materials, such as intracellular structures and engineered biofilms, and examine the design and applications of hybrid living materials, including living sensors, therapeutics, and electronics, as well as energy-conversion materials and living building materials.

1.1 Introduction

Biologically inspired engineering, also called biomimicry, takes its cues from the rich diversity of forms and functions found in nature and is applied across scales and disciplines;[1] for example, functional materials can be created by recapitulating design principles derived from nacre, spider silk, or gecko toes, using artificial building blocks[2,3]. Biomimetic approaches hold boundless potential for optimizing specific functionalities because synthetic building elements can outperform their natural analogs in terms of mechanical properties and are readily manufactured on a large scale. However, challenges remain for mimicking the responsiveness and adaptiveness of biological systems because it requires often complicated, top-down manufacturing tools that need to be coordinated with separate sensing and actuation modules[4,5]. Living creatures harness the evolved power of multiple subsystems based on universal building blocks, including nucleic acids, proteins, and polysaccharides. Insights into the meticulous architecture and function of cells, tissues, and organisms are shifting the paradigm to mimicking biology for engineering solutions[6].

Synthetic biology aims to program biological systems to perform user-defined functions[7]. Instead of computer codes, nucleic acid or protein sequences are used as scripts to direct the behavior of biological systems from the subcellular to the organism level. Engineering principles, such as modular design, standardized parts, and computational simulation have fueled the rapid advancement of synthetic biology, and with the invention of the genetic toggle switch[8] and repressilator[9] in 2000, synthetic biology has emerged as a full-fledged engineering field. Engineering principles can be adopted for biological systems to transform cells into designed living machines; for example, on-off state changes and oscillating protein concentrations can be engineered in bacteria, such as *Escherichia coli*. The same principle has facilitated the development of quantitative techniques to probe biological problems. Concepts such as control theory[10] and elements such as logic gates[11] and modular parts[12] have been implemented in developing genetic circuits with predictable behaviors, substantially expanding the programmability of biological phenomena (Figure 1). After two decades of intensive tool development, massive genetic circuits can now be built that perform sophisticated decision-making processes involving multiple inputs and outputs[13].

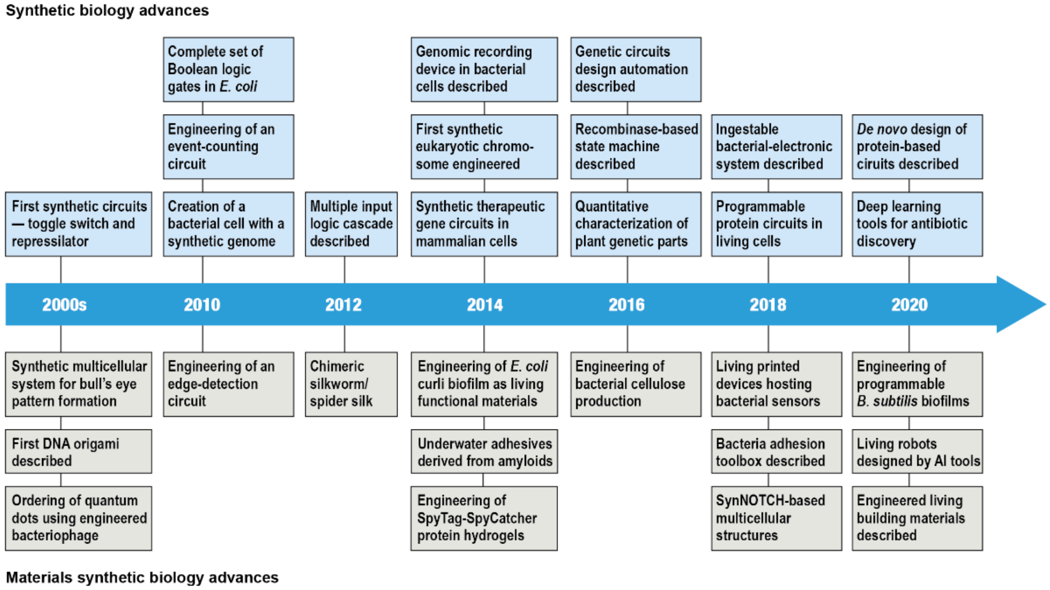

Figure 1 | **Timeline of major milestones in synthetic biology tool development and the advances of materials synthetic biology.** AI, artificial intelligence.

Complex biological functions created with model circuitry can further be modified with artificial functionalities. Advances in bioinformatics and the decreasing cost of DNA sequencing and synthesis have given rise to de novo biological systems that integrate sensing, computing, and recording to perform specific tasks[14–16]. The applications of these technologies range from biomedicine[14] to agriculture[17].

Synthetic biology has also extended its impact to materials science and engineering (Figure 1). Engineered biomaterials have great potential in various areas, including medicine[18], civil and environmental engineering[19], architecture[20], and product design[21]. Living organisms continually interface with their surrounding environment through the biomaterials they produce[22]. The properties of natural biomaterials are related to their biological function; for example, as living organisms grow and move, they generate extracellular matrices, cell walls, and other biopolymers that serve as templates for composite formation tailored to fit specific physiological functions[23]. In these dynamic processes, the spatial and temporal information required for the production of biomaterials is encoded in the genome. Therefore, the synthesis and performance of biomaterials can be directed by designing genetic circuits to tune gene expression and biomolecular interactions with exquisite spatiotemporal control[22]. Indeed, synthetic biology can be applied to generate geometrical patterns[24] and to introduce new functionalities into model material systems, such as *E. coli* biofilms[25]. Insights into gene regulation mechanisms in more complex organisms have further allowed the design of self-organizing multicellular structures using synthetic cell-cell signaling, for example, for the asymmetric differentiation of mammalian cells[26].

Traditionally, genetic engineering has been used to create modified or fusion proteins that can be purified and processed into protein-based materials[27]. Similarly, metabolic engineering has allowed the synthesis of chemicals that can serve as monomers for the downstream production of polymeric materials[28]. However, although these materials are engineered in cells, they do not fully exploit the features of living biological systems[27–29]. Thus, to better capture the emphasis on the dynamics of living systems, we propose to denote the concept of designing materials with synthetic biology' materials synthetic biology'. In materials synthetic biology, living systems are used to produce dynamic and responsive materials for user-defined applications. These materials can be endowed with new functions using programmable features, such as self-regeneration, remodeling in response to environmental cues, and evolution[22].

In materials synthetic biology, designer cells, and genetic circuitries are employed to engineer functional materials, marking a paradigm shift in materials design. The use of smart, programmable biomolecular or cellular devices cannot only improve our ability to replicate and harness the properties of natural materials but also improve artificial materials by incorporating biologically derived or inspired functionalities[23]. Therefore, synthetic biology holds great promise for material design; however, this area remains underexplored because, historically, synthetic biology has focused on biomedicine. Furthermore, the concept of genetic circuits has only recently been introduced in materials science, which has mainly applied genetic engineering thus far. Materials synthetic biology also sheds light on mechanisms of biomaterial formation, which are difficult to decipher using traditional reverse engineering approaches.

In this Chapter, we discuss the integration of synthetic biology and materials science tools for the development of self-organizing functional materials and hybrid living materials. We highlight their specific advantages and challenges, and investigate how materials synthetic biology can exploit unconventional biological systems for the design of new materials and applications. We also discuss how active biomolecular or living cellular components can improve the performance of artificial materials and how they can be used to build living hybrid composites with programmable functionalities. Finally, we outline the structure of the experimental part of this Thesis.

1.2 Synthetic biology for material design

Computational tools, in combination with gene sequencing, synthesis, and editing technologies, enable the precise engineering of biomolecular and cellular functions. From the simple toggle switch to automated genetic circuit design, synthetic biology tools and design concepts for prokaryotic and eukaryotic systems have become increasingly sophisticated (Figure 1)[7,30]. These genetic tools allow rational intervention in cellular processes, including genome replication, transcription, translation, and post-translational modifications[7]. Genetic circuits can be implemented for the production of chemicals and biopolymers (such as DNA or proteins), produced either constitutively or in response to environmental cues, which can then be used for the engineering of materials. For the production of chemicals, a cellular metabolic network can be modified to redistribute the fluxes or to create new pathways for metabolite synthesis[31]. Modular engineering of biomolecular domains enables the engineering of distinct functionalities and hierarchical assemblies of biopolymers, for example, proteins with non-canonical amino acids[32], self-assembling DNA[33], and protein complexes[34]. The fine-tuning of the dynamic features of biomolecules using genetic circuits endows living systems with computer-like capabilities, including sensing, computing, recording, and other programmable functions[35–37]. Programmable protein and nucleic acid materials can also be designed and produced by in vitro purification and post-processing; although equally important, these materials do not require genetic circuits and thus, they are not the focus of ours.

1.2.1 *Genetic circuits*

Genetic circuits, which essentially perform computation inside a cell or in a cell-free reaction mix, can operate at the transcriptional, post-transcriptional, translational, or post-translational levels[7]. In each case, the inputs are the presence (or absence) of various environmental cues, whereas the outputs are the initiation (or inhibition) of RNA synthesis, protein synthesis, or amino acid residue functionalization. Transcriptional circuits are the most commonly used tools to manipulate gene expression by controlling the efficiency of RNA synthesis. The binding of a transcription factor (regulator) to a specific DNA sequence (operator) upstream of the gene of interest can either recruit RNA polymerase (RNAP) to initiate transcription, or block RNAP attachment and thus, prevent gene expression[7] (Figure 2a). Depending on its mode of action, a transcriptional regulator can be either an activator or a repressor. In an inducible system, activation or deactivation by the regulator is determined by a conformational change or oligomerization triggered by certain inputs, such as exposure to light[38], temperature change[39], or binding to a chemical[40]. The DNA sequence that contains the operators with an affinity for the regulators is called an inducible promoter, which controls downstream gene expression based on environmental cues[35]. Alternatively, constitutive promoters can independently drive gene expression at a fixed level, which depends on the strength of the promoter[41]. A basic genetic circuit, or a transcriptional unit, is constructed by combining a regulator, the corresponding promoter, a gene of interest, and a terminator sequence that ends transcription[42]. In materials synthetic biology, the genes of interest often encode proteins that influence the microscopic or macroscale properties of the material (Figure 2b). Multiple transcriptional units can be linked or layered by connecting the output of the upstream transcriptional unit to the input of the downstream transcriptional unit; the resulting complex circuits can execute Boolean logic computation[43], amplify or integrate signals[44] or introduce delays in a cascade of processes[45].

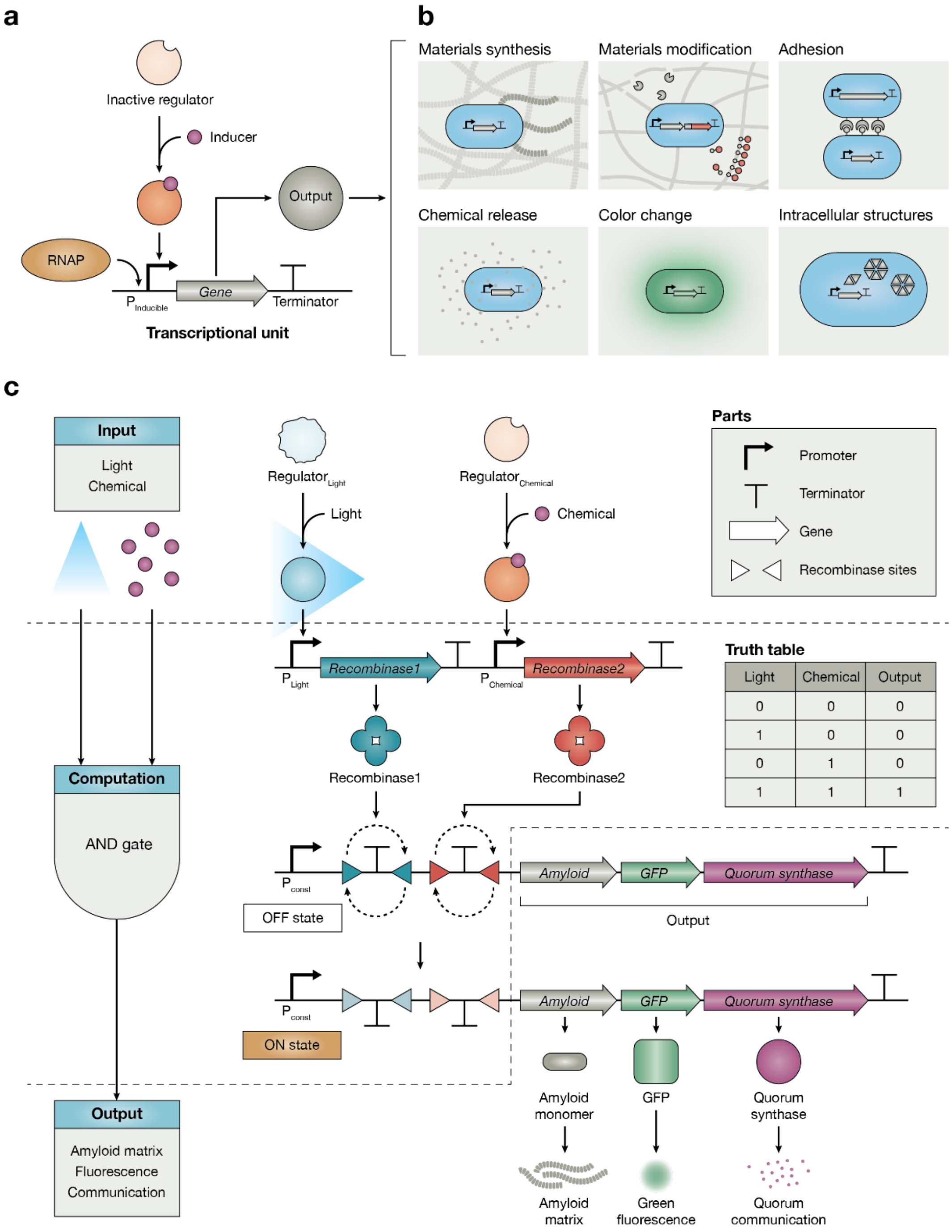

Truth table

Light	Chemical	Output
0	0	0
1	0	0
0	1	0
1	1	1

Figure 2 | **Examples of genetic circuits. (a)** The basic architecture of a simple inducible circuit. A transcriptional unit is a DNA fragment that has a promoter, a gene of interest, and a terminator. An inducer, such as a small molecule, binds to a transcriptional regulator and activates its ability to recruit the RNA polymerase (RNAP) to the promoter and starts gene expression, generating an output. **(b)** Outputs of genetic circuits can be functional proteins that are relevant to material applications. **(c)** An example of an AND gate that computes based on two inputs and generates an output consisting of three proteins. At the input level, two transcriptional regulators can sense two orthogonal inputs, light and a chemical, and control the expression of two different recombinases. When both inputs are present, recombinase1 and recombinase2 bind to their corresponding recognition sites on the output circuit and invert the terminators. The output proteins are only "ON" and produced when both terminators upstream from the genes are inverted, removing the obstacles preventing the RNAP from starting transcription (see the truth table).

The functionality of transcriptional circuits can be expanded using additional genetic tools. For example, memory can be introduced into the circuit design by incorporating recombinases. Recombinases excise or invert DNA fragments flanked by specific recognition sites[46], and thus, they can be used to manipulate the presence and direction of promoters, genes of interest, and terminators. For example, the excision or inversion of the coding sequence of a particular gene can completely shut down its expression[47]. Similarly, removing a terminator placed between a promoter and a gene of interest lifts the inhibition imposed by the terminator, turning the circuit from the OFF to the ON state (Figure 2c). Recombinases are useful for building switches and memory circuits, because they introduce permanent changes in the circuit topology, enabling digital control of gene expression states[48] and on-demand switching of material production[49]. Powerful tools based on the CRISPR-Cas system can also be used for the tuning of the transcription status[50]. With the help of a guide RNA targeting a specific DNA sequence, an inactivated Cas9 protein can precisely bind to a promoter and interfere with RNAP function (that is, CRISPR interference (CRISPRi)), or, if fused with an activator, help to recruit extra RNAP (that is, CRISPR activation (CRISPRa))[51]. In contrast to the 'digital switch' nature of recombinases, CRISPR-Cas-derived tools offer a more analog 'tuning knob' to knock down or ramp up gene expression[13]. Tuning is potentially useful for the fabrication of materials with gradient features; for example, materials that undergo a gradual change in properties, such as stiffness or coloration.

Most materials designed by synthetic biology have been based on transcriptional circuits thus far, which are easy to implement, well-characterized, and versatile[52]. However, circuits operating at the translational and post-translational levels[53,54], such as RNA-based circuits involving miRNAs and toehold switches, are also being explored for the design of materials for theranostics[55,56]. Alternatively, protein-based circuits using phosphorylation, functional fusion peptides, and polymerization provide prompt output responses to inputs, because they skip the rate-limiting protein translation step[53]. Therefore, materials synthesized by a combination of multiple circuit types could accomplish highly sophisticated tasks, for example, fast and ultra-sensitive detection of a massive array of inputs while simultaneously performing computation, data storage, and even mechanical actuation. Such materials would outperform responsive materials made purely of artificial components.

1.2.2 Genetic parts

The choice of regulator-promoter pair determines the sensing capability of materials equipped with transcriptional genetic circuits. Inducible transcriptional units can respond to natural chemicals, light, temperature change, and electrical and mechanical stimuli, and have been optimized to be modular and universal in prokaryotic[7] and eukaryotic systems[30]. Alternatively, sensing modules can be generated de novo to create new inputs, such as artificial chemicals. De novo generation requires extensive genome mining or haphazard mutagenesis, and thus, remains an immense challenge. However, protein-directed evolution techniques have shown great promise in expanding the current repertoire of inducible regulators[57].

The output of a genetic circuit modifies the physical and chemical properties of a material, resulting in distinct functionalities (Figure 2b). In genetic circuits with sensing capabilities, the response of the circuit can be detected by a change in color or opacity. For example, fluorescent or chromatic proteins, pigments, or enzymes that generate bioluminescence can be expressed upon exposure to environmental inputs, without adding significant biomass to materials[58–61]. Hybrid materials with artificial and natural features can be created by combining biological sensors with abiotic materials[62]. To generate biomolecular materials, naturally occurring polymers can directly serve as outputs of synthetic circuits. However, technical difficulties in recreating the native microenvironment for the in situ assembly of biomolecular materials—for example, for spider silk fiber spinning[63]—have limited the toolbox to simpler systems thus far, such as metabolites, carbohydrate polymers, structural protein monomers, enzymes, and amyloid fibers.

To achieve higher complexity in the material architecture, biochemical processes would have to be coordinated by genetic circuits. At the base level, digital computation based on ON and OFF states is commonly used for the detection of a specific cue from the environment or from an upstream cellular process. By linking multiple transcriptional units, simple Boolean operators, such as AND, OR, and NOT gates, can be constructed using transcriptional regulators[64], recombinases,[48] and CRISPR-related tools[65]. Building on top of these parts, universal logic gates, such as NAND and NOR, can be constructed, enabling the development of logic gates with multiple inputs[43]. The computational result of logic gates either leads to an immediate output or can be registered on a recombinase-based state machine (RSM), for which the combination and order of inputs determine a specific state of the system[66]. The states and the controllable transition between states have laid the foundation for building multi-material systems, in which different elements can be produced in a specific order defined by the input sequence. Furthermore, RSMs can be designed to mimic the cell differentiation process or the evolution of cell states and thus, could be used to direct the growth and morphogenesis of cell-based living materials.

Cell-cell communication is essential for layered circuit design and pattern formation to allow applications in materials at the systems level. Molecules, such as metabolites, peptides, and proteins, can serve as signals indicating cell population density and physical proximity[67,68]. Therefore, quorum-sensing molecules, mating factors, and cell surface receptors, which facilitate signal transduction between cells, can be repurposed as circuit outputs that are exported to the cell surface or the extracellular space, where they act on other cells as inputs initiating responses. For example, N-acyl homoserine lactone, the primary quorum-sensing molecule in Gram-negative bacteria, can amplify upstream signals[69] and create patterned biofilm materials[25].

1.2.3 Choice of organism

Using living systems as chassis for material design builds on native cellular machineries, which have evolved as self-replicating entities that respond to the environment[22]. However, for applications that require a high degree of homogeneity and predictivity, purified biomolecules and cell-free systems may be preferable[27,29]. The extent to which an organism can be engineered depends on the availability of its genomic sequence. Computational tools support the prediction and annotation of promoters, genes, and terminators based on genome databases[70]. An ideal chassis is characterized by a thorough characterization of its genetic parts (native or foreign) and the availability of tools for genetic transformation, because developing new tools is laborious and time-consuming. Therefore, pioneering work on materials powered by synthetic biology has primarily focused on model microorganisms, such as *E. coli* and *Saccharomyces cerevisiae*. These organisms usually have rapid growth rates, and an extensive collection of genetic tools is already available, making them ideal organisms for prototyping genetic circuits and for expressing foreign biomolecules in a plug-and-play fashion. Genetic circuits use the resources of the host cell to perform tasks, and thus, the compatibility of circuit parts with the host cellular machinery (transcription, translation, or molecule secretion) needs to be individually optimized. Otherwise, unexpected resource competition, cross-talk, and toxicity may lead to failures in material functions[13].

Biofilms produced by model microorganisms demonstrated great promise in proof-of-concept work; however, they often lack macroscale structural robustness, and they need to be combined with artificial scaffolds. Thus, there has been a shift towards engineering unconventional organisms that natively produce large amounts of extracellular matrix (ECM); for example, acetic acid bacteria, which naturally exhibit a high yield of ECM consisting of bacterial cellulose— a material with exceptional mechanical properties[71]. Species such as *Gluconacetobacter xylinus* and *Komagataeibacter rhaeticus* have also gained popularity for the development of genetic tools because they can be programmed by genetic circuits transplanted from *E. coli*[72,73]. Similarly, mycelium-producing fungi, such as *Ganoderma lucidum* and other mushrooms, which are used commercially as structural and packaging materials[74], can be genetically engineering using CRISPR-Cas9, which makes them an attractive platform for the production of responsive materials equipped with programmable gene circuits[75]. Alternatively, co-culture of a model organism with a material-producing organism could provide a balance between engineerability and bulk biopolymer production, such as fermented food with a symbiotic community of yeast cells. For example, a synthetic kombucha pellicle can host engineered yeast and wild-type acetic acid bacteria, forming co-cultures that function as biosensing cellulosic materials[76].

Engineering multicellular systems that include animal or plant cells is technically more challenging than building microbial systems. Slower growth rates and more stringent culture conditions make it more difficult to rapidly prototype eukaryotic cells[77,78]. However, animals and plants are relevant to real-world applications, and therefore, building biomaterials with their cellular components is a key focus of living functional materials research[26,79]. For example, genetic circuits allow animal cells to form 3D tissue-like structures made of multiple cell types, paving the path towards tunable autonomous organoids[80] and living robots[81]. Similarly, circuit-equipped plants can gain additional functionalities, such as desalination and detection of hazardous agents in the environment; these functionalities build upon the native ability of plants to produce bulk cellulose and lignin composites[82,83], as well as recalcitrant biopolymers, including suberin[84] and sporopollenin[85]. Complex circuits with powerful computation capabilities validated in simple microbial systems could realize their full potential in engineered animal and plant living materials in the future.

1.2.4 Design parameter space

Self-organizing functional materials and hybrid living materials differ in their biomaterial composition. Self-organizing functional materials contain only biomolecules or living cells, whereas hybrid living materials also incorporate synthetic components, for example, artificial scaffolding matrices. Self-organizing functional materials include non-living and living materials, whose structural components are directly generated or derived from biological systems rather than from artificial sources (Figure 3). Functions generated by recombinant genes or genetic circuits can be harvested for the design of self-organizing multifunctional materials[52], for example, non-living materials, such as underwater protein adhesives recapitulating features of natural marine glues[86], and living materials, such as engineered living functional materials based on biofilms[87,88], bacterial cellulose[76] or intracellular assemblies[89], for diverse applications, such as bioremediation[90], biomedicine[18], and adhesion[91]. By contrast, hybrid living materials integrate living cells with non-biological components; for example, engineered cells can be combined with artificial matrices and biomanufacturing tools to form living devices with defined geometry and size[92,93]. In theory, such hybrid living materials can comprise components whose functions can combine and even synergize, which enables the integration of living attributes of cells with synthetic scaffolds and thus, new applications not currently associated with synthetic materials.

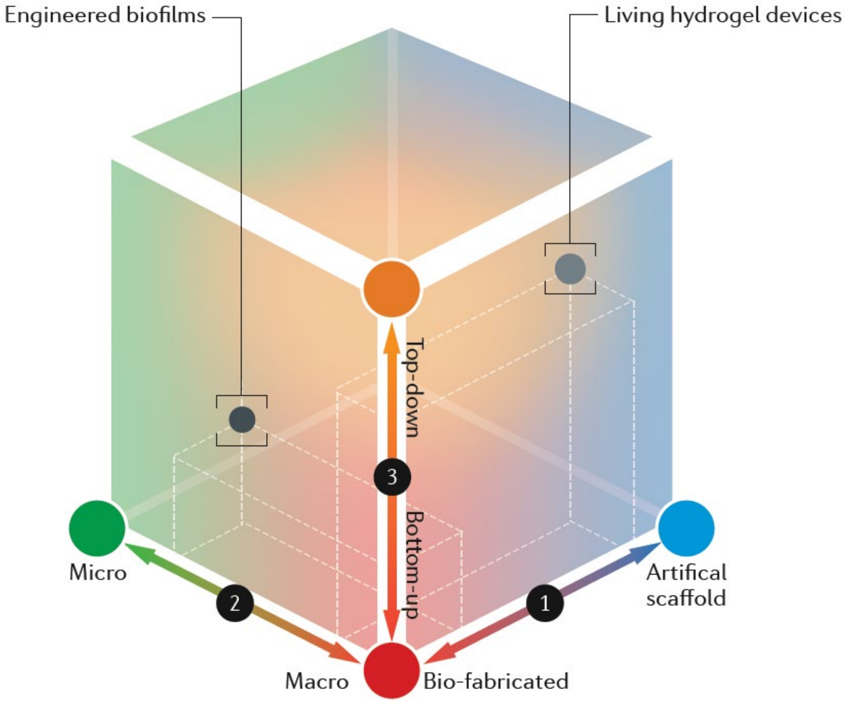

Figure 3 | **Design parameter space for materials synthetic biology.** The cube represents the design space determined by three major axes of the parameter. First (red to blue), the matrices in materials can either be fabricated by biological processes carried out in living cells, or they can be produced on abiotic artificial scaffolds. This axis defines the two main categories discussed in this Review. The second axis (green to red) describes the materials based on their length scale, from microscopic to macroscopic. Finally, the third axis (red to orange) differentiates materials that are assembled with bottom-up approaches from those shaped by top-down methods. Engineered biofilms (black dot) produce their matrix with biopolymers from cells self-organized at the microscale. Hydrogel wearable device hosting engineered whole-cell biosensors (brown dot), on the other hand, are manufactured in pre-defined geometries at the macroscale.

The design parameter space is also related to the degree to which artificial scaffolds are used, the length scale at which they operate, ranging from microscale (biofilms)[87] to macroscale (building materials)[20], and to the design approach, for example, bottom-up morphogenesis[25] versus top-down design (casting and 3D printing) (Figure 3)[92].

1.3 Self-organizing functional materials

Biological systems have self-assembly mechanisms that create functional materials across a broad spectrum of length scales using basic building blocks[94] (Figure 4). At the nanoscale, the structure and function of biomacromolecules, such as nucleic acids and proteins, are determined by the sequential arrangement of nucleotides and amino acids, respectively. Similarly, at the population level, cells organize themselves into ordered architectures, based on genetic instructions encoded in their genome that orchestrate cell differentiation. Therefore, extracted or synthesized biopolymers (that is, nucleic acids, bioplastics, and proteins) can be used for the fabrication of self-organizing non-living functional materials[27,28,95,96]. Importantly, synthetic biology tools can be applied to the engineering of programmable living materials.

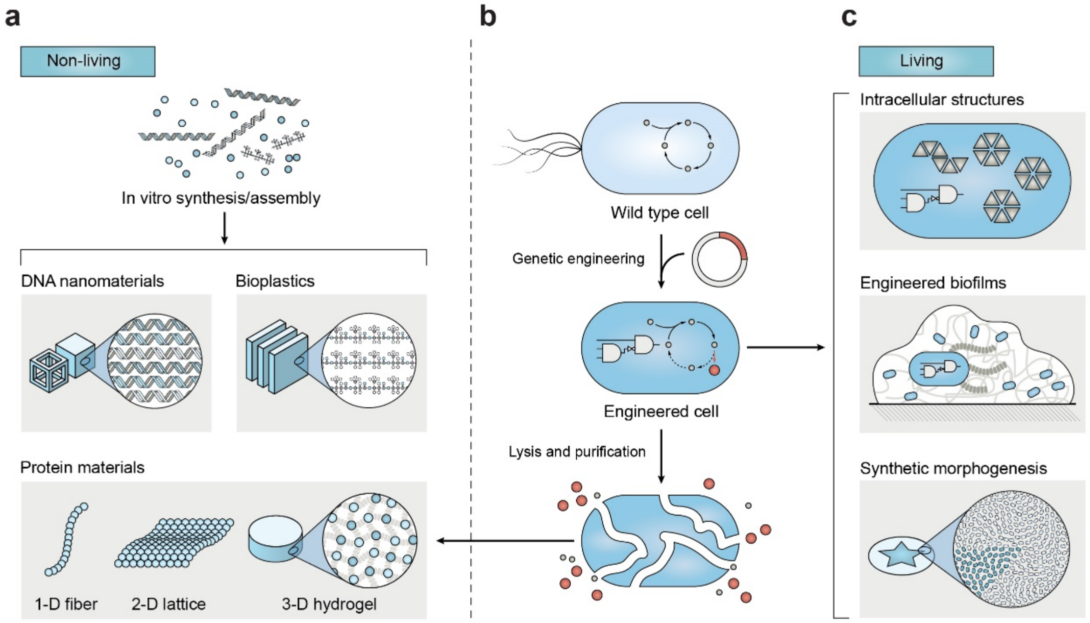

Figure 4 | **Types of non-living and living self-organized materials. (a)** Non-living DNA nanomaterials and bioplastics are usually synthesized artificially using chemicals or purified monomers from bioreactors. Protein materials, ranging from one-dimensional (1D) fibers to two-dimensional (2D) lattices and three-dimensional (3D) hydrogels, are mostly produced by processing purified proteins from genetically modified living cells. **(b)** Cells undergo genetic engineering and acquire DNA-encoded information for producing precursors for bioplastics and monomers for protein materials. **(c)** These engineered cells can also be used directly as living materials with functionalities programmed by genetic circuits that can create intracellular structures, enhance the responsiveness of biofilms, and direct synthetic pattern formation and morphogenesis.

1.3.1 Non-living materials

Non-living functional materials can be made from self-organizing biomolecules (for example, nucleic acids, bioplastic precursors, and proteins), derived from artificial synthesis or metabolic engineering[28,97] (Figure 4a). For material production, synthetic biology provides numerous natural or artificially designed modules with various functions, and enables their rational reassembly for customized applications[27,98,99]. For example, programmable CRISPR-responsive DNA hydrogels constructed by integrating CRISPR-associated nucleases with structural DNA elements, which can convert biological information (that is, guide RNA) into particular properties of materials (for example, conductivity or the ability to detect a virus)[100], or hierarchical strong underwater adhesives made from rationally designed recombinant proteins, composed of cohesive (amyloid self-assembling proteins) and adhesive domains (3,4-dihydroxy-L-phenylalanine (DOPA)-containing mussel foot proteins)[86,101]. In addition, synthetic biology provides solutions for the in vivo production and functionalization of engineered materials in genetically modified organisms with remodeled metabolic pathways[28,95,102–105] (Figure 4b), for example, genetically encoded DNA nanostructures[33], mechanics-tunable bioplastics[106] and recombinant proteins with modified functional moieties[107].

1.3.2 Living materials

In contrast to non-living materials, engineered living materials are composites of biopolymers and genetically modified cells (Figure 4c). The living organisms hosting the genetic circuits in these materials can perform sensing, computation, and actuation, allowing them to synthesize or modify the materials in response to environmental cues[23]. In addition to performing complex tasks, engineered living materials self-replicate and evolve, which makes them autonomous, adaptive, and very versatile[22]; for example, the assembly of intracellular structures, the enhancement of biofilms by secreted materials, or pattern formation by populations of cells.

1.3.2.1 Intracellular structures

Cells build intracellular structures for diverse purposes, including the formation of diffusion barriers or compartments for local confinement of biomolecules, enabling site-specific cellular functions[108]. Similar to organelles, these nano- or microstructures are constructed through the self-organization of biomolecules, such as proteins and lipids. Investigation of the self-assembly mechanisms of protein complexes, amyloids, and viral capsids has generated knowledge from which design principles for intracellular structures can be discerned[109], providing a blueprint for the reprogramming of protein materials using modular designs for the de novo creation of form-function relationships. For example, protein-based hydrogels[110] and phase-separated clusters[34] can be constructed in living cells by rationally designing the intermolecular interactions between peptide and protein modules. These droplet-like hydrogel materials, which provide an ideal microenvironment for biochemical reactions, are responsive to inputs, such as proteases and light[109]. In addition to influencing metabolism, intracellular protein assemblies, such as ferritin aggregates[111], reflectin-based structures[112], and gas vesicles[89,113], endow the cell with inducible material properties, including magnetism, opacity, and acoustics.

1.3.2.2 Engineered biofilms

Microorganisms often exist in biofilms composed of living cells, embedded in a self-produced ECM. Secreted ECM polymers, such as proteins and polysaccharides, form 3D structures that protect cells against environmental challenges and provide a medium for nutrient exchange[114]. The underlying mechanisms of biofilm formation have been extensively studied because biofilm formation is intrinsic to many persistent, antimicrobial-resistant bacterial infections[114,115]. The increase in understanding of the protein and polysaccharide secretion machinery enables the repurposing of biofilms into assembly lines for functional material production[23,52]. Synthetic biology tools, such as genetic circuits, modular protein design, and metabolic engineering, allow the creation of a broad spectrum of programmable functional biofilms.

Intracellular and extracellular amyloid fibers are formed by highly ordered protein aggregates[116]. In addition to their roles in the pathogenesis of neurodegenerative diseases, amyloids often act as functional protein structures in microorganisms[117]. For example, in enterobacteria, such as *E. coli* and *Salmonella* spp., curli amyloid fibers are the main component of the ECM, facilitating surface binding and promoting host colonization[118]. The CsgA protein monomer, which is the basic building block of *E. coli* curli fibers, served as one of the earliest chassis for biofilm engineering[87]. The production of curli fibers can be precisely tuned by putting the expression of CsgA under the control of inducible promoters; for example, promotors responding to small molecules[25]. Similarly, optical inputs can drive the on-demand production of curli fibers, allowing light-patterning of adhesive biofilms[119]. To further functionalize the biofilm, exogenous protein modules can be fused to the amyloid-forming domain of CsgA, leading to curli fibers capable of electrical conduction[120,121], enzymatic catalysis[122,123], bioremediation[90,124] and templating inorganic materials[125,126]. To enable more complex tasks, functionalized curli fibers can work in concert with computation and communication modules, achieving simple Boolean decision making[49] and intra-fiber patterning[25]; for example, to promote wound healing in animals[18]. In addition to the *E. coli* curli system, programmable TasA amyloid fibers in *Bacillus subtilis* can also be engineered into functional materials, demonstrating that modular design is a universal feature of amyloid-forming proteins[91]. Engineered *B. subtilis* biofilms exhibit hydrogel-like viscoelastic behaviors, making them ideal for the manufacturing of protrusion-based additives[88]. Besides amyloids, surface-layer proteins, such as RsaA of *Caulobacter crescentus*, can be engineered using protein fusion to create functionalized lattice-based 2D living materials[127].

Polysaccharides, including bacterial cellulose, are the main constituents of most mechanically strong biofilms[114]. The chemical and physical properties of polysaccharides can be altered by genetically modifying the pathways synthesizing the constituent monosaccharide building blocks[128]. However, this approach requires detailed knowledge of the polymerization-secretion machinery and well-developed genetic engineering techniques, which are often lacking in non-model, ECM-rich microorganisms. The development of genetic toolkits for *K. rhaeticus* has greatly improved the engineerability of cellulose-producing strains, making inducible bacterial cellulose production possible[73,129]. Alternatively, co-culture systems consisting of a potent polysaccharide-producing species and an engineerable model species bypass the hurdle of producing secreted polysaccharides[76]. For example, a kombucha-inspired living material has been engineered using *K. rhaeticus*, which generates a bacterial cellulose matrix, and *S. cerevisiae*, which provides programmable functionalities, such as light sensing and catalytic activity[76].

Living materials are currently mainly engineered using endogenous biomacromolecules for ECM synthesis; however, non-biological monomers can also be applied for building polymers in the extracellular space[130–132]. *Shewanella oneidensis*, an electroactive bacterium with a built-in extracellular electron transfer machinery, allows metabolically controlled atom-transfer radical polymerization using non-biological monomers and metal catalysts[131]. Such technologies, coupled with genetic circuits, could substantially broaden the biochemical spectrum for biofilm engineering.

1.3.3 Synthetic morphogenesis

Biological materials are rarely formed by a single cell type or a homogeneous population of cells. Living organisms self-organize into various spatial patterns that translate into the heterogeneity of material properties. By analyzing natural biomaterials, macroscopic forms and functions can be mapped to distinctive cell types on the microscale. The ability to develop patterns and translate them into material properties has enabled organisms to optimize their biomaterials, which is difficult to translate to artificial biomimetic products. The process of materials production in living cells is guided by spatially and temporally controlled functions determined by DNA-encoded information, which eventually leads to cell differentiation and morphogenesis[133–135]. For example, hierarchically self-organized functional cellular assemblies differentiating from the same progenitor cells can form skin tissue or insect exoskeletons, both of which have desirable mechanical properties that have emerged from different cell types. Technologies to precisely manipulate microscale components in synthetic materials are still in development. Alternatively, engineered living cellular factories can be equipped with coordinated synthetic genetic circuits to create autonomously self-organized materials[52,136]. Ideally, a seed cell carrying a genetic blueprint could replicate and differentiate into synthetic multicellular systems to perform pre-programmed functions while adapting to the surrounding environment, without external human intervention or guidance[137].

Programming morphogenesis has long been the holy grail for synthetic biologists[138]. Constructing genetic circuitry for the bottom-up orchestration of a series of biological events is extremely difficult, owing to the inevitable error propagation and restricted parameter space in living systems. As a starting point, simple synthetic optical inputs can be used to direct pigment-based pattern formation in biofilms[38]. This strategy can be expanded to produce multiplexed inputs[139] and functional outputs[140,141]. The same approach can also be applied for chemical inputs[73] and further enhanced by computer-aided design to generate complex patterns[21]. Coupled with quorum-sensing molecules, these simple inputs can trigger downstream cell-to-cell communication, leading to semi-autonomous patterns, such as bullseye[24], stripes[142], and edge detection[143]. Furthermore, inspired by the reaction-diffusion model[144], stochastic Turing patterns can be constructed in biofilms using quorums with different diffusivities[145]. Tools such as repressilators[146] and synthetic asymmetric cell division[147,148] can also serve as orthogonal mechanisms that could be used in parallel to achieve greater design complexity.

Adhesion between cells plays a pivotal role in determining the final multicellular geometry of 3D structures. Modular cell-to-cell adhesion enabled by synthetic adhesins provides a tool to rationally define the morphology of bacterial microstructures[149]. In mammalian systems, programmed cell adhesion combined with the synNOTCH juxtacrine signaling platform results in self-organizing, multilayered structures capable of sequential assembly and differentiation[26]. Aided by computational tools powered by artificial intelligence, robust and autonomous living tissues or materials could soon become a reality.

The mechanisms underlying pattern formation in natural, sophisticated materials or structures (for example, diatom frustules) are being increasingly deciphered, and artificial pattern-generating circuits are being invented. Thus, it may soon be possible to create artificial living materials recapitulating the hierarchically ordered architectures and the outstanding material properties of their natural counterparts.

1.4 Hybrid living materials and devices

Hybrid living systems incorporate cellular ‘factories’ and abiotic environmental components, which form composites with new properties[23]. For example, porous silica structures encapsulating single diatom cells (diatom frustules) not only provide the organism with robust mechanical support but they also take part in cellular metabolic processes, such as chlorophyll synthesis[150]. Synthetic materials manufactured by energy-intensive, top-down processes may exhibit specific user-designed properties, but lack biological responsiveness and adaptability. For artificial materials to acquire specific biological properties, such as self-adjustment, self-regeneration, self-healing, and environmental responsiveness, synthetic materials can be coupled with living systems. In turn, the incorporation of high-performance synthetic components improves the performance and practical utility of living materials. Thus, hybrid living materials have the advantages of artificial components and living cells, broadening the application scope of conventional hybrid materials (Figure 5a), including sensing, therapeutics, electronics, energy conversion, and building materials.

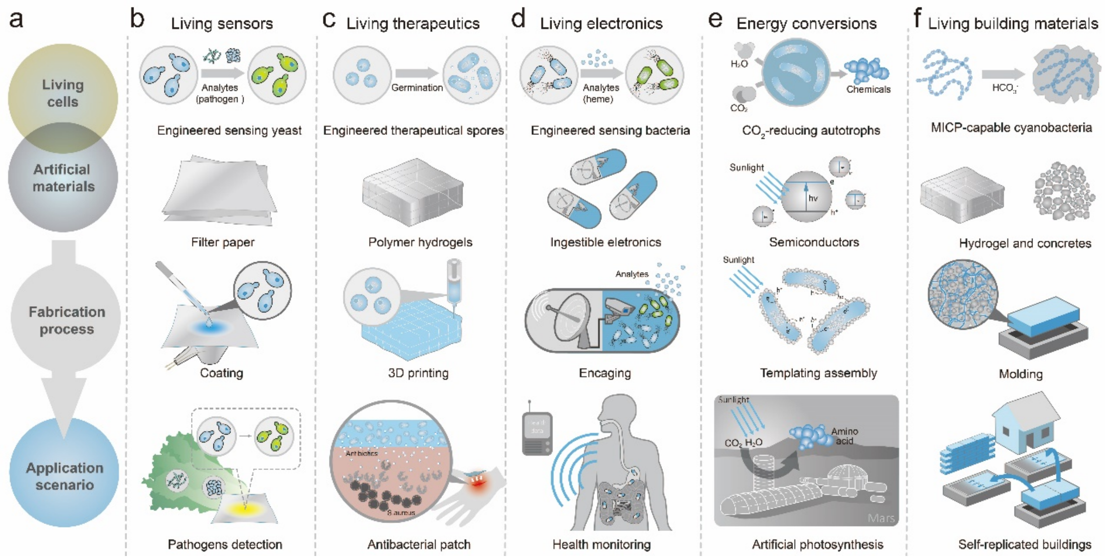

Figure 5 | **Representative examples of hybrid living materials. (a)** General forms of hybrid living materials. **(b)** Living paper dipsticks for detecting pathogens. Pathogen-detection yeasts coated on filter paper were used for checking vegetable pollutants. **(c)** Living therapeutic patches for blocking wound infection. The 3D printed patch containing antibiotic-secreting *B. subtilis* spores inhibits pathogen infection. **(d)** Living electronics for monitoring gastrointestinal health. Blood inducible microbial sensors encased in microelectronic devices for diagnosing gastrointestinal diseases. **(e)** Renewable energy production via artificial photosynthesis. Non-photosynthetic autotrophs interfacing with light-harvesting semiconductors were employed for chemical production in space. **(f)** Self-replicated living bricks. Cyanobacteria with microbial induced calcium carbonate precipitation (MICP) capabilities enabled the bio-fabrication of living building bricks.

1.4.1 Living sensors

The efficient, innate sense-and-response mechanisms in living cells, coupled with genetic modularity engineered by synthetic biology, offer vast possibilities for the construction of whole-cell biosensors[151]. Compared with traditional physical or chemical sensing methods, the manipulation of biosensors does not require sophisticated lab instruments or professional personnel. In contrast to cell-free sensing systems[152], the living components, which colonize the surroundings, enable on-site signal readout. Living biosensors are currently applied in various areas, including monitoring of metabolic production[153], environmental hazards[154], and disease signals[14].

Hybrid living sensors can be built by integrating genetically encoded microorganisms with biocompatible scaffolding materials. For example, dipsticks produced by vacuum-filtering G protein-coupled receptor (GPCR)-refactored *S. cerevisiae* onto cellulose filter paper enable visible color readouts upon contact with specific fungal mating peptides. This living sensor provides a scalable and economical platform for global surveillance of fungal pathogens[155] (Figure 5b). Long-term detection can be achieved using biocompatible hydrogel materials infused with water and nutrients to provide semi-liquid environments that can sustain cell survival and the exchange of molecules[156]. Owing to their tunable viscoelastic properties, these materials can be processed with various fabrication tools, such as molding and 3D printing, making them interesting scaffolds for field-deployable biosensors[92,157]. In addition to their protective role, hydrogel materials can also help to reduce potential risks of environmental pollution from leaked genetically modified microorganisms. For example, a bilayer hydrogel comprising a robust, porous hydrogel shell and a bacteria-containing alginate core can serve as effective biocontainment to inhibit the escape of genetically encoded microbes[93].

However, living sensing materials also have several shortcomings, including limited detection sensitivities and operational ranges, which are determined by the cells[158]. These limitations can be addressed by optimizing the sensing modules, for example, by modifying the strength of transcriptional promoters[159], adjusting translational levels[160], or controlling post-translational degradation[44]. Alternatively, signal-cascade genetic circuits[44] can be amplified and cellular consortia[161] can be constructed to achieve ultrasensitive detection thresholds and tunable input and output operational ranges.

1.4.2 Living therapeutics

Native and genetically modified microorganisms have been traditionally employed in the industry to produce bioactive metabolites. Viable cells equipped with drug-producing genetic modules constitute living therapeutics, engineered to prevent or treat diseases in vivo[162]. Living therapeutics can be administered for the sustained and long-term treatment of chronic diseases (such as cancer, diabetes, and some gastrointestinal diseases); however, to avoid immune responses (immunosuppression) associated with the uncontrolled cell growth of free-floating microorganisms in the body, the organisms have to be encapsulated within biocompatible scaffolding materials[163].

Similar to hybrid biosensors, biocompatible nutrient-containing hydrogels with proper mechanical strength and selective penetrability are the preferable artificial materials for fabricating living therapeutic devices. For example, soft, biocompatible agarose hydrogels can support the survival of genetically modified *E. coli*, which secretes drugs into culture media in response to light. Owing to the optoregulation of metabolic pathways, the composite material can be dynamically tuned by light to regulate reporter production, localization, and dose release[164,165]. Similarly, biopolymer-based microcapsules and nanoporous membranes can provide matter exchange, cell blocking, and continuous nutrient supply[166,167].

Hybrid living therapeutics can not only deliver drugs inside the body, but they can also be applied for the treatment of pathogen infections in vitro. Antibiotic-producing microbes entrapped in soft, hydrated hydrogels can be used as cost-effective medical bandages with long-term or on-demand antimicrobial properties. For example, a 3D-printed wound-shaped hydrogel patch that contains *B. subtilis* spores excreting lysostaphin and thiocillin can be applied to skin wounds to detect and kill *S. aureus*[168] (Figure 5c). Genetically modified bacteria can also manipulate mammalian cell behaviors by secreting metabolites[169], and thus, they could also be used in regenerative medicine. For example, the non-pathogenic bacterium *Lactococcus lactis*, which can be engineered to display recombinant human fibronectin (FNIII7-10)[170] on extracellular biofilms, colonizes organic or inorganic surfaces and forms ‘living biointerfaces’, which support the differentiation of human mesenchymal stem cells[171–173].

Synthetic biology offers possibilities to engineer living systems with custom-built functions by rewiring genetic circuits[7]. Therefore, drug-releasing cells could also be developed for other healthcare applications, such as low-cost cosmetics or face masks with virolytic capability. In addition to the dynamic features of engineered living systems, artificial synthetic materials can also endow hybrid composites with customized properties (for example, responsiveness). For example, a smart, adaptable gel made of thermo-responsive polymer Pluronic F-127 that contains living *B. subtilis* spores can be applied to treat superficial fungal infections. This gel converts from the liquid to the hydrogel state when the temperature rises to 37°C[174].

1.4.3 Living electronics

Programmable cells can be integrated with electrical devices to simplify detection processes of biosensors and to enable remote and real-time control of living materials; for example, an ingestible micro-bio-electronic device composed of encapsulated bacteria and electronic photodetectors[175] can monitor gastrointestinal health. Upon sensing a particular biomarker, for example, heme, N-acyl homoserine lactone, or thiosulfate, the bacteria within the device produce luminescence, which is detected by a photodetector that wirelessly transmits photocurrent data in vivo to an external device for real-time monitoring. This device, although still at an early stage of development, may be beneficial for diagnosing and monitoring otherwise difficult-to-detect health conditions (Figure 5d). In addition to photodetector-embedded microelectronics, the integration of electrochemical electrodes[176], field-effect transistor devices[177], or directly programming electrode reduction microbial strains[178] also enable environmental monitoring and health diagnostics by converting cellular biochemical changes to easily detectable electrical signals.

Electronic devices can also remotely control the behavior of engineered living materials. For example, a 'HydrogeLED' implant connects the digital signal of a far-red light-emitting diode (LED) to optogenetically responsive cells. The implanted device can release drugs in vivo for the treatment of diabetes, and can be remotely controlled by smartphones[179]. In this device, cell behavior is directly linked to electrical stimulation. Electron-triggered gene expression has also been explored for an *E. coli* SoxR-mediated transcription system in an electrogenetic device[180]. However, the bacteria require anaerobic culturing environments, and the system may be too toxic for in vivo applications[180]. External digital electronic inputs can modulate mammalian cells that contain depolarization-based genetic circuits[181]. Electrogenetic interfaces can be constructed by coupling electrosensitive insulin-secreting β cells with a wireless electrical device, enabling electro-triggered insulin delivery in vivo[181]. These examples of living bioelectronics demonstrate the potential of materials synthetic biology for real-time sensing applications.

1.4.4 Energy-conversion materials

Hybrid living devices are being explored for the generation of renewable energy, providing an important contribution to mitigating the global energy and environmental crisis. For example, microbial fuel cells, which rely on viable exoelectrogens, can convert energy from organic matter into electrical power[182]. Exoelectrogens, such as the model bacteria *S. oneidensis* or *Geobacter* spp., transport electrons via redox proteins attached to the outer membrane or pili nanowires and via indirect redox electron shuttles[183]. The efficiency of electron transfer from the cytoplasm to the external electrode is crucial for the performance of microbial fuel cells. Synthetic biology can be applied to improve electron generation from exoelectrogens and optimize their conductive pathways[184]. Artificial materials, including 3D porous bio-affinity anodes[185] and conductive coating materials (such as reduced graphene oxide or polypyrrole), can be used to form artificial biofilms, which further improve electron delivery[186].

Biological photovoltaics derived from microbial fuel cells use photosynthetic microorganisms, such as microalgae or cyanobacteria, to harvest and convert solar energy into electricity. However, in this type of energy conversion device, the efficiency of transferring photo-excited electrons to electrodes remains limited[187]. Similar to microbial fuel cells, hybridization of conductive substrates and the addition of biocompatible soluble mediators can improve the electron transfer between cells and electrodes[188]. Considering that only 45% of the solar spectrum (visible light) can be absorbed by photosynthetic cells[189], complementing living cells with additional light-capturing materials (such as plasmonic hybrid nanostructures, for example, ZnO NR/Au NP[190]) can help harvest solar energy from broad wavelength ranges. The intra- and extracellular electron transportation can also be improved by introducing electron-exporting conduits from exoelectrogens into photosynthetic cells using synthetic biology; however, the metabolic bottleneck of the corresponding heme-containing proteins remains a challenge for the engineering of cyanobacteria[191].

Artificial photosynthetic systems, which consist of native autotrophic microbes and semiconducting materials or external light-harvesting devices, enable highly selective solar-to-chemical energy conversion[192]. For example, photo-excited electrons from light-absorbing semiconductor nanoparticles can be used by the non-photosynthetic acetogen *Moorella thermoacetica* to create reducing equivalents, accelerating the CO_2 fixation process[193] (Figure 5e). Synthetic biology can be applied to introduce engineered solar-to-chemical metabolic pathways into model microorganisms. For example, *E. coli* encoding hydrogenase can be loaded onto light-capturing materials to catalyze the production of H_2 in anaerobic illuminated environments[194]. Electrons can also be photogenerated by yeast-bound inorganic semiconductors for the regeneration of the redox cofactor nicotinamide adenine dinucleotide phosphate (NADPH), enabling the efficient synthesis of high-value-added metabolites[195]. These living energy-conversion materials are typically built by coupling engineered strains with non-living semiconductor components. To improve their performance, the components and cells need to be integrated through an interface, which will require a better fundamental understanding of electron transfer between the components.

1.4.5 Living building materials

Living systems can also be applied for building construction. For example, inspired by the phenomenon of microbially induced calcium carbonate precipitation, bacterial bricks were invented by directly culturing calcium carbonate precipitating bacteria with mortar in brick molds[196]. Biomineralization directly occurs in the mixture and promotes the aggregation of separate inorganic particles, leading to the formation of bricks with high mechanical strengths. This process avoids traditional clay-heating procedures and massive carbon emissions, and the final products are eco-friendly and able to self-replicate if placed under benign conditions (appropriate temperature and humidity)[20] (Figure 5f). Building materials that contain viable mineral-precipitating microorganisms also exhibit self-healing properties[197]. If the concrete surface is damaged, dormant bacteria exposed to cracks germinate upon contacting the outside air and moisture, which triggers specific metabolic activities, such as ureolysis, methane oxidation, and photosynthesis. The metabolic changes lead to an increase in the precipitation of the surrounding calcium carbonate and thus, enable damage repair[197]. Long-term survival of microbes is the most salient factor in determining the performance of these self-healing materials. Owing to the inhospitable conditions (dehydration, low oxygen, and high alkali) in concrete materials, calcium carbonate precipitating microbes have to tolerate high pH and heat, and they should have the ability to form spores. Biocompatible carriers, such as microcapsules and hydrogels, can function as protective shelters[198]. In addition, synthetic biology can be applied to introduce anti-desiccation components—for example, from tardigrades[199] or by stress-selective evolution[200]—which improve the resilience of microbes. Moreover, biomineralization-relevant metabolic pathways could be modified or nucleating sites could be engineered on biofilms to improve the mechanical strength and to shorten the healing process.

Fast-growing mycelium can also be applied to construction. The divergent filaments of mycelia can function as self-organized ropes that can robustly bind substrate particles (for example, wood chips) to composite materials with advantageous properties (that is, compostable, lightweight, fire-resistant, and soundproof)[201]. In mycelium-based materials, the filaments spread to autonomously and rapidly form an integrated material. This approach could be particularly useful in low-resource areas (for example, to build airport runways in wartime). Only a few genetically modified mycelium materials have been explored thus far; however, advances in fungal genome editing[75], inhibiting mushroom fruiting bodies[202] and developing synthetic sense-to-response circuits[35] will contribute to the creation of living buildings with user-defined functions, such as the release of fragrance or absorption of external toxic or greenhouse gases. Mycelium-based materials are also currently limited by low compressive strength and low stiffness[203]. To overcome these limitations, inspiration can be taken from plants, which possess outstanding mechanical strength and toughness, owing to the oriented arrangement of polysaccharide cellulose and the formation of lignin-carbohydrate complexes[204]. The incorporation of structural order and molecular interactions by synthetic biology may provide a viable route to improving the mechanical performance of fungi-based materials.

1.5 Motivation and thesis structure

In 2014, when I decided to pursue living functional materials as my thesis topic, there were multiple well-received publications reporting living material based on microscopic *E. coli* biofilms as well as chemical biocontainment strategies. They were pioneering work with revolutionizing concepts but unfortunately limited by low yield and non-zero mutation rates. These papers laid a sturdy foundation for my thesis proposal and showed several key limitations, shedding light on important future directions for improvement. These problems came to my attention during the first year of my Ph.D. study when I was searching for impactful projects to work on. While the majority of researchers around me focused their research on biomedical uses such as diagnostics and therapeutics, I found that humankind and our planet Earth could also benefit tremendously from the emergence of synthetic biology. I decided to dedicate my career to developing robust living functional materials and devices that can sense and respond to their surrounding environment. Most importantly, I wanted my research to be translational and ready for the market.

Emerging ELMs created by microorganisms are strong competitors for next-generation materials applications because of their high modularity, low carbon footprint, and cost-effectiveness. However, a significant gap remains between research work and its practical uses since the majority of research was conducted using model organisms in well-controlled laboratory conditions. In field applications where ELMs need to be deployed, this distinction becomes even more significant. Of all the challenges ahead, scalability and safe deployment are among the most pressing ones and need to be addressed with top priority. First, most model microorganisms cannot produce a macroscale matrix to sustain themselves as standalone devices. The field of ELM aims to recapitulate the remarkable properties of natural biology to create novel, growable, multi-functional materials using genetically-engineered organisms. Nevertheless, most relevant pioneering work was created using nano- to micro-scale biofilm, which has rather small yields and usually requires costly post-production modification. Second, releasing genetically modified microorganisms (GMMs) into the field for food, water, or agricultural applications is often considered highly risky due to the uncertainty of wild-type organisms acquiring undesirable traits, such as antibiotic-resistance, from the GMMs. To address these unmet needs, I needed to tackle these two major problems directly, even though relevant resources were limited. I was lucky enough to meet great collaborators who brought me the tools I needed: biofilm production at a large scale and tough hydrogel-based physical containment technologies.

My Ph.D. work specifically contributes to the scalability and safe deployment challenges to bridge the concept-to-application gap. Such improvement would bring the ELM field much closer to the market. In the following Chapters, I will show our explorations towards implementing living functional materials with high scalability and safety. In Chapter 2, we transformed high-yield kombucha pellicles into programmable materials using just tea and sugar. In Chapter 3, we combined chemical and physical containments to develop a near-perfect biocontainment platform technology for deployment of GMMs. Next, in Chapter 4, we created hydrogel-based wearables devices housing GMMs for real-world sense-and-response applications. Lastly, in Chapter 5, we consider the prospects and challenges of current living functional materials technologies and identify potential future applications.

Chapter 2

Self-Organizing Living Functional Materials Grown from Microbial Co-Cultures

Biological systems assemble living materials that are autonomously patterned, can self-repair and can sense and respond to their environment. The field of engineered living materials aims to create novel materials with properties similar to those of natural biomaterials using genetically engineered organisms. Here we describe an approach to fabricate functional bacterial cellulose-based living materials using a stable co-culture of *S. cerevisiae* yeast and bacterial cellulose-producing *K. rhaeticus* bacteria. Yeast strains can be engineered to secrete enzymes into bacterial cellulose, generating autonomously grown catalytic materials and enabling DNA-encoded modification of bacterial cellulose bulk properties. Alternatively, engineered yeast can be incorporated within the growing cellulose matrix, creating living materials that can sense and respond to chemical and optical stimuli. This symbiotic culture of bacteria and yeast is a flexible platform for the production of bacterial cellulose-based engineered living materials with potential applications in biosensing and biocatalysis.

2.1 Introduction

The nascent field of engineered living materials (ELMs) aims to recapitulate desirable properties of natural living biomaterials to create useful new materials using genetically engineered organisms[22,23,52,205]. Existing ELMs exhibit a remarkable range of functions, but often require intensive manual processing steps for purification, functionalization or patterning[25,87,117,120,121,126,141,206–208]. Others make use of the multiple functionalities of living cells by embedding them within man-made hydrogels[157,167,209–212]. However, a long-term goal of ELMs research is to use engineered cells, rationally reprogrammed with DNA, to both make the material and incorporate novel functionalities into it at the same time—thus 'growing' functional biomaterials in situ[23].

Natural living materials often rely on division of labor between specialized cells performing particular functions to achieve such self-assembly. Plant leaves, for example, are self-assembling living materials in which specialized cells are responsible for different traits (Figure 6a). Inspired by this, we sought to develop a microbial ELM that utilized a similar approach, dividing bulk material production and functional modification between co-cultured cell types suited for each specialism and thus enabling complex ELMs to be self-assembled in situ.

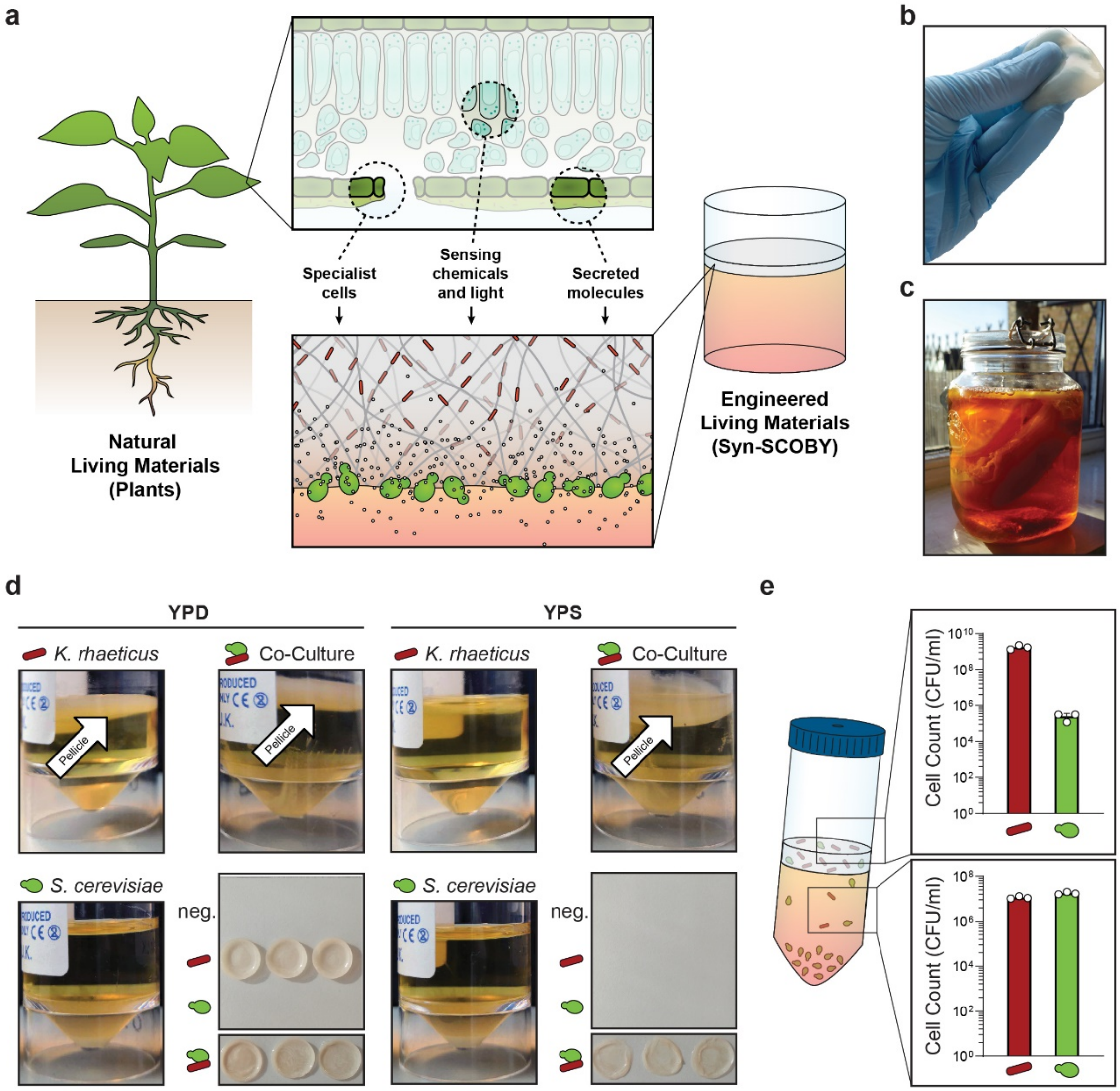

Figure 6 | **Generating Syn-SCOBY co-cultures with *S. cerevisiae* and *K. rhaeticus*. (a)** Schematic showing analogies between natural living materials (plants) and engineered living Syn-SCOBY materials, yeast cells depicted in green and bacteria depicted in red. **(b)** An image of a BC pellicle, a flexible but tough material. **(c)** Home-brewed kombucha tea. Both a large submerged mass of BC from previous rounds of fermentation as well as a newly formed thinner layer at the surface can be seen. **(d)** Images of monocultures and co-cultures of *K. rhaeticus* and *S. cerevisiae* grown in YPS and YPD medium for 3 days. Dense *S. cerevisiae* growth can be seen as a sediment at the base of the culture. *K. rhaeticus* growth results in a thick pellicle layer at the air-water interface (white arrow). **(e)** Cell counts of a co-culture consisting of *K. rhaeticus* Kr RFP and *S. cerevisiae* yWS167, grown in YPS media. Cell counts were determined by plating and counting the numbers of cells present in the two phases of co-cultures—the liquid layer and the pellicle layer. Samples prepared in triplicate, data represent the mean ±1 SD.

Bacterial cellulose (BC) has recently emerged as a promising bulk material for ELM production due to high production yields that achieve >10 grams per liter from just a few days of growth in low cost, simple sugar media[213]. Various species of Gram-negative acetic acid bacteria—particularly members of the *Komagataeibacter* and *Gluconacetobacter* genera—produce high quantities of extracellular cellulose. When grown in shallow trays containing static cultures, they yield continuous BC sheets with large surface areas. Numerous individual glucan chains are first secreted, then bundled into cellulose fibrils. Over several days, a thick floating mat called a pellicle forms, consisting of a network of BC fibrils around embedded BC-producing bacteria. The resulting material (Figure 6b) is a dense network of ribbonlike cellulose fibrils, each ~50 nm wide and up to 9 μm in length, held together tightly by van der Waals forces and hydrogen bonds[214].

The ultrapure nature and high crystallinity of BC afford excellent mechanical properties, with individual nanofibers estimated to have a tensile strength of at least 2 GPa and Young's modulus of ~138 GPa[215,216]. BC has high porosity, high water retention, and a very large surface area. It is both biodegradable and biocompatible and can be made at scale with minimal equipment and low environmental impact and cost. Consequently, BC-based materials have attracted interest for use as surgical and wound dressings, as acoustic diaphragms for headphones and speakers, as battery separators, as additives to cosmetics, and as scaffolds for tissue engineering[217]. Several BC-based materials have been commercially developed for medical and cosmetic applications, for example, as wound-dressings for the treatment of burns and ulcers[218].

Genetic modification of BC-producing bacteria has previously been used to alter BC material properties, for instance, by generating non-native chitin-cellulose[72] and curdlan-cellulose[128] co-polymer materials or optimizing cellulose yields to enable the production of battery separators[219]. Modular genetic toolkits for engineering BC-producing bacteria have also been developed but remain minimal in comparison to those for model organisms[73,129,220,221]. Crucially, there is a lack of genetic tools and knowledge to enable recombinant protein secretion from BC-producing bacteria, and their ability to be reprogrammed to sense external cues is also poor. These factors severely limit the engineerability and versatility of BC-based ELMs.

To create an ELM system that leverages specialist engineered cells among bulk-producer cells, we took inspiration from kombucha tea. Kombucha is a fermented beverage produced by a microbial community commonly referred to as a symbiotic culture of bacteria and yeast (SCOBY) (Figure 6c). SCOBYs typically consist of BC-producing bacteria and at least one species of yeast. Notably, one of the yeast species often found in kombucha fermentation is the yeast model organism *Saccharomyces cerevisiae*[222].

Here we recreate co-cultures of a BC-producing bacterium, *K. rhaeticus*[73], with engineered lab strains of *S. cerevisiae* in order to develop a novel ELM system, which we call a Synthetic SCOBY (Syn-SCOBY). Stable co-cultivation of yeast during the cellulose biofilm production phase provides a host cell that can easily be rationally programmed with DNA for dedicated tasks (Figure 6a). Engineered *S. cerevisiae* act as specialist cells in the system, secreting proteins, sensing chemical and physical signals, and modifying the material properties of surrounding cellulose. In light of the goals of ELMs research, we show that all these functionalities can be achieved in Syn-SCOBY materials that grow and self-assemble in their entirety from only simple growth media in a few days.

2.2 Establishing conditions for stable Syn-SCOBY growth

To introduce yeast as specialist cells within a bacterial culture used for BC material production, we first identified conditions in which *K. rhaeticus* and *S. cerevisiae* can be efficiently co-cultured. This required screening for growth at a range of inoculation ratios and in different growth media (A.1 Notes). An initial screen revealed that *K. rhaeticus* grew poorly in sucrose-containing media compared to glucose-containing media, failing to form a pellicle after 3 days (Figure 6d and A.2 Figure 20). However, co-culturing *K. rhaeticus* with *S. cerevisiae* in the same sucrose media enabled growth and pellicle formation, leading to our Syn-SCOBY co-culture protocol in which BC formation was dependent on the continued presence of the yeast (A.2 Figure 21). Under these conditions, the majority of *K. rhaeticus* cells were found in the pellicle layer, while the majority of *S. cerevisiae* cells were found in the liquid layer (Figure 6e). We characterized a range of other co-culture parameters, including pellicle yields, co-culture stability, cell distribution, and reproducibility (see A.1 Notes and A.2 Figure 22-27). Notably, we provide evidence that the growth enhancement conferred by yeast is based on the secretion of invertase enzyme, which hydrolyses sucrose to monosaccharide sugars that are more efficiently metabolized by the bacteria (A.2 Figure 25).

2.3 Engineering Syn-SCOBY yeast to functionalize BC

Having developed a robust *S. cerevisiae-K. rhaeticus* co-culture, we set out to engineer *S. cerevisiae* to act as specialist cells conferring novel functional properties (Figure 7a). Unlike BC-producing bacteria, yeasts have a high capacity for the secretion of recombinant proteins. Therefore, the presence of yeast in Syn-SCOBY co-cultures offers a route to BC functionalization by engineering S. cerevisiae strains to secrete proteins that form part of grown BC materials (Figure 7b). We assessed this capability with the β-lactam hydrolyzing enzyme TEM1 β-lactamase (BLA). Using the yeast toolkit (YTK) system for modular genetic engineering[223], the BLA catalytic region was cloned downstream of the mating factor alpha (MFα) secretion signal peptide under the control of a strong constitutive promoter to create yeast strain yCG04 (Figure 7c). However, as the pellicle makes up only a part of the co-culture volume, we hypothesized that fusion of a cellulose-binding domain (CBD) to this enzyme might increase the proportion of secreted protein incorporated within the BC layer. Therefore, a second strain (yCG05) was engineered in which a CBD was fused to the C-terminus of the BLA protein (Figure 7c). The 112 amino acid region from the C-terminus of the Cex exoglucanase from *Cellulomonas fimi* (CBDcex)[224] was chosen based on previous work demonstrating its ability to bind BC30. Monocultures of yCG04 and yCG05 were screened for BLA activity using the colorimetric nitrocefin assay (Figure 7d), confirming secretion of active BLA and BLA-CBD, respectively (A.2 Figure 28). Next, co-cultures of wild type, yCG04 or yCG05 *S. cerevisiae* strains with *K. rhaeticus* bacteria were grown, and the resultant BC pellicles were screened for β-lactamase activity. While pellicles grown with wild type yeast showed no BLA activity, clear activity was observed from pellicles co-cultured with BLA-secreting and BLA-CBD-secreting strains (Figure 7e), demonstrating direct BC functionalization. Notably, fusion of the CBD to the enzyme resulted in an increase in observed β-lactamase signal from the BC samples. In addition, BLA-CBD functionalized pellicles appeared to retain catalytic activity more strongly after washing than those with only BLA (A.2 Figure 29). Whether these observations originate from a difference in the number of bound BLA and BLA-CBD proteins in the material requires further exploration.

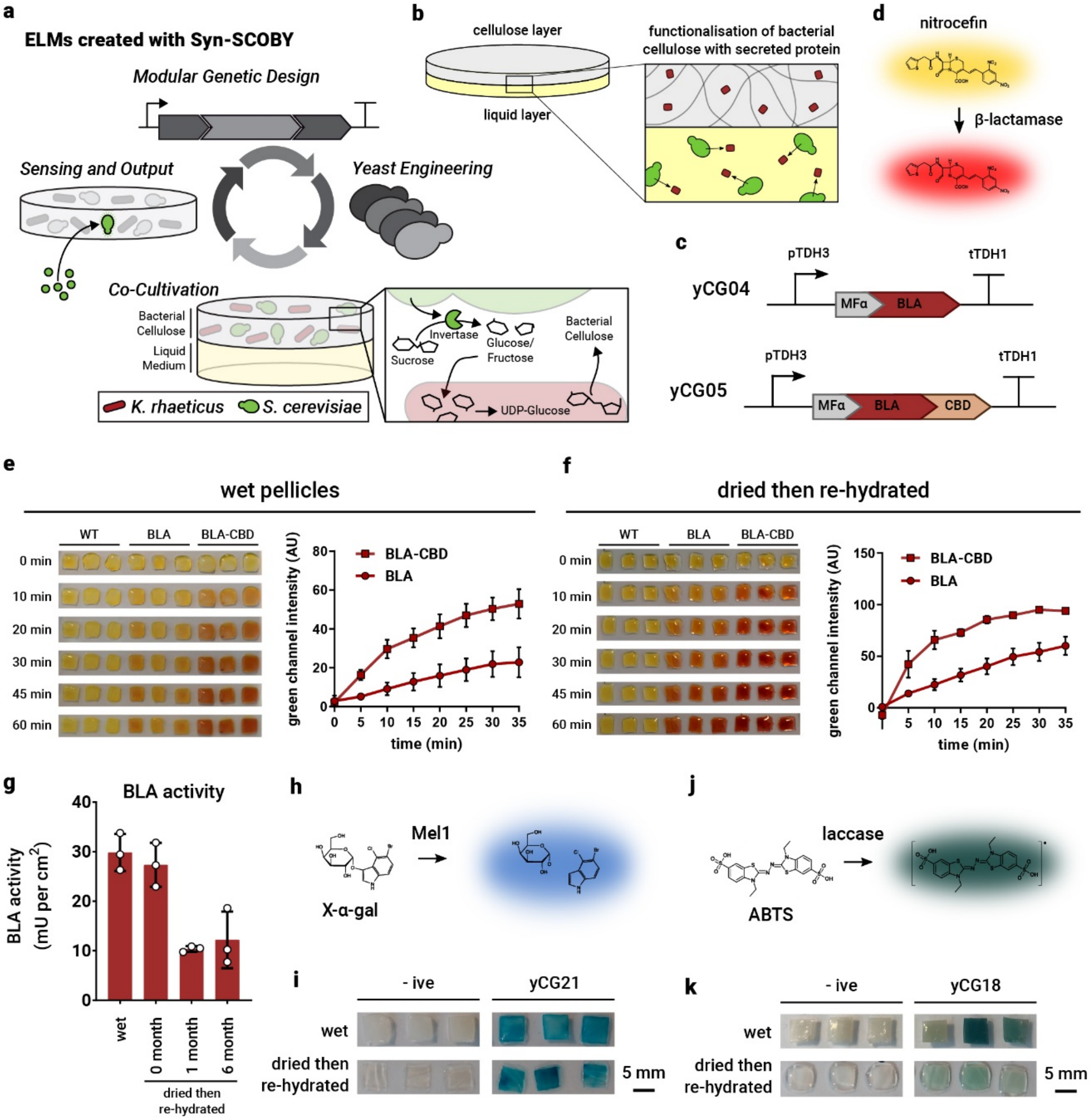

Figure 7 | **Syn-SCOBYs can produce enzyme-functionalized BC materials. (a)** Schematic summary of Syn-SCOBY ELMs. **(b)** Schematic illustrating the concept of functionalization. *S. cerevisiae* cells (green) secrete a protein (red) that incorporates into the BC layer (grey). **(c)** Genetic design of BLA-secreting yeast strains yCG04 (BLA) and yCG05 (BLA-CBD). **(d)** Nitrocefin is converted from a yellow substrate to a red product by β-lactamase. The nitrocefin assay was performed with cut 5x5 mm native wet pellicle samples **(e)** or with dried then re-hydrated pellicle samples **(f)**. In both cases, co-cultures were prepared with *S. cerevisiae* BY4741 (WT), yCG04 (BLA), and yCG05 (BLA-CBD). Images are of pellicles after indicated time points during the assay. The yellow-to-red color change was quantified and plotted. Samples prepared in triplicate; data represent mean ±1 SD. **(g)** Absolute β-lactamase activities were calculated from native hydrated pellicles (wet) and from pellicles dried then re-hydrated after the indicated time periods. Samples presented here are from pellicles grown in co-culture with yCG05. As pellicle liquid volume is altered by drying, β-lactamase activity is represented by enzyme activity units per unit of pellicle area. Samples prepared in triplicate; data represent mean ±1 SD. **(h)** X-α-gal is converted from a colorless substrate to a blue product by Mel1 enzyme. **(i)** The X-α-gal assay was performed with wet and dried then re-hydrated pellicle samples from co-cultures with the GFP-secreting strain yCG01 (-ive) or a strain that secretes Mel1 (yCG21), samples prepared in triplicate. **(j)** ABTS is converted from a colorless substrate to a green product by laccase enzyme. **(k)** The ABTS assay was performed with wet and dried then re-hydrated pellicle samples from co-cultures with the GFP-secreting strain yCG01 (-ive) or a strain that secretes CtLcc1 (yCG18), samples prepared in triplicate.

We then tested whether enzyme-functionalized BC that had been dried and re-hydrated retaining catalytic activity. Pellicles produced by co-culturing were dried to create thin, paper-like materials (A.2 Figure 30) and later rehydrated and assayed for β-lactamase activity. Rehydrated pellicles functionalized with both BLA and BLA-CBD demonstrated clear activity (Figure 7f). For absolute quantification of BLA activity, assays were run with pellicles derived from co-cultures with wild-type (WT) yeast spiked with known concentrations of commercial BLA enzyme to create standard curves (A.2 Figure 31). This revealed that the drying process itself had little effect on the BLA activity of the material: 29.8 ±3.7 mU/cm2 before drying and 27.3 ±4.4 mU/cm2 after (Figure 7g). Identical assays were performed following storage of materials for 1 month or 6 months at room temperature without desiccant. After storage, enzymatic activity was retained, although reduced to one-third the original level (Figure 7g). Overall, these experiments show that functionalized materials can be grown and stored at room temperature, retaining their activity for later rehydration and deployment.

To demonstrate the generalizability of our approach, we generated BC functionalized with two other enzymes: an α–galactosidase (Mel1) and a laccase from *Coriolopsis troggi* (CtLcc1)[225] (see A.1 Notes and A.2 Figure 32 and 33). Yeast secreting these enzymes were co-cultured with *K. rhaeticus* and the resultant pellicles assayed for enzyme activity. Laccase and α–galactosidase activities were detected in native, wet pellicles and were retained after drying and rehydration (Figure 7i and Figure 7k).

The Syn-SCOBY approach enables the self-assembly of enzyme-functionalized BC materials grown under mild conditions from simple raw materials. Importantly, these materials retain activity following drying and rehydration after storage under ambient conditions, suggesting this approach could be applied to the production of immobilized enzyme materials used in various industrial processes (see A.1 Notes).

2.4 Modifying BC physical properties via enzyme secretion

The presence of living cells within ELMs would allow cells to be programmed to modify the physical properties of the material as it is grown or used. To enable this, we first developed a method that increases the number of yeast cells incorporated into the BC pellicle by ~340-fold through tuning the density of the Syn-SCOBY culture medium with an inert culture medium additive called OptiPrep (see A.1 Notes and A.2 Figure 34-41).

Using this protocol, we engineered cellulase secretion from yeast to attempt to modify the bulk physical properties of the Syn-SCOBY BC. We constructed a yeast strain, yCelMix, in which cellobiohydrolases (CBH1 and CBH2), endoglucanase (EGL2), β-glucosidase (BGL1), and lytic polysaccharide monooxygenases (LPMO) are optimized to be secreted simultaneously for synergistic cellulose degradation, as described previously[226,227] (Figure 8a-b and A.2 Figure 42). Co-cultures of *K. rhaeticus* and yCelMix yeast formed pellicles after two days, albeit with slightly decreased dried weight (Figure 8c), indicating that rates of cellulase secretion and action were slower than the rate of BC biosynthesis. Extending incubation to five days did not further reduce the BC mass, potentially due to the limited diffusion of enzymes, low pH, local accumulation of reaction products, or cellulase deactivation at the air-liquid interface in static culture[228]. Cellulase secretion did not enhance leakage of yeast cells from pellicles but resulted in a smaller total surface area and changes in the fiber network packing (see A.1 Notes and A.2 Figure 43-45).

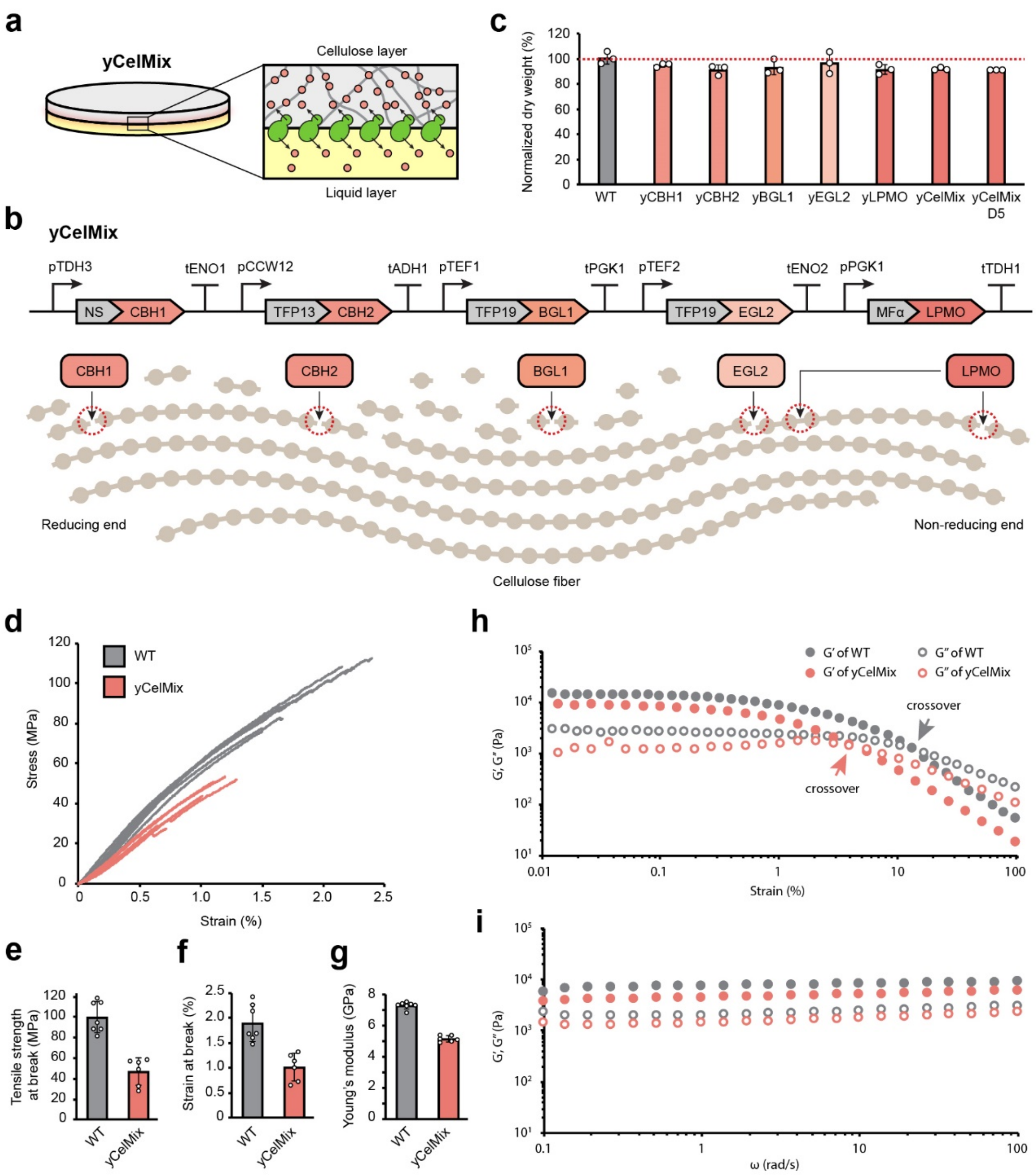

Figure 8 | **Modifying BC physical material properties. (a)** Schematic showing yCelMix cells secreting cellulases into the surrounding microenvironment from the bottom surface of the pellicle. **(b)** Schematic illustrating architecture of yCelMix cellulase secretion strain. Expression of each cellulase is controlled by a distinct combination of strong promoter and terminator to prevent homologous recombination. CBH1 (cellobiohydrolase from *Chaetomium thermophilum*), CBH2 (cellobiohydrolase from *Chrysosporium lucknowense*), BGL1 (β-glucosidase from *Saccharomycopsis fibuligera*), and EGL2 (endoglucanase from *Trichoderma reesei*) are fused with optimal secretion signals as determined by Lee *et al.*[227] while LPMO (LPMO9H from *Podospora anserine*)[226] was fused with *S. cerevisiae* MFα signal peptide. Signal peptides are colored grey (NS: native signal sequence; TFP13: translational fusion partner 13; TFP19: translational fusion partner 19). Cleavage sites for the cellulases on cellulose polymer are marked as red circles. Each circle represents a monosaccharide unit in the cellulose polymer. **(c)** Normalized pellicle dried weight after 2-day growth of *K. rhaeticus* with different cellulase-secreting *S. cerevisiae*. Red line is weight of wildtype (WT) yeast pellice. yCelMix D5 is after 5-day growth. Samples prepared in triplicate, data represent mean ±1 SD. **(d)** Stress-strain curves of dried WT and yCelMix pellicles. Samples are from 7 WT and 6 yCelMix co-cultures. **(e-g)** Tensile strength at break, strain at break, and Young's modulus calculated from the data in **(d)**. Data represent mean ±1 SD. **(h, i)** Rheological properties of WT and yCelMix pellicles measured by **(h)** strain sweep at 1 rad/s and **(i)** frequency sweep at 1% strain. Arrows in **(i)** indicate the crossover of the storage modulus (G', elastic deformation) and loss modulus (G", viscous deformation).

Although BC yield was not reduced by cellulase secretion, the mechanical properties of the pellicles were altered. Stress-strain curves from tensile tests demonstrated a clear difference between wild-type (WT) pellicle and yCelMix pellicle (Figure 8d). Specifically, while both were brittle (as determined by fracture strength), the yCelMix pellicle could only sustain 45.7 MPa while the WT pellicle can bear 98.3 MPa of stress before fracturing (Figure 8e). The yCelMix pellicle could also only be stretched to half the length that the WT pellicle could be elongated to before breaking (Figure 8f). Furthermore, secreted cellulases reduced the stiffness of the matrix, lowering the Young's modulus from 7.2 GPa (WT) to 5.1 GPa (yCelMix) (Figure 8g and A.2 Figure 46). Although the underlying mechanisms by which these enzymes modify the material properties require further investigation, our results are consistent with others who report that the continuity of the cellulose fibrils and integrity of network structure are essential for the strength and stiffness of BC materials[229,230].

The weakening of the microstructure in the yCelMix pellicle was also reflected by its rheological properties. In strain sweep experiments (Figure 8h), both pellicles showed gel-like behavior at low strain, as G' always dominates over G". The G' and G" of yCelMix pellicle were both lower than those of WT pellicles, confirming that cellulases reduced the stiffness of the BC material (Figure 8h) in a frequency-independent fashion (Figure 8i). As the applied strain increased beyond the G' G" crossover point, where microcracks accumulated and major rupture appeared, the pellicles switched to a viscoelastic liquid and started to flow. Notably, yCelMix pellicle had an earlier onset of crossover, indicating a faster breakdown of network structure in the matrix. The more pronounced G" maximum in the yCelMix pellicle (Figure 8i) also demonstrates that deformation energy was converted into friction heat from the free broken fibrils near the microcracks, which originated from a disintegrated and weaker cellulose network. Our results suggest cellulases secreted from the yeast can weaken the mechanical and viscoelastic properties of BC materials, complementing recent studies showing carbohydrate binding domain (CBD) protein additives can enhance the strength of cellulosic materials[231,232].

2.5 Engineering living materials to sense and respond

S. cerevisiae strains are routinely engineered in synthetic biology as biosensors that sense external stimuli and respond with changes in gene expression. Our modular co-culture Syn-SCOBY approach enables easy incorporation of biosensor yeast strains into grown BC materials (Figure 9a). We selected a chemically inducible system where the estrogen steroid hormone β-estradiol (BED) triggers activation of transcription from a target promoter[233,234]. Specifically, we used an *S. cerevisiae* strain (yGPH093) expressing the BED-activated synthetic transcription factor Z_3EV and a GFP reporter under the control of the Z_3EV-responsive promoter (Figure 9b)[235]. Pellicles produced by *K. rhaeticus*-yGPH093 co-cultures generated a strong GFP signal when exposed to exogenous BED (Figure 9c), demonstrating that the Syn-SCOBY approach produces living BC materials that sense-and-respond to environmental stimuli.

To test the viability of Syn-SCOBY living materials after drying and long-term storage (Figure 9d), pellicles containing a GFP-expressing yeast were grown from co-culture, dried, and stored at room temperature. They were then degraded enzymatically and viable cell counts of *S. cerevisiae* determined by plating. Although drying resulted in a substantial loss of viable yeast within the BC, viable cells could be recovered even after 1 month of storage (A.2 Figure 47).

To demonstrate that the remaining viable cells were still sufficient for biosensor materials to remain functional, pellicles grown with yGPH093 were dried, stored, and revived by incubating in fresh media for 24 hours in the presence or absence of BED. Rehydrated pellicles containing yGPH093 once again yielded a clear GFP signal in the presence of BED (Figure 9e), even after ambient storage of dried pellicles for 4 months (Figure 9f). While these sense-and-response functions require the addition of growth media, diverse sample types could be used by supplementing with concentrated nutrient stocks. A similar approach has previously enabled *S. cerevisiae* biosensor strains to function in blood, urine, and soil[155]. As a demonstration of further biosensor capabilities, we grew and verified a BC sensor where engineered yeasts sense a protein via a G protein coupled receptor (GPCR) (see A.1 Notes and A.2 Figure 48).

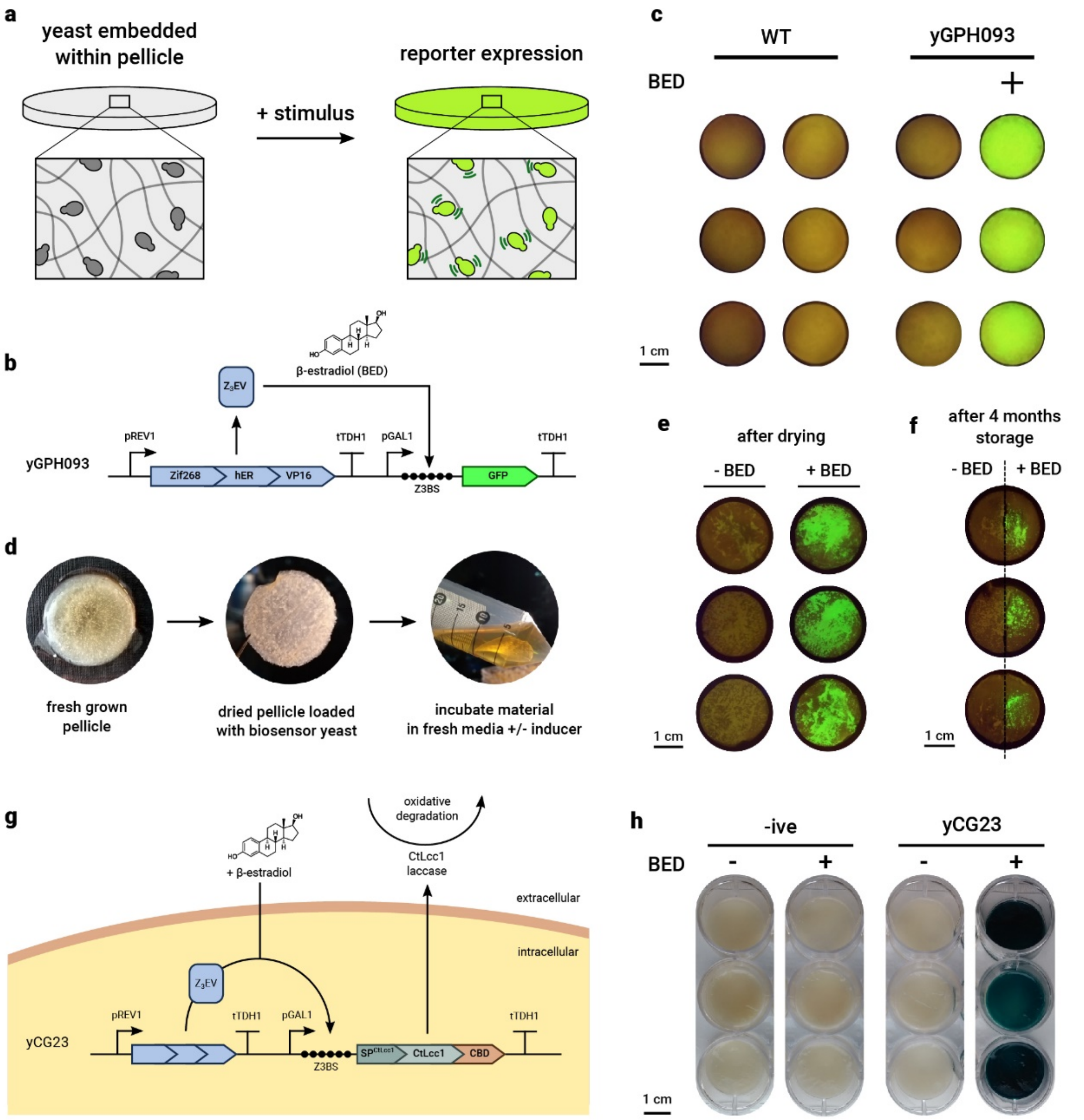

Figure 9 | **Syn-SCOBY materials can sense-and-respond. (a)** Schematic illustrating sense-and-respond pellicle function. Pellicles were grown containing engineered *S. cerevisiae* capable of detecting environmental stimuli and responding by gene expression. **(b)** Schematic showing genetic yGPH093 circuit. The engineered *S. cerevisiae* (yGPH093) senses the presence of the chemical inducer β-estradiol (BED) and in response, produces the reporter protein GFP. The Z_3EV synthetic transcription factor is expressed from constitutive promoter pREV1. On addition of β-estradiol Z_3EV binds Z_3EV binding sites (Z3BSs) in the pGAL1 promoter activating GFP expression. **(c)** Testing biosensor pellicles. Pellicles with either BY4741 (WT) or β-estradiol (BED) responsive (yGPH093) yeast incorporated within the BC matrix were grown. Triplicate samples were incubated with or without BED and imaged for GFP fluorescence by transilluminator after 24 h. **(d)** Pellicles into which *S. cerevisiae* have been incorporated can be dried, stored, and then revived by incubating in fresh media with or without inducer. Dried pellicles into which yGPH093 was incorporated, were incubated in fresh media in the presence or absence of BED following ambient storage for 1 day **(e)** or 4 months **(f)**. After 24 h, pellicles were imaged for GFP fluorescence by transilluminator. Samples prepared in triplicate. **(g)** Schematic illustrating yCG23 construct design. Similar to yGPH093, yCG23 enables BED-inducible expression of secreted CtLcc1 laccase. Extracellular laccases can then be used to oxidize a broad range of substrates, enabling the degradation of environmental pollutants. **(h)** Native wet pellicles from YPS-OptiPrep co-cultures of the GFP-secreting yCG01 strain (-ive) and yCG23 were harvested, washed, and inoculated into fresh medium with or without BED. After 24 h growth, pellicles were again harvested and washed, and assayed for laccase activity using the colorimetric ABTS assay. Samples prepared in triplicate.

A goal of ELMs research is to generate materials that are dynamic, adapting in response to environmental changes. To demonstrate a step towards this, we linked yeast biosensors to the production of a functional response. Since laccase enzymes have been previously shown to degrade BED[236], we engineered yeast strain yCG23 to secrete laccase from the BED-inducible promoter (Figure 9g and A.2 Figure 49). Co-culture of *K. rhaeticus* and yCG23 produced a BC-based living material that could both detect the presence of BED and in response secrete active laccase enzyme (Fig. 4h). Notably, BED is an important environmental pollutant, with potential effects on exposed aquatic species and humans[237,238]. The Syn-SCOBY approach can, therefore, be used to grow materials programmed to sense changes in their environment and respond accordingly.

2.6 Spatial patterning of living materials by optogenetics

As an alternative to sensing chemical inputs, we used optogenetics to develop light-responsive BC-based ELMs. We implemented and optimized a blue light sensing system in *S. cerevisiae* based on the CRY2/CIB transcription system[239] (see A.1 Notes and A.2 Figure 50 and 51a). The light-inducible promoter was engineered to trigger the expression of NanoLuc, a luciferase reporter enzyme. Two versions were designed, a yNSurface strain that displays NanoLuc on the yeast cell surface, and yNCellulose which secretes a NanoLuc-CBD version into the culture to bind to BC (Figure 10a and b).

To demonstrate that Syn-SCOBY pellicles can be engineered to respond to an optical input, *K. rhaeticus* was co-cultured with each strain, with or without exposure to white light. After 3 days of incubation in light, BC pellicles grown from both co-cultures formed material layers that exhibited high bioluminescence. Equivalent pellicles grown in the dark for 3 days showed nearly zero luciferase activity (Figure 10c). The yNCellulose pellicle exhibited evenly distributed NanoLuc activity across the material surface, whereas the yNSurface pellicle had localized foci, corresponding to yeast distribution. This demonstrates that the local distribution of protein functionalization in BC materials can be genetically programmed into the co-cultured yeast.

We further explored the responsiveness of these pellicles to light patterns created by masking and projecting. With Syn-SCOBYs containing either yNSurface or yNCellulose yeast, we grew 'living films' in the dark for 3 days before further growth with light exposure (Figure 10d). With light patterning by masking, both BC pellicles exhibited bright foci within their patterns, likely due to insufficient time for NanoLuc to diffuse away from yeast in this experiment. When the pattern was instead projected, the projected patterns were closely reproduced in the final luciferase activity output (Figure 10e). Here, yNSurface produced a sharper pattern compared with yNCellulose, which is expected due to the ability of NanoLuc to diffuse in the latter case.

We anticipate that this system could be readily expandable to multicolor optogenetics by further incorporating alternative light-based dimerizing systems[239] and linking these to other enzymatic outputs, enabling spatially segregated enzymatic cascade in BC materials.

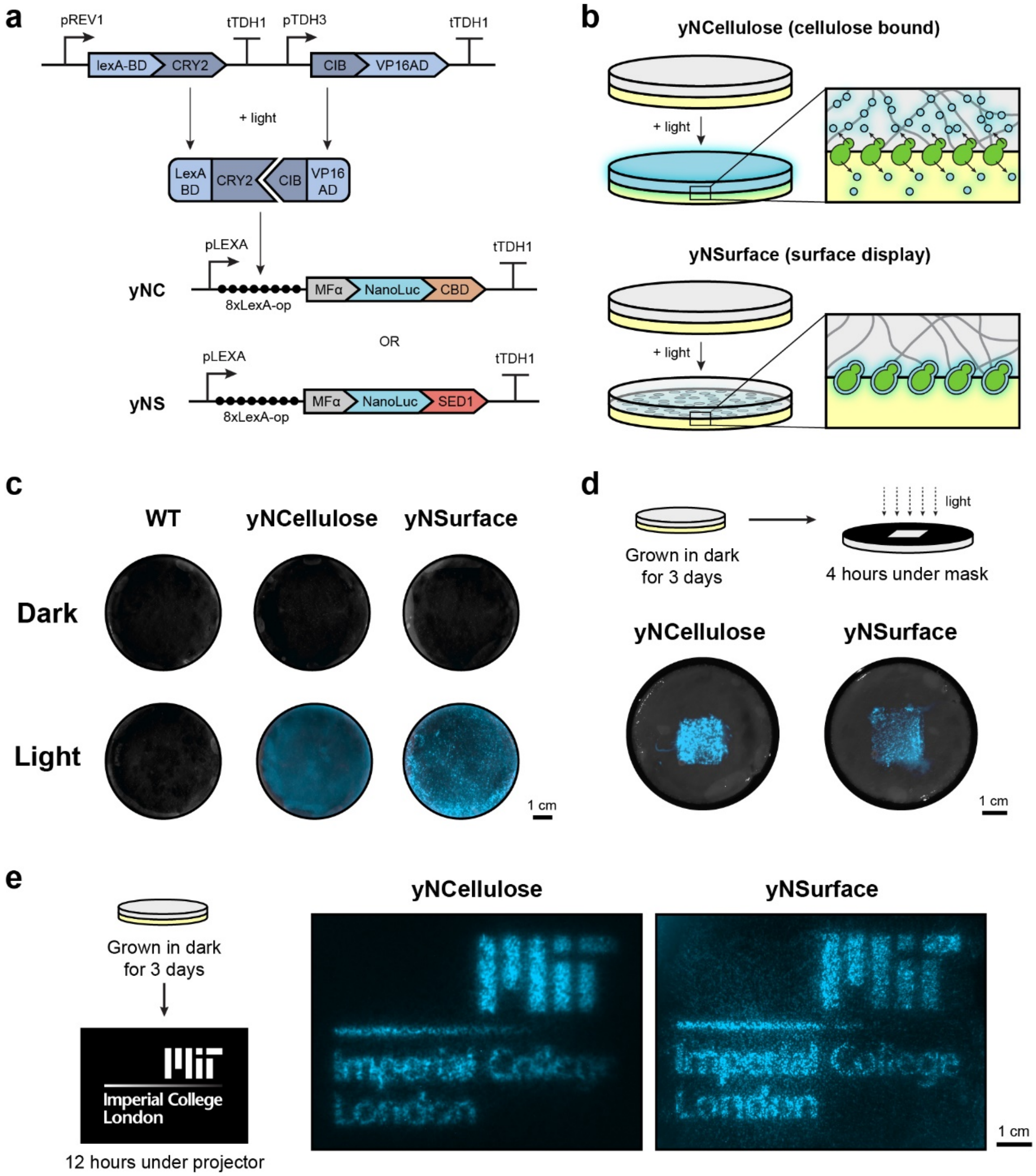

Figure 10 | **Optical patterning of enzymatically functionalized BC materials. (a)** Schematic showing the optogenetic circuit. Engineered *S. cerevisiae* strains (yNCellulose and yNSurface) sense blue light and in response express the reporter protein NanoLuc. The LexA-CRY2 and VP16-CIB synthetic transcription factors are expressed from constitutive promoters pREV1 and pTDH3, respectively. Upon exposure to light, the dimer binds LexA-binding-sites (8xLexA-op) in the pLEXA promoter, activating transcription of the NanoLuc gene. **(b)** Schematic illustrating the two modes of functionalisation. The yNCellulose strain secrete NanoLuc-CBD which diffuse into and eventually binds the surrounding cellulose matrix, while the yNSurface strain display NanoLuc-

SED1 on the yeast cell surface. **(c)** The pellicles grown in dark or light after 3 days. **(d)** yNCellulose and yNSurface pellicles were grown in dark and then exposed to light under a mask for 4 hours. Pellicles were flipped so that the lower surface, where the majority of yeast cells are localized, was closest to the light source. NanoLuc substrate was applied in the end for visualization of the pattern created by masking. **(e)** yNCellulose and yNSurface pellicles grown in the dark were exposed to a complicated pattern created by a projector. NanoLuc substrate was applied in the end for visualization of the pattern created by masking.

2.7 Discussion

BC materials are biocompatible, produced by growth under mild conditions with simple culture media, and made in high yield at little cost from microbes already commonly used in both the food and healthcare industries. As such, BC is a promising biological material for the development of ELMs. Our Syn-SCOBY approach represents a significant improvement in the engineerability of BC, bringing many potential applications into scope.

The functionalized BC materials we generated here could be applied to the degradation of environmental pollutants such as β-lactam antibiotics or estrogen hormones present in wastewater streams. An advantage of our approach is that secreted enzymes functionalized the material as it forms, so separate steps for protein purification and enzyme-material chemical bonding are not needed in the manufacturing process. This approach is also highly adaptable; numerous other protein targets—enzymes, binding or adhesion proteins, or even structural proteins—could be secreted from *S. cerevisiae* to add desired properties to BC. Importantly, the feasibility of this will depend on the secretion yield for a given protein—which may be lower under static growth conditions compared to shake-flask or bioreactor growth—as well as the stability of the protein outside the cell or after any required sterilization procedures.

Our approach also offers a fast, simple method to generate biosensor materials. Sense-and-respond ELMs could find application in a variety of contexts, in biosensing, bioremediation, or creation of patterned materials. Again, numerous existing *S. cerevisiae* biosensor strains able to detect pathogens[155], environmental pollutants[240], or biomarkers[241] could be plugged into the Syn-SCOBY approach.

Organisms are remarkable material-producing systems, capable of self-assembling complex materials with diverse chemical and physical properties starting only from simple feedstocks. Simultaneously, living cells within these materials control their morphology over multiple length scales and remodel material properties in response to environmental cues. Synthetic material systems capable of recreating all of these behaviors do not exist. As such, the ability to genetically control the process of material self-assembly with the same level of sophistication seen in natural biological materials could revolutionize the manufacture of products for use in numerous arenas of human life and society. The Syn-SCOBY approach showcases the viability of microbial co-cultures combined with synthetic biology tools to design, grow, and test functional living materials.

Chapter 3

Dual-Mode Biocontainment Strategies for Engineered Organisms in Hybrid Living Materials

Genetically modified microorganisms (GMMs) can enable a wide range of important applications, including environmental sensing, precision therapeutics, and responsive materials. However, the containment of GMMs to prevent environmental escape and satisfy regulatory requirements is a bottleneck for real-world use. While biochemical strategies have been developed to restrict unwanted growth and replication of GMMs in the environment, there is a need for deployable physical containment technologies to achieve redundant, multilayered, and robust containment. In addition, form factors that enable easy retrieval would be useful for environmental sensing. To address this challenge, we developed a hydrogel-based encapsulation system for GMMs that incorporates a biocompatible multilayer tough shell and an alginate-based core. This DEployable Physical COntainment Strategy (DEPCOS) allows no detectable GMM escape, bacteria to be protected against environmental insults, including antibiotics and low pH, controllable lifespan, and easy retrieval of genetically recoded bacteria. To highlight the versatility of a DEPCOS, we demonstrated that robustly encapsulated cells can execute useful functions, including performing cell-cell communication with other encapsulated bacteria and sensing heavy metals in water samples from the Charles River. We envisioned that our multilayered physical and chemical containment strategy will facilitate the realization of a wide range of real-world applications for 'living' biosensors.

3.1 Introduction

Genetically modified microorganisms (GMMs) are being developed and used for bioremediation[242], agriculture[243], and the production of biofuels[244] and pharmaceuticals[245]. However, the potential for GMMs to escape into the environment has created a need for strategies to contain these organisms and prevent their uncontrolled release[246–249].

Chemical biocontainment utilizes chemical barriers to impede the escape and survival of microorganisms in the environment[246–248]. Several strategies have been developed for the chemical containment of GMMs[250–253]. For example, GMMs can carry gene circuits that require specific chemical combinations to prevent cell death by inhibiting toxin production[254], rescue cells from being killed by a constitutively expressed toxin by producing the corresponding antitoxin[255], or multi-layered safeguards that modulate the expression of essential genes and toxins[256]. In addition, microbes can be engineered with auxotrophies so that they require synthetic amino acids for survival[257,258]. However, chemical strategies alone are imperfect for containment because mutation rates of GMMs, while low, are never zero, thus resulting in escape mutants. This implies that the number of chemically contained GMMs that can be deployed is intrinsically limited by its mutation rate[258]. Thus, it would be beneficial to combine biological containment strategies and physical encapsulation such that functional redundancy further reduces any chance of inadvertent escape.

To address this challenge, we created a DEployable Physical COntainment Strategy (DEPCOS) that prevents GMM escape while providing a tunable protective environment in which GMMs can execute engineered functions. DEPCOS erects a physical barrier to prevent GMMs from escaping into their surroundings, limits horizontal gene transfer between GMMs and natural species in the environment and allows for easy retrieval of bacterial communities.

Hydrogels are desirable materials for encapsulating living cells as they provide an aqueous environment that can be infused with nutrients, allowing for cell growth[259,260] and sensing[261], while also protecting against environmental hazards[262]. Alginate forms hydrogels in the presence of di-cationic solutions (e.g., Ca^{2+}, Ba^{2+}) and has been used in various biomedical applications[263–265] because of its low cost, negligible cytotoxicity, and mild gelation conditions. However, weak mechanical properties and susceptibility to multiple chemical conditions (such as low pH, citrate, and phosphate) make alginate, as well as other traditional hydrogels, poor solutions for robust physical containment when used on their own[266–268].

Core-shell designs that include an alginate core and a polymer-based protective shell have emerged as a potential design for alginate-based microbial biosensors[267,269]. Nonetheless, there is a major need for a mechanically tough shell that is also highly permeable to analytes for sensing. Our DEPCOS design for bacterial encapsulation consists of two parts: 1) an alginate-based hydrogel core and 2) a tough hydrogel shell (Figure 11) that combines both a stretchy polymer network (polyacrylamide) and an energy dissipation network (alginate, through the unzipping of ionic crosslinking between polymer chains)[270]. This shell material is extremely tough and resistant to fracture yet retains permeability for small molecules[157]. Herein, we test the biocompatibility of this hydrogel and further expand upon its physical characterization for core-shell particle form factors.

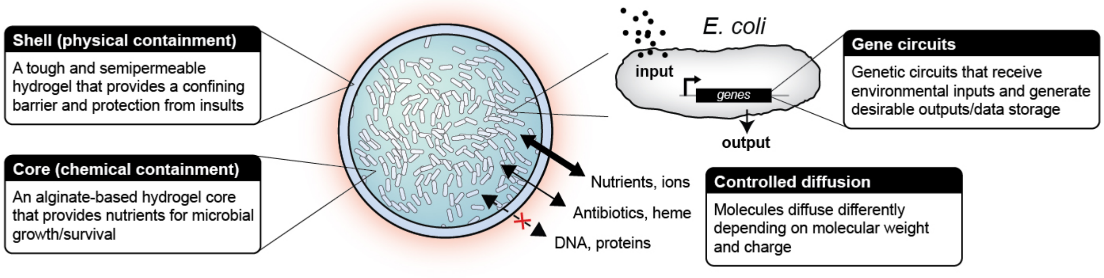

Shell (physical containment)
A tough and semipermeable hydrogel that provides a confining barrier and protection from insults

Core (chemical containment)
An alginate-based hydrogel core that provides nutrients for microbial growth/survival

Gene circuits
Genetic circuits that receive environmental inputs and generate desirable outputs/data storage

Controlled diffusion
Molecules diffuse differently depending on molecular weight and charge

Figure 11 | Schematic of the DEPCOS platform. The DEployable Physical COntainment Strategy (DEPCOS) platform provides secure biocontainment by using a core-shell hydrogel design. The key components and their features are presented in the textboxes.

3.2 Manufacturing the DEPCOS hydrogel beads

To incorporate living cells into the particle core, liquid cultures of *E. coli* were mixed with alginate in 50 μl or 100 μl droplets that were crosslinked with calcium ions to form spheres. The cell-containing alginate hydrogel was easily shaped by a mold or cut into different geometries (B.1 Figure 52). Cores were then coated with the tough polyacrylamide-alginate hydrogel layer[270] (Figure 12). In our core-shell system, the alginate core is pre-loaded with nutrients to support growth, while the hydrogel shell provides mechanical protection for the entire bead. For downstream analyses after deployment, cells can easily be retrieved from the beads by removing the shell with a razor blade and homogenizing the core (B.1 Figure 53). Due to the observed toxicity of the chemical crosslinkers (B.1 Figure 54), a 12-hour outgrowth step was performed to replenish the CFU count before the following experiments (B.1 Figure 55).

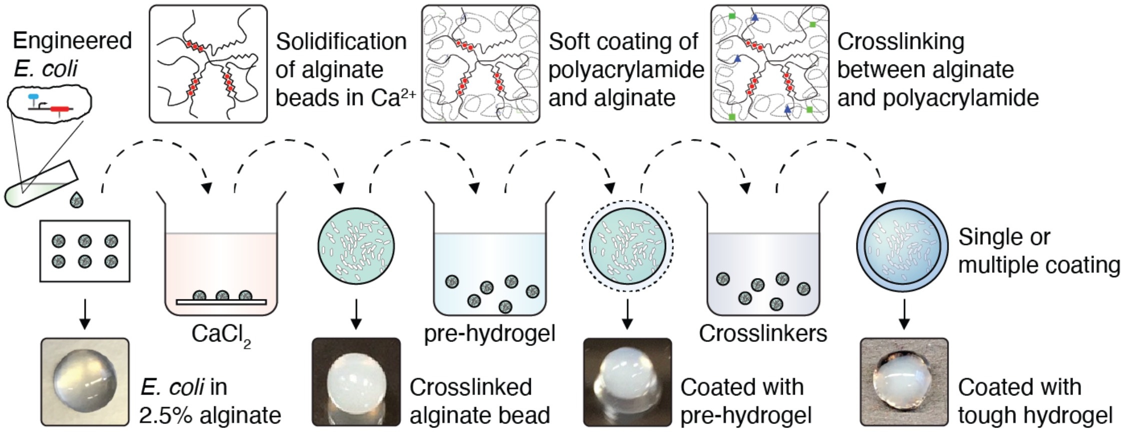

Figure 12 | **Cell encapsulation in tough hydrogel capsules.** The process of core-shell encapsulation of cells. Droplets of 2.5% alginate with engineered E. coli were crosslinked in a calcium solution to form the soft core of the beads, which were then coated with a layer of alginate/polyacrylamide to form a tough hydrogel shell. The process can be repeated to achieve multiple coatings.

3.3 Tough hydrogel shell provides robust physical containment

We hypothesized that the tough hydrogel layer would serve as a containment mechanism because its pore size (5-50 nm) is too small for *E. coli* to penetrate[271]. To test this hypothesis, we measured the containment efficiency of hydrogel beads by incubating *E. coli*-encapsulated beads at the optimal temperature for bacterial growth (37°C) with shaking. Specifically, we encapsulated a concentration of ~10^9 bacteria/mL in each bead. Beads lacking a tough shell allowed bacteria to escape into the surrounding media and to grow to high densities after overnight incubation, whereas there was no physical escape of bacteria from coated beads even after 72 hours of incubation (Figure 13a and B.1 Figure 56). In this assay, we plated all of the media (5 mL) surrounding the beads, with a lower limit of detection (LLOD) of 1 CFU in 5 mL. Furthermore, the tough hydrogel shell maintained zero escape under physical insult such as prolonged shaking at 200 rpm, outperforming alginate and agarose, two common coating materials for core-shell cell encapsulation (B.1 Figure 57).

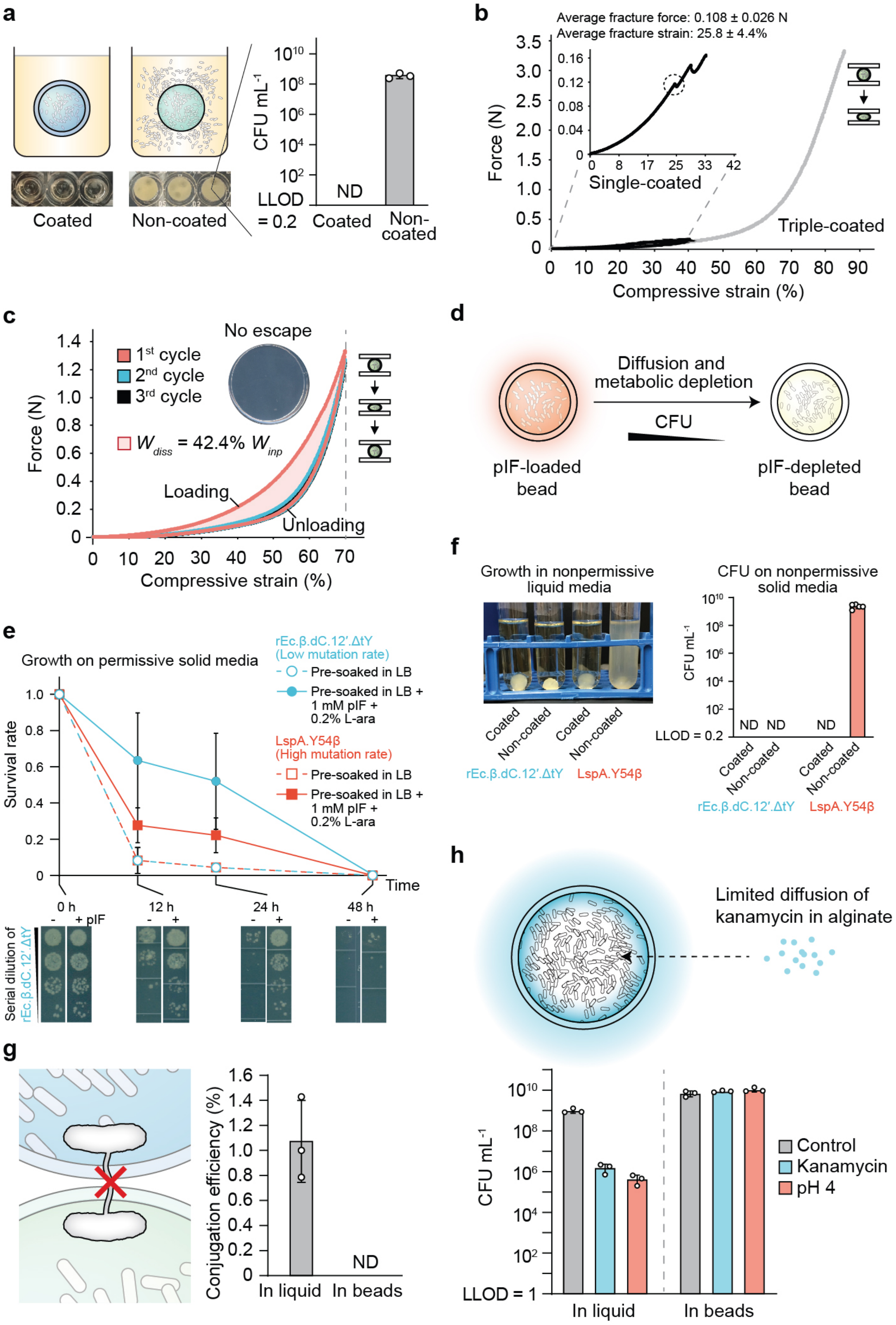
a
Coated
Non-coated
CFU mL^{-1}
10^{10}
10^{8}
10^{6}
10^{4}
10^{2}
LLOD = 0.2
ND
Coated
Non-coated
b
Average fracture force: 0.108 ± 0.026 N
Average fracture strain: 25.8 ± 4.4%
Force (N)
Compressive strain (%)
Single-coated
Triple-coated
3.5
3.0
2.5
2.0
1.5
1.0
0.5
0
0.16
0.12
0.08
0.04
0
8
17
25
33
42
10
20
30
40
50
60
70
80
90
c
No escape
1st cycle
2nd cycle
3rd cycle
W_{diss} = 42.4% W_{inp}
Loading
Unloading
Force (N)
Compressive strain (%)
1.4
1.2
1.0
0.8
0.6
0.4
0.2
0
0
10
20
30
40
50
60
70
d
Diffusion and metabolic depletion
CFU
pIF-loaded bead
pIF-depleted bead
e
Growth on permissive solid media
rEc.β.dC.12′.ΔtY (Low mutation rate)
Pre-soaked in LB
Pre-soaked in LB + 1 mM pIF + 0.2% L-ara
LspA.Y54β (High mutation rate)
Pre-soaked in LB
Pre-soaked in LB + 1 mM pIF + 0.2% L-ara
Survival rate
1.0
0.8
0.6
0.4
0.2
0
Time
0 h
12 h
24 h
48 h
- + pIF
Serial dilution of rEc.β.dC.12′.ΔtY
f
Growth in nonpermissive liquid media
Coated
Non-coated
Coated
Non-coated
rEc.β.dC.12′.ΔtY
LspA.Y54β
CFU on nonpermissive solid media
CFU mL^{-1}
10^{10}
10^{8}
10^{6}
10^{4}
10^{2}
LLOD = 0.2
ND
ND
ND
Coated
Non-coated
Coated
Non-coated
rEc.β.dC.12′.ΔtY
LspA.Y54β
g
Conjugation efficiency (%)
1.6
1.4
1.2
1.0
0.8
0.6
0.4
0.2
0
ND
In liquid
In beads
h
Limited diffusion of kanamycin in alginate
CFU mL^{-1}
10^{10}
10^{8}
10^{6}
10^{4}
10^{2}
LLOD = 1
Control
Kanamycin
pH 4
In liquid
In beads

Figure 13 | **Combining chemical and physical strategies for optimal biocontainment. (a)** Encapsulated bacteria escaped from non-coated beads at high rates but did not escape from tough-hydrogel-coated beads at detectable levels after 72h. Inset shows media in which non-coated and coated bead were grown for 24h (lower limit of detection (LLOD) = 1 CFU / 5 mL). ND = not detectable. Samples prepared in triplicate; data represent the mean ±1 SD. **(b)** Typical force-displacement curves of single-layer tough-hydrogel-coated beads subjected to 40% (black) compressive strain and triple-coated beads subjected to compression up to 85% (gray) compression. Inset zooms in on the single-coated bead stress-strain curve. The average maximum strain and force before fracture for the single-layer coating were 25.8 % and 0.108 N, respectively. Triple-coated beads showed no fracture under compression. Samples prepared in n = 14. **(c)** Cyclic compression of triple-layer coated beads showed hysteresis in the stress-strain curve between the first and second cycles due to plastic deformation. Work dissipated W_{diss} in the first cycle was calculated as 42.4% of the total work Win. Stress-strain curves are representative of at least 6 independent experiments. Inset shows there was no escape: plating the surrounding media of a bead after cyclic compression yielded no colonies. Samples prepared in triplicate. **(d)** Schematic of combining chemical and physical biocontainment strategies. The number of viable cells in the beads decreases as p-iodo-l-phenylalanine (pIF) in permissive media is consumed or diffuses away. **(e)** Comparison of cell survival in beads between two genomically recoded organism (GRO) strains with different containment efficiencies. Survival rate calculated by the number of encapsulated GRO in tough-hydrogel beads that were pre-soaked in permissive media (lysogeny broth (LB) + 1 mM pIF + 0.2% L-ara) (closed circles and solid lines) versus encapsulated GRO in tough-hydrogel beads that were pre-soaked in nonpermissive media (LB only) (open circles and dashed lines) before incubation of the beads in LB. Survival rates were calculated by normalizing colony forming units (CFU) from samples inside the beads, plated on permissive solid media at each time point to CFU at 0 h. Dilution series of the rEc. β .dC.12'. Δ tY at different incubation time points are shown at the bottom. Samples prepared in triplicate; data represent the mean ±1 SD. **(f)** Left: Escape of GROs into 5 mL of nonpermissive media (LB only) surrounding the coated versus non-coated beads containing the GROs after shaking the tough-hydrogel beads at 200 rpm for 3 days. Right: The surrounding media was plated on nonpermissive solid media in order to obtain CFU counts (ND: not detectable with LLOD = 1 CFU/5 mL). Samples prepared in n = 5, data represent the mean ±1 SD. **(g)** The tough hydrogel shell prevents horizontal gene transfer by direct cell-to-cell conjugation. Conjugation efficiency is calculated as the ratio of recipient strain that acquired the F' plasmid over the total number of recipient cells in media. ND = not detectable. Samples prepared in triplicate; data represent the mean ±1 SD. **(h)** Survival of bacteria after subjecting liquid bacterial cultures or bacteria in tough-hydrogel-coated beads to environmental challenges such as antibiotics (30 µg/mL kanamycin for 2 hours), low pH (pH 4 for 4 hours), and untreated controls (LLOD = 200 CFU/mL). Samples prepared in triplicate; data represent the mean ±1 SD.

Next, we used compression testing to characterize the mechanical robustness of the hydrogel-bacteria beads (radius = 3-4 mm) with varying shell layers. We found that beads with a single-layer shell coating

(B.1 Figure 58) could sustain 25% compressive strains and forces up to ~0.1 N before the fracture occurred (Figure 13b and B.1 Figure 59a). We further improved the mechanical properties of the beads by creating multilayer shells via repetitive coating. With beads that were coated with three layers of tough polyacrylamide-alginate hydrogel, we did not observe any fracture when the beads were subjected to up to 85% compressive strains and forces up to ~3.3 N (Figure 13b and B.1 Figure 59a). The bead capsules were also subjected to cyclic compression at 70% strain, revealing a pronounced hysteresis due to plastic deformation and energy dissipation (Figure 13c and B.1 Figure 59b). Based on the dimensions of the beads, the cyclic effective compressive stress was calculated as ~70 kPa (B.1 Figure 59b), which is equivalent to pressure at ~7 m depth underwater and ~4 m depth under dry soil[272], and is comparable to our previously published ingestible hydrogel device[273]. This result suggests that these beads could sustain much stronger stresses higher than the maximum gastric pressure (~10 kPa)[274], highlighting their potential for in vivo biosensing. Thus, multilayer coating with elastic tough hydrogel around an alginate core provides mechanical robustness to the entire capsule, a phenomenon which is observed with other stiff polymer coatings[275]. Importantly, zero CFU counts were detected when plating the surrounding media that was incubated with compressed single- and triple-coated beads, suggesting that the capsules withstood successive compressions without fracturing and maintained perfect containment needed for safe environmental deployment (Figure 13c, inset). In the liquid environment, the beads showed ~25% swelling after day 1 and remained stable over the course of 14 days (B.1 Figure 60a). This swelling has a limited impact on the beads' mechanical properties measured by compression (B.1 Figure 60b). However, swelling might be a potential challenge for long-term deployment in the low-salt environment and could be minimized by replacing the salt-sensitive alginate with swelling-resistant PEG-containing hydrogels[276].

3.4 Synergistic containment ensures zero GMM escape

Since extreme forces could potentially compromise our hydrogels and permit bacterial escape, we hypothesized that chemical containment could be employed to enforce an additional layer of control over encapsulated cells. Genomically recoded organisms (GROs, microbes with synthetic autotrophies)[258] can be contained because the growth of these microbes is dependent on the supply of synthetic amino acids (enabling a permissive environment). Here, we sought to combine physical and chemical strategies for biocontainment by encapsulating two GROs auxotrophic for the synthetic amino acid p-iodo-L-phenylalanine (pIF, β) in tough hydrogel beads (Fig. 3d). The *E. coli* strains rEc.β.dC.12'.ΔtY (mutation rate $<4.9 \times 10^{-12}$) and LspA.Y54β (mutation rate = 1.86×10^{-5}) have amber codons (TAG) inserted in three (Lsp, DnaX, SecY) and in one (Lsp) essential genes[258], respectively, to restrict growth to permissive media (containing pIF). We showed that: 1) chemical containment in the beads enables the programmable loss of cellular viability after 48 hours, which prevents undesirable growth once a given time frame has expired; and 2) physical containment adds another layer of protection over chemically contained microbes, which is necessary for applications that require extremely high standards of biocontainment.

First, beads encapsulating the pIF-auxotroph GROs, rEc.β.dC.12'.ΔtY and LspA.Y54β were pre-soaked in lysogeny broth (LB) in the absence (non-permissive media) or presence (permissive media) of 1 mM pIF and 0.2% L-arabinose (L-ara), which is required for aminoacyl-tRNA synthetases (aaRS) expression in these strains[258]. We hypothesized that in non-permissive media, the GROs would be unable to synthesize functional essential proteins and thus, lose viability. Indeed, beads pre-soaked in non-permissive media failed to sustain cell growth and showed less than 10% survival after 12 hours in LB only (Fig. 3e, cells were plated on permissive solid media), with no survival detected at 24 h. On the other hand, pre-soaking encapsulated beads in permissive media greatly prolonged cell survival. Greater than 50% of the rEc.β.dC.12'.ΔtY population and >25% of the LspA.Y54β population remained viable after 24h of incubation. Nearly all cells (>99%) lost viability after 2 days of incubation, which we believe is due to pIF and L-ara depletion by cells, as well as passive diffusion of these molecules out of the encapsulated hydrogel. Because many chemical induction and sensing responses in *E. coli* require less than 24 hours to complete, this defined survival window could be used to prevent the undesirable growth of cells upon completion of tasks.

We demonstrated the benefit of combining physical and chemical containment (Fig. 3f) by placing beads in non-permissive liquid media and then plating samples from the liquid media on non-permissive solid media. This experiment allowed us to screen for escape mutants. For beads with tough hydrogel coating encapsulating either GRO strain (1.2×10^7 cells), no viable cells were observed in the surrounding non-permissive media at the end of a 3-day shaking incubation period, indicating complete containment (Fig. 3f). When rEc.β.dC.12'.ΔtY cells (low mutational escape rate, $<4.9 \times 10^{-12}$)[258] were encapsulated in beads without the tough hydrogel coating, no viable cells were observed in the non-permissive media. On the other hand, when LspA.Y54β cells (higher mutational escape rate, $\sim 1.86 \times 10^{-5}$)[258] were encapsulated in beads without the tough hydrogel coating, mutational escape was observed, and cells grew in the non-permissive media. These results demonstrate that physical containment can complement chemical containment strategies to achieve near-zero escape rates (chemical plus physical). Furthermore, we can program a "biological timer" system that ceases to grow in the absence of artificial chemicals and eliminates potential bacterial growth outside the bead even when the hydrogel shell is compromised.

3.5 DEPCOS prevents the exchange of genetic materials and protects GMMs from insults.

Horizontal gene transfer (HGT) of engineered genes into the environment and disruption of native ecosystems is a major regulatory concern regarding the deployment of GMMs. Since DNA is much smaller than bacteria, we sought to explore whether DEPCOs could prevent HGT. We used a bacterial conjugation assay (Fig. 3g) where the conjugation efficiency of an F-plasmid carrying a chloramphenicol (Cm) resistance marker from an F+ donor strain was measured for transfer into a recipient bacteria strain (F-) that lacks Cm resistance. In liquid media, we measured conjugation efficiency to be ~1%. When the F+ donor strain was encapsulated within tough hydrogel beads and incubated with recipient bacteria in the surrounding media (2 mL), no transconjugants were detected after 24 hours of co-incubation (LLOD: 1 CFU/2 mL). In addition to conjugation, GMM-derived DNA might reach the environment through diffusion from decayed GMM after cell death. We encapsulated DNA molecules at high concentration (3×10^9 copy/μL) in the beads and measured DNA copy number in the surrounding media using quantitative PCR. There was no DNA molecules leakage as they were perfectly contained (Supplementary Fig. 10) by the alginate-containing DEPCOS, which effectively blocked the diffusion of large biomacromolecules such as DNA[277].

We then investigated the protective effects of the beads on bacterial cells by comparing the resistance of encapsulated cells versus planktonic cells (without bead encapsulation) to a series of chemical and biological stresses (Fig. 3h). Encapsulated bacteria survived to a much greater extent than planktonic cells in the presence of the aminoglycoside antibiotic kanamycin. Surprisingly, encapsulation also helped cells survive acidic environments (pH 4). Such protection became more prominent as the size of the alginate core increase because the killing is localized near the surface of the alginate core (Supplementary Fig. 11). Thus, our robust hydrogels can prevent bacterial conjugation-based HGT and enhance GMM survivability in certain stressful conditions.

3.6 Sensing, recording, and communication capabilities powered by genetic circuits

During the outgrowth step (B.1 Figure 55), the number of cells in the beads increased by ~10^5 fold (~16-17 doublings) and reached stationary phase after 12 hours of incubation, corresponding to a doubling time of ~40 minutes. These data indicate that bacterial cells within the beads are metabolically active and able to divide in the alginate core, which is important for GMMs that must carry out active biological functions[278].

The nanoporous structures of the hydrogel shell and alginate core should allow rapid diffusion of small molecules and ions[263,279] while blocking out large biopolymers such as DNA (B.1 Figure 61) and proteins[263]. The anionic nature of alginate in both components further restricts the diffusion of highly charged molecules such as tobramycin[280] and kanamycin (Figure 13f). Combining the tough hydrogel shell and the alginate core as a whole system, we observed that mildly charged small molecules could quickly diffuse into the beads (B.1 Figure 63), which also suggests that the H^+ ions could diffuse at an even faster rate. To determine whether encapsulated bacteria can respond to these stimuli, we encapsulated bacteria containing a genetic construct that expresses GFP in response to aTc induction.

We then incubated the beads at 37°C in the absence of aTc or in the presence of 200 ng/mL aTc. We found that encapsulated cells exposed to aTc exhibited a 35-fold increase in green fluorescence compared with encapsulated cells not exposed to aTc, which was lower than the fold-induction seen in liquid cultures (Figure 14a), potentially due to the limited diffusion within the core. Thus, gene expression in cells encapsulated in tough hydrogels can be exogenously controlled by chemical inducers. In addition, activation of gene expression could still be observed in ready-to-use beads stored at 4°C for 14 days (B.1 Figure 64), which is comparable to current state-of-the-art whole-cell biosensors for field applications[281,282], such as hydrogel-based[268,283] and liquid-in-a-cartridge devices[284]. Additionally, to demonstrate the sensing versatility of our system, we showed that a larger and more charged molecule (heme, physiological charge: 3^+) with physiological importance could be easily detected using an engineered probiotic *E. coli*[175] (Figure 14b).

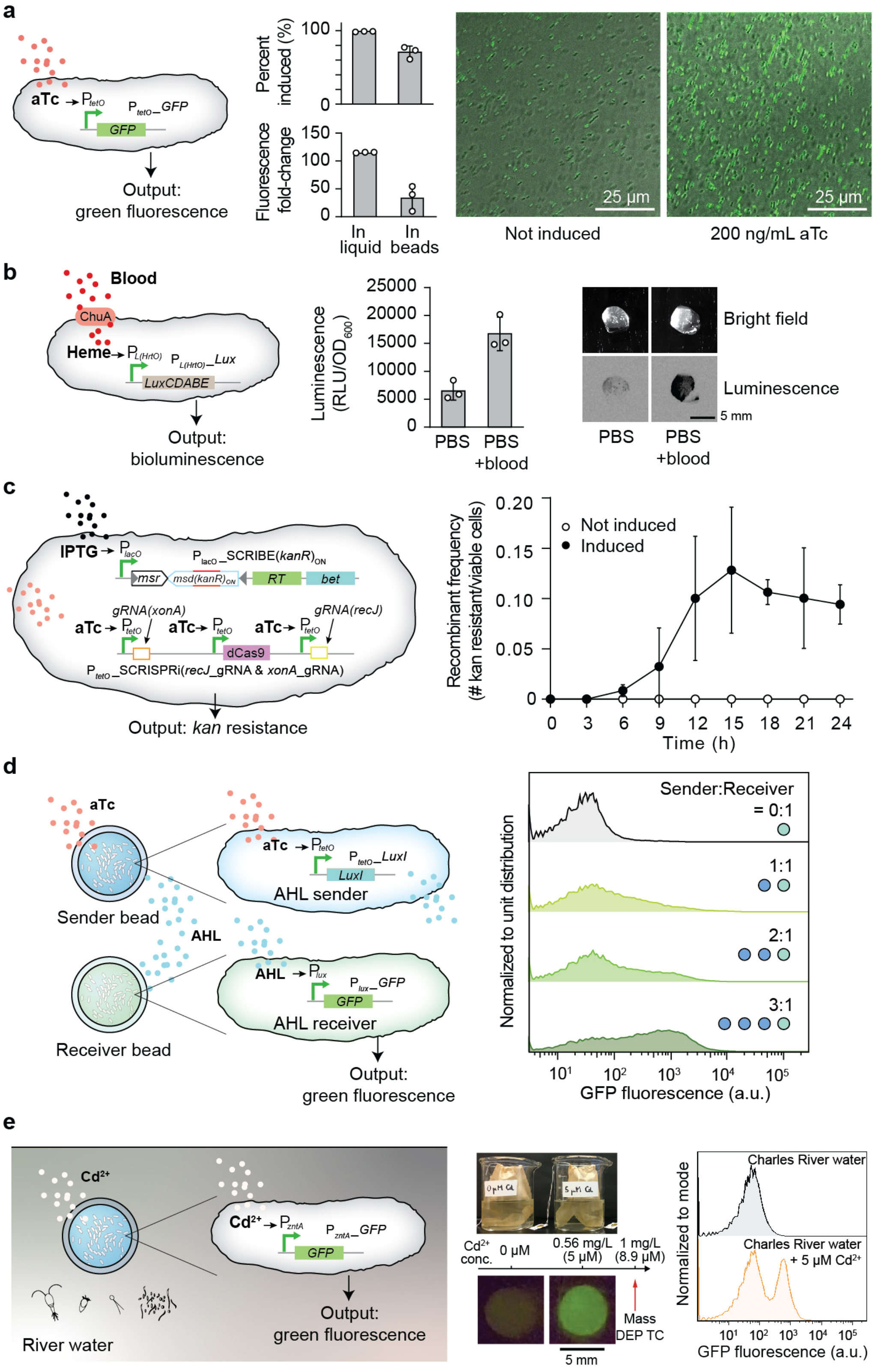
a
aTc → P_tetO
P_tetO_GFP
GFP
Output:
green fluorescence
Percent induced (%)
100
0
Fluorescence fold-change
150
100
50
0
In liquid
In beads
25 µm
25 µm
Not induced
200 ng/mL aTc
b
Blood
ChuA
Heme → P_L(HrtO)
P_L(HrtO)_Lux
LuxCDABE
Output:
bioluminescence
Luminescence (RLU/OD600)
25000
20000
15000
10000
5000
0
PBS
PBS +blood
Bright field
Luminescence
5 mm
PBS
PBS +blood
c
IPTG → P_lacO
P_lacO_SCRIBE(kanR)ON
msr
msd(kanR)ON
RT
bet
gRNA(xonA)
gRNA(recJ)
aTc → P_tetO
aTc → P_tetO
aTc → P_tetO
dCas9
P_tetO_SCRISPRi(recJ_gRNA & xonA_gRNA)
Output: kan resistance
Recombinant frequency (# kan resistant/viable cells)
0.20
0.15
0.10
0.05
0
○ Not induced
● Induced
0 3 6 9 12 15 18 21 24
Time (h)
d
aTc
Sender bead
AHL
Receiver bead
aTc → P_tetO
P_tetO_LuxI
LuxI
AHL sender
AHL → P_lux
P_lux_GFP
GFP
AHL receiver
Output:
green fluorescence
Normalized to unit distribution
Sender:Receiver = 0:1
1:1
2:1
3:1
10¹ 10² 10³ 10⁴ 10⁵
GFP fluorescence (a.u.)
e
Cd²⁺
River water
Cd²⁺ → P_zntA
P_zntA_GFP
GFP
Output:
green fluorescence
0 µM Cd
5 µM Cd
Cd²⁺ conc.
0 µM
0.56 mg/L (5 µM)
1 mg/L (8.9 µM)
Mass DEP TC
5 mm
Normalized to mode
Charles River water
Charles River water + 5 µM Cd²⁺
10¹ 10² 10³ 10⁴ 10⁵
GFP fluorescence (a.u.)

Figure 14 | **Responses of encapsulated bacterial cells to external stimuli.** **(a)** Left: Schematic of GFP expression under the control of an aTc-inducible promoter. Center: Flow cytometry analysis of GFP expression in liquid culture and in hydrogel beads. Samples prepared in triplicate; data represent the mean ±1 SD based on analyses of 30000 events. The percentage data were calculated by dividing the numbers of GFP ON cells by the total cell counts. The fold-change data were derived from the mean of fluorescence. Right: Confocal microscopy images of beads encapsulating the aTc-sensing *E. coli* strain with and without 200 ng/mL aTc. **(b)** Left: A Heme sensing strain which senses heme and generates bioluminescence as an output[175]. The heme released from blood is transported into the cell by ChuA. Middle: Cells retrieved from beads showed a significant increase in luciferase activity. Right: The resulting bioluminescence can be detected with high sensitivity from intact beads. Samples prepared in triplicate; data represent the mean ±1 SD. **(c)** Left: An improved SCRIBE strain using CRISPRi to knock down cellular exonucleases (*xonA* and *recJ*) for enhanced genome editing efficiency via SCRIBE in DH5αPRO[285]. Right: Recombinant frequencies of beads containing the high-efficiency SCRIBE strain induced for a total of 24 hours with or without aTc and IPTG. Samples prepared in triplicate; data represent the mean ±1 SD. **(d)** Left: An AHL sender strain responds to aTc and produces AHL as an output, which later reaches an AHL receiver strain through diffusion and induces GFP expression. Right: Cells retrieved from receiver beads showed various levels of induction corresponding to different AHL sender bead to AHL receiver bead ratios. The data is representative of three independent experiments and normalized to unit distribution (area under the curve). The sender:receiver numbers represent actual number of beads, each contains ~10^9 cells. **(e)** Left: Schematic of GFP expression under the control of a cadmium-inducible promoter. Center: Photograph of the heavy metal sensing experiment setup (top). Tea bags containing five beads each were incubated in beakers containing Charles River water with and without 5 μM $CdCl_2$. The Massachusetts Department of Environmental Protection toxic limit for $CdCl_2$ is 1 mg/L, corresponding to 8.9 μM. Beads retrieved after 6 hours showed green fluorescence (bottom). Right: Flow cytometry analysis of encapsulated cells responding to cadmium ions in Charles River water ($n \geq 3$ for all panels). The three flow cytometry panels are each representative of at least four experiments with similar results. Data are normalized to mode (peak value).

We then tested whether bacteria containing a genomically encoded memory system that requires cell division to function would be able to record information within the beads. Recording information on genomic DNA is advantageous in that DNA is a highly stable information storage medium (turnover time up to weeks in aquatic environments and years in soil[286]), information can be retrieved after cell death, and is amenable to multiplexing[287]. We used our SCRIBE platform[278,285] for targeted in vivo genome editing to record information in encapsulated GMMs. The SCRIBE circuit was designed so that IPTG and aTc controlled the expression of Beta recombinase and the CRISPRi system, respectively; in this design, gene editing of the *kanR* gene records chemical exposure (Figure 14c, left).

We exposed beads containing SCRIBE bacteria to IPTG and aTc over 48 hours and found increasing numbers of bacteria acquired kanamycin resistance over the first 12 hours (Figure 14c, right). The high recombinant frequency (~10%) by 12 hours is comparable to results obtained using liquid cultures of non-encapsulated bacteria[278,285], and the plateau in recombination frequency after 12 hours corresponds to growth saturation (B.1 Figure 55). This DNA-encoded memory is stable and can be retrieved at the end of the testing period and even after cell death without constant monitoring by electronics.

Communication between GMMs in beads can be used to implement computation with higher complexity, division of labor, and signal integration/amplification[288,289]. To demonstrate this capability, we showed that different *E. coli* strains contained within beads could communicate with each other via quorum-sensing molecules. An acyl-homoserine lactone (AHL) sender strain[24] and an AHL receiver strain were encapsulated in separate beads and incubated together in 1 mL of Luria-Bertani (LB) media plus carbenicillin (Figure 14d, left). Upon receiving externally added aTc, the sender bead produced AHL, which induced GFP expression in the neighboring receiver bead. The receiver beads exhibited intensified fluorescence (4-, 12-, and 21-fold-increase for 1, 2, and 3 sender beads to receiver beads ratio, respectively) as more sender beads were used (Figure 14d right, and B.1 Figure 65). These results demonstrate that DEPCOS can enable a modular and distributed strategy for the collective execution of complex tasks based on cell-to-cell communication using multiple beads with different GMMs.

3.7 DEPCOS bead can sense contaminants in real-world river water

Finally, to demonstrate that encapsulated bacteria can function in a real-world setting, we used an *E. coli* strain to detect the presence of metal ions in water samples from the Charles River, such as cadmium. Cd^{2+} is a well-known and widespread environmental contaminant that can adversely affect human health[290]. Specifically, we used ZntR, a transcriptional regulator activated by metal ions (Zn^{2+}, Pb^{2+}, Cd^{2+}) and activates the promoter P*zntA*, to express GFP[291]. We characterized the induction of P*zntA* by Zn^{2+}, Pb^{2+}, and Cd^{2+} in liquid cultures of *E. coli* harboring the plasmid pEZ074 (P*zntA*-GFP construct) (Figure 14e, B.1 Figure 66a and B.1 Figure 67). While encapsulated in hydrogel beads and incubated in LB media for a total of three hours, cells produced green fluorescence intensities proportional to Cd^{2+} concentrations (B.1 Figure 66b and B.1 Figure 67).

Next, hydrogel-bacteria beads (pre-soaked in 4x LB) were incubated in water samples extracted from the Charles River having exogenously added Cd^{2+} (Figure 14e, center). The hydrogel-bacteria beads were placed in tea bags to facilitate easy deployment and retrieval. Exposure to 5 μM $CdCl_2$ resulted in the emergence of a cell population expressing high levels of GFP (Figure 14e, right), indicating successful detection of cadmium ions. These results were confirmed visually under blue light: beads exposed to 5 μM $CdCl_2$ exhibited strong green fluorescence (Figure 14e, center and right, and Supplementary Fig. 11c, $p < 0.05$; Student's t-test). Importantly, the high sensitivity of this system to detect 5 μM $CdCl_2$ is relevant to real-world use, as it is below the 8.9 μM (1 mg/L) standard defined by the Massachusetts Department of Environmental Protection as the maximum concentration of cadmium allowed in waste water[32]. Thus, these results highlight the potential of physically biocontained bacteria to detect toxic levels of heavy metals in environmental settings.

3.8 Discussion

To date, the only commercially available GMMs used as environmental sensors are confined in sealed vials into which water samples are manually injected[293]. To enable the environmental deployment of GMMs as biosensors and bioremediation devices, new strategies are needed that allow for interactions with the surrounding environment while maintaining the containment of GMMs. Tough hydrogel scaffolds provide a highly hydrated environment that can sustain cell growth, protect cells from external stresses, and allow small molecules to diffuse between the interior and exterior of the device. Although previous work showed the long-term physical containment of bacteria by core-shell hydrogel microparticles, it did not demonstrate biological activity, robust sensing, or high mechanical toughness[267,280,294]. To the best of our knowledge, no reports have demonstrated robust physical containment while still permitting sensing and cell growth, thus overcoming the major limitations for the deployment of GMMs into the real world.

By combining two types of hydrogels into a core-shell structure, we have developed a reliable strategy for the physical containment and protection of microbes that are genetically engineered with heterologous functions. We showed that encapsulated cells could sense environmental and biomedical stimuli, record exogenous signals into genomically encoded memory, and communicate with each other via quorum-sensing molecules. Finally, we showed that heavy-metal-sensing bacteria can be incorporated into our hydrogel beads and successfully detect cadmium ions in Charles River water samples.

We anticipate that the DEPCOS containment platform can enable the deployment of microbes engineered with synthetic gene circuits into real-world scenarios. For example, encapsulated GMMs could be used to detect explosives[156] or monitor exposure time to toxic chemicals[295] without potential escape into the wild. In addition, the geometry of DEPCOS could be adapted to meet the design specifications of desired applications, such as wearables[157]. Future work will be focused on automating the manufacturing process to provide precise control over the device size and geometries in order to accommodate various physical environments and improve the miniaturization and scalability of the platform. We will also explore the incorporation of selective diffusion barriers and extreme pH resistance capabilities into the hydrogels to enable encapsulated microbial populations to survive in harsh environments, such as during transit through the human GI tract for detecting disease-relevant biomarkers. Another future challenge lies in devising large-scale standardized tests to determine whether encapsulated organisms can be contained, yet function robustly in harsh real-world scenarios, and not just in simulated laboratory settings.

Chapter 4

Living Wearables Combining Material Design and Synthetic Biology

Living systems, such as bacteria, yeasts, and mammalian cells, can be genetically programmed with synthetic circuits that execute sensing, computing, memory, and response functions. Integrating these functional living components into materials and devices will provide powerful tools for scientific research and enable new technological applications. However, it has been a grand challenge to maintain the viability, functionality, and safety of living components in freestanding materials and devices, which frequently undergo deformations during applications. Here, we report the design of a set of living materials and devices based on stretchable, robust, and biocompatible hydrogel–elastomer hybrids that host various types of genetically engineered bacterial cells. The hydrogel provides sustainable supplies of water and nutrients, and the elastomer is air-permeable, maintaining long-term viability and functionality of the encapsulated cells. Communication between different bacterial strains and with the environment is achieved via diffusion of molecules in the hydrogel. The high stretchability and robustness of the hydrogel–elastomer hybrids prevent leakage of cells from the living materials and devices, even under large deformations. We show functions and applications of stretchable living sensors that are responsive to multiple chemicals in a variety of form factors, including skin patches and glove-based sensors.

4.1 Introduction

Genetically engineered cells enabled by synthetic biology have accomplished multiple programmable functions, including sensing[296], responding[297], computing[298], and recording[299]. Powered by this emerging capability to program cells into living computers[25,73,296–299], the integration of genetically encoded cells into freestanding materials and devices will not only provide new tools for scientific research but also, lead to unprecedented technological applications[300]. However, the development of such living materials and devices has been significantly hampered by the demanding requirements for maintaining viable and functional cells in materials and devices, plus biosafety concerns toward the release of genetically modified organisms into environments. For example, gene networks embedded in paper matrices have been used for low-cost rapid virus detection and protein manufacturing[296]. However, such gene networks are based on freeze-dried extracts from genetically engineered cells to operate, partially because the paper substrates cannot sustain long-term viability and functionality of living cells or prevent their leakage. As another example, by seeding cardiomyocytes on thin elastomer films, biohybrid devices have been developed as soft actuators[301] and biomimetic robots[302]. However, because the cells are not protected or isolated from the environment, the biohybrid devices need to operate in media, and the cells may detach from the elastomer films. Thus, it remains a grand challenge to integrate genetically encoded cells into practical materials and devices that can maintain long-term viability and functionality of the cells, allow for efficient chemical communications between cells and with external environments, and prevent cells from escaping the materials or devices. A versatile material system and a general method to design living materials and devices capable of diverse functions[167,296,301,302] remain a critical need in the field.

As polymer networks infiltrated with water, hydrogels have been widely used as scaffolds for tissue engineering[303] and vehicles for cell delivery[304] owing to their high water content, biocompatibility, biofunctionality, and permeability to a wide range of chemicals and biomolecules[260]. The success of hydrogels as cell carriers in tissue engineering and cell delivery shows their potential as ideal matrices for living materials and devices to incorporate genetically engineered cells. However, common hydrogels exhibit low mechanical robustness[305] and difficulty in bonding with other materials and devices[306], which have posed challenges to using them as matrices for living materials and devices[167].

Significant progress has been made toward designing hydrogels with high mechanical toughness and stretchability[305,307,308] and robustly bonding hydrogels to engineering materials, such as glass, ceramics, metals, and elastomers[306,309,310]. Combining programmed cells with robust biocompatible hydrogels has the potential to enable the creation of new living materials and devices, but this promising approach has not been explored yet.

Here, we show the design of a set of living materials and devices based on stretchable, robust, and biocompatible hydrogel–elastomer hybrids that host various types of genetically engineered bacterial cells. We show that our hydrogels can sustainably provide water and nutrients to the cells, whereas our elastomers ensure sufficient air permeability to maintain viability and functionality of the bacteria. Communication between different types of genetically engineered cells and with the environment is achieved via the transportation of signaling molecules in hydrogels. The high stretchability and robustness of the hydrogel–elastomer hybrids prevent leakage of cells from the living materials and devices under repeated deformations. We show applications uniquely enabled by our living materials and devices, including stretchable living sensors responsive to multiple chemicals, interactive genetic circuits, a living patch that senses chemicals on the skin, and a glove with living chemical detectors integrated at the fingertips. A quantitative model that couples transportation of signaling molecules and responses of cells is further developed to help the design of future living materials and devices.

4.2 Design of living materials and devices

We propose that encapsulating genetically engineered cells in biocompatible, stretchable, and robust hydrogel–elastomer hybrid matrices represents a general strategy for the design of living materials and devices with powerful properties and functions. The design of a generic structure for the living materials and devices is illustrated in Figure 15a. In brief, layers of robust and biocompatible hydrogel and elastomer were assembled and bonded into a hybrid structure[306]. Patterned cavities of different shapes and sizes were introduced on the hydrogel–elastomer interfaces to host living cells in subsequent steps. The hydrogel–elastomer hybrid was then immersed in culture media for 12 h, so that the hydrogel can be infiltrated with nutrients. Thereafter, genetically engineered bacteria suspended in media were infused into the patterned cavities through the hydrogel, and the injection points were then sealed with drops of fast-curable pregel solution (C.1 Figure 70). Because the hydrogel was infiltrated with media and the elastomer is air-permeable, hydrogel–elastomer hybrids with proper dimensions can provide sustained supplies of water, nutrient, and oxygen (if needed) to the cells. By tuning the dimensions of hydrogel walls between different types of cells and between cells and external environments, we can control the transportation times of signaling molecules for cellular communication. Furthermore, the high mechanical robustness of the hydrogel, elastomer, and their interface confers structural integrity to the matrix even under large deformations, thus preventing cell escape in dynamic environments.

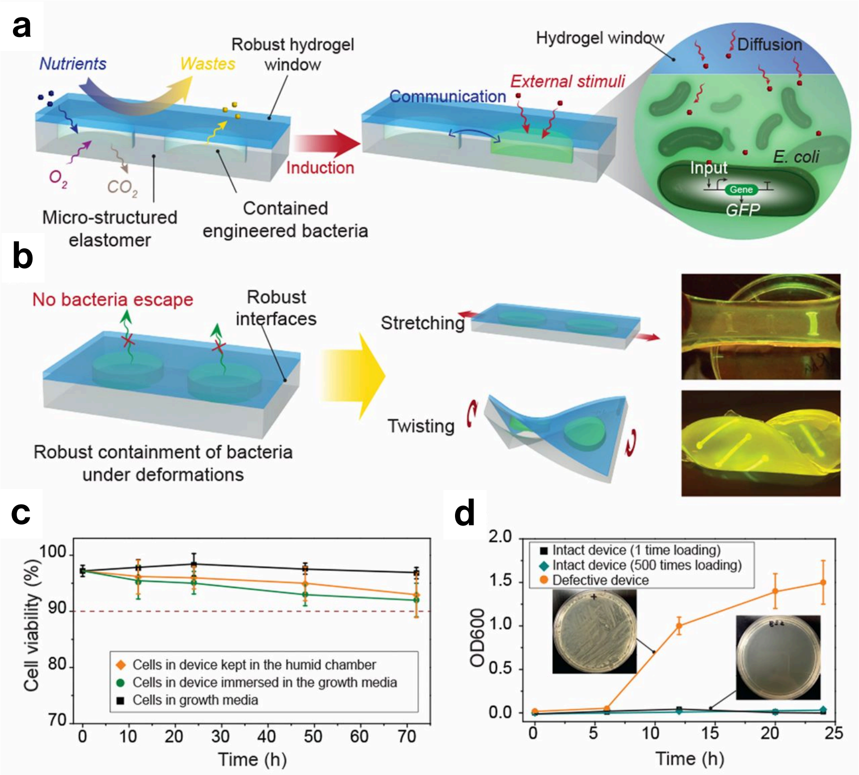

Figure 15 | **Design of living materials and devices. (a)** Schematic illustration of a generic structure for living materials and devices. Layers of robust and biocompatible hydrogel and elastomer were assembled and bonded into a hybrid structure, which can transport sustained supplies of water, nutrient, and oxygen to genetically engineered cells at the hydrogel–elastomer interface. Communication between different types of cells and with the environment was achieved by diffusion of small molecules in hydrogels. **(b)** Schematic illustration of the high stretchability and high robustness of the hydrogel–elastomer hybrids that prevent cell leakage from the living device, even under large deformations. Images show that the living device can sustain uniaxial stretching over 1.8 times and twisting over 180° while maintaining its structural integrity. **(c)** Viability of bacterial cells at room temperature over 3 d. The cells were kept in the device placed in the humid chamber without additional growth media (yellow), in the device immersed in the growth media as a control (green), and in growth media as another control (black; n = 3 repeats). **(d)** OD_{600} and (insets) streak plate results of the media surrounding the defective devices (yellow) and intact devices at different times after 1 (black) or 500 times (green) deformation of the living devices and immersion in media (n = 3 repeats).

In this study, we chose polyacrylamide (PAAm)-alginate hydrogel[306,308] and polydimethylsiloxane (Sylgard 184; Dow Corning) or Ecoflex (Smooth-On) silicone elastomer to constitute the robust hydrogel and elastomer, respectively. The biocompatibility of these materials has been extensively validated in various biomedical applications[311,312]. The sufficient gas permeation of the silicone elastomer enables oxygen supply for the bacteria[313–315]. If a higher level of oxygen is required, one may choose elastomers with higher permeability, such as Silbione[316], or microporous elastomers[314]. In the hydrogel, the covalently cross-linked PAAm network is highly stretchable, and the reversibly cross-linked alginate network dissipates mechanical energy under deformation, leading to tough and stretchable hydrogels[305,308,317]. More robust devices can be fabricated by using fiber-reinforced tough hydrogel[318]. Robust bonding between the hydrogel and elastomer can be achieved by covalently anchoring the PAAm network on the elastomer substrate[306,309,317]. The *E. coli* bacterial strains were engineered to produce outputs [e.g., expressing GFP] under the control of promoters that are inducible by cognate chemicals. For example, the 2,4-diacetylphloroglucinol$_{\text{Receiver}}$ (DAPG$_{\text{RCV}}$)/GFP strain produces GFP when the chemical inducer DAPG is added and received by the cells. The cell strains used in this study included DAPG$_{\text{RCV}}$/GFP, N-acyl homoserine lactone$_{\text{RCV}}$ (AHL$_{\text{RCV}}$)/GFP, isopropyl β-D-1-thiogalactopyranoside$_{\text{RCV}}$ (IPTG$_{\text{RCV}}$)/GFP, rhamnose$_{\text{RCV}}$ (Rham$_{\text{RCV}}$)/GFP, and anhydrotetracycline$_{\text{RCV}}$ (aTc$_{\text{RCV}}$)/AHL. The DAPG, AHL, IPTG, Rham, and aTc are small molecules with biochemical activities and used as the signaling molecules in this study.

To evaluate the viability of cells in living materials and devices, we placed the hydrogel–elastomer matrices containing Rham$_{\text{RCV}}$/GFP cells (Figure 15a) in a humid chamber (relative humidity > 90%) without the addition of growth media or immersed the living materials in the growth media at room temperature (25°C) for 3 d. We also directly cultured the cells in growth media as a control. Thereafter, we used the live/dead stain and performed flow cytometry analysis for bacteria retrieved from the living device to test the cell viability. As shown in Figure 15c and C.1 Figure 71, the viability of cells in the device placed in a humid chamber maintains above 90% over 3 d without the addition of media to the device. This viability is similar to that of cells in the device immersed in media or cells directly cultured in media at room temperature over 3 d.

To test whether bacteria could escape from the living devices, we deformed the hydrogel–elastomer hybrids containing Rham_{RCV}/GFP bacteria in different modes (i.e., stretching and twisting) as illustrated in Figure 15b, and then immersed the device in media for a 24-h period. As shown in Figure 15b and C.1 Figure 72, the living device made of Ecoflex and tough hydrogel sustained a uniaxial stretch over 1.8 times its original length and a twist over 180° while maintaining its structural integrity. Furthermore, after immersing the device in media for 6, 12, 20, and 24 h, we collected the media surrounding the device and measured the cell population in the media over time via OD_{600} by UV spectroscopy (Figure 15d); 200 μL media were streaked on agar plates after 24 h to check for cell escape and growth (Figure 15d, Insets). Fig. 1D shows that bacteria did not escape the hydrogel–elastomer hybrid even under repeated mechanical loads (500 cycles). As controls, we intentionally created defective devices (with weak hydrogel–elastomer bonding) and observed significant escape and overgrowth of bacteria after immersing the samples in media (yellow curve in Figure 15d). Because agar hydrogels have been widely used for cell encapsulation, we fabricated an agar-based control device that encapsulated Rham_{RCV}/GFP bacteria with the same dimensions as the hydrogel–elastomer hybrid. In Fig. S4, it can be seen that these agar devices underwent failures even under moderate deformation (e.g., a stretch of 1.1 or a twist of 60°). Moreover, cell leakage from the agar devices occurred regardless of the presence of any deformation, likely because of the large pore sizes and sol-gel transition of the agar gel, allowing for the escape of encapsulated bacteria (C.1 Figure 74). These results indicate that our hydrogel–elastomer hybrids can provide a biocompatible, stretchable, and robust host for genetically engineered bacteria.

4.3 Stretchable living sensors for chemical sensing

We next show functions and applications enabled by the living materials and devices. Figure 16a illustrates a hydrogel–elastomer hybrid with four isolated chambers that each hosted a different bacterial strain: DAPG$_{\mathrm{RCV}}$/GFP, AHL$_{\mathrm{RCV}}$/GFP, IPTG$_{\mathrm{RCV}}$/GFP, and Rham$_{\mathrm{RCV}}$/GFP. The genetic circuits in these bacterial strains can sense their cognate inducers and express GFP (C.1 Figure 75), which can be visible under blue light illumination. As mentioned above, the DAPG$_{\mathrm{RCV}}$/GFP strain exhibits green fluorescence when receiving DAPG but is not responsive to other stimuli. Similarly, the AHL$_{\mathrm{RCV}}$/GFP strain expresses GFP only induced by AHL, IPTG selectively induces GFP expression in the IPTG$_{\mathrm{RCV}}$/GFP strain, and Rham selectively induces the green fluorescence output of the Rham$_{\mathrm{RCV}}$/GFP strain (Figure 16b). We show that each inducer, diffusing from the environment through the hydrogel into cell chamber, can trigger GFP expression of its cognate strain inside the device, which could be visualized by the naked eye or microscope (Figure 16c and C.1 Figure 76). This orthogonality makes the hydrogel–elastomer hybrid with encapsulated bacteria into a living sensor that can simultaneously detect multiple chemicals in the environment (Figure 16c). About 2 h is required for each strain to produce significant fluorescence. Parameters that affect response times for the living sensor are discussed with a quantitative model below.

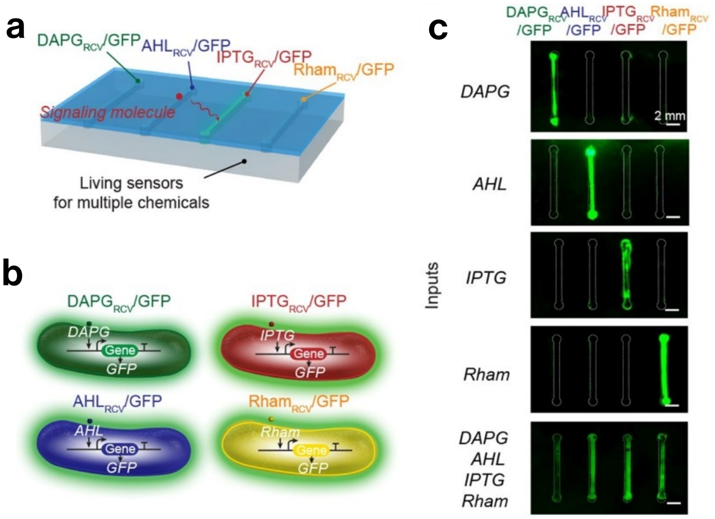

Figure 16 | **Stretchable living sensors can independently detect multiple chemicals.** **(a)** Schematic illustration of a hydrogel–elastomer hybrid with four isolated chambers to host bacterial strains, including DAPGRCV/GFP, AHLRCV/GFP, IPTGRCV/GFP, and RhamRCV/GFP. Signaling molecules were diffused from the environment through the hydrogel window into cell chambers, where they were detected by the bacteria. **(b)** Genetic circuits were constructed in bacterial strains to detect cognate inducers (i.e., DAPG, AHL, IPTG, and Rham) and produce GFP. **(c)** Images of living devices after exposure to individual or multiple inputs. Cell chambers hosting bacteria with the cognate sensors showed green fluorescence, whereas the noncognate bacteria in chambers were not fluorescent. Scale bars are shown in images.

4.4 Interactive genetic circuits

Next, we integrated cells containing different genetic circuits into a freestanding living device to study cellular signaling cascades. We designed two bacterial strains that can communicate via the diffusion of signaling molecules through the hydrogel, although both were separated by an elastomer barrier within discrete chambers of the device (Figure 17a). Specifically, we used a transmitter strain (aTc_{RCV}/AHL) that produces the quorum-sensing molecule AHL when induced by aTc and a receiver strain (AHL_{RCV}/GFP) with AHL-inducible GFP genes[25]. We triggered this device with aTc from the environment to induce the transmitter cells, which resulted in AHL production and stimulation of receiver cells to synthesize GFP (Figure 17c). In Figure 17b, we plot the normalized fluorescence of bacteria in different cell chambers (i.e., transmitter and receiver in Figure 17a) as a function of time after aTc was added outside the device. Because there is no GFP gene in the transmitter cells (aTc_{RCV}/AHL), their chambers showed no fluorescence over time (Figure 17b). It took a longer response time (~5 h) for the receiver cells in the middle chamber to exhibit significant fluorescence compared with the cells in simple living sensors (Figure 16a). Two diffusion processes (i.e., aTc from the environment to the two side chambers and AHL from the two side chambers to the central chamber) and two induction processes (i.e., AHL production induced by aTc in transmitters and GFP expression induced by AHL in receivers) were involved in the current interactive genetic circuits. As a control, when the transmitters (aTc_{RCV}/AHL) in the device were replaced by a cell strain containing aTc-inducible GFP (aTc_{RCV}/GFP) that cannot communicate with AHL_{RCV}/GFP, no fluorescence was observed in the receiver (AHL_{RCV}/GFP) chamber (Figure 17d). Overall, the integrated devices containing interactive genetic circuits provide a platform for the detection of various chemicals and the investigation of cellular interaction among physically isolated cell populations.

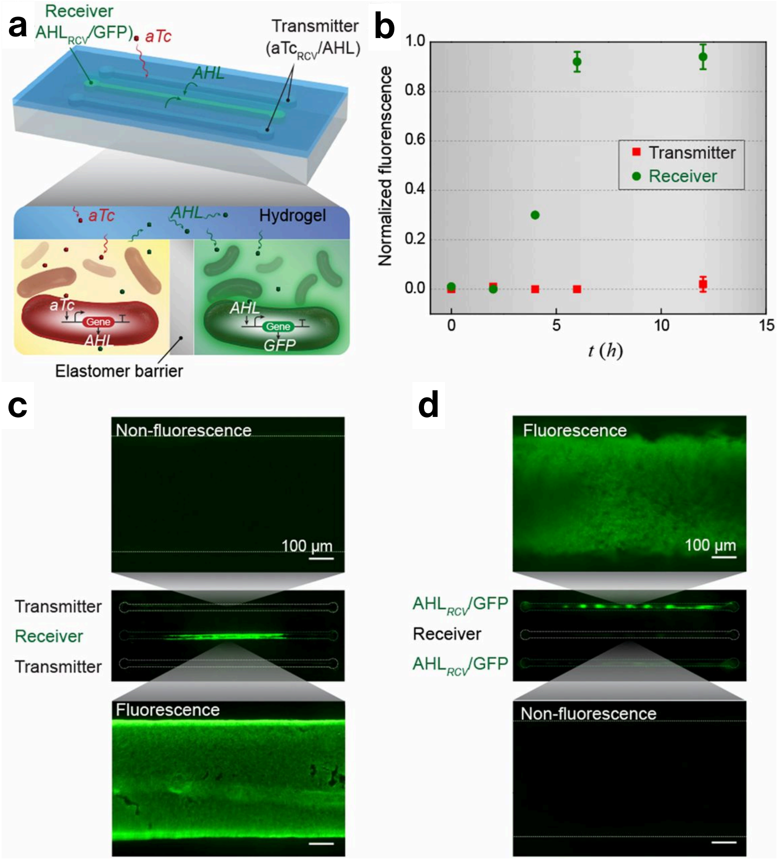

Figure 17 | **Interactive genetic circuits.** **(a)** Schematic illustration of a living device that contains two cell strains: the transmitters (aTc$_{RCV}$/AHL strain) produce AHL in the presence of aTc, and the receivers (AHL$_{RCV}$/GFP strain) express GFP in the presence of AHL. The transmitters could communicate with the receivers via diffusion of the AHL signaling molecules through the hydrogel window, although the cells are physically isolated by the elastomer. **(b)** Quantification of normalized fluorescence over time (n = 3 repeats). All data were measured by flow cytometry, with cells retrieved from the device at different times. **(c)** Images of the device and microscopic images of cell chambers 6 h after addition of aTc into the environment surrounding the device. The side chambers contain transmitters, whereas the middle one contains receivers. **(d)** Images of the device and microscopic images of cell chambers 6 h after aTc addition in the environment. The side chambers contain aTc$_{RCV}$/GFP instead of transmitters, whereas the middle one contains receivers. Scale bars are shown in images.

4.5 Living wearable devices

To further show practical applications of living materials and devices, we fabricated a living wearable patch that detects chemicals on the skin (Figure 18a-d). The sensing patch matrix consists of a bilayer hybrid structure of tough hydrogel and silicone elastomer. The wavy cell channels could cover a larger area of the skin with a limited quantity of bacterial cells (Figure 18a). The living patch can be fixed on the skin by clear Scotch tape, with the hydrogel exposed to the skin and the elastomer exposed to the air. The compliance and stickiness of the hydrogel promote conformal attachment of the living patch to human skin, whereas the silicone elastomer cover effectively prevents the dehydration of the sensor patch (C.1 Figure 77)[306]. As shown in Figure 18b-d, the inducer Rham was smeared on the skin of a forearm before we adhered the living patch. The channels with Rham_{RCV}/GFP in the living patch became fluorescent within 4 h, whereas channels with AHL_{RCV}/GFP did not show any difference. As controls, no fluorescence was observed in any channels in the absence of any inducer on the skin (C.1 Figure 78a), whereas all channels became fluorescent in the presence of both AHL and Rham (C.1 Figure 78b). Although the inducers are used as mock biomarkers here, more realistic chemical detections, such as components in human sweat or blood, may be pursued with living devices for scientific research and translational medicine in the future.

As another application, a glove with chemical detectors integrated at the fingertips was fabricated (Figure 18e). The stretchable hydrogel and tough bonding between hydrogel and rubber allow for robust integration of living monitors on flexible gloves. To show the capability of this living glove, a glove-wearer held cotton balls that have absorbed inducers. Those chemicals from the cotton ball would diffuse through the hydrogel and induce fluorescence in the engineered bacteria (Figure 18f-h). For example, gripping a wet cotton ball that contained IPTG and Rham resulted in fluorescence at two of three bacterial sensors that contained IPTG_{RCV}/GFP (Figure 18g and h, *) and Rham_{RCV}/GFP (Figure 18g and h, ***) on the glove within 4 h. The middle sensor containing AHL_{RCV}/GFP (Figure 18g and h, **) remained unaffected. The living patch and biosensing glove show the potential of living materials as low-cost and mechanically flexible platforms for healthcare and environmental monitoring. Looking forward, we envision the design of living devices that can be wearable, ingestible, or implantable for applications, such as water quality alert, disease diagnostics, and therapy.

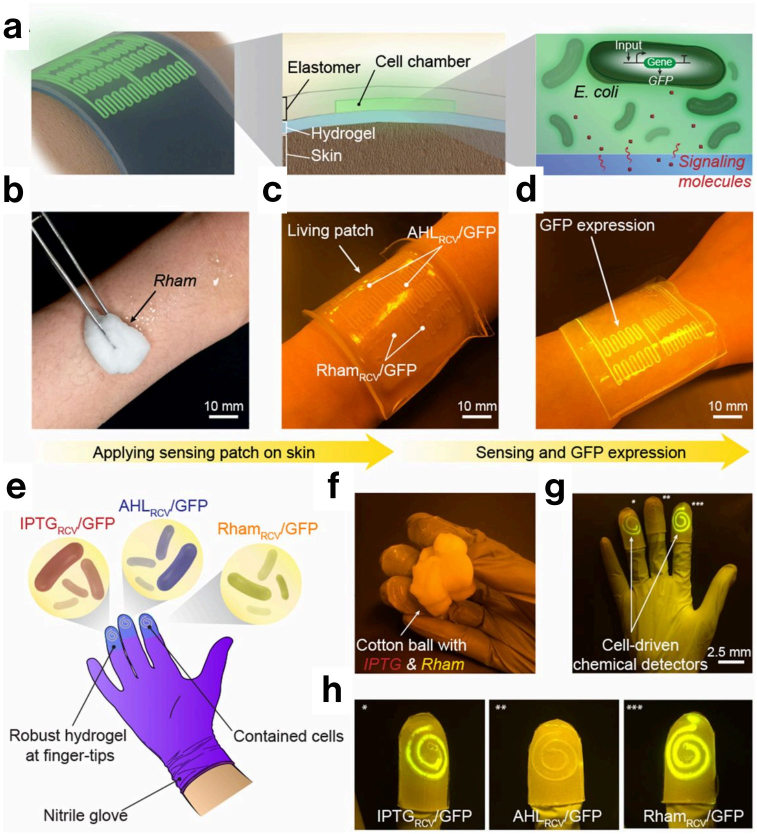

Figure 18 | **Living wearable devices.** **(a)** Schematic illustration of a living patch. The patch adhered to the skin with the hydrogel side and the elastomer side was exposed to the air. Engineered bacteria inside can detect signaling molecules. **(b–d)** Rham solution was smeared on the skin, and the sensor patch was conformably applied on the skin. The channels with Rham$_{RCV}$/GFP in the living patch became fluorescent, whereas channels with AHL$_{RCV}$/GFP did not show any differences. Scale bars are shown in images. **(e)** Schematic illustration of a glove with chemical detectors robustly integrated at the fingertips. Different chemical-inducible cell strains, including IPTG$_{RCV}$/GFP, AHL$_{RCV}$/GFP, and Rham$_{RCV}$/GFP, were encapsulated in the chambers. **(f–h)** When the living glove was used to grab a wet cotton ball containing the inducers, GFP fluorescence was shown in the cognate sensors IPTG$_{RCV}$/GFP (*) and Rham$_{RCV}$/GFP (***) on the gloves. In contrast, the noncognate sensor AHL$_{RCV}$/GFP (**) did not show any fluorescence. Scale bars are shown in images.

4.6 Discussion

We have integrated genetically engineered cells as programmable functional components with stretchable, robust, and biocompatible hydrogel–elastomer hybrids to create a set of stretchable living materials and devices. These living materials and devices can be programmed with desirable functionalities by designing the genetic circuits in the cells as well as the structures and micropatterns of the hydrogel–elastomer hybrids. Moreover, we developed a quantitative model that accounts for the coupling between physical and biochemical processes in living materials. We further identified two critical timescales that determine the speed of response of the living materials and devices and provide guidelines for the design of future systems. This work has the potential to open technological avenues that capitalize on advances in synthetic biology and soft materials to implement stretchable, wearable, and portable living systems with important applications in the monitoring of human health[296] and environmental conditions[319] and the treatment and prevention of diseases[297].

Chapter 5

Outlook

Synthetic biology has facilitated the development of a new class of smart materials for biomedical, environmental, and consumer applications. These smart materials display a wide range of length scales, design approaches, and matrix types. However, limitations remain owing to inherent problems related to biological engineering (Figure 19).

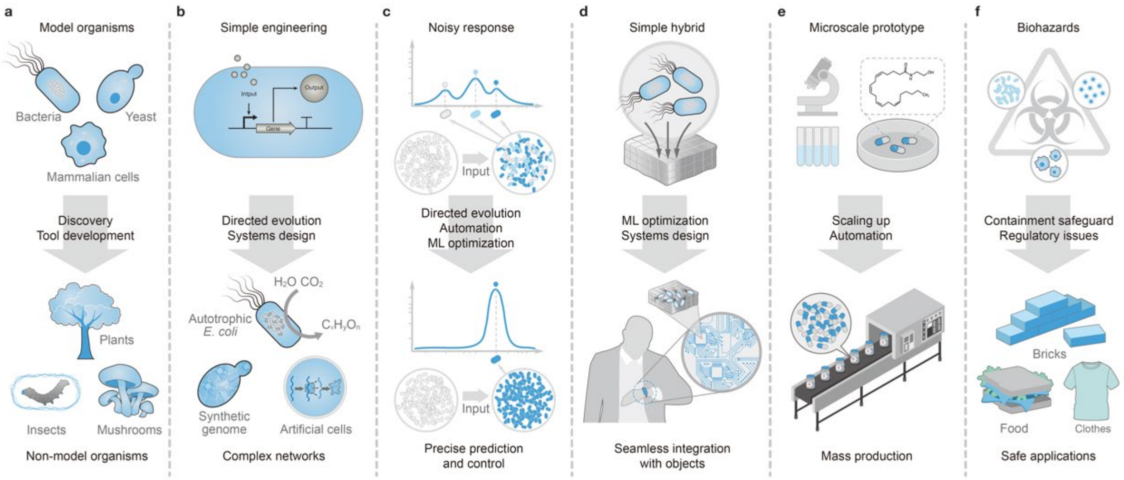

Figure 19 | **Challenges and future directions of materials synthetic biology. (a)** Research in materials synthetic biology is currently limited to well-characterized model systems that were chosen because of high engineerability. As more genetic tools are discovered and developed, unconventional organisms, which are potent material producers, are predicted to become the major organisms in the field. **(b)** Using directed evolution and systems design, large-scale and complex circuitry can be computationally generated and replace simple designs with few transcriptional units. **(c)** Biological input-output functions are often noisy and error-prone.

Optimization using machine learning (ML) and automation at design and test levels will greatly improve the precision of cellular responses and benefit computational simulations. **(d)** Instead of a simple mixture of artificial materials and engineered cells, future living devices will seamlessly integrate biotic and abiotic parts that work in concert to perform complex tasks. **(e)** To bring an early-stage prototype to the market, manufacturing processes need to be redesigned with a focus on scalability and automation, which are often lacking in a laboratory setup. **(f)** Biocontainment safeguards and relevant regulations need to be implemented to ensure the safe application of materials in the real world.

Currently, mainly model organisms, such as *E. coli*, are used as chassis for materials production or as the active component in composites. However, model organisms are often chosen because they are easy to engineer, not because they are competent material producers. Genetic engineering tools can also be applied to modify non-model organisms; however, they heavily depend on reliable genome sequences and efficient transformation and screening methods, whose development is often time- and labor-intensive. Advances in sequencing and genome editing technologies will enable the engineering of non-model organisms, for example, silkworms[320], mushrooms[75], and vascular plants[77], with great potential for robust biopolymer generation (Figure 19a). Organisms exhibiting complicated dynamic multicellular behaviors, such as slime molds[321], are also potential candidates for active material development. In addition, mining newly sequenced genomes is likely to lead to the discovery of genetic parts with new properties, such as regulator-promoter pairs for the sensing of chemicals that are currently not detectable by biosensors[322].

New functionalities may also be generated by modifying genetic parts using directed evolution. By iterating mutagenesis followed by careful screening—for example, for enzymatic activities—cells can be modified to metabolize nonconventional substrates and produce chemicals for biomaterials synthesis more efficiently[323,324] (Figure 19b). For example, by employing metabolic rewiring coupled with directed evolution, engineered *E. coli* can use carbon dioxide as the only carbon source, which makes it autotrophic and thus ideal for sustainable biomaterials production[325]. Similar selective concepts could also be applied to attributes such as adhesiveness and stiffness, which will require tailored optimization for high-throughput screening. In addition to engineering proteins that directly contribute to material properties, directed evolution can also be applied to optimize promoter-regulator pairs to reduce background activation, increase sensitivity, and expand the dynamic range[35]. Such improvements would benefit the construction of computational models for genetic circuits, which require the precise quantification of input-output functions (Figure 19c).

As predictive power has increased, the complexity and scale of genetic circuitry in model organisms have grown exponentially. Upscaling poses challenges at the circuitry level, because the assembly of layers of genetic units often results in failures with unknown causes. Integrating modules from various sources requires a tremendous amount of characterization, design, and fine-tuning, which are often laborious processes if done manually. Thus, standardized genetic parts and syntaxes play crucial roles in creating a universal programming language that operates across platforms and species[70]. Using automated computer-aided genetic parts[326], circuit design[327], and modular DNA assembly[328], large and multi-layer networks can be implemented to design materials that cannot be engineered with simple topologies and a limited number of transcriptional units; for example, synthetic genomes[329] and artificial cells[330] could be constructed. Generalizing the high-throughput characterization of individual parts, coupled with automation[327], is necessary at the in silico circuit design level and at the testing stages, to cover materials-related parts, in particular because biomass-generating outputs often create a substantial metabolic burden and can lead to resource competition with other modules in the circuit architecture[331,332]. An automated workflow assisted by robotics[333] to characterize the responses of material-related circuits would enable the production of a large amount of data for establishing quantitative models from data-driven computational tools.

The rapid growth of machine learning and artificial intelligence has also impacted materials engineering and synthetic biology[334,335]. The large training datasets generated by automated experimental platforms allow machine learning techniques to predict biomolecular behaviors without the need to understand the underlying mechanisms[336]. In particular, protein materials engineering benefits from deep learning, which has enabled the rational design of structures and functions despite limited knowledge of protein folding[337]. Similarly, machine learning could outperform current mechanistic models for the systems design of complex genetic networks. Beyond the cellular level, the collective behavior of a population of cells and its emerging material properties are difficult to predict, because cell populations are dynamic and influenced by the environment. This complexity is reflected in the gap between proof-of-concept hybrid materials, such as simple mixtures of cells and hydrogels, and mature products, which require the systematic amalgamation of living and non-living components, often on a much larger scale. In particular, cell growth, packaging, and communication with the device, demand systems that take all relevant parameters into consideration (Figure 19d). With the help of machine learning and artificial intelligence, we envision that the seamless integration of cells and objects could soon become a reality, and engineered cells interfacing with electronics could lead to products for medical and environmental applications.

For real-world applications, scalability and safety remain major concerns for materials powered by synthetic biology. Unicellular microorganisms, such as *E. coli*, *B. subtilis* and *S. cerevisiae*, which are the current focus of research in biopolymer precursor production[29] and biofilm-based functional materials[52], are among the primary candidates entering the industry for biomaterials production. In chemical production, cell cultures grown in a small batch of test tubes exhibit drastically different behaviors compared to cell cultures grown in industrial bioreactors. Optimizing growth conditions, such as accessibility to gas and nutrient transport at high liquid volumes, to enable maximal metabolic flux is greatly improved by high-throughput screening and automation with robotics[338]. However, industrial optimization has not yet been achieved for the mass production of engineered biofilm-derived materials, which have only been demonstrated at the nano- and microscale thus far (Figure 19e). Finally, safety issues are important hurdles preventing genetically modified organisms from entering the market. Chemical containment—for example, kill switches[252] and synthetic auxotrophy[339]—can prohibit the propagation of engineered cells outside controlled environments. In addition, physical containment strategies using abiotic materials can prevent the escape of engineered cells[93]. Regulations must be carefully developed alongside technological advances, and impacts at the social, ethical, economic, and environmental levels need to be considered[340–342] (Figure 19f). A well-established regulatory system for materials synthetic biology could also facilitate the standardization of manufacturing procedures and outcomes.

Living functional material design by synthetic biology opens the possibility of creating a new class of materials with tailored morphologies and functions. The cores of these materials are living cells or biomolecules that can perform sensing, computation, and actuation. The interdisciplinary field of materials synthetic biology has tremendous potential for the sustainable fabrication of smart biomaterials.

Appendix A

Additional Information and Protocols for Chapter 2

A.1 Notes

Screening S. cerevisiae–K. rhaeticus co-culture conditions

To find optimal conditions for co-culture we screened a panel of conditions for *K. rhaeticus* and *S. cerevisiae* growth. Specifically, we screened growth over a range of *S. cerevisiae* inoculation ratios and in two different media: standard rich yeast medium with glucose (YPD) or sucrose (YPS) as the carbon source and standard medium for cultivation of BC-producing bacteria with glucose (HS-glucose) or sucrose (HS-sucrose) as the carbon source (A.2 Figure 20). Our screen led to a number of observations regarding the growth of *S. cerevisiae* and *K. rhaeticus*. Firstly, we found that, at low *S. cerevisiae* inoculation densities, co-cultures could be established in all media types. Secondly, thicker BC pellicles were obtained in yeast media (YPS and YPD) than in HS media. Thirdly, in both glucose and sucrose media, high inoculation densities of *S. cerevisiae* abolished pellicle formation, consistent with either nutrient competition or suppression of BC production by *S. cerevisiae*. Lastly, we found that, in monoculture, *S. cerevisiae* grew well in all media types, forming a dense sediment at the base of the culture well. In contrast, in sucrose-containing media, *K. rhaeticus* grew poorly compared to glucose-containing media, failing to form a pellicle after 3 days. But, when co-cultured with *S. cerevisiae* inoculated at low density, the growth of *K. rhaeticus* in sucrose media was substantially increased, indicating that the presence of *S. cerevisiae* has some stimulatory effect on the growth of *K. rhaeticus*.

Given our aim of establishing a robust method for co-culturing *S. cerevisiae* alongside *K. rhaeticus*, the observed beneficial interaction between *K. rhaeticus* and *S. cerevisiae* in sucrose media can be considered a useful trait. Specifically, since *K. rhaeticus* growth is dependent on the growth of *S. cerevisiae*, these co-culture conditions effectively ensure that *K. rhaeticus* cannot outcompete *S. cerevisiae*. Co-culture in YPS following this protocol was therefore defined as our standard co-culture condition.

This interaction likely represents either a commensal symbiotic relationship, where one partner benefits from the interaction while the other is unaffected, or a parasitic symbiotic relationship, in which one partner benefits from the interaction while the other is detrimentally affected. A more desirable co-culture system might incorporate an obligate mutualistic symbiosis, where both species are unable to survive without the other. In this case, neither species can outcompete the other, resulting in a stable co-culture system. Although we do not explore this here, in the future it may be possible to engineer further co-dependence between *K. rhaeticus* and *S. cerevisiae*.

Co-culture characterization

First, we followed a time course of pellicle formation to determine the optimal incubation time. Co-cultures yields plateaued after 3 days at a level approximately equivalent to 2.25 g/L (A.2 Figure 22).

Next, since yeast and bacterial communities co-exist stably over many cycles of passage during kombucha tea brewing, we wished to determine to what extent our co-culture system constitutes a similarly stable co-culture. To assay long-term co-culture dynamics, our co-culture consisted of genetically engineered versions of *K. rhaeticus* (Kr RFP) and *S. cerevisiae* (yWS167) that respectively express red and green fluorescent proteins (RFP and GFP) and so can be individually visualized. We used a serial passage approach, in which the liquid below mature pellicles was inoculated into fresh YPS media and allowed to grow for 3 days (A.2 Figure 23a). This process was repeated over 16 rounds (48 days). During each round of serial passage, cultures produced new BC pellicles, confirming the presence of *K. rhaeticus* throughout serial passage (A.2 Figure 23b). To confirm that *S. cerevisiae* was also maintained throughout passage and to rule out the possibility of contamination with another yeast species, samples from the liquid below the pellicle and from pellicles degraded with commercial cellulase enzyme were plated onto YPD-agar and the resultant colonies imaged for GFP expression (Supplementary Fig. 4c). We observed that the original GFP-tagged *S. cerevisiae* strain, yWS167, was indeed maintained throughout the 16 rounds of serial passage. In addition, in a repeat of the passage experiment, changes in yeast cell counts and pellicle dry weight over 10 passages indicated an increase in the number of *S. cerevisiae* compared to *K. rhaeticus* (A.2 Figure 24).

We next wished to investigate the possible causes for the observed stimulatory effect of *S. cerevisiae* on the growth of *K. rhaeticus* in sucrose medium. Notably, *K. rhaeticus* grows well in glucose-containing medium, but much worse in similar sucrose-containing media. One possible explanation is that *S. cerevisiae* converts sucrose to a carbon source, which *K. rhaeticus* can consume more efficiently. Although the exact nature of the interactions between kombucha microbes remains unclear, yeasts in kombucha fermentation are known to hydrolyze the majority of carbon source, sucrose, to form extracellular glucose and fructose through the action of the secreted enzyme invertase (A.2 Figure 25a)[343]. To explore whether the conversion of sucrose to glucose and fructose might cause the observed symbiotic interaction, we tested whether purified *S. cerevisiae* invertase could enhance *K. rhaeticus* growth in YPS medium (A.2 Figure 25b). As before, *K. rhaeticus* failed to produce a pellicle when grown in YPS. However, when grown in YPS spiked with invertase enzyme, *K. rhaeticus* produced thick BC pellicles after 3 days of incubation, like those produced under co-culture in YPS. This is consistent with a mechanism in which the secretion of invertase by *S. cerevisiae*, results in the accumulation of extracellular glucose and fructose, which *K. rhaeticus* can more efficiently metabolize.

Another key property of our co-culture system affecting the downstream development of BC ELMs is the distribution of *S. cerevisiae* and *K. rhaeticus* between the liquid below the pellicle and the pellicle layer itself. To assess the distribution of cells, monocultures and co-cultures of Kr RFP bacteria and yWS167 yeast were prepared and counts of viable cells obtained from the liquid and pellicle layers. Importantly, as described in the methods section, since the degraded pellicle volume was not measured, cell counts in pellicles were estimated by assuming a fixed material volume. In all conditions, the majority of *K. rhaeticus* cells were found in the pellicle layer, while the majority of *S. cerevisiae* cells were found in the liquid layer (Figure 6e, A.2 Figure 26). As before, *K. rhaeticus* formed no pellicle in monoculture in YPS. Notably, *K. rhaeticus* reached similar estimated cell densities in both the pellicle and liquid layers when grown in monoculture in YPD and in co-culture in YPS. By contrast, *S. cerevisiae* grew to a reduced cell density when co-cultured with *K. rhaeticus* in YPS compared to monoculture in YPS, indicating that *K. rhaeticus* either competes with *S. cerevisiae* for some nutrient in the medium or creates conditions in the co-culture that inhibit *S. cerevisiae* growth. Importantly, *S. cerevisiae* still grows to reasonably high cell densities under co-culture conditions, reaching a cell density in the liquid layer of 1.78 x 10^7 cells/mL (± 2.42 x 10^6 cells/mL).

Finally, to give an idea of the robustness of our co-culture method, we set out to determine reproducibility. To achieve this, identical co-cultures were prepared following our standard protocol on three separate occasions, and two parameters were measured: pellicle yields and cell counts (Note: one of the three data sets is the same data set presented in Supplementary Fig. 7b). We found that pellicle yields tended to be consistent within triplicate samples, but variable between co-cultures set up on different occasions (A.2 Figure 27a). Estimated cell counts for *K. rhaeticus* were consistent in the pellicle layer, where the majority of cells were detected, but varied by up to an order of magnitude in the liquid layer (A.2 Figure 27c and e). Similarly, *S. cerevisiae* cell counts were consistent in the liquid layer, where the majority of cells were detected, but more variable in the pellicle layer (A.2 Figure 27d and f).

Engineering secretion of alpha-galactosidase and laccase secretion from yeast

Testing the broad-applicability of the Syn-SCOBY approach for BC functionalization required us to explore whether additional enzymes could be secreted from yeast and incorporated into BC. We chose to investigate two enzymes: α-galactosidase enzyme Mel1 (a native *S. cerevisiae* secreted protein) and laccase enzymes from *Myceliophthora thermophila* (MtLcc1) and *Coriolopsis troggi* (CtLcc1). All were cloned with a C-terminal cellulose-binding domain (CBD) and either their native secretion signal peptide or the *S. cerevisiae* MFα signal peptide at the N-terminus (A.2 Figure 32a and A.2 Figure 33a). Colorimetric plate-based assays were used to screen for the highest-yielding strains based on the intensity of halos of colored substrates surrounding colonies. We found that yeast secreting Mel1 fused to the MFα signal peptide and yeast secreting CtLcc1 fused to its native signal peptide exhibited the highest secretion yields (A.2 Figure 32b and A.2 Figure 33b). As a result, we selected these two strains for BC functionalization experiments (Figure 7i and k).

Potential applicability of the Syn-SCOBY functionalization approach

The Syn-SCOBY enzyme functionalization approach could be applied to the production of immobilized enzyme materials used in various industrial processes, such as lipases in the interesterification of food fats and oils[344], laccases in bioremediation of industrial waste products[345–349] or β-lactamases in decontamination of antibiotic-contaminated soil and wastewater[350,351]. We found that an engineered GFP-expressing strain using an identical promoter continually produced functional protein over the course of 16 passages (48 days), indicating our system might allow simple scalable production for many days by passaging (A.2 Figure 23). This kind of biological material assembly process is likely to be more sustainable than alternative methods, as it occurs autonomously, using simple chemical feedstocks under mild conditions and without the need for complex manufacturing steps, such as separate enzyme purification and chemical bonding to the material. However, evaluating whether the approach is more cost-effective than traditional synthetic methods at large scale will require further, case-by-case characterization and calculation.

OptiPrep enables incorporation of S. cerevisiae within BC materials

We sought to develop a method to increase the number of yeast cells incorporated into the BC pellicle during its production. *S. cerevisiae* settles to the bottom of static liquid culture as the density of yeast cells is greater than that of water: ~1.11 g/mL compared to 1 g/mL[352]. We hypothesized that increasing the density of the culture medium to >1.11 g/mL would float *S. cerevisiae* cells to the surface, forcing their incorporation into the newly forming pellicle at the air-water interface (A.2 Figure 34a).

To increase the density of the YPS medium we used OptiPrep, a metabolically inert aqueous solution of 60% iodixanol with a density of 1.32 g/mL. An initial screen, in which increasing concentrations of OptiPrep were added to YPS medium, revealed that higher density media showed less cell sedimentation (A.2 Figure 35). Based on this, co-cultures grown in media with 45% OptiPrep (v/v) were compared to those grown without, and images were taken of resulting materials. Under both conditions, BC pellicles formed, with pellicle thicknesses and yields slightly reduced when grown with OptiPrep (A.2 Figure 34b and A.2 Figure 36). When pellicles were removed from the cultures, there was a complete absence of sediment in the YPS-OptiPrep medium, in contrast to dense sediment in standard YPS medium (A.2 Figure 34b). Compared to the homogenous surface of pellicles grown in YPS, pellicles grown in YPS-OptiPrep had a speckled appearance due to embedded yeast colonies (A.2 Figure 34c). Addition of OptiPrep gave a ~340-fold increase in estimated *S. cerevisiae* cell count within the pellicle layer, from 5.50 x 10^4 CFU/mL (±4.58 x 10^4) to 1.87 x 10^7 CFU/mL (±1.15 x 10^6) (A.2 Figure 34d).

Further characterization of Syn-SCOBYs formed with OptiPrep supplementation

To explore whether alternative, low-cost reagents could be used in place of OptiPrep, we tested the ability of reagents with various molecular weights, including alginate and polyethylene glycol, to promote yeast incorporation into BC. However, only OptiPrep allowed efficient incorporation of yeast without interfering with the pellicle formation (A.2 Figure 37). Although commercial sources of OptiPrep are relatively expensive, wholesale sources of non-clinical-grade purity iodixanol, used to make OptiPrep, are orders of magnitude less expensive.

We found that pellicles formed with OptiPrep present exhibited a larger total surface area, as determined by Brunauer-Emmett-Teller (BET) measurement (A.2 Figure 34e). This increase may benefit BC enzyme functionalization applications as the internal catalytic surface in the cellulose network is expanded. Our observations were confirmed by scanning electron microscopy (SEM) images of dried pellicles and pellicle cross-sections where enlarged macroporous structures are seen when grown in YPS-OptiPrep (A.2 Figure 34f and A.2 Figure 38). Furthermore, when grown in YPS, small numbers of *S. cerevisiae* cells were loosely attached to the bottom surface of the pellicle. In contrast, when grown in YPS+OptiPrep, yeast cells were again localized to the bottom surface of pellicles, but now formed larger foci reminiscent of colonies, containing many cells covered by cellulose fibrils.

To ensure that the drying process did not change the native structure of the pellicles, we also imaged pellicles without lyophilization by environmental SEM (A.2 Figure 39) and observed the same surface morphologies and localization of yeast at the bottom surface. However, different drying conditions are known to affect the material properties of BC[353].

Stable incorporation of yeast cells, with little or no leakage, may permit applications in which the escape of engineered yeast cells is not permitted. Fluorescence scans of a pellicle containing mScarlet-expressing yeast showed a punctate, colony-like lateral distribution suggestive of physically confined pockets of yeast (A.2 Figure 40). Even after washing of these pellicles, more than half of the yeast were still present, demonstrating stable incorporation of part of the total yeast population within the BC material (A.2 Figure 41).

Effect of cellulase secretion on yeast cell leakage and pellicle morphology

Although the secretion of cellulases might be anticipated to loosen the BC fiber network, there was no significant difference in cell leakage when both wildtype and yCelMix pellicles were subjected to prolonged wash in liquid (A.2 Figure 43). Notably, after the first wash in PBS, ~20% of yeast cells dissociated from the pellicles, likely the loosely attached cells from the pellicle bottom surface. In all following washes, the leakage of embedded yeast cells into the surrounding environment was less than 3%. Interestingly, the total surface area of yCelMix pellicles was smaller than that of pellicles grown with normal wildtype yeast (A.2 Figure 44). This may result from a decrease in structure due to cellulose degradation. Indeed, SEM imaging of yCelMix reveals that a loose fibrous network replaces the densely packed cellulosic matrix at both the top and bottom surfaces (A.2 Figure 45).

Testing a GPCR-based Syn-SCOBY biosensor

To demonstrate the broad applicability of the Syn-SCOBY sense and response approach, we grew and verified sense and response BC materials using a G protein coupled receptor (GPCR)-based yeast biosensor. Specifically, we used biosensor strain yWS890 to detect the *S. cerevisiae* MFα peptide and produce GFP in response[354] (A.2 Figure 48). GPCRs are the major class of membrane protein receptors across eukaryotes and detect a remarkable range of different chemical and physical stimuli. Our modular approach opens up the possibility of porting previously developed biosensing strains into the Syn-SCOBY approach to generate a range of grown biosensor materials[155,240,355]. However, it should be noted that depending on the sensor used, the kinetics of sensing behavior of the cells in BC materials could differ from that of their planktonic counterparts, and so may require additional optimization.

Spatial patterning of catalytic living materials

To optimize the behavior of the light-inducible promoter system, we investigated the effect of different strength promoters driving the expression of the DNA-binding component (LexA-CRY2), and the transcriptional activation component (VP16-CIB1) had on system performance (A.2 Figure 50a). We found that light-induced GFP expression exhibited the lowest background and highest expression levels when driving LexA-CRY2 expression with a weak constitutive promoter (pREV1) and VP16-CIB1 with a strong constitutive promoter (pTDH3) (A.2 Figure 50b). Using this information, we constructed yeast strains in which the GFP output was replaced with the luciferase enzyme, NanoLuc. Two strains were generated, each with an N-terminal MFα signal peptide and C-terminal fusions partners of either SED1 for cell surface display[356] (yNSurface strain) or CBD for cellulose binding (yNCellulose strain) (Figure 10a and b). Notably, the luciferase reporter output outperforms the previous fluorescence output, since the catalytic step greatly increases the sensitivity and reduces background noise (A.2 Figure 51a).

When using projection to pattern Syn-SCOBY materials, we noted that areas more intricately patterned showed poorer resolution, possibly due to the internal light scattering from the opaque cellulose matrix. In addition, changing the *S. cerevisiae* density in the co-culture by either slowing down yeast growth rate or increasing the incubation time in the dark was able to decrease (A.2 Figure 51b), or increase (A.2 Figure 51c) the resolution of the patterns, respectively. These knobs, along with different patterning modes (light mask for rapid, large-scale prototyping and projection for complicated patterning), provide a basic toolset for optogenetic control of the functionalization of BC-based ELMs.

A.2 Supplementary figures

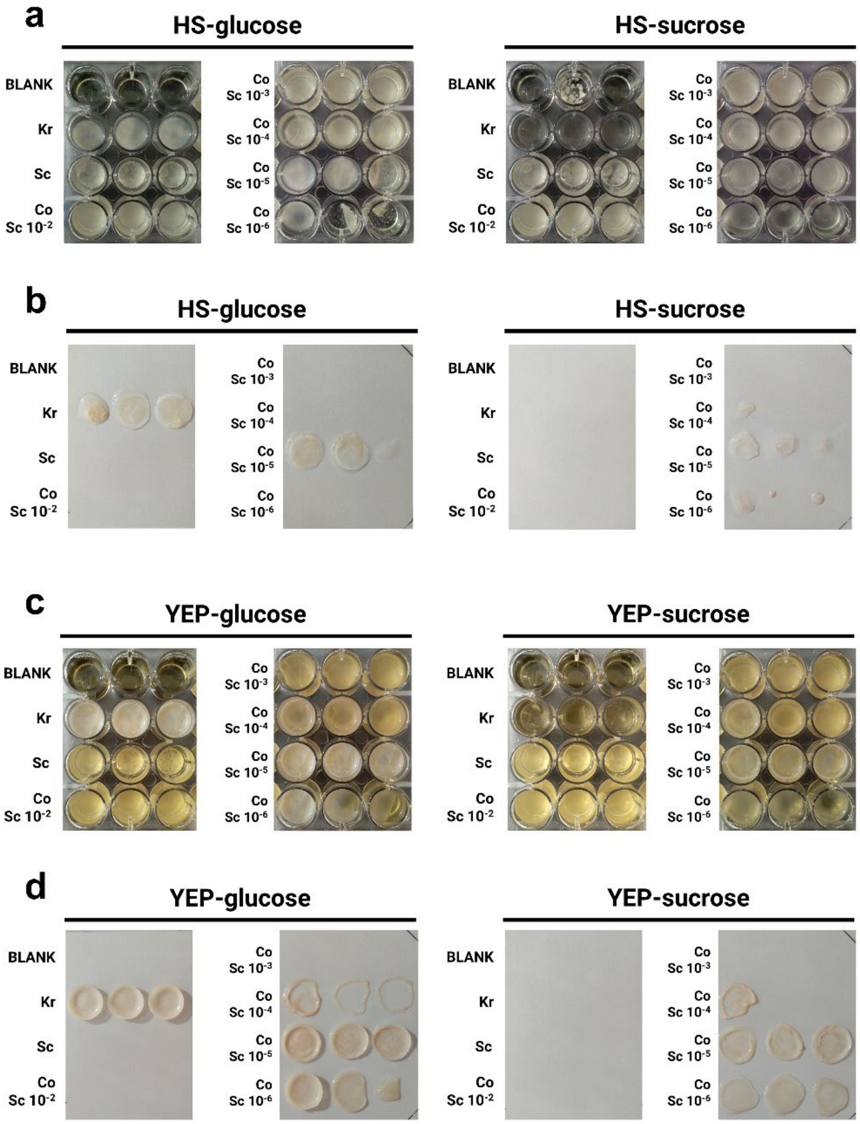

Figure 20 | **Images of cultures and pellicles from the co-culture condition screen.** *S. cerevisiae* (Sc) and *K. rhaeticus* (Kr) were inoculated in monoculture or co-culture (Co) in rich yeast media (YEP) or BC-producing bacteria media (HS) with either glucose or sucrose as the carbon source. For co-cultures, the Sc pre-cultures were diluted into fresh medium over a range from 1/100 (Sc 10^{-2}) to 1/106 (Sc 10^{-6}). In monoculture, Sc pre-cultures were diluted 1/100, and Kr pre-cultures were diluted 1/50. As a control for contamination, wells were included in which no cells were inoculated (BLANK). After 4 days of incubation at 30°C, images were taken of cultures and then of isolated pellicle layers, where present. Cultures **(a)** and pellicles **(b)** produced in HS media and cultures **(c)** and pellicles **(d)** produced in YEP media.

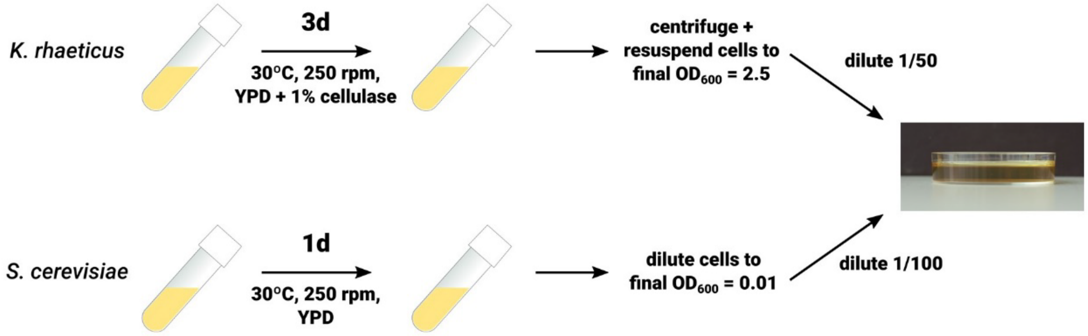

Figure 21 | **Defining and testing a standard protocol for co-culturing *S. cerevisiae* and *K. rhaeticus*.** Schematic outlining the standard co-culture protocol. *K. rhaeticus* and *S. cerevisiae* are grown in monoculture under agitation. *K. rhaeticus* cultures are then centrifuged and resuspended in YEP-sucrose (YPS) medium to a final OD_{600} = 2.5; this step removes trace amounts of cellulase enzyme and normalizes cell density. *S. cerevisiae* cultures are normalized by diluting to an OD_{600} = 0.01 in YPS. Normalized *K. rhaeticus* and *S. cerevisiae* cultures are then inoculated into fresh YPS by diluting 1/50 and 1/100, respectively.

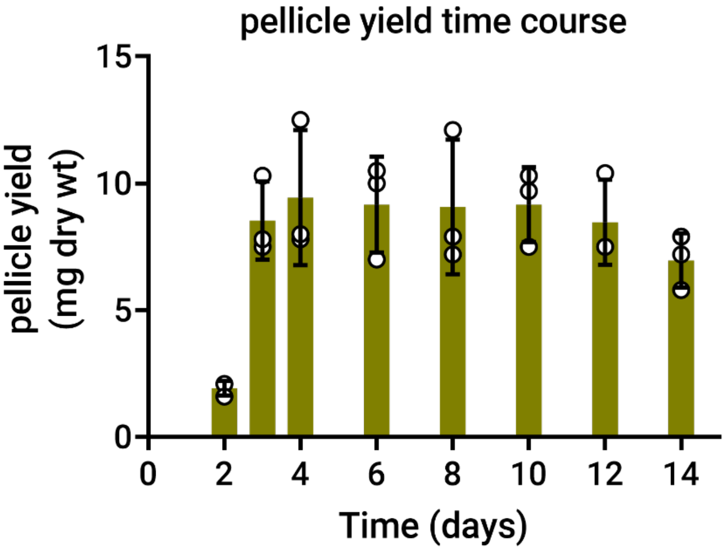

Figure 22 | **Measuring co-culture pellicle yields.** To follow BC production dynamics over time, co-cultures were prepared following our standard protocol and left incubating over several days. At each time point, pellicle layers were removed and dried. Once dried, pellicles were weighed to determine the pellicle yield. Notably, since pellicles were not treated to lyse and remove cells, this measurement includes the contribution from both BC yield and entrapped cells. Pellicle yield rapidly increased between 2 and 3 days, at which point it plateaued. Samples prepared in triplicate; data represent the mean ±1 SD.

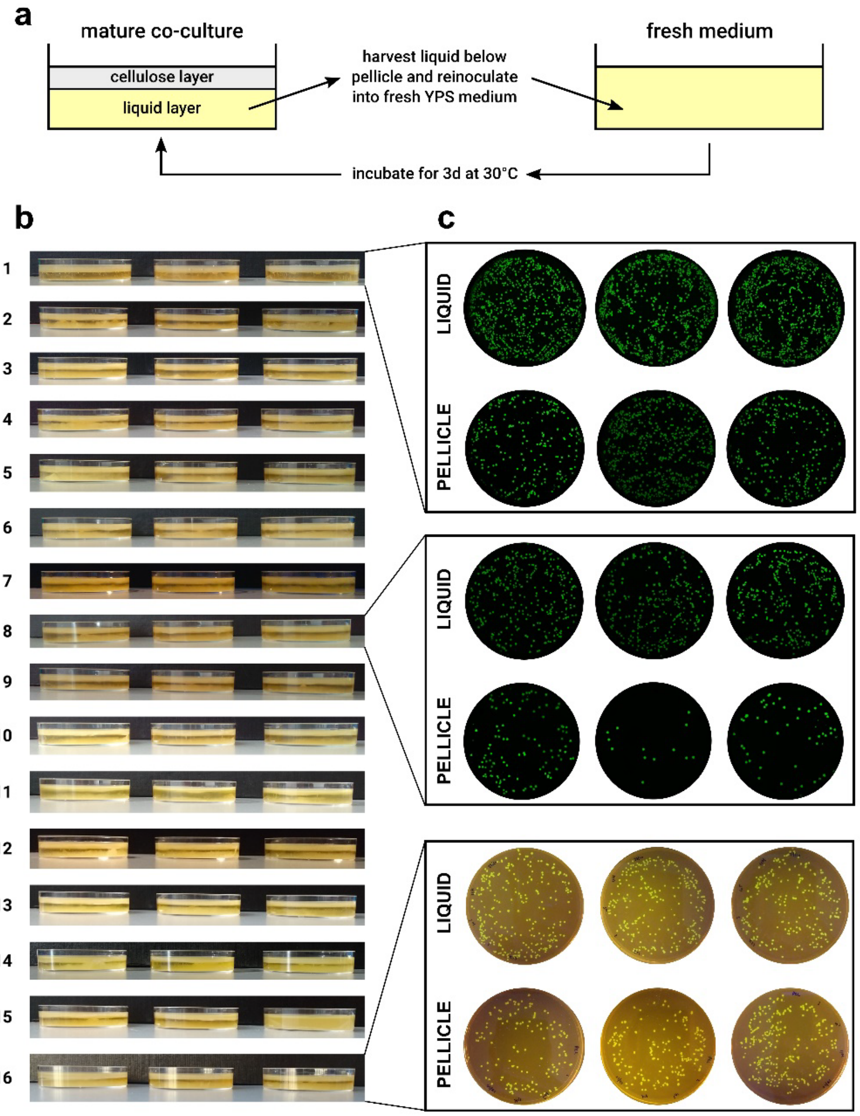

Figure 23 | **Investigating co-culture stability by passage.** **(a)** Co-cultures of *S. cerevisiae* yWS167 and *K. rhaeticus* Kr RFP were passaged by iteratively back-diluting liquid from below the pellicle layer in mature co-cultures into fresh YPS medium. **(b)** At each stage, mature pellicles were imaged. Pellicle formation was constant, indicating *K. rhaeticus* was growing well. In addition, a clear sediment was formed below the pellicle, consistent with *S. cerevisiae* growth. **(c)** To confirm the presence of the initial *S. cerevisiae* strain, which expresses GFP, in passage co-cultures, samples of the liquid below the pellicle (LIQUID) and enzymatically degraded pellicles (PELLICLE) were plated and imaged for GFP fluorescence. In the interest of clarity, plates from only three time points are shown here. The appearance of the final time point is different, as it was imaged for fluorescence using different equipment (fluorescence scanner versus imaging under a transilluminator). All images show that the initial GFP-expressing *S. cerevisiae* strain was maintained throughout passage.

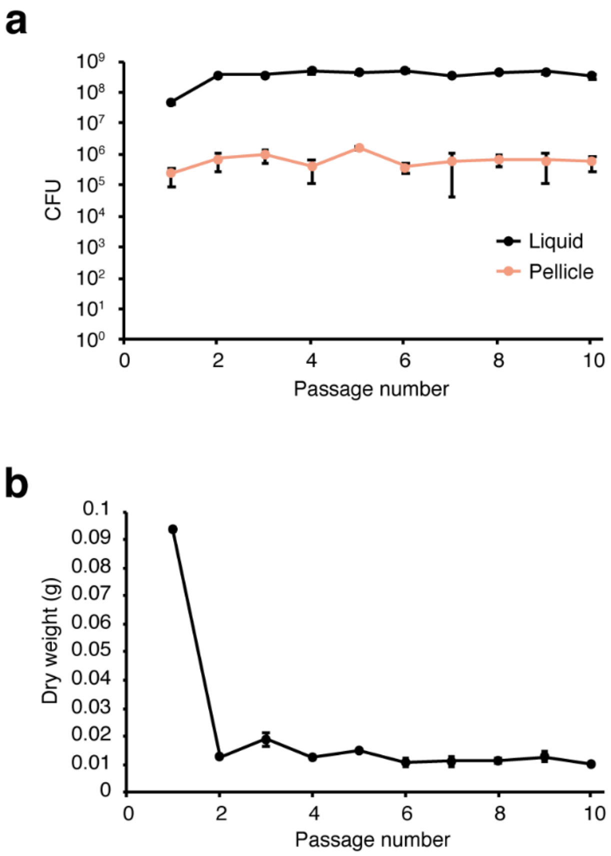

Figure 24 | **Yeast cell count and pellicle dry weight across 10 passages. (a)** Yeast colony forming unit (CFU) of pellicle from the first passage to the tenth passage. Each passage was inoculated using liquid from the previous passage. Data represent the mean ±1 SD from biological triplicates. **(b)** Pellicle dry weight from the first passage to the tenth passage. Pellicles were freeze-dried using a lyophilizer. Data represent the mean ±1 SD from biological triplicates.

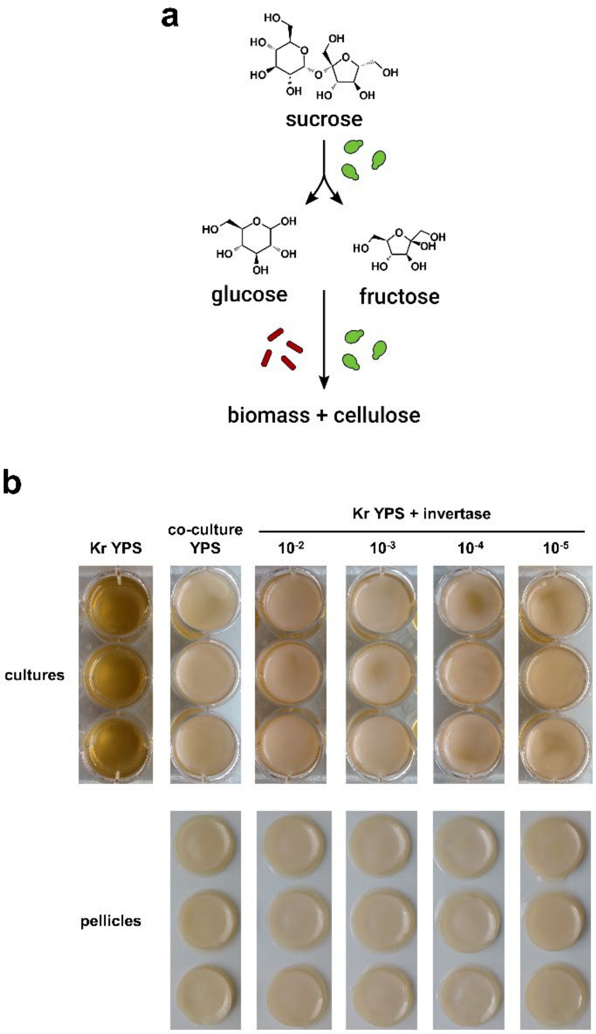

Figure 25 | **A putative metabolic mechanism for *S. cerevisiae* stimulation of *K. rhaeticus* growth. (a)** Various studies report that yeast (green) in kombucha microbial communities degrade extracellular sucrose to glucose and fructose, which both yeast and BC-producing bacteria (red) consume to produce biomass. **(b)** A variety of cultures were prepared in YPS: *K. rhaeticus* Kr RFP monoculture (Kr YPS), co-cultures of Kr RFP and *S. cerevisiae* yWS167 (co-culture YPS), and monocultures of *K. rhaeticus* Kr RFP spiked with a range of dilutions of a stock solution of commercial *S. cerevisiae* invertase at 5000 U/mL concentration (1/100, 1/1000. 1/10,000 and 1/100,000). Images were taken of cultures and, where present, isolated pellicles after 3 days of incubation at 30°C.

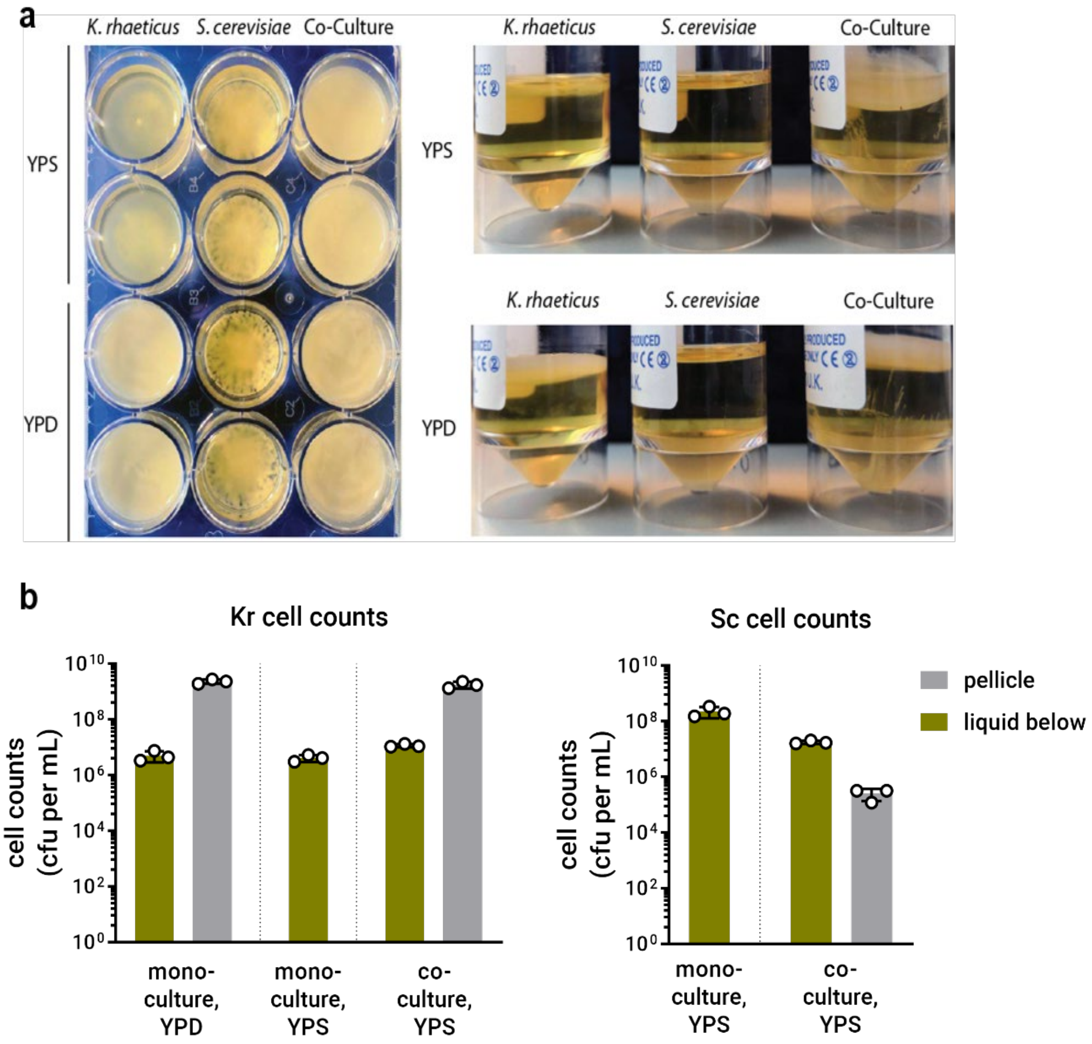

Figure 26 | **Growing co- and monocultures of engineerable *S. cerevisiae* and *K. rhaeticus* in YPD and YPS media. (a)** Images of monocultures and co-cultures of *K. rhaeticus* and *S. cerevisiae* grown for 3 days. *S. cerevisiae* grows well in both YPD and YPS media, forming a sediment at the base of the culture. *K. rhaeticus* grew well in YPD medium, forming a thick pellicle layer at the air-water interface, but failed to form a pellicle in YPS medium. When co-cultured, in both YPD and YPS, a thick pellicle layer was formed as well as a sediment layer at the base of the culture, indicating both *S. cerevisiae* and *K. rhaeticus* had grown. The left panel shows a top view from the different cultures in a 24-well plate. The right panel shows a side view of the different cultures incubated in 20 mL reaction tubes. **(b)** Cell counts of *K. rhaeticus* Kr RFP and *S. cerevisiae* yWS167 were determined by plating and counting the numbers of cells present in the two phases of co-cultures – the liquid layer and the pellicle layer. Cell counts were determined for *K. rhaeticus* grown in monoculture in YPD (Kr YPD) or YPS (Kr YPS) or in co-culture with *S. cerevisiae* in YPS (Co YPS). Cell counts were determined for *S. cerevisiae* grown in monoculture in YPS (Sc YPS) or in co-culture with *K. rhaeticus* in YPS (Co YPS). Samples prepared in triplicate; data represent the mean ±1 SD.

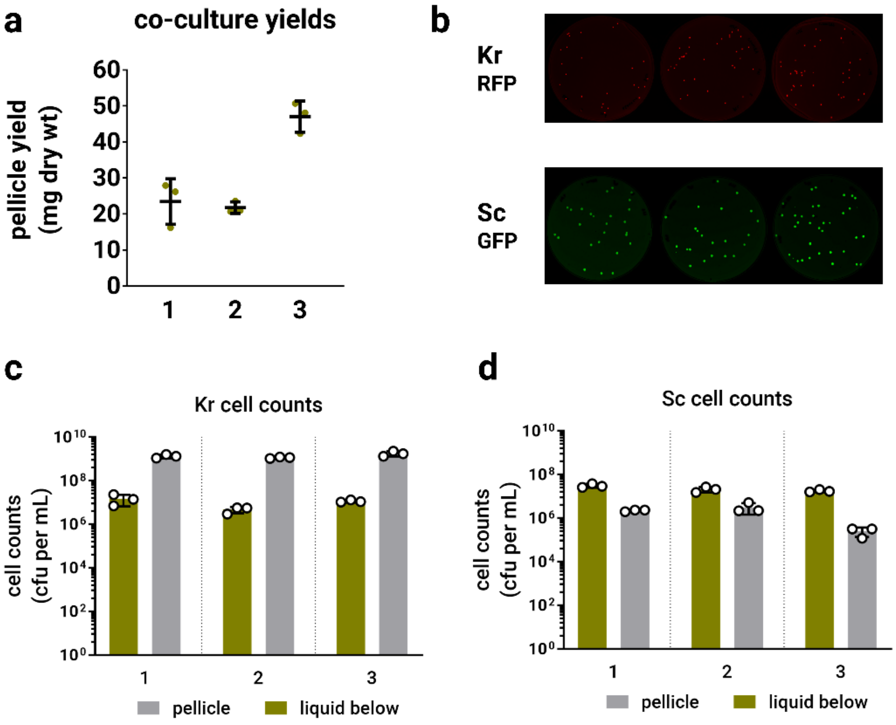

e

Kr cell counts

	liquid			pellicle		
	1	2	3	1	2	3
mean cell counts (cfu/mL)	1.47E+07	4.75E+06	1.14E+07	1.33E+09	1.14E+09	1.77E+09
standard deviation (cfu/mL)	8.02E+06	1.53E+06	1.46E+06	2.60E+08	8.43E+07	4.82E+08

f

Sc cell counts

	liquid			pellicle		
	1	2	3	1	2	3
mean cell counts (cfu/mL)	3.10E+07	2.09E+07	1.78E+07	2.23E+06	3.16E+06	2.53E+05
standard deviation (cfu/mL)	6.24E+06	5.80E+06	2.42E+06	2.08E+05	1.70E+06	1.15E+05

Figure 27 | **Reproducibility of co-culture pellicle yields and cell densities.** **(a)** Pellicle yields were measured on three separate occasions. For each repeat, samples were prepared in triplicate; horizontal bars represent the mean ±1 SD, green circles represent the values of individual samples. **(b)** Cell counts from co-cultures were prepared on three separate occasions by plating onto selective media and scanning for RFP fluorescence for *K. rhaeticus* and GFP fluorescence for *S. cerevisiae*. Cell counts were recorded from both the liquid and pellicle layers for both *K. rhaeticus* **(c)** and *S. cerevisiae* **(d)**. Data are presented from three separate experiments prepared on different occasions. The third dataset (labeled 3) uses the same data presented in Supplementary Figure 7. Samples were prepared in triplicate; data represent the mean ±1 SD. Since logarithmic scales can mask some of the variations, numerical values of cell counts are included for both *K. rhaeticus* **(e)** and *S. cerevisiae* **(f)**.

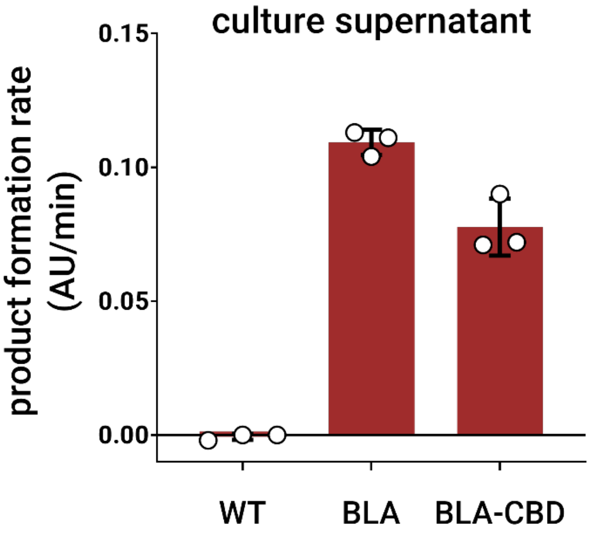

Figure 28 | **Secreted β-lactamase activity in *S. cerevisiae* monoculture.** Culture supernatants from WT, BLA, and BLA-CBD strains were assayed for β-lactamase activity using the colorimetric nitrocefin substrate. The product formation rate was measured using a plate reader. Samples prepared in triplicate; data represent the mean ±1 SD. Notably, the activity detected from the BLA-CBD secreting strain, yCG05, was reduced compared to the BLA secreting strain, yCG04. Since this assay was performed using undiluted supernatants from 24h cultures, the observed activity will be affected by multiple factors. Therefore, the decrease in β-lactamase activity for BLA-CBD could be due to decreased growth rate, decreased secreted protein yields, or an effect of fusion of the CBD to BLA enzyme decreasing its activity by causing steric hindrance, for example.

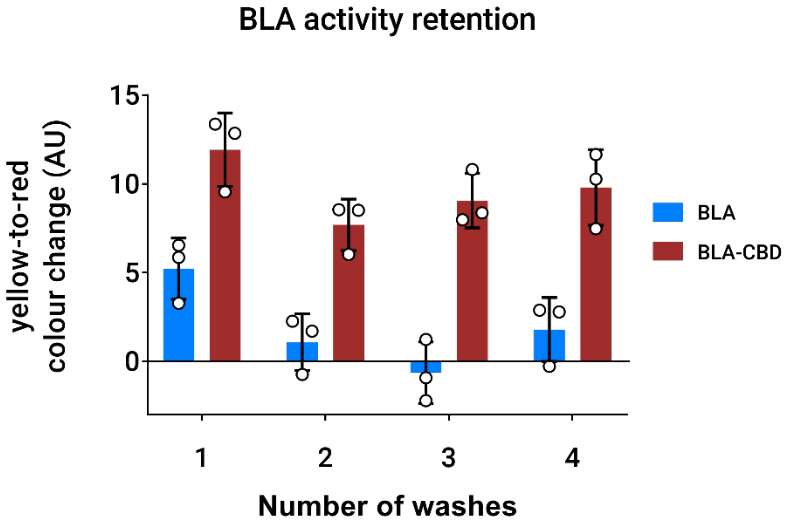

Figure 29 | **Retention of β-lactamase within functionalized material after washing.** As the BLA enzyme is passively incorporated within the BC matrix by diffusion and the BLA-CBD fusion is specifically bound through the CBD-cellulose interaction, it might, be anticipated that BLA enzyme could leach out of the BC material over time, while BLA-CBD would remain bound stably. To test this, dried pellicles functionalized with BLA and BLA-CBD were subjected to multiple rounds of washes in PBS buffer and then assayed for β-lactamase activity. The activity of β-lactamase in BLA-functionalized pellicles (by nitrofecin assay) fell sharply after washing, by contrast, BLA-CBD-functionalized pellicles retained a greater proportion of their original β-lactamase activity after washing. Samples prepared in triplicate; data represent the mean ±1 SD.

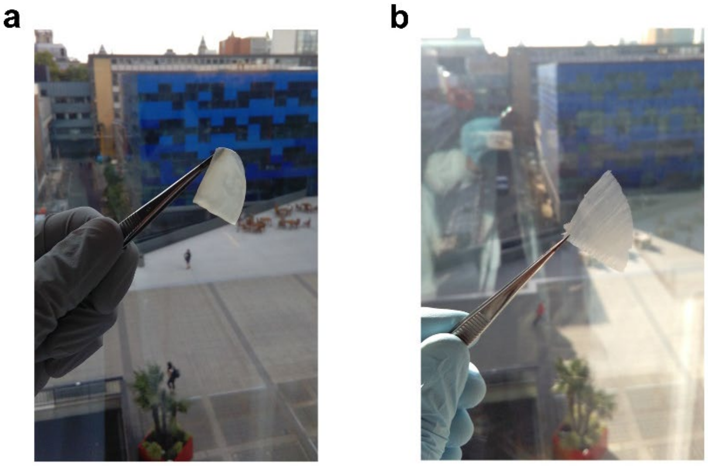

Figure 30 | **Images of wet and dried BC pellicles. (a)** A piece of BC pellicle in its native, wet stated. **(b)** A piece of a BC pellicle following drying using the sandwich method. Dried pellicles are much thinner than wet pellicles due to water loss and are similar in appearance to thin sheets of paper.

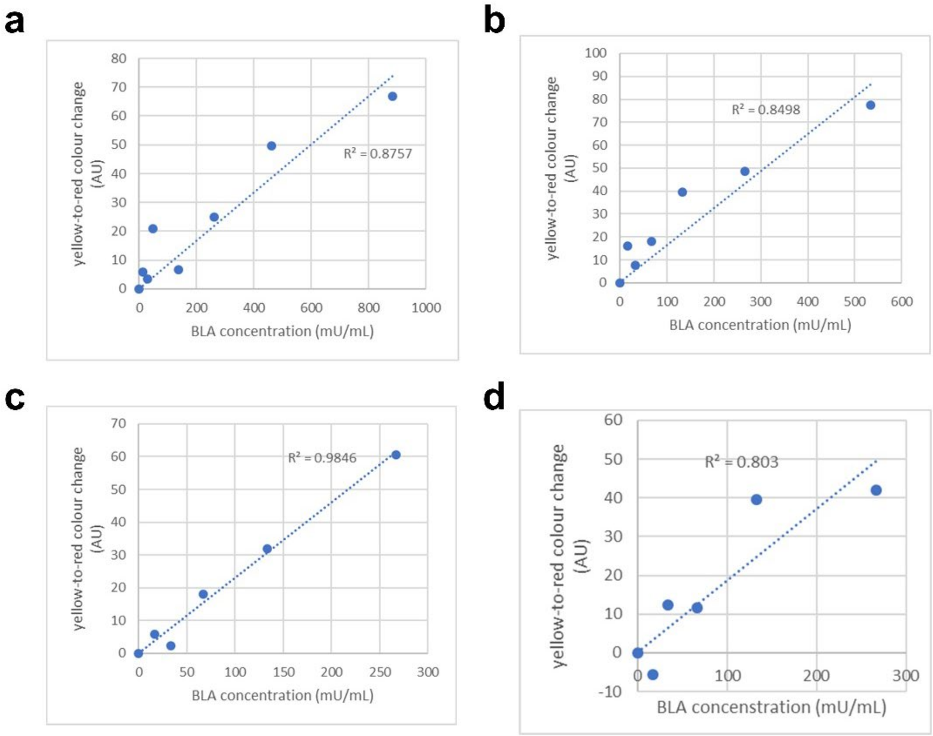

Figure 31 | **BLA assay standard curves.** To calculate absolute β-lactamase activities, standard curves were run alongside wet **(a)**, dry 0 days **(b)**, dry 1 month **(c)** and dry 6 month **(d)** samples. To prepare standard curves, pellicles from co-cultures prepared with WT yeast were treated exactly as sample pellicles (i.e., used wet, dried, or dried and then stored). Pellicles were then supplemented with the indicated amounts of commercial *E. coli* β-lactamase enzyme to create known standards. Assays were performed in parallel with samples and images processed identically to generate standard curves as above.

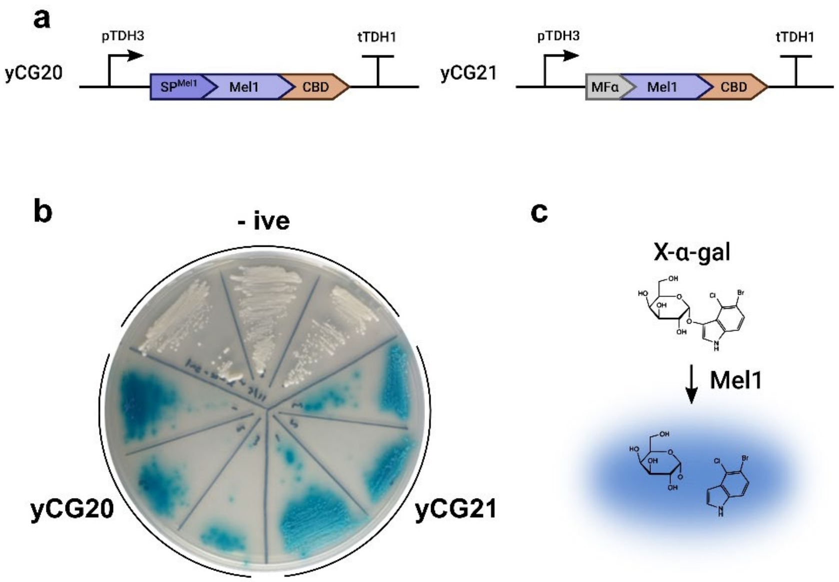

Figure 32 | **Secretion of the alpha-galactosidase Mel1. (a)** Two engineered strains were generated for Mel1 secretion. The first possessed the Mel1 N-terminal signal peptide and Mel1 catalytic region fused to CBDcex (yCG20). The second possessed the MFα signal peptide fused to the Mel1 catalytic region and CBDcex (yCG21). In both constructs, expression was driven by the strong constitutive promoter pTDH3. **(b)** Strains were screened for Mel1 secretion by a plate-based colorimetric assay. Transformants were re-streaked in triplicates on SC URA^- agar supplemented with the colorimetric reporter X-α-gal. After two days growth activity was detectable in the form of halos of blue pigment around colonies of both yCG20 and yCG21. No blue pigment was formed around colonies of the negative control strain, GFP-secreting yCG01 (-ive). Since the growth rate of yCG20 was severely reduced compared to that of yCG21 and yCG01, yCG21 was taken forwards for BC material functionalization. **(c)** X-α-gal is a colorimetric reporter for Mel1; in the presence of active α-galactosidase enzymes, X-α-gal is converted from a colorless substrate to a blue pigment.

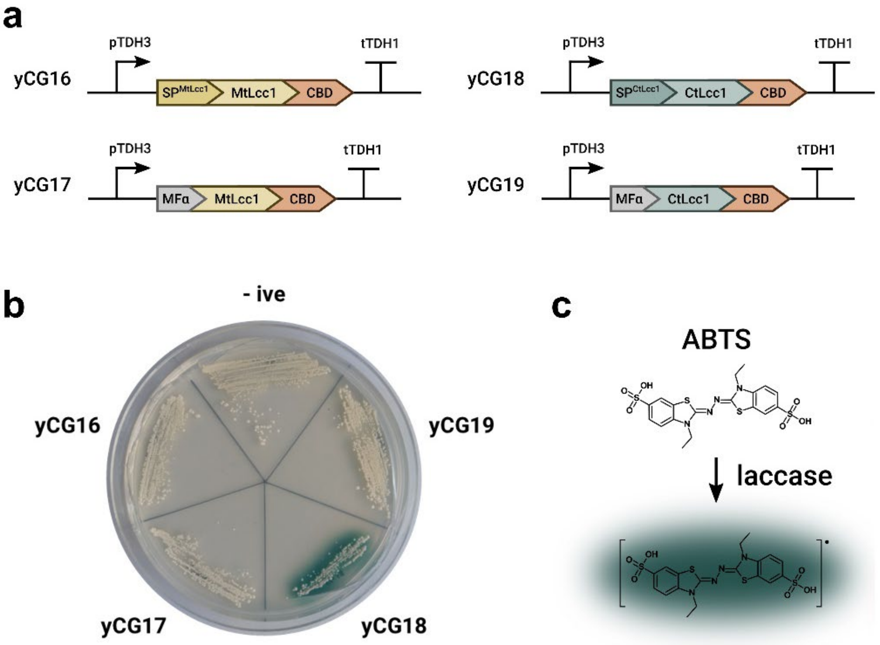

Figure 33 | **Secretion of fungal laccase enzymes. (a)** Four engineered strains were constructed for laccase enzyme secretion. Two strains were engineered to secrete a laccase from *Myceliophthora thermophila* (MtLcc1) with either the native signal peptide (yCG16) or the MFα signal peptide (yCG17). Two strains were engineered to secrete a laccase from *Coriolopsis trogii* (CtLcc1) with either the native signal peptide (yCG18) or the MFα signal peptide (yCG19). All constructs possessed a C-terminal CBD fusion and were expressed from the strong constitutive promoter pTDH3. **(b)** Strains were screened for laccase secretion by a plate-based colorimetric assay. Transformants were re-streaked on SC URA^- agar supplemented with the colorimetric reporter 2,2'-azino-bis(3-ethylbenzothiazoline-6-sulphonic acid) (ABTS) and $CuSO_4$. After two days growth activity was detectable in the form of halos of green pigment around colonies of only yCG18. By contrast, no green pigment was formed around colonies of the negative control strain, GFP-secreting yCG01 (-ive) nor yCG16, yCG17 or yCG19 (although low level activity could be detected after longer incubation times). Therefore, yCG18 was taken forwards for BC material functionalization. **(c)** ABTS is a colorimetric reporter for laccase activity; in the presence of active laccase enzyme, ABTS is converted from a colorless substrate to a green pigment.

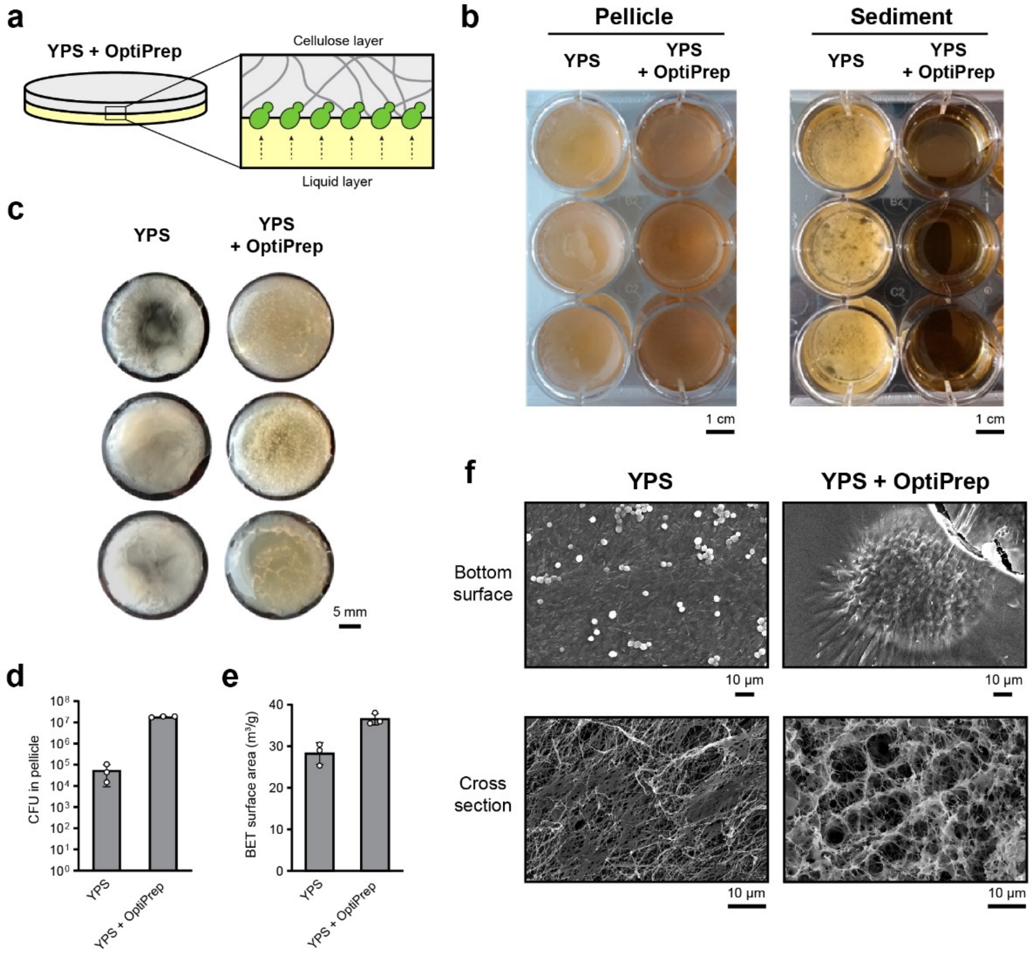

Figure 34 | **Incorporation of *S. cerevisiae* cells within BC material (a)** Schematic demonstrating that modified media density facilitates the incorporation of *S. cerevisiae* cells into the pellicle. **(b)** Co-cultures of *K. rhaeticus* Kr RFP and *S. cerevisiae* yWS167 were prepared in YPS media with or without 45% OptiPrep. Images show the pellicles formed at the air-water interface and the liquid below the pellicle, following pellicle removal. **(c)** Isolated pellicles from YPS and YPS+OptiPrep co-cultures of *K. rhaeticus* Kr RPF and *S. cerevisiae* yWS167. Pellicles isolated from co-cultures with OptiPrep have a speckled appearance due to *S. cerevisiae* colonies. **(d)** Yeast colony forming unit (CFU) counts from pellicles grown in YPS and YPS+OptiPrep using *K. rhaeticus* Kr RPF and *S. cerevisiae* yWS167. Samples prepared in triplicate; data represent mean ±1 SD. **(e)** Brunauer-Emmett-Teller (BET) surface area of the pellicles. Samples prepared in triplicate; data represent mean ±1 SD. **(f)** Sample SEM images of the bottom surface (top) and cross-section (bottom) of pellicles (representative of n = 3).

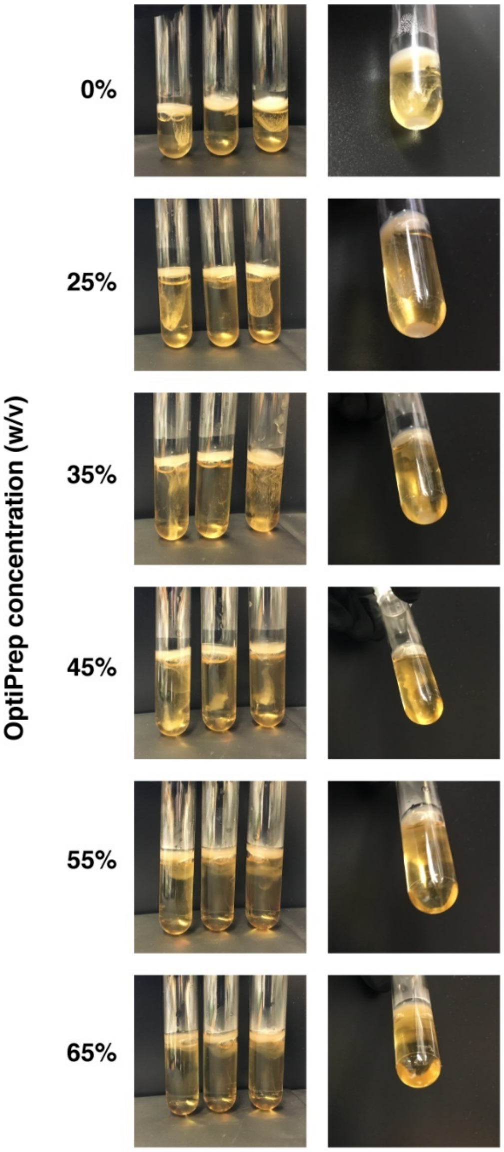

Figure 35 | **The effect of increasing concentrations of OptiPrep on the sedimentation of cells in co-cultures.** Co-cultures (Sc BY4741 and Kr) were prepared in YPS medium supplemented with the indicated concentrations of OptiPrep. After 3 days of growth, samples were imaged in triplicate, and the bottoms of individual tubes were imaged. The cell sediment is only apparent at OptiPrep concentrations less than 35%.

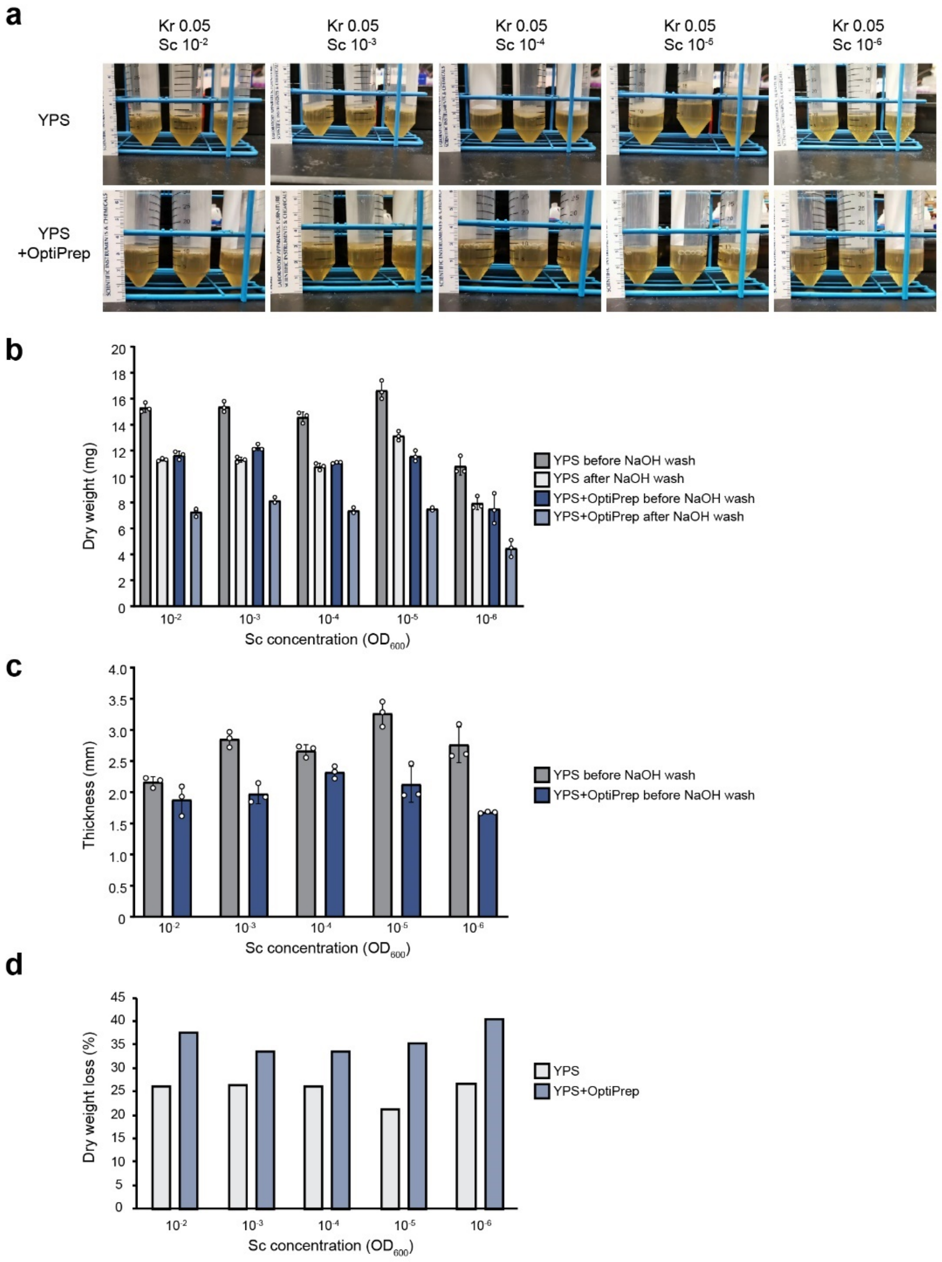

Figure 36 | **Comparison of co-culture behavior in YPS compared to YPS+OptiPrep media. (a)** Side view of pellicles grown for 3 days with different starting Sc concentrations (unit: OD_{600}). **(b)** Dry weights of pellicles grown in YPS and YPS+OptiPrep before and after NaOH wash. (c) Thickness of pellicles grown in YPS and YPS+OptiPrep. (d) Loss in dry weight (% of weight before NaOH wash) of pellicles grown in YPS and YPS+OptiPrep. The extra weight loss in YPS+OptiPrep might originate from the yeast cells incorporated into the bottom surface. Samples prepared in triplicate; data represent the mean ±1 SD.

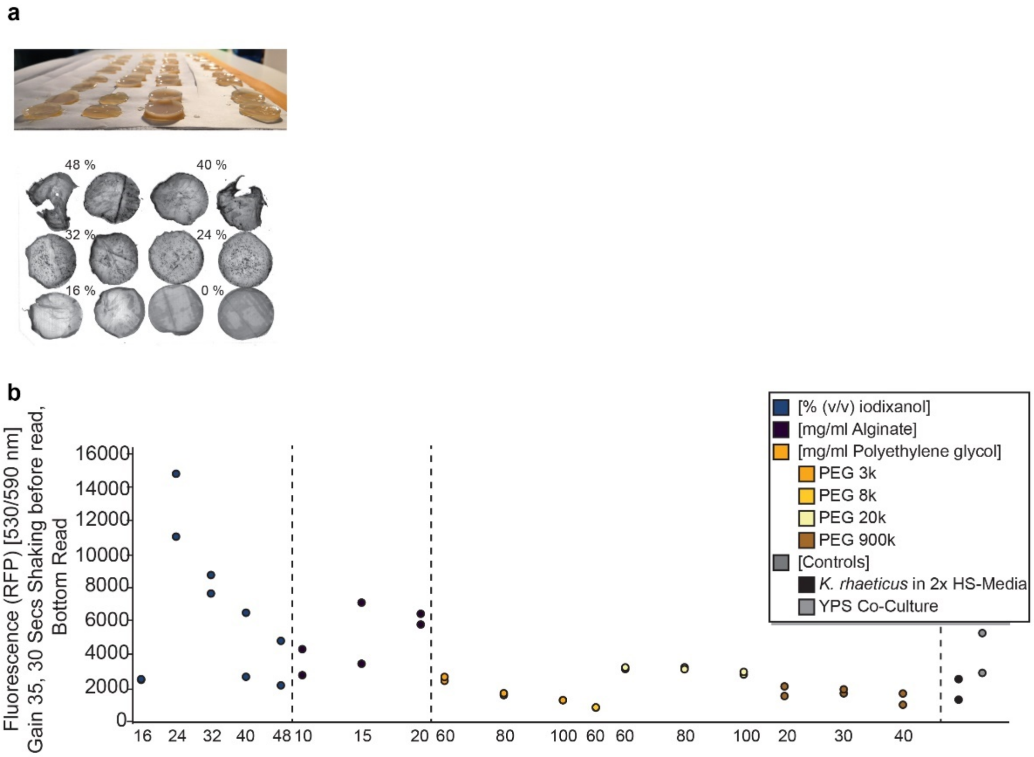

Figure 37 | **Overview of different media supplements and their influence on yeast incorporation in BC pellicles. (a)** Top: A photo of pellicles grown for 3 days under static condition. Bottom: A fluorescent laser scan of the dried cellulose sheets grown in different concentrations of iodixanol. **(b)** After digestion of the pellicle, the overall fluorescence of the cell (yeast cells constitutively expressed an RFP) sediment was determined as a benchmark for yeast incorporation efficiency. Samples prepared in duplicate.

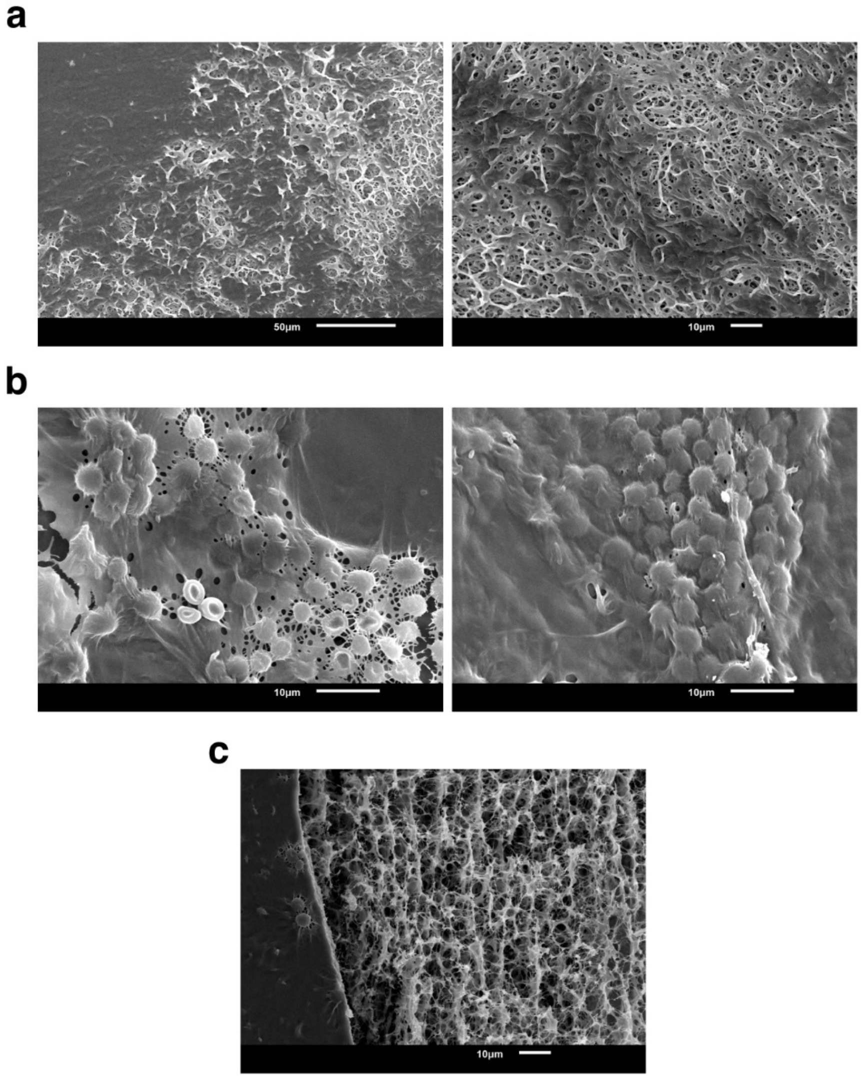

Figure 38 | **Additional SEM images of dried pellicles grown in YPS+OptiPrep. (a)** The top surface of the pellicle. **(b)** The bottom surface of the pellicle. Spherical yeast cells are trapped in the cellulose matrix produced by rod-shaped *K. rhaeticus*. **(c)** Cross-section of the pellicle. Part of the bottom surface is presented on the left. Notably, the top surface of pellicles is largely evenly covered with *K. rhaeticus* cells, while the lower surface contains numerous yeast cells localized in colony-like foci (representative of n = 3 pellicles).

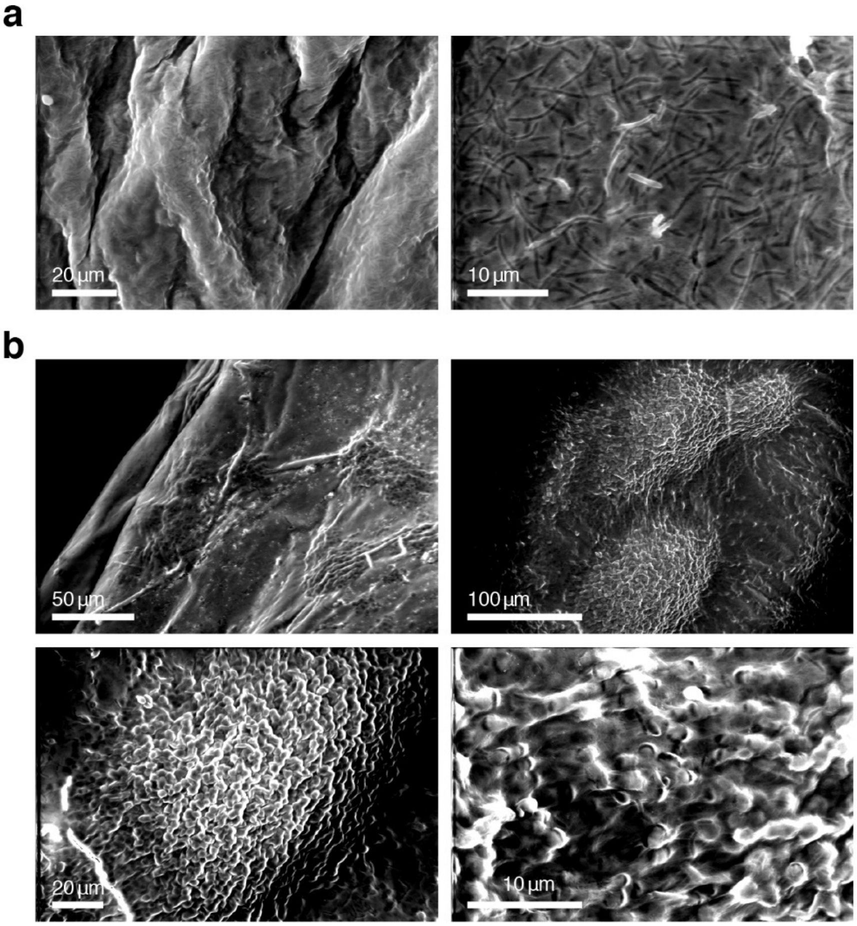

Figure 39 | **Environmental SEM (eSEM) images showing the native, hydrated structure of pellicles grown in YPS+OptiPrep. (a)** The top surface, where rod-shaped *K. rhaeticus* cells covering the entire surface can be easily observed. **(b)** The bottom surface, where numerous yeast cells are localized in colony-like foci (representative of n = 3 pellicles).

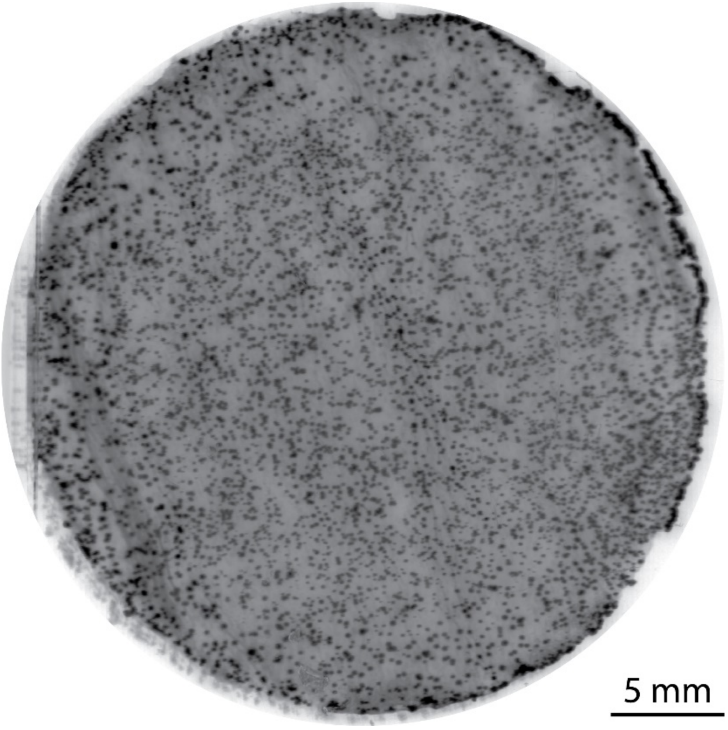

Figure 40 | **Fluorescence scan of a dried cellulose pellicle containing yeast expressing mScarlet-I.** After 3 days of growth of a static co-culture in YPS media supplemented with 40% (v/v) iodixanol, the pellicle was removed from the culture and dried between absorbent papers. The pellicle was then imaged with a laser scanner to obtain a 2D distribution landscape of the incorporated yeast cells. The image was inverted to enhance the visibility of the fluorescent yeast colonies (in black). The darker the spots are, the higher is the fluorescence. The pellicle has a diameter of ca. 30 mm as it was grown in a Falcon 50 mL tube.

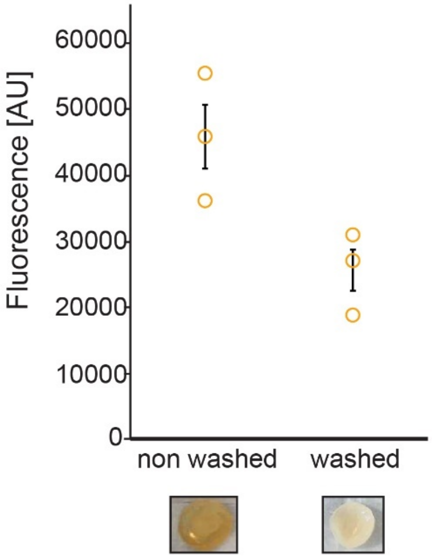

Figure 41 | **Fluorescence measurement of cell sediment after cellulase digestion of the harvested and dried BC pellicle grown in YPS+OptiPrep.** The co-culture was inoculated in 2 mL media with yeast (final OD700=0.0001) and *K. rhaeticu*s (final OD700=0.05) at the same time and grown statically at 30°C for three days in 24-well plates. Three pellicles (washed with 0.75 x PBS and not washed) were digested separately, and the fluorescence of the freed, RFP-expressing yeast cells was determined. The fluorescence was measured with a Synergy HT (BioTek) from the bottom of the plate at 530 nm excitation and 590 nm emission with a gain of 55. The plate was shaken for 30 seconds before measuring. Error bars represent the standard deviation of three different digested pellicles and were placed in the middle of the mean value.

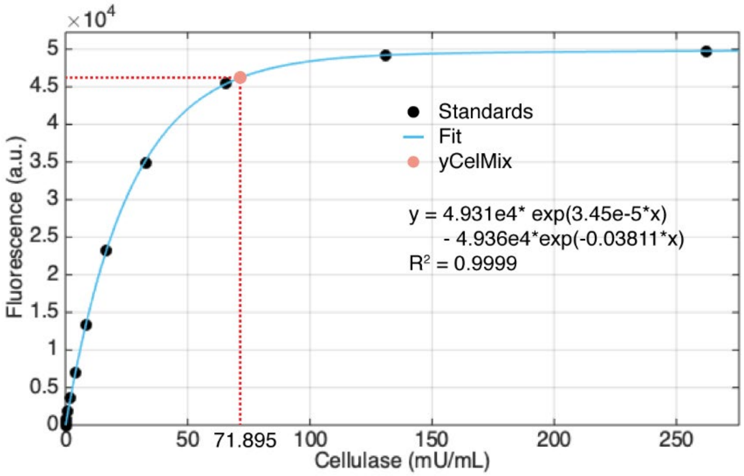

Figure 42 | **Total cellulase activity of yCelMix.** The total cellulase activity of yCelMix saturated culture was calculated from standards prepared with *T. reesei* cellulase mix. Data represent the mean from biological triplicates.

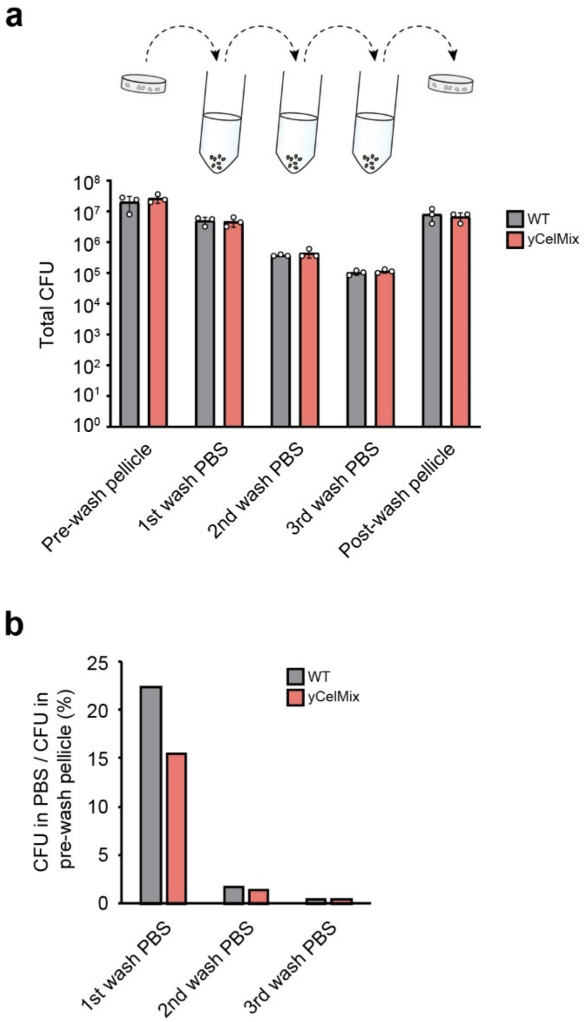

Figure 43 | **Cell leakage in wildtype (WT) and yCelMix pellicles.** Pellicles grown for 3 days were subjected to 3 rounds of 24-hour wash in PBS and characterized for the number of yeast cells escaped. **(a)** Total CFU count of yeast cells in pre-wash pellicles, in PBS after each round of wash, and in post-wash pellicles. **(b)** Cell leakage ratio normalized to CFU in pellicles before wash. Samples prepared in triplicate; data represent the mean ±1 SD.

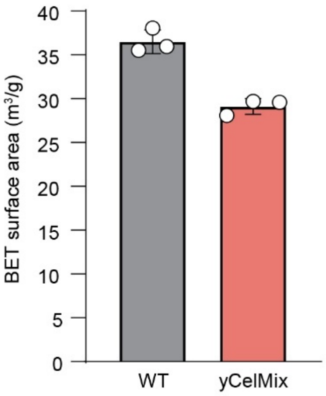

Figure 44 | **BET surface area is decreased in yCelMix pellicle.** Total BET surface area was calculated from dried pellicles. Samples prepared in triplicate; data represent the mean ±1 SD.

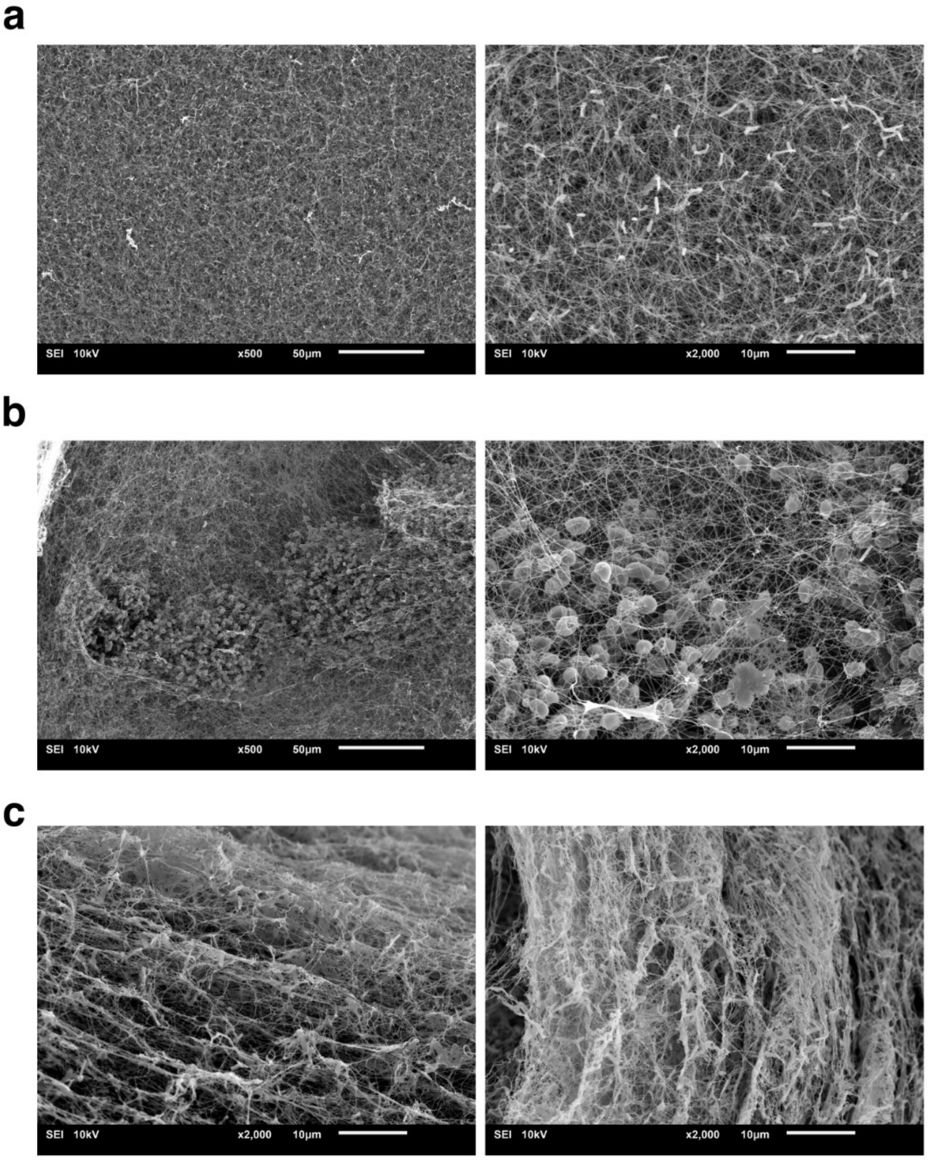

Figure 45 | **SEM images of dried yCelMix pellicles grown in YPS+OptiPrep. (a)** The top surface of the pellicle. **(b)** The bottom surface of the pellicle. Spherical yeast cells are trapped in the loose cellulose matrix, which is partially degraded by the cellulase cocktail. **(c)** Cross-sections of the pellicle (representative of n = 3 pellicles).

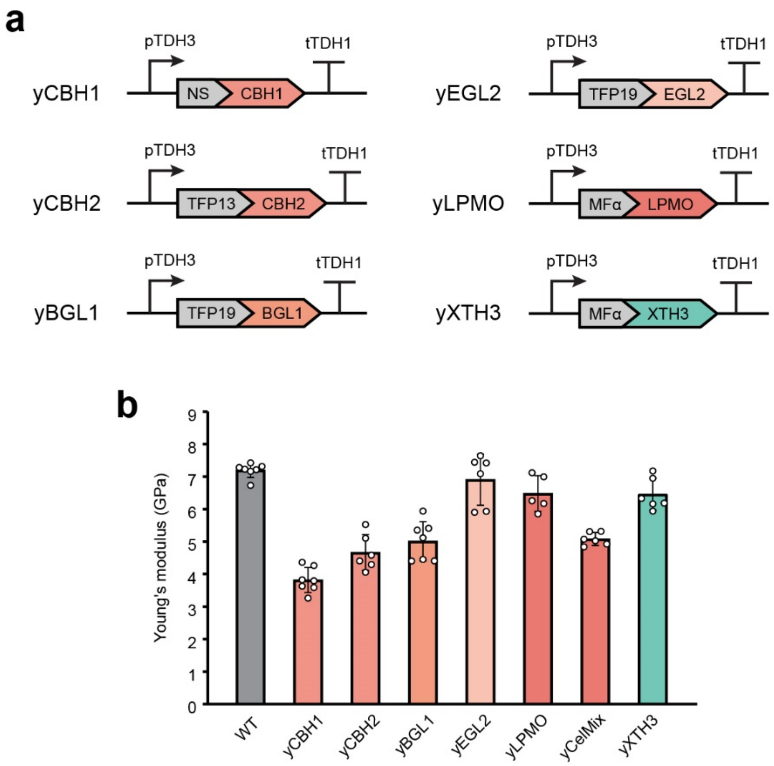

Figure 46 | **Single cellulase secretion strains and their effect on BC stiffness. (a)** Schematic illustrating the construction of single cellulase secretion strains. XTH3 is an *Arabidopsis thaliana* cell-wall enzyme which catalyzes covalent cross-linking between cellulose[357]. The expression of individually secretion-tagged cellulases is driven by the strong constitutive promoter pTDH3. **(b)** Young's moduli of dried pellicles from single cellulase secretion strains and from a cross-linking enzyme secretion strain. Samples prepared in triplicate; data represent the mean ±1 SD.

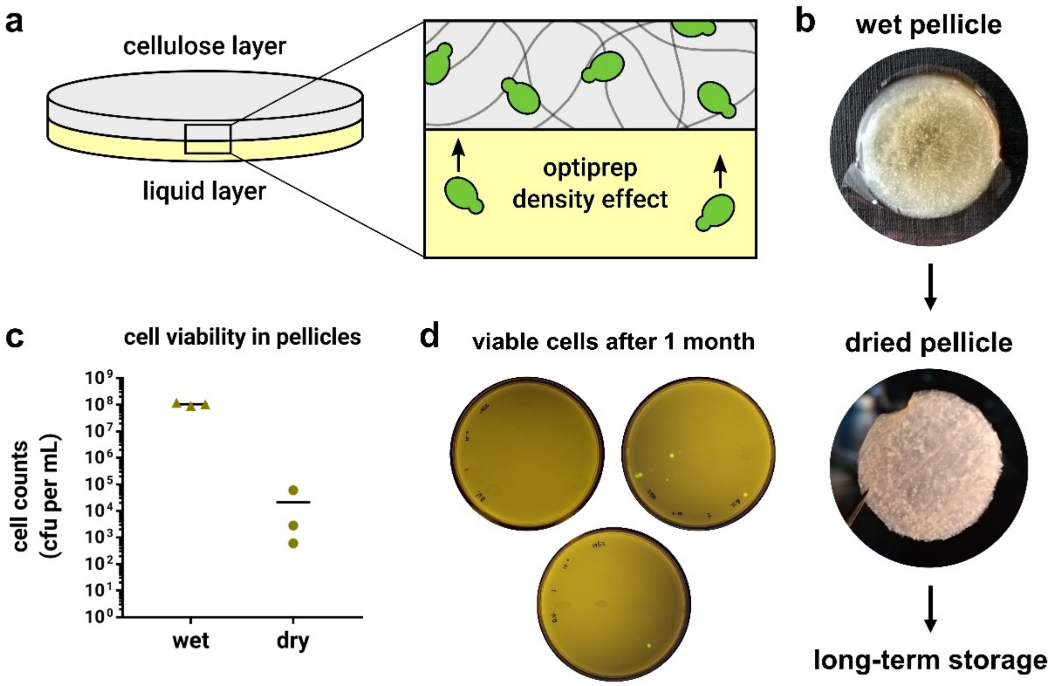

Figure 47 | **Cell viability in dried pellicles. (a)** Schematic illustrating the effect of OptiPrep in the culture medium. By increasing culture medium density, *S. cerevisiae* cells become buoyant, rise to the surface, and become incorporated into the BC matrix. **(b)** Pellicles into which *S. cerevisiae* cells have been incorporated can be dried and stored. **(c)** Cell viability was compared between wet and dried pellicles by enzymatically degraded pellicles, plating, and obtain counts of fluorescent *S. cerevisiae* cells. Bars represent the mean and green dots represent individual values. **(d)** After storage for 1 month, dried pellicles were enzymatically degraded and 100 μL samples plated without dilution. The resultant plates are shown here, imaged for GFP fluorescence under translumination. Viable cells were obtained on two of three plates, indicating that a small number of *S. cerevisiae* cells survive even after 1 month of storage at room temperature.

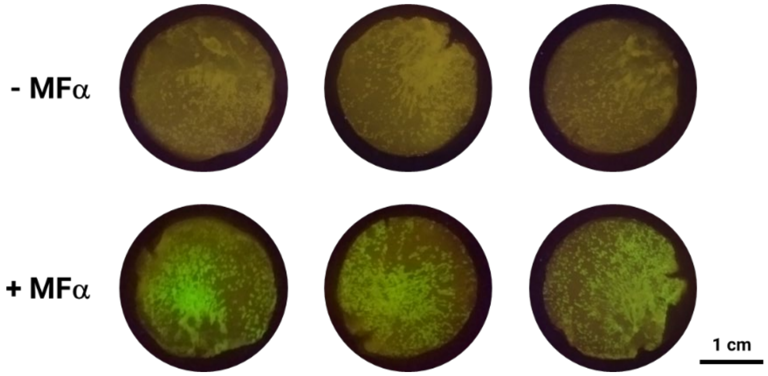

Figure 48 | **Sense-and-response BC materials using a GPCR-based biosensor strain.** Dried pellicles, into which the GPCR-based, MFα-responsive *S. cerevisiae* strain (yWS890) was incorporated, were incubated in fresh YPD medium without agitation in the presence or absence of MFα. After 24 hours, biosensor pellicles were imaged for GFP fluorescence under a transluminator. Samples prepared in triplicate.

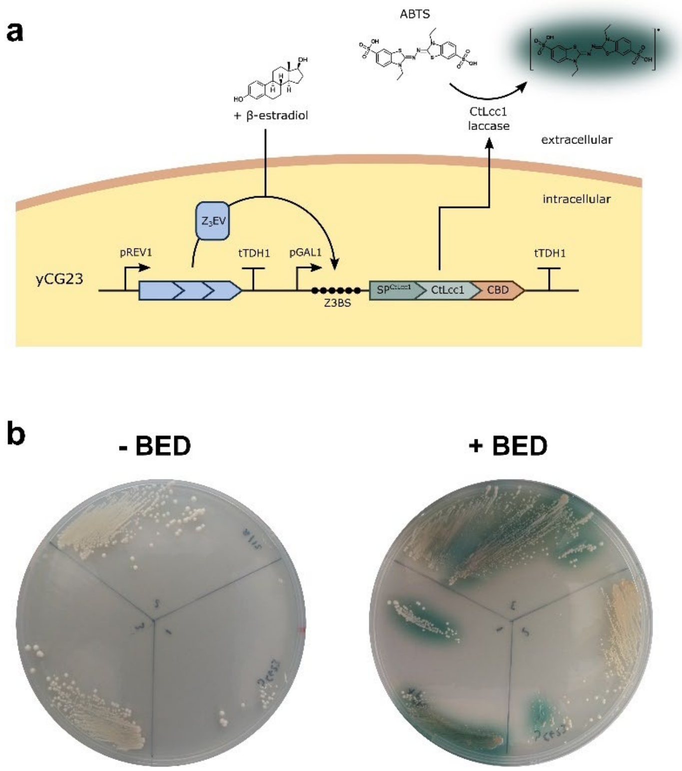

Figure 49 | **BED-inducible CtLcc1 laccase secretion. (a)** A strain, yCG23, was constructed for engineered CtLcc1 secretion in response to the presence of β-estradiol (BED). A two-gene construct was assembled using the YTK cloning system. The first gene encoded constitutive expression of the BED-responsive synthetic transcription factor Z_3EV. The second gene encoded a fusion of the CtLcc1 signal peptide and catalytic region fused to a C-terminal CBDcex domain, all under control of the Z_3EV-responsive promoter. In the presence of BED, Z_3EV will translocate to the nucleus, bind the Z3 binding sites (Z3BS) upstream of the CtLcc1-CBD ORF and induce transcription. CtLcc1-CBD secretion directed by the MFα signal peptide enables extracellular oxidation of the ABTS substrate to a colorimetric product. **(b)** Transformants were re-streaked in triplicate onto agar containing the colorimetric reporter of laccase activity, ABTS and $CuSO_4$ in the presence or absence of BED. After 3 days of growth, a clear halo of green pigment was observed only in the presence of BED, indicating successful induction of CtLcc1 secretion.

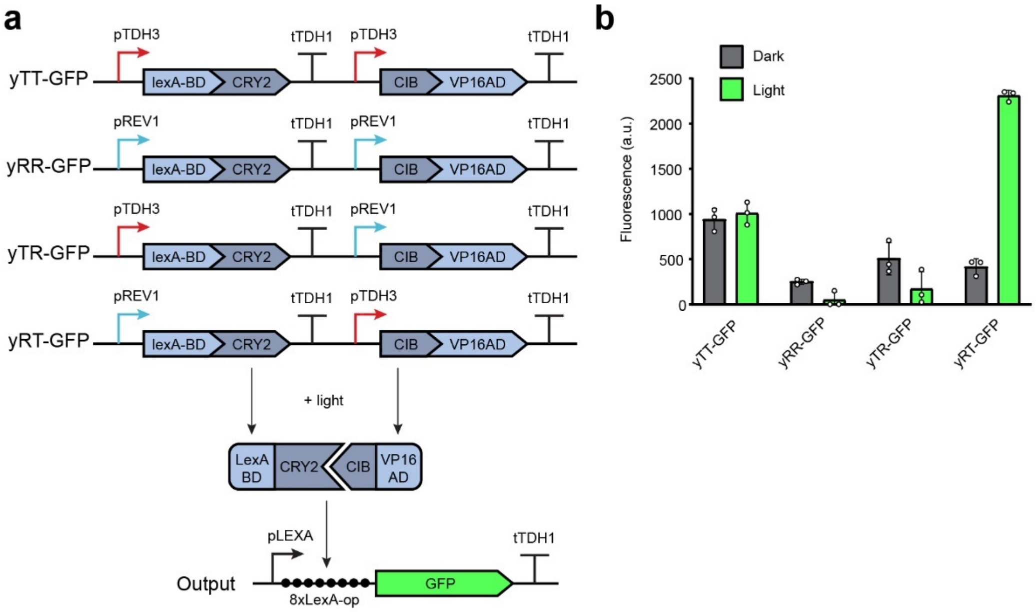

Figure 50 | **Optimization of light induction. (a)** Schematic illustrating the design of four combinations of promoter strength pairs. The strong constitutive promoter (pTDH3) is marked in red and the weak constitutive promoter (pREV1) is marked in blue. They drive the expression of the DNA-binding component and activation component, which together drive the expression of GFP in the presence of light. **(b)** GFP expression of yeast culture in liquid in the dark or after 4 hours of light induction. Data represent the mean ±1 SD from biological triplicates.

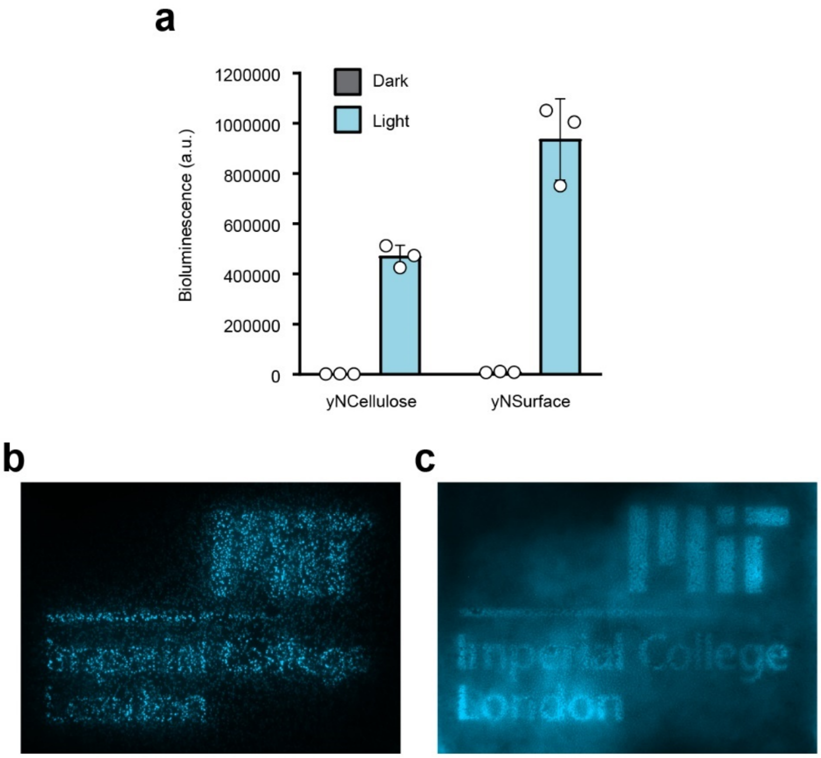

Figure 51 | **Light induction of luciferase expression and the tuneable resolution on BC living films.** **(a)** Bioluminescence of yNCellulose and yNSurface liquid culture after 4 hours of light induction. Data represent the mean ±1 SD from biological triplicates. **(b)** yNSurface ΔSED1 pellicle after 12 hours of exposure to a projected pattern. This knockout strain showed slower growth compared to yNSurface. Less foci were formed and they are unable to provide enough resolution to reflect the pattern. **(c)** yNCellulose pellicle after 1-day outgrowth followed by 12 hours of exposure. Increased yeast cell number on the surface provides a higher resolution for patterning. Higher background activity reflects the diffusion of NanoLuc-CBD within the BC material.

A.3 Supplementary tables

Table 1 | Strains used in this study

Strains	Description and phenotype	Source
Komagataeibacter rhaeticus iGEM	BC-producing bacterium isolated from kombucha tea	Florea et al.[73]
K. rhaeticus Kr RFP	Constitutive mRFP expression. *K. rhaeticus* transformed with J23110-mRFP1-331Bb.	Florea et al.[73]
Sc BY4741	MATa his3Δ1 leu2Δ0 met15Δ0 ura3Δ0	Dharmacon yeast collection
Sc YSC6273	BY4741 sed1Δ::KanMX	Dharmacon yeast collection
Sc yWS167	Constitutive GFP expression, BY4741 transformed with integrative plasmid pWS702	This work
Sc yCG01	Constitutive secretion of MFa-sfGFP, BY4741 transformed with integrative plasmid pCG01	This work
Sc yCG04	Constitutive secretion of MFa-BLA, BY4741 transformed with integrative plasmid pCG04	This work
Sc yCG05	Constitutive secretion of MFa-BLA-CBDcex, BY4741 transformed with integrative plasmid pCG05	This work
Sc yCG16	Constitutive secretion of MtLcc1 signal peptide-MtLcc1-CBDcex, BY4741 transformed with integrative plasmid pCG16	This work
Sc yCG17	Constitutive secretion of MFa signal peptide-MtLcc1-CBDcex, BY4741 transformed with integrative plasmid pCG17	This work
Sc yCG18	Constitutive secretion of CtLcc1 signal peptide-CtLcc1-CBDcex, BY4741 transformed with integrative plasmid pCG18	This work
Sc yCG19	Constitutive secretion of MFa signal peptide-CtLcc1-CBDcex, BY4741 transformed with integrative plasmid pCG19	This work
Sc yCG20	Constitutive secretion of Mel1 signal peptide-Mel1-CBDcex, BY4741 transformed with integrative plasmid pCG20	This work
Sc yCG21	Constitutive secretion of MFa signal peptide-Mel1-CBDcex, BY4741 transformed with integrative plasmid pCG21	This work
Sc yCG23	β-estradiol inducible secretion of CtLcc1 laccase. BY4741 transformed with integrative plasmid pCG23	This work
Sc yGPH093	β-estradiol inducible GFP expression. BY4741 transformed with integrative plasmid pGPY093	Pothoulakis et al.[235]
Sc yWS890	Alpha-factor-inducible GFP expression. "Design 4" strain from Shaw el at. (2019): BY4741 sst2Δ0 far1Δ0 bar1Δ0 ste2Δ0 ste12Δ0 gpa1Δ0 ste3Δ0 mf(alpha)1Δ0 mf(alpha)2Δ0 mfa1Δ0 mfa2Δ0 gpr1Δ0 gpa2Δ0 LexO(6x)-pLEU2m-sfGFP-tTDH1-LEU2 pCCW12-STE2-tSSA1-pPGK1-GPA1-tENO2-pRAD27-LexA-PRD-tENO1-URA3	Shaw et al.[354]
Sc yCelMix	Constitutive secretion of CtCbh1, ClCbh2, SfBgl1, and PaLPMO9H, BY4741 transformed with integrative plasmid pCelMix	This work
Sc yCBH1	Constitutive secretion of CtCbh1, BY4741 transformed with integrative plasmid pCBH1	This work
Sc yCBH2	Constitutive secretion of ClCbh2, BY4741 transformed with integrative plasmid pCBH2	This work

Sc yBGL1	Constitutive secretion of SfBgl1, BY4741 transformed with integrative plasmid pBGL1	This work
Sc yEGL2	Constitutive secretion of TrEgl2, BY4741 transformed with integrative plasmid pEgl2	This work
Sc yLPMO	Constitutive secretion of PaLPMO9H, BY4741 transformed with integrative plasmid pLPMO	This work
Sc yXTH3	Constitutive secretion of AtXth3, BY4741 transformed with integrative plasmid pXTH3	This work
Sc yTT-GFP	Blue light inducible GFP expression. BY4741 transformed with integrative plasmid pTT-GFP	This work
Sc yRR-GFP	Blue light inducible GFP expression. BY4741 transformed with integrative plasmid pRR-GFP	This work
Sc yTR-GFP	Blue light inducible GFP expression. BY4741 transformed with integrative plasmid pTR-GFP	This work
Sc yRT-GFP	Blue light inducible GFP expression. BY4741 transformed with integrative plasmid pRT-GFP	This work
Sc yNCellulose	Blue light inducible NanoLuc-CBD secretion. BY4741 transformed with integrative plasmid pNCellulose	This work
Sc yNSurface	Blue light inducible NanoLuc surface display. BY4741 transformed with integrative plasmid pNSurface	This work
Sc yNSurfaceΔSED1	Blue light inducible NanoLuc surface display. YSC6273 transformed with integrative plasmid pNSurface	This work
Sc yWO68	Constitutive expression of mScarlet-I, BY4741 (ΔAga1, ΔAga2) transformed with integrative plasmid pWO68.	This work

Table 2 | Plasmids used in this study.

Plasmid	Construct details	Source
J23110-mRFP1-331Bb	Constitutive mRFP1 expression from the pSEVA-331Bb backbone plasmid. Expression is driven by the low strength J23110 promoter. Addgene #78277	Florea et al.[73]
pYTK001	YTK entry vector into which new DNA parts can be cloned using BsmBI golden gate reactions, verified and stored for later assemblies.	Lee et al.[358]
pYTK096	Pre-assembled YTK plasmid containing genetic elements enabling cloning in *E. coli* and later integrative transformation into the URA3 locus in *S. cerevisiae*. Golden gate assembly allows insertion of YTK type 2-3-4 parts.	Lee et al.[358]
pWS041	Pre-assembled YTK acceptor plasmid into which single gene cassettes can be cloned, consisting of an sfGFP dropout part flanked by YTK connectors ConS and Con1. Backbone enabling propagation in *E. coli*	This study
pWS042	Pre-assembled YTK acceptor plasmid into which single gene cassettes can be cloned, consisting of an sfGFP dropout part flanked by YTK connectors Con1 and ConE. Backbone enabling propagation in *E. coli*	This study
pWS702	YTK single gene cassette plasmid for constitutive GFP expression, pTDH3-sfGFP-tTDH1. Backbone enabling propagation in *E. coli* and markerless integration at the HO locus in *S. cerevisiae*	This study
pCG01	YTK single gene cassette plasmid for constitutive sfGFP secretion, pTDH3-MFa-sfGFP-tTDH1. Backbone enabling propagation in *E. coli* and integration at the URA3 locus in *S. cerevisiae*	This study
pCG04	YTK single gene cassette plasmid for constitutive BLA secretion, pTDH3-MFa-BLA-tTDH1. Backbone enabling propagation in *E. coli* and integration at the URA3 locus in *S. cerevisiae*	This study
pCG05	YTK single gene cassette plasmid for constitutive BLA-CBD secretion, pTDH3-MFa-BLA-CBD-tTDH1. Backbone enabling propagation in *E. coli* and integration at the URA3 locus in *S. cerevisiae*	This study
pCG16	YTK single gene cassette plasmid for constitutive MtLcc1-CBD secretion, pTDH3-MtLcc1^{SP}-MtLcc1-CBD-tTDH1. Backbone enabling propagation in *E. coli* and integration at the URA3 locus in *S. cerevisiae*	This study
pCG17	YTK single gene cassette plasmid for constitutive MtLcc1-CBD secretion, pTDH3-MFa-MtLcc1-CBD-tTDH1. Backbone enabling propagation in *E. coli* and integration at the URA3 locus in *S. cerevisiae*	This study
pCG18	YTK single gene cassette plasmid for constitutive CtLcc1-CBD secretion, pTDH3-CtLcc1^{SP}-CtLcc1-CBD-tTDH1. Backbone enabling propagation in *E. coli* and integration at the URA3 locus in *S. cerevisiae*	This study
pCG19	YTK single gene cassette plasmid for constitutive CtLcc1-CBD secretion, pTDH3-MFa-CtLcc1-CBD-tTDH1. Backbone enabling propagation in *E. coli* and integration at the URA3 locus in *S. cerevisiae*	This study
pCG20	YTK single gene cassette plasmid for constitutive Mel1-CBD secretion, pTDH3-Mel1^{SP}-Mel1-CBD-tTDH1. Backbone enabling propagation in *E. coli* and integration at the URA3 locus in *S. cerevisiae*	This study
pCG21	YTK single gene cassette plasmid for constitutive Mel1-CBD secretion, pTDH3-MFa-Mel1-CBD-tTDH1. Backbone enabling propagation in *E. coli* and integration at the URA3 locus in *S. cerevisiae*	This study
pCG22	YTK single gene cassette plasmid for expression of CtLcc1 signal peptide-CtLcc1-CBD driven by the pZ3 promoter: pZ3-CtLcc1SP-CtLcc1-CBDcex-tTDH1. Backbone enabling propagation in *E. coli*	This study
pCG23	YTK multi gene cassette plasmid for β-estradiol inducible CtLcc1-CBD secretion, cassette 1: pREV1-Z$_3$E-VP16^{AD}-tTDH1, cassette 2: pGAL1^{6xZ3BS}-	This study

	CtLcc1 signal peptide-CtLcc1-CBD-tTDH1. Backbone enabling propagation in *E. coli* and integration at the URA3 locus in *S. cerevisiae*	
pGPY093	YTK multi gene cassette plasmid for β-estradiol inducible GFP expression, cassette 1: pREV1-Z$_3$E-VP16^{AD}-tTDH1, cassette 2: pGAL1^{6xZ3BS}-sfGFP-tTDH1. Backbone enabling propagation in *E. coli* and integration at the URA3 locus in *S. cerevisiae*	Pothoulakis et al.[235]
pGPY074	YTK single gene cassette plasmid for expression of Z$_3$EV driven by the weak constitutive promoter pREV1: pREV1-Z$_3$E-VP16^{AD}-tTDH1. Backbone enabling propagation in *E. coli*	Pothoulakis et al.[235]
pGPY085	YTK single gene cassette plasmid for expression of sfGFP driven by the pZ3 promoter: pZ3-sfGFP-tTDH1. Backbone enabling propagation in *E. coli*	This study
pWS032	YTK position 3b part containing the *E. coli* TEM1 beta-lactamase BLA (UniProt: Q6SJ61) mature protein, lacking signal peptide	This study
pWS033	YTK position 3 part containing sfGFP	Shaw et al.[354]
pWS034	YTK position 3b part containing sfGFP	This study
pWS433	YTK position 3a part containing the S. cerevisiae mating-factor alpha (UniProt: P01149) signal peptide	This study
pWS930	YTK position 3a part containing a fusion of the Zif268 DNA binding domain and the ligand binding domain of the human estrogen receptor	Pothoulakis et al.[235]
pWS935	YTK position 3b part containing the VP16 transcriptional activation domain	Pothoulakis et al.[235]
pPPK027	YTK position 4a part containing the CBDcex cellulose binding domain from the *Cellulomonas fimi* Cex exoglucanase (UniProt: P07986)	This study
pPPK041	YTK position 3a part containing the *Myceliophthora thermophila* laccase Lcc1 (UniProt: Q9HDQ0) signal peptide	This study
pPPK042	YTK position 3a part containing the *Coriolopsis trogii* laccase Lcc1 (UniProt: G2QG31) signal peptide	This study
pPPK043	YTK position 3a part containing the *S. cerevisiae* alpha-galactosidase Mel1 (UniProt: P04824) signal peptide	This study
pWS1078	YTK position 2 part containing a modified GAL1 promoter containing six Zif268 binding sequences	Pothoulakis et al.[235]
pPPK044	YTK position 3b part containing the *Myceliophthora thermophila* laccase Lcc1 (UniProt: Q9HDQ0) mature protein, lacking signal peptide	This study
pPPK045	YTK position 3b part containing the *Coriolopsis trogii* laccase Lcc1 (UniProt: G2QG31) mature protein, lacking signal peptide	This study
pPPK046	YTK position 3b part containing the *S. cerevisiae* alpha-galactosidase Mel1 (UniProt: P04824) mature protein, lacking signal peptide	This study
pWS473	Pre-assembled YTK plasmid containing genetic elements enabling cloning in *E. coli* and later markerless integrative transformation into the HO locus in S. cerevisiae. Golden gate assembly allows insertion of YTK type 2-3-4 parts.	This study
pCelMix	YTK multi gene cassette plasmid for constitutive cellulase cocktail secretion, cassette 1: pTDH3-NS-CtCbh1-tENO1, cassette 2: pCCW12-TFP13-ClCbh2-tADH1, cassette 3: pTEF1-TFP19-SfBgl1-tPGK1, cassette 4: pTEF2-TFP19-TrEgl2-tENO2, cassette 5: pPGK1-MFa-PaLPMO9H-tTDH1. Backbone enabling propagation in *E. coli* and integration at the URA3 locus in *S. cerevisiae*	This study
pLSR1-CBH1	YTK single gene cassette 1 plasmid for constitutive Cbh1 secretion, pTDH3-NS-CtCbh1-tENO1 inserted onto pYTKLSR1DO	This study
pL1R2-CBH2	YTK single gene cassette 2 plasmid for constitutive Cbh2 secretion, pCCW12-TFP13-ClCbh2-tADH1 inserted onto pYTKL1R2DO	This study
pL2R3-BGL1	YTK single gene cassette 3 plasmid for constitutive Bgl1 secretion, pTEF1-TFP19-SfBgl1-tPGK1 inserted onto pYTKL2R3DO	This study

pL3R4-EGL2	YTK single gene cassette 4 plasmid for constitutive Egl2 secretion, pTEF2-TFP19-TrEgl2-tENO2 inserted onto pYTKL3R4DO	This study
pL4RE-LPMO	YTK single gene cassette 5 plasmid for constitutive LPMO secretion, pPGK1-MFa-PaLPMO9H-tTDH1 inserted onto pYTKL4REDO	This study
pBGL1	YTK single gene cassette plasmid for constitutive Bgl1 secretion, pTDH3-TFP19-SfBgl1-tTDH1. Backbone enabling propagation in *E. coli* and integration at the URA3 locus in *S. cerevisiae*	This study
pCBH1	YTK single gene cassette plasmid for constitutive Cbh1 secretion, pTDH3-NS-CtCbh1-tTDH1. Backbone enabling propagation in *E. coli* and integration at the URA3 locus in *S. cerevisiae*	This study
pCBH2	YTK single gene cassette plasmid for constitutive Cbh2 secretion, pTDH3-TFP13-ClCbh2-tTDH1. Backbone enabling propagation in *E. coli* and integration at the URA3 locus in *S. cerevisiae*	This study
pEGL2	YTK single gene cassette plasmid for constitutive Egl2 secretion, pTDH3-TFP19-TrEgl2-tTDH1. Backbone enabling propagation in *E. coli* and integration at the URA3 locus in *S. cerevisiae*	This study
pLPMO	YTK single gene cassette plasmid for constitutive LPMO secretion, pTDH3-MFa-PaLPMO9H-tTDH1. Backbone enabling propagation in *E. coli* and integration at the URA3 locus in *S. cerevisiae*	This study
pXTH3	YTK single gene cassette plasmid for constitutive Xth3 secretion, pTDH3- MFa-AtXTH3-tTDH1. Backbone enabling propagation in *E. coli* and integration at the URA3 locus in *S. cerevisiae*	This study
pYTK-CBH1	YTK position 3 part containing the *Chaetomium thermophilum* cellobiohydrolase with native signal peptide (NS-CtCbh1)[227], codon-optimized for expression in *S. cerevisiae*	This study
pYTK-CBH2	YTK position 3 part containing the *Chrysosporium lucknowense* cellobiohydrolase with translational fusion partner 13 (TFP13-ClCbh2)[227], codon-optimized for expression in *S. cerevisiae*	This study
pYTK-BGL1	YTK position 3 part containing the *Saccharomycopsis fibuligera* β-glucosidase with translational fusion partner 19 (TFP19-SfBgl1)[227], codon-optimized for expression in *S. cerevisiae*	This study
pYTK-EGL2	YTK position 3 part containing the *Trichoderma reesei* endoglucanase with translational fusion partner 19 (TFP19-TrEgl2)[227], codon-optimized for expression in *S. cerevisiae*	This study
pYTK-LPMO	YTK position 3 part containing the *Podospora anserina* lytic polysaccharide monooxygenases with MFalpha signal peptide (MFa-LPMO)[226], codon-optimized for expression in *S. cerevisiae*	This study
pYTK-XTH3	YTK position 3 part containing the *Arabidopsis thaliana* xyloglucan endotransglucosylase/hydrolase with MFalpha signal peptide (MFa-XTH3)[357], codon-optimized for expression in *S. cerevisiae*	This study
pTT-GFP	YTK multi gene cassette plasmid for light-inducible GFP expression, cassette 1: pTDH3-LexABD-CRY2-tTDH1, cassette 2: spacer, cassette 3: pLEXA-yeGFP-tTDH1, cassette 4: spacer, cassette 5: pTDH3-VP16-CIB1-tTDH1. Backbone enabling propagation in *E. coli* and integration at the URA3 locus in *S. cerevisiae*	This study
pRR-GFP	YTK multi gene cassette plasmid for light-inducible GFP expression, cassette 1: pREV1-LexABD-CRY2-tTDH1, cassette 2: spacer, cassette 3: pLEXA-yeGFP-tTDH1, cassette 4: spacer, cassette 5: pREV1-VP16-CIB1-tTDH1. Backbone enabling propagation in *E. coli* and integration at the URA3 locus in *S. cerevisiae*	This study
pTR-GFP	YTK multi gene cassette plasmid for light-inducible GFP expression, cassette 1: pTDH3-LexABD-CRY2-tTDH1, cassette 2: spacer, cassette 3: pLEXA-yeGFP-tTDH1, cassette 4: spacer, cassette 5: pREV1-VP16-CIB1-tTDH1. Backbone enabling propagation in *E. coli* and integration at the URA3 locus in *S. cerevisiae*	This study

pRT-GFP	YTK multi gene cassette plasmid for light-inducible GFP expression, cassette 1: pREV1-LexABD-CRY2-tTDH1, cassette 2: spacer, cassette 3: pLEXA-yeGFP-tTDH1, cassette 4: spacer, cassette 5: pTDH3-VP16-CIB1-tTDH1. Backbone enabling propagation in *E. coli* and integration at the URA3 locus in *S. cerevisiae*	This study
pNCellulose	YTK multi gene cassette plasmid for light-inducible Nanoluc-CBM3 secretion, cassette 1: pREV1-LexABD-CRY2-tTDH1, cassette 2: spacer, cassette 3: pLEXA-MFa-NanoLuc-CBD-tTDH1, cassette 4: spacer, cassette 5: pTDH3-VP16-CIB1-tTDH1. Backbone enabling propagation in *E. coli* and integration at the URA3 locus in *S. cerevisiae*	This study
pNSurface	YTK multi gene cassette plasmid for light-inducible Nanoluc-SED1 surface display, cassette 1: pREV1-LexABD-CRY2-tTDH1, cassette 2: spacer, cassette 3: pLEXA-MFa-NanoLuc-Sed1-tTDH1, cassette 4: spacer, cassette 5: pTDH3-VP16-CIB1-tTDH1. Backbone enabling propagation in *E. coli* and integration at the URA3 locus in *S. cerevisiae*	This study
pLSR1-T-LexABD-CRY2	YTK single gene cassette 1 plasmid for strong constitutive LexABD-CRY2 expression, pTDH3-LexABD-CRY2-tTDH1 inserted onto pYTKLSR1DO	This study
pLSR1-R-LexABD-CRY2	YTK single gene cassette 1 plasmid for weak constitutive LexABD-CRY2 expression, pREV1-LexABD-CRY2-tTDH1 inserted onto pYTKLSR1DO	This study
pL1R2-spacer	YTK single gene cassette 2 plasmid where an empty spacer is inserted on pTYKL1R2DO	This study
pL2R3-LexA-GFP	YTK single gene cassette 3 plasmid for light-inducible GFP expression, pLEXA-yeGFP-tTDH1 inserted onto pYTKL2R3DO	This study
pL2R3-LexA-Nluc-CBM3	YTK single gene cassette 3 plasmid for light-inducible NanoLuc-CBM3 secretion, pLEXA-MFa-Nluc-CBM3-tTDH1 inserted onto pYTKL2R3DO	This study
pL2R3-Nluc-SED1	YTK single gene cassette 3 plasmid for light-inducible NanoLuc-SED1 surface display, pLEXA-MFa-Nluc-Sed1-tTDH1 inserted onto pYTKL2R3DO	This study
pL3R4-spacer	YTK single gene cassette 4 plasmid where an empty spacer is inserted on pTYKL3R4DO	This study
pL4RE-T-VP16-CIB1	YTK single gene cassette 5 plasmid for strong constitutive VP16-CIB1 expression, pTDH3- VP16-CIB1-tTDH1 inserted onto pYTKL4REDO	This study
pL4RE-R-VP16-CIB1	YTK single gene cassette 5 plasmid for weak constitutive VP16-CIB1 expression, pREV1- VP16-CIB1-tTDH1 inserted onto pYTKL4REDO	This study
pYTK-LexABD-CRY2	YTK position 3 part containing the LexA DNA binding domain and optical dimerizing partner CRY2 (LexABD-CRY2)[239], codon-optimized for expression in *S. cerevisiae*	This study
pYTK-VP16-CIB1	YTK position 3 part containing the VP16 activation domain and optical dimerizing partnerr CIB1 (VP16-CIB1)[239], codon-optimized for expression in *S. cerevisiae*	This study
pYTK-PLEXA	YTK position 2 part containing a modified CYC1 minimal promoter containing eight LexA binding sequences	This study
pYTK-yeGFP	YTK position 3 part containing yeGFP	This study
pYTK-Nluc	YTK position 3b part containing the NanoLuc luciferase reporter, codon-optimized for expression in *S. cerevisiae*	This study

pYTK-CBM3	YTK position 4a part containing the *Hungateiclostridium thermocellum* cellulosome anchoring protein cellulose-binding module (CBM3), codon-optimized for expression in *S. cerevisiae*	This study
pYTK-SED1	YTK position 4a part containing the *S. cerevisiae* Sed1 protein for surface display	This study
pYTKLSR1DO	Pre-assembled YTK acceptor plasmid into which single gene cassettes can be cloned, consisting of an sfGFP dropout part flanked by YTK connectors ConS and Con1. Backbone enabling propagation in *E. coli*	This study
pYTKL1R2DO	Pre-assembled YTK acceptor plasmid into which single gene cassettes can be cloned, consisting of an sfGFP dropout part flanked by YTK connectors Con1 and Con2. Backbone enabling propagation in *E. coli*	This study
pYTKL2R3DO	Pre-assembled YTK acceptor plasmid into which single gene cassettes can be cloned, consisting of an sfGFP dropout part flanked by YTK connectors Con2 and Con3. Backbone enabling propagation in *E. coli*	This study
pYTKL3R4DO	Pre-assembled YTK acceptor plasmid into which single gene cassettes can be cloned, consisting of an sfGFP dropout part flanked by YTK connectors Con3 and Con4. Backbone enabling propagation in *E. coli*	This study
pYTKL4REDO	Pre-assembled YTK acceptor plasmid into which single gene cassettes can be cloned, consisting of an sfGFP dropout part flanked by YTK connectors Con4 and ConE. Backbone enabling propagation in *E. coli*	This study
pWO68	YTK single gene cassette plasmid for constitutive mScarlet-I expression, pCCW12-mScarlet-I-tTDH1. Backbone enabling propagation in *E. coli* and integration at the HIS3 locus in *S. cerevisiae*	This study
pWS1766	YTK position 3 part encoding the mScarlet-I protein	This study
pWS065	Pre-assembled YTK acceptor plasmid into which single gene cassettes can be cloned, consisting of an sfGFP dropout part flanked by YTK connectors ConS and ConE. Backbone enabling propagation in *E. coli*	This study

Table 3 | **Composition of YTK single gene constructs used in this study**

	Parts					
Plasmid	2	3a	3b	4a	4b	Backbone
pWS702	pYTK009	pWS033		pYTK056		pWS473
pCG01	pYTK009	pWS433	pWS034	pYTK056		pYTK096
pCG04	pYTK009	pWS433	pWS032	pYTK056		pYTK096
pCG05	pYTK009	pWS433	pWS032	pPPK027	pYTK066	pYTK096
pCG16	pYTK009	pPPK041	pPPK044	pPPK027	pYTK066	pYTK096
pCG17	pYTK009	pWS433	pPPK044	pPPK027	pYTK066	pYTK096
pCG18	pYTK009	pPPK042	pPPK045	pPPK027	pYTK066	pYTK096
pCG19	pYTK009	pWS433	pPPK045	pPPK027	pYTK066	pYTK096
pCG20	pYTK009	pPPK043	pPPK046	pPPK027	pYTK066	pYTK096
pCG21	pYTK009	pWS433	pPPK046	pPPK027	pYTK066	pYTK096
pCG22	pWS1078	pPPK042	pPPK045	pPPK027	pYTK066	pWS042
pGPY74	pYTK027	pWS930	pWS935	pYTK056		pWS041
pGPY85	pWS1078	pWS033		pYTK056		pWS042
pCBH1	pYTK009	pYTK-CBH1		pYTK056		pYTK096
pCBH2	pYTK009	pYTK-CBH2		pYTK056		pYTK096
pBGL1	pYTK009	pYTK-BGL1		pYTK056		pYTK096
pEGL2	pYTK009	pYTK-EGL2		pYTK056		pYTK096
pLPMO	pYTK009	pYTK-LPMO		pYTK056		pYTK096
pXTH3	pYTK009	pYTK-XTH3		pYTK056		pYTK096
pWO68	pYTK010	pWS1766		pYTK056		pWS065

Table 4 | **Composition of YTK multi gene constructs used in this study**

Plasmid	Cassette 1	Cassette 2	Cassette 3	Cassette 4	Cassette 5	Backbone
pCG23	pGPY074	pCG22	NA	NA	NA	pYTK096
pGPY093	pGPY074	pGPY085	NA	NA	NA	pYTK096
pCelMix	pLSR1-CBH1	pL1R2-CBH2	pL2R3-BGL1	pL3R4-EGL2	pL4RE-LPMO	pYTK096
pTT-GFP	pLSR1-T-LexABD-CRY2	pL1R2-spacer	pL2R3-LexA-GFP	pL3R4-spacer	pL4RE-T-VP16-CIB1	pYTK096
pRR-GFP	pLSR1-R-LexABD-CRY2	pL1R2-spacer	pL2R3-LexA-GFP	pL3R4-spacer	pL4RE-R-VP16-CIB1	pYTK096
pTR-GFP	pLSR1-T-LexABD-CRY2	pL1R2-spacer	pL2R3-LexA-GFP	pL3R4-spacer	pL4RE-R-VP16-CIB1	pYTK096
pRT-GFP	pLSR1-R-LexABD-CRY2	pL1R2-spacer	pL2R3-LexA-GFP	pL3R4-spacer	pL4RE-T-VP16-CIB1	pYTK096
pNCellulose	pLSR1-R-LexABD-CRY2	pL1R2-spacer	pL2R3-LexA-Nluc-CBM3	pL3R4-spacer	pL4RE-T-VP16-CIB1	pYTK096
pNSurface	pLSR1-R-LexABD-CRY2	pL1R2-spacer	pL2R3-LexA-Nluc-SED1	pL3R4-spacer	pL4RE-T-VP16-CIB1	pYTK096

A.4 Materials and methods

Strains, constructs, and DNA assembly

Strains used in this study are listed in A.3 Table 1. All plasmids used in this study are listed in A.3 Table 2, with links provided to their complete sequences. All plasmids constructed in this study were constructed using standard cloning techniques. Oligonucleotides were obtained from IDT. Restriction endonucleases, Phusion-HF DNA polymerase and T7 DNA ligase were obtained from NEB. Unless stated, all plasmids were transformed into *E. coli* turbo (NEB) for amplification and verification before transforming into *S. cerevisiae* for protein expression and secretion. Constructs were verified by restriction enzyme digestion and Sanger sequencing (Source Bioscience).

S. cerevisiae constructs and strains were generated using the yeast toolkit (YTK) system developed by the Dueber lab[358]. The YTK system uses Golden Gate assembly to combine pre-assembled, defined parts into single gene cassettes and multi-gene cassettes. The final positions of pre-assembled parts within constructs are determined by the sequences of 4 bp overhangs created by digestion with type IIS restriction enzymes (BsaI or BsmBI). Users can therefore pick and choose from pre-assembled promoter, terminator and protein-coding parts to create expression cassettes. The identity of constituent YTK DNA parts used for all single-gene and multi-gene cassettes are listed in A.3 Table 3 and 4, respectively. All parts were cloned into pre-assembled backbone plasmids containing genetic elements enabling cloning in *E. coli* and later integrative transformation into the URA3 locus (pYTK096) or the HO locus (pWS473) in *S. cerevisiae*. Type 2, 3 and 4 parts were cloned into pre-assembled backbones. To create more complex fusion proteins, additional subparts were used (e.g. 3a and 3b parts). New parts were codon optimized for *S. cerevisiae* expression, synthesized commercially by GeneArt or IDT and cloned into the YTK system entry vector, pYTK001, for storage and verification. All other parts were taken from the YTK or from published work. Golden Gate assembly reactions were performed as described in Lee et al.[358]

Culture conditions and media

Yeast extract peptone dextrose (YPD) and yeast extract peptone sucrose (YPS) media were prepared with 10 g/L yeast extract, 20 g/L peptone from soybean and 20 g/L glucose or sucrose. Synthetic complete (SC) dropout media were prepared with 1.4 g/L yeast synthetic dropout medium supplements, 6.8 g/L yeast nitrogen base without amino acids and 20 g/L glucose. Depending on the required selection, SC media were supplemented with stock solutions of one or more of uracil (final concentration 2 g/L), tryptophan (final concentration 50 mg/L), histidine (final concentration 50 mg/L) and leucine (final concentration 0.1 g/L). Hestrin–Schramm (HS) media were prepared with 5 g/L yeast extract, 5 g/L peptone from soybean, 2.7 g/L Na_2HPO_4, 1.5 g/L citric acid and 20 g/L glucose or sucrose. Where required, media were supplemented with 20 g/L bacteriological agar.

E. coli was grown in LB medium at 37°C, supplemented with appropriate antibiotics at the following concentrations: chloramphenicol 34 µg/mL, kanamycin 50 µg/mL. For biomass accumulation, *K. rhaeticus* was grown at 30°C in yeast extract peptone dextrose (YPD) medium supplemented with 34 µg/mL chloramphenicol and 1% (v/v) cellulase from *T. reesei* (Sigma Aldrich, C2730). Notably, we found that the growth of *K. rhaeticus* liquid cultures was significantly more reliable when inoculated from glycerol stock, rather than from colonies. Therefore, unless otherwise indicated, all *K. rhaeticus* cultures were inoculated from glycerol stocks. *S. cerevisiae* was grown at 30°C in rich YPD medium or selective SC medium lacking the appropriate supplements, each supplemented with 50 µg/mL kanamycin.

Co-culture condition screen

Triplicate samples of *K. rhaeticus* Kr RFP were inoculated from glycerol stocks into 5 mL YPD medium supplemented with cellulase (1% v/v) and grown in shaking conditions for 3 days. Triplicate samples of *S. cerevisiae* yWS167 were inoculated from plates into 5 mL YPD medium and grown in shaking conditions for 24 hours. To prepare screens, *K. rhaeticus* and *S. cerevisiae* were inoculated into 2 mL volumes of YPD, YPS, HS-glucose or HS-sucrose media in 24-well cell culture plates. *K. rhaeticus* cultures were diluted 1/50 into fresh media. *S. cerevisiae* cultures were inoculated over a range of dilutions: 1/100, 1/1000, 1/10,000, 1/100,000 and 1/1,000,000. To enable pellicle formation, plates were incubated for 4 days under static conditions at 30°C. After 4 days of incubation, cultures were photographed under identical conditions. Where present, pellicle layers were removed from the culture surface and photographed.

OptiPrep concentration screen

Triplicate samples of *K. rhaeticus* Kr were inoculated from glycerol stocks into 5 mL YPD medium supplemented with cellulase (1% v/v) and grown in shaking conditions for 3 days. Triplicate samples of *S. cerevisiae* BY4741 were inoculated from plates into 5 mL YPD medium and grown in shaking conditions for 24 hours. To prepare screens, *K. rhaeticus* and *S. cerevisiae* were inoculated into 10 mL volumes of YPS or YPS plus 0%, 25%, 35%, 45%, 55%, 65% (w/v) OptiPrep in 10 mL tubes. *K. rhaeticus* cultures were diluted 1/50 into fresh YPS media. *S. cerevisiae* cultures were inoculated at dilution of 1/10,000. To enable pellicle formation, tubes were incubated for 3 days under static conditions at 30°C. After 3 days of incubation, cultures were photographed under identical conditions.

OptiPrep co-culture condition screen

Triplicate samples of *K. rhaeticus* Kr were inoculated from glycerol stocks into 5 mL YPD medium supplemented with cellulase (1% v/v) and grown in shaking conditions for 3 days. Triplicate samples of *S. cerevisiae* BY4741 were inoculated from plates into 5 mL YPD medium and grown in shaking conditions for 24 hours. To prepare screens, *K. rhaeticus* and *S. cerevisiae* were inoculated into 10 mL volumes of YPS or YPS plus 40% (w/v) OptiPrep in 50 mL tubes with breathable caps. *K. rhaeticus* cultures were diluted 1/50 into fresh YPS media. *S. cerevisiae* cultures were inoculated over a range of dilutions: final OD_{600} = 1/100, 1/1000, 1/10,000, 1/100,000 and 1/1,000,000. To enable pellicle formation, tubes were incubated for 3 days under static conditions at 30°C. After 3 days of incubation, cultures were photographed under identical conditions. Pellicles were collected and washed/shaken in deionized water at 4°C for 12 hours, twice, Clean pellicles were subjected to lyophilization for 3 days and measured for dry weight. To remove *S. cerevisiae* and *K. rhaeticus* cells associated with the cellulosic matrix, pellicles were immersed in 0.1 M NaOH at 65°C for 4 hours. Washed pellicles were again washed/shaken in H_2O at 4°C for 6 hours, subjected to lyophilization for 3 days, and measured for dry weight.

Testing of different supplements

Starter cultures of *K. rhaeticus* were grown in 2x HS-Media (supplemented with 2 % (v/v) cellulases) at 30°C, 250 rpm for three days. The OD700 was adjusted to 2.5 and the co-culture inoculated with a 1:50 dilution of the adjusted starter culture. *S. cerevisiae* starter culture was grown overnight at 30°C, 250 rpm in YPS media. The OD700 of yeast was adjusted to 0.01 and the co-culture was inoculated with 1:100 dilution.

In order to screen different supplements the co-culture media was composed of 5x YPS (adjusted to a final concentration of 1x), autoclaved water and the different supplements (Polyethylene glycol with a molecular weight of 3000, 8000, and 20000 to a final concentration of 100, 80, and 60 mg/mL, PEG 900000 to a final concentration of 40, 30, and 20 mg/mL, alginate to a final concentration of 20, 15 and 10 mg/mL and iodixanol (OptiPrep) to a final concentration of 48, 40, 32, 24, and 16 % (v/v)).

After mixing of the components the media was aliquoted in 12-well plates with 3 mL in each well and inoculated with a master mix of the starter co-culture already diluted. The static co-culture was incubated at 30°C for days.

Pellicles, if formed, were removed from the top of the static co-culture and dried through pressing them between adsorbent paper for 1 day. Dried pellicles were imaged with the fluorescence laser scanner (FLA-5000, Fujifilm). This was possible as the yeast cells were expressing mScarlet-I, a red fluorescent protein (yWO68). After imaging the pellicles were digested by incubating individual pellicles in 2 mL of 1x PBS supplemented with 5 % (v/v) cellulases at room temperature overnight. Next, the digestion mix was centrifuged (6500 g, 5 min) and the supernatant removed. The pellet was solely formed by the biomass of yeast and *K. rhaeticus*. The cell pellet was resuspended in 400 µL 1x PBS and pipetted into 2 wells of a 96-well plate. The red fluorescence was determined with a spectrophotometer (BioTek Synergy HT) and used as overall yeast incorporation value.

Standard co-culture protocol

Unless otherwise stated, all co-cultures were prepared using *K. rhaeticus* Kr RFP and *S. cerevisiae* yWS167 strains, allowing facile strain-specific detection through fluorescence measurements. Triplicate samples of *K. rhaeticus* were inoculated from glycerol stocks into 5 mL YPD medium supplemented with cellulase (1% v/v) and grown in shaking conditions for 3 days. Triplicate samples of *S. cerevisiae* were inoculated from plates into 5 mL YPD medium and grown in shaking conditions for 24 hours. To enable inoculation of co-cultures with equivalent cell densities of different samples, OD_{600} measurements were made and used to normalize pre-culture densities. *K. rhaeticus* pre-cultures were centrifuged at 3220 x g for 10 min and cell pellets resuspended in sufficient volume of YPS medium to result in a final OD_{600} of 2.5. *S. cerevisiae* pre-cultures were diluted in YPS medium to a final OD_{600} of 0.01. To prepare final co-cultures, resuspended *K. rhaeticus* samples were diluted 1/50 and pre-diluted *S. cerevisiae* samples were diluted 1/100 into fresh YPS medium. In instances where strains were inoculated into various different final media, *K. rhaeticus* pellets were resuspended in PBS buffer and *S. cerevisiae* cultures were pre-diluted in PBS buffer. To prepare OptiPrep-containing co-cultures, OptiPrep (D1556, Sigma-Aldrich) was added to YPS media to a final concentration of 45% (v/v). Co-cultures were grown in either 55 mm Petri dishes (15 mL) or 12 well cell culture plates (4 mL). Co-cultures were incubated for 3 days at 30°C under static conditions. It is important to ensure that culture vessels are not mechanically disturbed during the incubation period as this can partially submerge the growing BC layer, resulting in the formation of multiple, disconnected BC layers.

Determining BC pellicle yields

To determine the yields of BC pellicles, pellicle layers were removed from the surfaces of cultures and dried using the 'sandwich method'. Here, pellicles were sandwiched between sheets of greaseproof paper and then further sandwiched between multiple sheets of absorbent paper and finally placed under a heavy weighted object. After 24 hours, fresh sheets of absorbent paper were added, and pellicles left for an additional 24 hours. Pellicles dried in this way were then weighed to determine pellicle yields.

Importantly, pellicles were not treated with NaOH to lyse and remove cells embedded within the BC matrix. Since the cellular biomass constitutes an integral, functional part of BC-based ELMs is made up of, we chose not to perform NaOH washes.

This method was used to follow the yields of pellicle formation over time. Here, multiple co-cultures were prepared in triplicate using the standard co-culture procedure. Co-cultures were grown in 12 well plate format. At indicated time points, pellicle layers were removed to be dried and weighed.

Co-culture passage

To test whether co-cultures could be passaged, initial co-cultures were prepared in triplicate in 15 mL YPS cultures using the standard co-culture protocol. After 3 days incubation at 30°C, photographs were taken of the resultant cultures. To initiate new rounds of growth, pellicle layers were removed and the liquid below mixed by aspiration then diluted 1/100 into fresh samples of 15 mL YPS. This process was repeated over 16 rounds.

To confirm that the initial strain of GFP-expressing *S. cerevisiae* (yWS167) was maintained during passage, samples were plated at the end of each round. Samples from both the liquid below the pellicle and the pellicle layer itself were plated at various dilutions onto YPD-kanamycin plates. To enable plating, pellicles were first digested by shaking gently for 16 hours at 4°C in 15 mL of PBS buffer with 2% (v/v) cellulase from *T. reesei* (Sigma Aldrich, C2730). After 48 hours of incubation at 30°C, plates were imaged for GFP fluorescence. Dilutions were selected which enabled visualization of single colonies. Initially, plates were imaged using a Fujifilm FLA-5000 Fluorescent Image Analyser. However, due to equipment malfunction, later plates were photographed under a transluminator.

Determining cell distribution in co-cultures

Cell distributions were determined by plating samples of cells onto solid media and counting the resultant colonies. Pellicle samples were first gently rinsed by inverting ten times in 15 mL PBS and then digested by shaking gently for 16 hours at 4°C in 15 mL of PBS buffer with 2% (v/v) cellulase from *T. reesei* (Sigma Aldrich, C2730). Samples were diluted at various levels into PBS. For *S. cerevisiae* cell counts, samples were plated onto YPD-kanamycin media. For *K. rhaeticus* cell counts, samples were plated onto SC media lacking all four supplements essential for *S. cerevisiae* yWS167 growth (histidine, leucine, tryptophan, and uracil). In all instances, Kr RFP and yWS167 strains were used. Despite the use of selective growth conditions, to ensure the colonies counted were the target strains, plates were scanned for fluorescence using a Fujifilm FLA-5000 Fluorescent Image Analyser. Plate cell counts were used to calculate the original colony forming units (CFU) per unit volume for liquid samples. However, since the exact volumes of pellicle were not measured prior to degradation, it was not possible to calculate the exact cell counts in CFU per unit volume. To enable a rough approximation of the cell counts per unit volume, pellicle volumes were estimated at fixed levels and these values were used to calculate estimated CFU per unit volume. For 15 mL cultures, pellicle volumes were estimated at 4 mL. For 4 mL cultures in 12 well plates, pellicle volumes were estimated at 1 mL.

To compare cell counts from monocultures and co-cultures of *K. rhaeticus* and *S. cerevisiae*, pre-cultures of *K. rhaeticus* Kr RFP were pelleted and resuspended in PBS buffer, and pre-cultures of *S. cerevisiae* yWS167 were diluted in PBS buffer, according to the standard co-culture procedure. Various co-cultures and monocultures were then prepared in different media in 15 mL volumes. After 3 days of incubation at 30°C, pellicle and liquid samples were prepared, diluted, and plated for cell counts.

To determine the reproducibility of co-culture cell counts, co-cultures were prepared according to the standard co-culture protocol in 15 mL cultures on three separate occasions. After 3 days of incubation at 30°C, pellicle and liquid samples were prepared, diluted, and plated for cell counts.

Invertase supplementation experiment

Co-cultures and *K. rhaeticus* Kr RFP monocultures were prepared in YPS medium according to the standard co-culture procedure. Recombinant, purified *S. cerevisiae* invertase (Sigma-Aldrich, I9274) was resuspended in 100 mM citrate buffer, pH 4.5 to create a stock solution at a final concentration of 5 U/μL. This stock solution was diluted into YPS medium for a range of final invertase concentrations: 50 mU/mL (10^{-2}), 5 mU/mL (10^{-3}), 0.5 mU/mL (10^{-4}), 50 µU/mL (10^{-5}). After 3 days of growth at 30°C, cultures and, where present, pellicles were imaged.

Supernatant nitrocefin assay

For culture supernatant assays, WT BY4741, yCG04 and yCG05 *S. cerevisiae* strains were grown in triplicate overnight in YPD liquid medium with shaking. After 16 hours of growth, liquid cultures were back-diluted to final OD_{600} = 0.01 in 5 mL fresh YPS medium and grown for 24 hours with shaking. The resultant cultures were centrifuged at 3220 x g for 10 min and the supernatant fractions harvested. Supernatant samples were pipetted in 50 µL volumes into the wells of a 96 well plate. The colorimetric substrate, nitrocefin (484400, Merck-Millipore), was resuspended in DMSO to create a 10 mg/mL working stock. This stock was diluted to 50 µg/mL in nitrocefin assay buffer (50 mM sodium phosphate, 1 mM EDTA, pH 7.4). To start the reaction, 50 µL of nitrocefin at 50 µg/mL was added to each of the samples simultaneously, and the absorbance at 490 nm was measured over time. Active β-lactamase converts nitrocefin to a red substrate, increasing the absorbance of light at 490 nm. Therefore, to calculate the relative β-lactamase activity in samples, the rate of change in the absorbance of light at 490 nm was determined. Specifically, the product formation rates were calculated from the gradient over the linear region of a graph plotting fluorescence AU against time.

Pellicle nitrocefin assays

For initial pellicle assays (Fig. 2e and 2f), WT BY4741, yCG04, and yCG05 *S. cerevisiae* strains were co-cultured with *K. rhaeticus* (Kr RFP) in triplicate, according to the standard co-culture protocol. Following 3 days of growth, pellicles were removed and washed in 15 mL PBS buffer for 30 min with shaking at 150 rpm. Square pieces of pellicle, measuring 5 mm x 5 mm, were then cut using a scalpel. The remainder of the pellicle was dried using the sandwich method. Once dried, pellicles were again cut to produce 5 mm x 5 mm pieces. Dried pellicle pieces were rehydrated by adding 25 µL of PBS buffer and incubating for 30 min. Assays for both wet and dried samples were run by adding 10 µL of nitrocefin, diluted to 1 mg/mL in PBS buffer, to each of the pellicle pieces simultaneously. Initial assays were performed at room temperature. Photographs were taken of pellicles over the course of 35 min to follow the color change. To provide a quantitative measure of colour change, the ImageJ (NIH) image analysis software was used. Images were first split into individual color channels. Since yellow-to-red color change is caused by an increase in the absorbance of green light wavelengths, the green channel was selected. To quantify the yellow-to-red colour change, the green channel intensity was then measured from greyscale-inverted images of pellicle slices over time. Since preliminary results showed that WT pellicles exhibited no color change, the signal from WT pellicles was used as a baseline value to correct for background levels of green channel intensity.

To determine absolute levels of β-lactamase activity in wet and dried pellicles, a similar protocol was used to create standard curves. Standard curves were prepared using a commercial *E. coli* β-lactamase enzyme (ENZ-351, ProSpec). First, pellicles grown with WT BY4741 *S. cerevisiae* were washed in nitrocefin assay buffer (50 mM sodium phosphate, 1 mM EDTA, pH 7.4). Pellicle pieces measuring 5 mm x 5 mm were cut and weighed to enable the determination of the approximate volume of liquid within the pellicle. The remainder of the pellicles were dried using the sandwich method. Once dried, 5 mm x 5 mm pieces of pellicle were cut for dried pellicle standard curves. Dried pellicle pieces were rehydrated by adding 20 μL of nitrocefin assay buffer. Pre-diluted standard β-lactamase samples were then added to pellicle pieces in 5 μL volumes and allowed to diffuse throughout the BC for 30 min. To initiate the reaction, 5 μL aliquots of nitrocefin, diluted to 2 mg/mL in nitrocefin assay buffer, were added to each of the pellicle pieces simultaneously. Samples were incubated at 25°C and photographs taken over the course of the reaction. Again, ImageJ was used to quantify the yellow-to-red colour change at given time points. Time points were chosen to maximize the dynamic range, without reaching saturation. For wet pellicles, it was necessary to use measured weight of pellicle slices to determine the actual final concentration of the standard β-lactamase. Standard curves are shown in A.2 Figure 31. Standard curves using fresh wet pellicles, dried pellicles, and dried pellicles stored for 1 month or 6 months at room temperature were all prepared according to this method. For long-term storage, dried pellicles were stored in Petri dishes at room temperature and protected from light.

Alongside standard curves, pellicles grown with yCG05 *S. cerevisiae* were analyzed using an identical protocol. To enable cross comparison with standard curves, negative samples (pellicles from co-cultures with WT *S. cerevisiae*) and positive samples (pellicles from co-cultures with WT *S. cerevisiae* to which a known amount of β-lactamase standard had been added) were run with samples. For samples to which no standard β-lactamase was added, 5 μL of nitrocefin assay buffer was added to maintain equal final liquid volumes. Photographs taken at identical time points were then used with standard curves to calculate absolute values of β-lactamase activity. Again, ImageJ was used to quantify the yellow-to-red color change. For wet pellicles, it was necessary to use the measured weight of pellicle slices to determine the actual final concentration of enzyme. Again, fresh wet pellicles, dried pellicles, and dried pellicles stored for 1 month at room temperature were all assayed according to this method.

β-lactamase activity retention assay

To determine the retention of β-lactamase within BC following multiple rounds of washes, nitrocefin assays were performed. Pieces measuring 5 mm x 5 mm were cut from dried pellicles grown with yCG04 and yCG05. All pellicle pieces were rehydrated by incubating in 1 mL of PBS buffer. Pieces were subjected to a variable number of wash steps, where pellicle pieces were incubated in 4 mL PBS buffer at 25°C and 150 rpm for 30 min. After washing, pellicles were assayed for β-lactamase activity. Negative samples (pellicles from co-cultures with WT *S. cerevisiae*) and positive samples (pellicles from co-cultures with WT *S. cerevisiae* to which a known amount of β-lactamase standard had been added) were run alongside all samples. For samples to which no standard β-lactamase was added, 5 μL of PBS buffer was added to maintain equal final liquid volumes. As before, assays were initiated by adding 5 μL of nitrocefin, diluted to 2 mg/mL in PBS buffer, to each of the pellicle pieces simultaneously. Samples were run in batches based on the number of washes. Again, ImageJ was used to quantify the yellow-to-red color change at given time points. To enable cross-comparison between different assay runs, negative samples were used to subtract background signals, and positive samples were used to normalize signals. To ensure that yellow-to-red color change values were within a range in which there is a linear relationship between β-lactamase activity and the yellow-to-red color change signal, a standard curve was run. The standard curve ($r^2 = 0.9571$) confirmed that detected yellow-to-red color change values fell within the linear range.

X-α-gal α-galactosidase assays

A stock solution of X-α-galactosidase (Sigma-Aldrich, 16555) was prepared in DMSO at a concentration of 40 mg/mL. For plate assays, 100 µL of X-α-gal were spread on plates prior to cell plating and images taken after 3 days of growth at 30°C. For pellicle assays, pellicles grown with *K. rhaeticus* Kr RFP were harvested after 3 days of growth following the standard co-culture procedure. Pellicles were then washed in 15 mL 100 mM citrate buffer, pH 4.5 for 30 min with shaking at 150 rpm. Square pieces of pellicle, measuring 5 mm x 5 mm, were then cut using a scalpel. The remainder of the pellicle was dried using the sandwich method. Once dried, pellicles were again cut to produce 5 mm x 5 mm pieces. Dried pellicle pieces were rehydrated by adding 25 µL of 100 mM citrate buffer, pH 4.5 and incubating for 30 min. Assays for both wet and dried samples were run by adding 2.5 µL of X-α-gal stock solution and incubating at 25°C. Images were taken over the course of several hours.

ABTS laccase activity assays

Stock solutions were prepared of 2,2'-azino-bis(3-ethylbenzothiazoline-6-sulphonic acid) (ABTS) (Sigma-Aldrich, A1888) at a final concentration of 0.1 M and copper sulfate at a final concentration of 1 M. Laccases are copper-containing enzymes, requiring supplementation of copper for culture and assay conditions. For plate assays, 125 µL of 0.1 M ABTS and 25 µL of 1 M $CuSO_4$ were spread on plates prior to cell plating and images taken after 3 days of growth at 30°C. For pellicle assays, pellicles grown with *K. rhaeticus* Kr RFP were harvested after 3 days growth following the standard co-culture procedure. The only modification was the addition of 1 mM CuSO4 to the culture medium of both *S. cerevisiae* pre-cultures and co-cultures. Pellicles were then washed in 15 mL 100 mM citrate buffer, 1 mM $CuSO_4$, pH 4.5 for 30 min with shaking at 150 rpm. Square pieces of pellicle, measuring 5 mm x 5 mm, were then cut using a scalpel. The remainder of the pellicle was dried using the sandwich method. Once dried, pellicles were again cut to produce 5 mm x 5 mm pieces. Dried pellicle pieces were rehydrated by adding 25 µL of 100 mM citrate buffer, 1 mM $CuSO_4$, pH 4.5 and incubating for

30 min. Assays for both wet and dried samples were run by adding 5 µL of ABTS stock solution and incubating at 25°C. Images were taken over the course of several hours.

Scanning electron microscopy (SEM)

Pellicles were grown for 3 days following the co-culture procedure and washed with deionized water 3 times (shaking at 70 rpm at 4°C for 12 hours per wash) to remove residue YPS or OptiPrep. Washed pellicles were then freeze-dried with a lyophilizer for at least 48 hours before coated with a gold sputter. Images were taken with a JEOL 6010LA benchtop scanning electron microscope.

Environmental scanning electron microscopy (eSEM)

Pellicles were grown and washed as described in the SEM sample preparation. Instead of subjected to freeze-drying, washed pellicles were placed in 6-well plater suspended in transfer buffer containing 2.5% glutaraldehyde (10% EM grade from EMS, 16100) and 200 mM sodium cacodylate buffer at pH 7.2 (EMS, 11655). After 60 minutes of fixation, samples were rinsed twice with the cacodylate buffer, 5-10 minutes each at 4°C, followed by 3-4 times rinsing with distilled water. Rinsed samples should then be subjected to dehydration as soon as possible, where they were serially dehydrated with multiple rounds of EtOH, 5 minutes each (35%, 45%, 55%, 65%, 70%, 85%, 95%, and 100%). After dehydration, samples were transferred to 50% TMS (EMS, 21760) mixed with 50% EtOH and incubated for 15 minutes, followed by transferring to 80% TMS mixed with 20% EtOH and another 15-minute incubation. Finally, samples were transferred to 100% TMS and incubated for 5 minutes, repeated for 3 times, and air-dried overnight in the fume hood. Images were taken with a FEI XL30 ESEM used on low vacuum mode with a Backscatter detector (BSE). Dehydrated samples were placed on stub using double-sided conductive carbon tape (EMS). Parameters: Working height < 10 cm; Low pressure setting > 2.5 Torr; Accelerating voltage 15 kV; Magnification > 1000x; Spot size = 3.

Cell leakage from pellicles

Pellicles were grown in YPS on a 12-well plate for 3 days to reach ~900 mg in wet weight and then subjected to 3 rounds of wash in 20 mL PBS (shaking at 70 rpm at 4°C for 24 hours per wash). Total CFU counts per pellicle were obtained from cellulase-digested pre-wash pellicles, liquid (PBS) after each wash step, and post-wash pellicles.

Brunauer-Emmett-Teller (BET) surface area analysis

Free-dried pellicles were cut into 5 mm x 5 mm piece and placed in sample tube for 1 hour degas at 423 K using a Micromeritics (Atlanta, GA) ASAP 2020 analyzer. BET surface area and pore size were then determined with N_2 adsorption at 77 K using Brunauer–Emmett–Teller and Barrett–Joyner–Halenda analyses on the same machine.

Preparing and assaying sense-and-response pellicles

In yGPH093, transcription from the BED-inducible promoter is controlled by a synthetic transcription factor (Z_3EV) consisting of three domains: the Zif268 DNA-binding domain, the human estrogen receptor (hER) ligand binding domain, and the transcriptional activation domain of viral protein 16 ($VP16^{AD}$)[233]. When present, β-estradiol binds to the hER ligand binding domain of Z_3EV, releasing it from its basal sequestration in the cytosol and enabling it to translocate into the nucleus. Once in the nucleus, the Zif268 domain binds cognate DNA sequences in engineered promoters and the $VP16^{AD}$ domain activates transcription of downstream genes. As a preliminary test of *S. cerevisiae* sense-and-response in BC pellicles, co-cultures were prepared in triplicate according to the standard co-culture protocol using WT BY4741 and yGPH093 strains. Co-cultures were inoculated into 4 mL YPS-OptiPrep medium in 12 well cell culture plates. After 3 days of growth, pellicles were removed and washed by incubating at 25°C with shaking at 150 rpm in 15 mL PBS. Pellicles were then placed in fresh 15 mL of YPD medium in the presence or absence of 5 nM β-estradiol (E8875, Sigma-Aldrich) and incubated for 24 hours at 30°C and 150 rpm. During growth cells had 'escaped' from biosensor pellicles, making the medium surrounding the pellicles turbid. Therefore, to remove loosely associated cells, pellicles were washed twice by incubating for 30 min at 25°C and 150 rpm in 15 mL of PBS buffer. Finally, pellicles were imaged simultaneously for GFP fluorescence under a transilluminator.

Similarly, dried biosensor pellicles were prepared in triplicate according to the standard co-culture protocol using WT BY4741 and yGPH093 or WT BY4741 and yWS890 strains. Co-cultures were inoculated into 4 mL YPS-OptiPrep medium in 12 well cell culture plates. After 3 days of growth, pellicles were dried using the 'sandwich method'. Dried pellicles were then placed in fresh 15 mL of YPD medium in the presence or absence of 5 nM β-estradiol or 50 nM *S. cerevisiae* α–mating factor (RP01002, Genscript) and incubated 24 hours at 30°C. Notably, to more closely match the potential use of biosensors in an on-site detection setting, pellicles were incubated without agitation in this and all future experiments. Since static growth results in far less growth in the surrounding liquid, pellicles were only briefly washed after incubation by inverting ten times in 15 mL PBS buffer. Finally, pellicles were imaged side-by-side for GFP fluorescence under a transilluminator. To test for stability after long-term storage, pellicles were stored for 4 months at room temperature stored in Petri dishes protected from light. These pellicles were cut in half prior to induction, which was performed as above.

The BED-inducible CtLcc1-secreting strain yCG23 was initially screened for laccase induction using a plate-based ABTS assay. Transformants of yCG23 were re-streaked in triplicate on SC URA$^-$ plates supplemented with 125 µL of 0.1 M ABTS and 25 µL of 1 M $CuSO_4$. After 3 days of incubation at 30°C colonies were imaged. Co-cultures between *K. rhaeticus* Kr RFP and yCG01 or yCG23 were then prepared in triplicate in 12-well plate format, using YPS-OptiPrep medium supplemented with 1 mM $CuSO_4$. After 3 days of growth, pellicles were harvested and were washed by incubating for 30 min at 25°C and 150 rpm in 15 mL of 100 mM citrate buffer, 1 mM $CuSO_4$, pH 4.5. Pellicles were then inoculated into 15 mL of fresh YPD supplemented with 1 mM $CuSO_4$ in the presence or absence of 5 nM β-estradiol and incubated at 30°C for 24 hours statically. After incubation, pellicles were washed by incubating for 30 min at 25°C and 150 rpm in 15 mL of 100 mM citrate buffer, 1 mM $CuSO_4$, pH 4.5. Pellicles were then placed in a 12-well plate, and 75 µL of 0.1 M ABTS added to each well to assay for laccase activity. Pellicles were incubated at 25°C and imaged after 72 hours.

Determining the viability of S. cerevisiae in dried BC pellicles

Co-cultures were prepared in triplicate according to the standard co-culture protocol. Co-cultures were inoculated into 4 mL YPS-OptiPrep medium in 12 well cell culture plates. Counts of viable *S. cerevisiae* cells within wet and dried pellicles were determined as described in 'Determining cell distribution in co-cultures'. Dried pellicles were also stored for 1 month at room temperature, and then degraded and plated onto YPD medium. Since one of the triplicate samples produced no colonies, we could not calculate estimated cell counts within pellicles. However, images are presented of the three plates to show that viable cells were indeed recovered from the other two samples (A.2 Figure 47d).

Total cellulase activity assay

S. cerevisiae strains BY4741 and yCelMix were grown overnight in YPS in triplicate with shaking. After 16 hours of growth, liquid cultures were back-diluted to final OD_{600} = 0.1 in 5 mL fresh YPS medium with 2 mM L-ascorbic acid (A7506, Sigma-Aldrich) and grown for 24 hours with shaking. The resultant cultures were centrifuged at 3220 x g for 10 min and the supernatant fractions harvested. Supernatant samples were pipetted in 50 µL volumes into the wells of a 96 well plate. The EnzChek® Cellulase Substrate (E33953, Thermo-Fisher) was resuspended in 50% DMSO and diluted 5-fold in 100 mM sodium acetate (pH 5.0). To start the reaction, 50 µL of cellulase substrate was added to the supernatant and let incubated for 30 minutes in the dark at room temperature. To build an enzyme activity standard curve, the cellulase from *T. reesi* (C2730, Sigma-Aldrich) was used to prepare a serial dilution in YPS medium and mixed with the substrate at 1:1 ratio. Blue fluorescence (360/460) was detected using a plate reader (Synergy H1, BioTek) after 30 minutes incubation in the dark at room temperature. The data from enzyme standards was fit to an exponential model, a*exp(b*x) + c*exp(d*x) in MATLAB. This model was then used to calculate the total cellulase activity of the supernatant from yCelMix (using supernatant from BY4741 as a blank control).

Pellicle tensile test

Co-cultures were set up in 40 mL YPS+OptiPrep (plus 2 mM L-ascorbic acid) and grown in square plates (100 mm x 15 mm) for 2 days at 30°C. Pellicles were then washed in deionized water 3 times (shaking at 70 rpm at 4°C for 12 hours per wash) and dried using the sandwich method described previously but with an extended 3 days drying to ensure water removal. Dried pellicles were cut into 60 mm * 10 mm stripes and their thickness were measured with a micrometer. Tensile test was performed with a Zwick mechanical tester (BTC-ExMacro .001, Roell) following the ASTM D882 protocol at 1 mm/min speed.

Pellicle rheology analysis

The rheological properties of washed pellicles were characterized on a rheometer (AR2000, TA Instruments) with a 25 mm ETC aluminum plate (1 mm gap). The strain sweep measurements were taken from 0.01% to 100% strain amplitude at a constant frequency of 1 rad/s, while frequency sweep measurements were taken from 0.1 rad/s to 100 rad/s at a constant strain amplitude of 1%. Samples were kept fully hydrated with deionized water at 25°C on a Peltier thermoelectric plate.

Light-inducible circuit promoter characterization

Yeast strains were grown overnight in YPD in triplicate with shaking. After 16 hours of growth, liquid cultures were back-diluted to final OD_{600} = 0.2 in 100 µL fresh YPD and pipetted into the wells of two 96 well plates (duplicates). One of the two plates was wrapped in black aluminum foil as a dark control. Both plates were placed under a LED lamp at 30°C for 4 hours. Green fluorescence was then measured with a plate reader.

Light-inducible luciferase assay

Yeast strains were grown overnight in YPD in triplicate with shaking. After 16 hours of growth, liquid cultures were back-diluted to final OD_{600} = 0.2 in 15 µL fresh YPS and pipetted into the wells of two 96 well plates (duplicates for light and dark conditions, as previously described). Plates were placed under a LED lamp at 30°C for 4 hours. Substrate in buffer from Nano-Glo® Luciferase Assay System (N1120, Promega) were added to the culture at 1:1 ratio at the end of incubation. After incubation in the dark for 5 minutes, the bioluminescence of the samples was measured with a plate reader.

Light-inducible pellicle response assay

Co-cultures were set up using yeast strains BY4741, yNCellulose, and yNSurface along with wildtype *K. rhaeticus* in 10 mL YPS+OptiPrep. For the long-term exposure experiment, 60 mm Petri dishes were prepared as duplicates, one was wrapped in black aluminum foil while the other one was not. The plates were placed under a LED lamp at 30°C for 3 days. After the incubation, pellicles were flipped so the bottom side was facing up, and transferred onto YPD agar plates. 500 µL of Nano-Glo mix was applied onto the pellicles evenly through the entire surface. After incubation in the dark for 10 minutes, bioluminescence of the samples was detected with a ChemiDoc Touch imager (BioRad). For the short-term exposure experiment (masking), co-cultures were grown in the dark at 30°C for 3 days. Pellicles were flipped, so the bottom side was facing up and transferred onto YPD agar plates. A mask made of black aluminum foil with a carved pattern in the center was placed on top of the pellicles. Plates were placed under a LED lamp and incubated at 30°C for 4 hours. The mask was then removed and 500 µL of Nano-Glo mix was applied onto the pellicles evenly through the entire surface. After incubation in the dark for 10 minutes, bioluminescence of the samples was detected with a ChemiDoc Touch imager.

Light-patterning on pellicles

Co-cultures were grown in 100 mm square plates protected from light as previously described. Pellicles were rinsed in PBS, flipped, placed on YPD agar, and placed in an incubator with a projector mounted on top. After incubation under the projected pattern (with no lid to prevent water condensation) at 30°C for 12 hours or more, 3 mL of Nano-Glo mix was applied onto the pellicles evenly through the entire surface. Bioluminescence images was detected with a ChemiDoc Touch imager after 30 minutes of incubation in the dark.

Appendix B

Additional Information and Protocols for Chapter 3

B.1 Supplementary figures

Figure 52 | **Alginate cores in various geometries.** The alginate core used to encapsulate cells can be shaped into spheres with different radii through extrusion with syringes and needles on parafilm followed by crosslinking in calcium chloride solution. Alginate thread was produced by direct extrusion in calcium chloride solution. Disk, cube, and cylinder-like structures can be achieved through cutting.

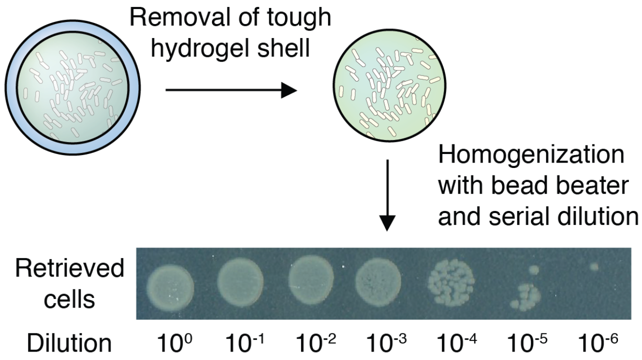

Figure 53 | **Retrieving encapsulated cells.** Retrieval of live cells from the beads immediately before the cross-linking step. Retrieval was performed through the removal of the tough shell followed by homogenization and showed nearly full recovery (~10^9 CFU per mL).

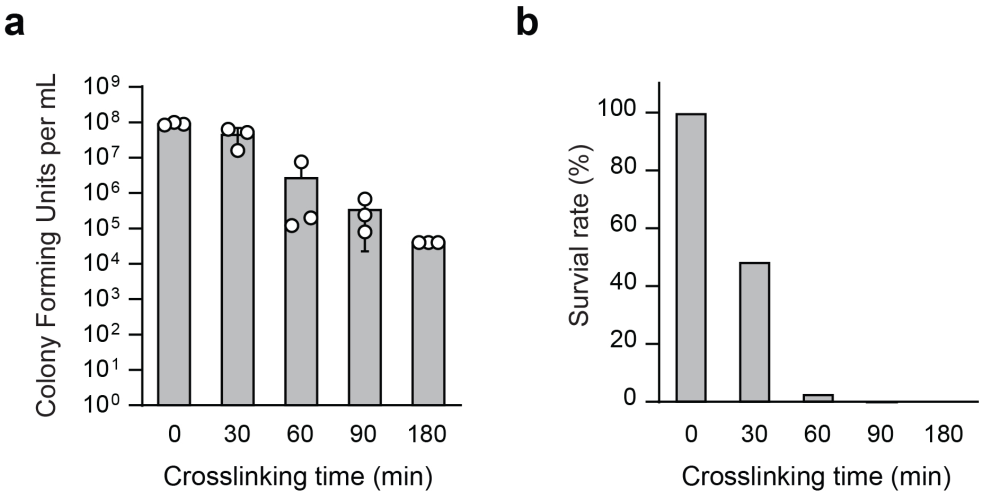

Figure 54 | **Toxicity of the chemical crosslinkers.** **(a)** CFU counts and **(b)** survival rates for cells retrieved from hydrogel beads after incubating in the crosslinking solution for different lengths of time. Samples prepared in triplicate; data represent the mean ±1 SD.

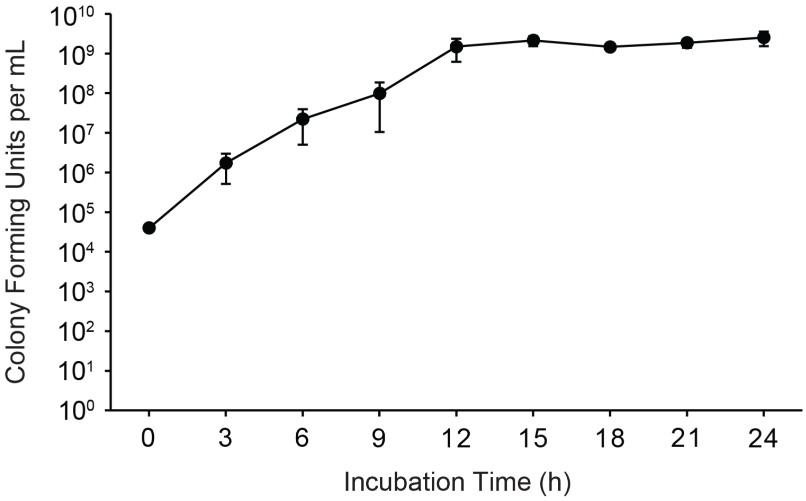

Figure 55 | **Growth curve of bacteria in hydrogel beads.** Cells encapsulated in beads were incubated in LB medium and retrieved at given time points to measure growth over 24 hours. Samples prepared in triplicate; data represent the mean ±1 SD.

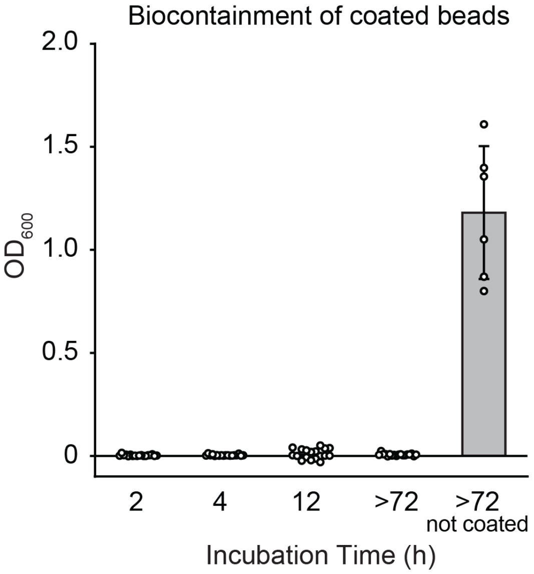

Figure 56 | **Long-term physical containment.** Optical density at 600 nm (OD_{600}) measurement demonstrating that the media surrounding coated beads showed no bacterial growth after 72 hours. Samples prepared in *n* = 18 for h = 2, 4, 12, and >72, and *n* = 6 for beads that are not coated. Data represent the mean ±1 SD.

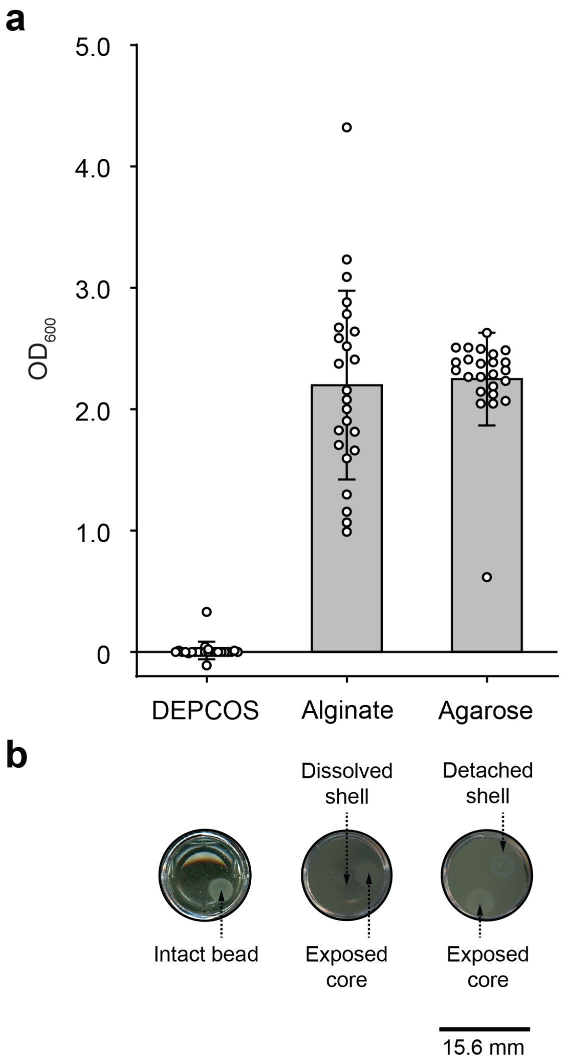

Figure 57 | **Physical containment under prolonged shaking.** **(a)** OD_{600} measurement demonstrating the bacterial growth in the media surrounding the beads after 12 hours of shaking at 200 rpm. Samples prepared in *n* = 24, data represent the mean ±1 SD. **(b)** Representative images of the beads and their surrounding media after shaking. The DEPCOS beads (left) remained intact and showed no signs of cell leakage (clear media). The shell of the alginate-coated beads (center) was dissolved after prolonged shaking and could not stop the core from exposing. Similarly, the shell of the agarose-coated beads broke and detached from the core, leaving it exposed and causing cell escape.

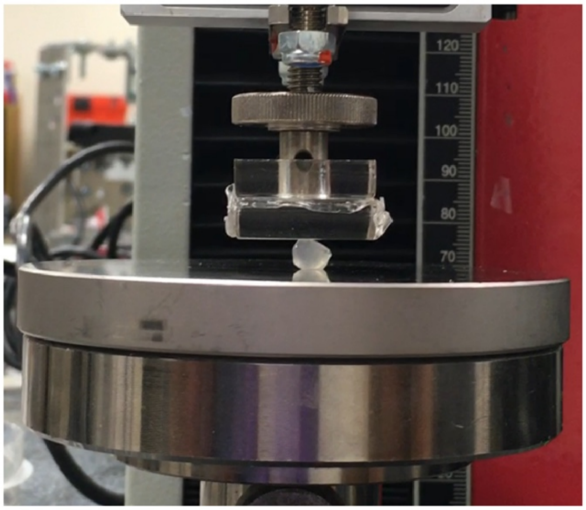

Figure 58 | **Compression test setup with Zwick mechanical tester.** A fully hydrated hydrogel bead (r = 3 mm) was placed between sterile surfaces and submitted to compressions.

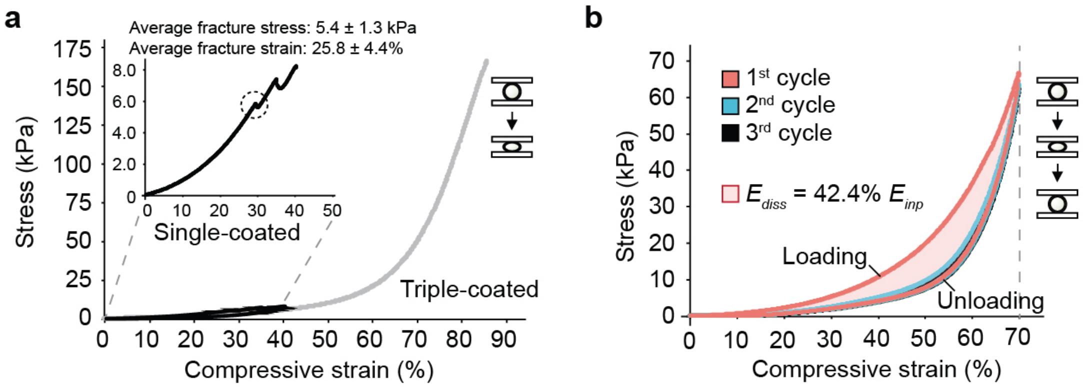

Figure 59 | **Effective stress-strain profiles of the hydrogel beads under compression. (a)** Effective stress-strain curves of single- and triple-coated beads. Samples prepared in *n* = 14. (**b**) Effective stress-strain curves of cyclic compression of triple-coated beads. Effective stress-strain curves were converted from force-displacement curves using the initial dimensions of the beads before compressions[273,359]. Samples prepared in triplicate.

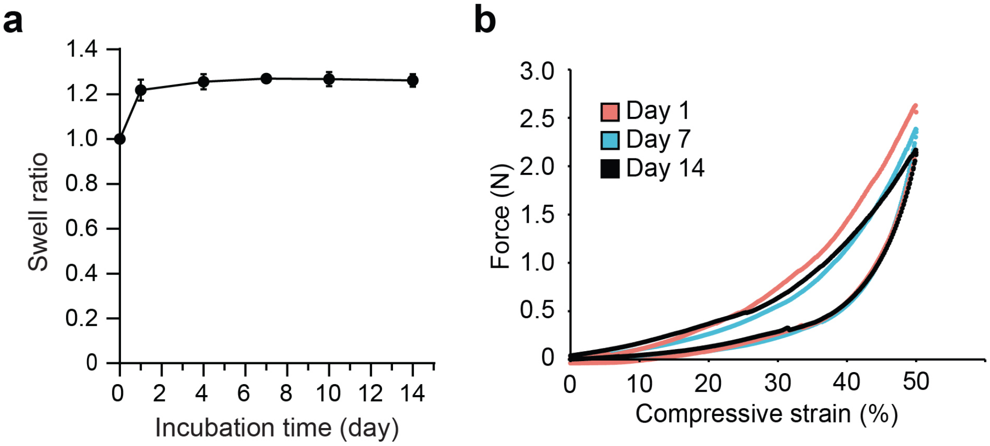

Figure 60 | **Swelling and mechanical properties of the hydrogel beads after prolonged incubation.** **(a)** The swelling behavior of beads over the course of 14 days. Samples prepared in *n* = 10, data represent the mean ±1 SD. **(b)** Typical force-displacement curves of single-layer coated bead (r = 3 mm) on day 1, 7, and 14 of incubation.

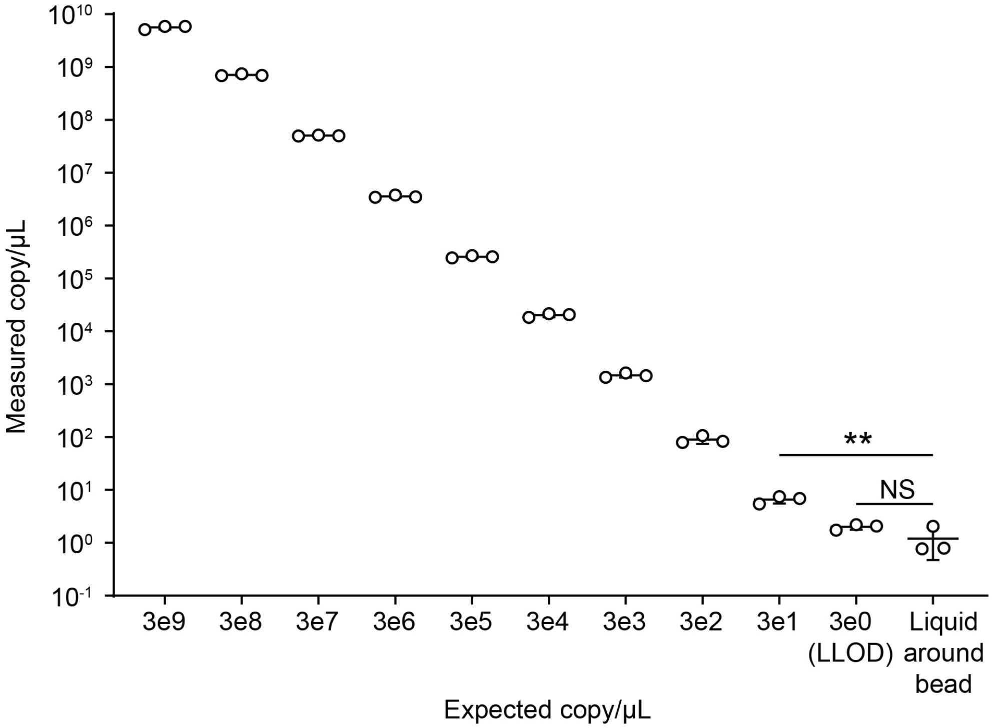

Figure 61 | **DNA containment inside the hydrogel beads.** Linear DNA fragments (977 bp) were PCR-amplified and encapsulated in the hydrogel beads at 3e9 copy/μL. Soluble DNA in the surrounding media after 72-hr incubation was quantified using qPCR. Standards were prepared by serial dilutions. Samples prepared in triplicate; data represent the mean ±1 SD. ***P* = 0.0018 (df = 4, 95% CI = -7.398 to -3.351), NS = not significant (*P* = 0.1460, df = 4, 95% CI =-2.035 to 0.4334). Statistics are derived using a two-tailed *t*-test. Lower limit of detection (LLOD) = 3 copy/μL.

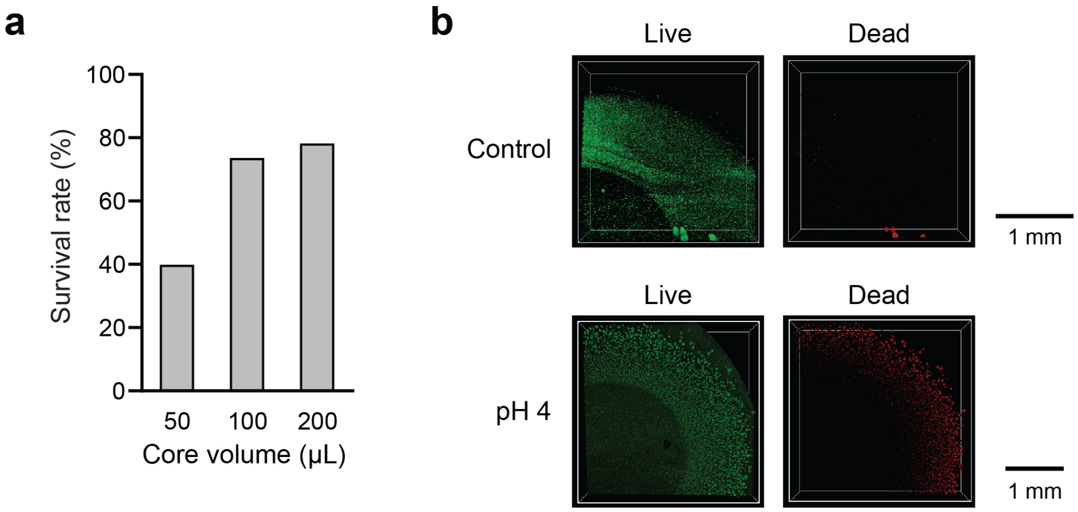

Figure 62 | **Viability of encapsulated cells at pH 4. (a)** Survival rates of cells encapsulated in alginate cores of different sizes after 4 hours of shaking incubation at pH 4. The final diameters of the beads after outgrowth are approximately 6 mm, 6.5 mm, and 8 mm for initial core volumes of 50 μL, 100 μL, and 200 μL, respectively. Data are calculated from triplicates incubated in original LB and LB adjusted to pH 4. **(b)** Spatial distribution of live (green) and dead (red) cells in the 50 μL alginate cores after 4 hours of shaking incubation at pH 4. The depth of the Z-stack is 580 μm for the control bead images and 800 μm for the pH 4 bead images.

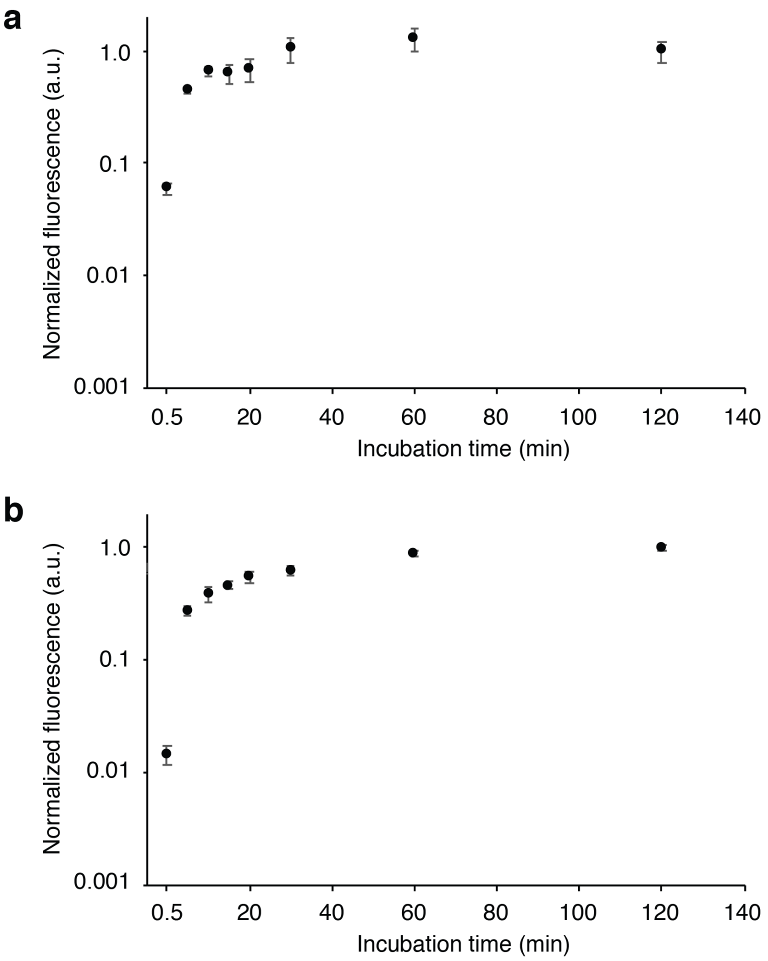

Figure 63 | **Diffusion of small molecules into the hydrogel beads.** **(a)** Diffusion of a positively charged dye, rhodamine, into the hydrogel beads over the course of two hours. **(b)** The diffusion profile of a negatively charged dye, fluorescein. Samples prepared in triplicate; data represent the mean ±1 SD.

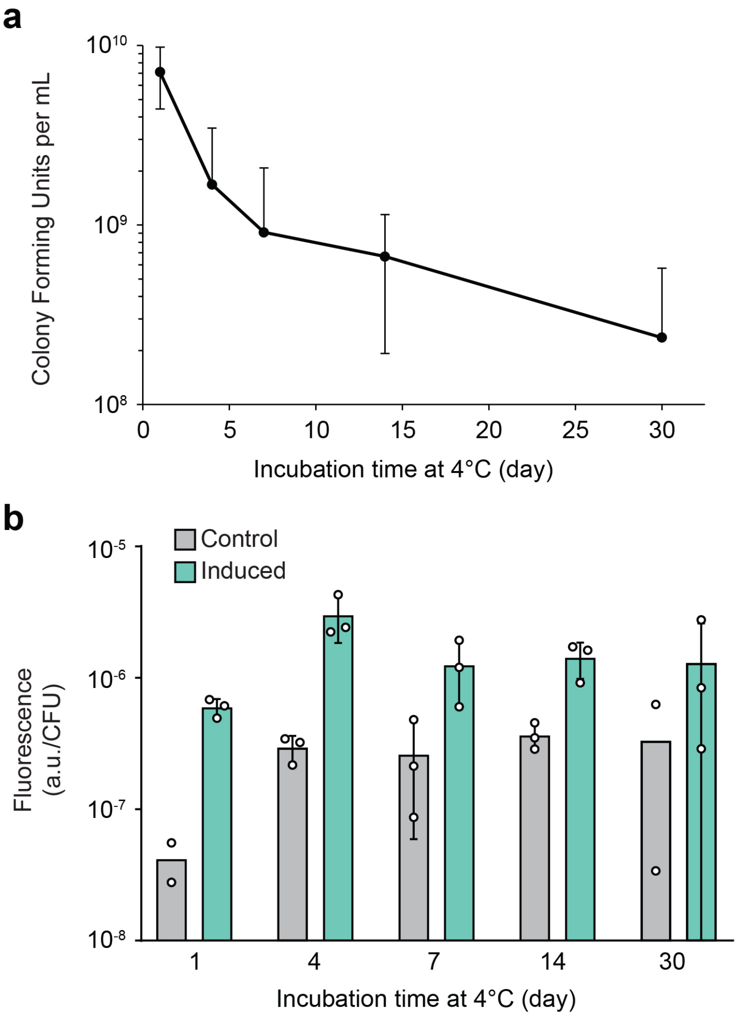

Figure 64 | **Cell survival and inducibility after storage at low temperature. (a)** CFU counts for cells retrieved from hydrogel beads after storage in a refrigerator (4°C) across 30 days **(b)** Comparison of aTc-induced fluorescence profiles of retrieved cells after storage at 4°C for various time periods. Samples prepared in triplicate; data represent the mean ±1 SD.

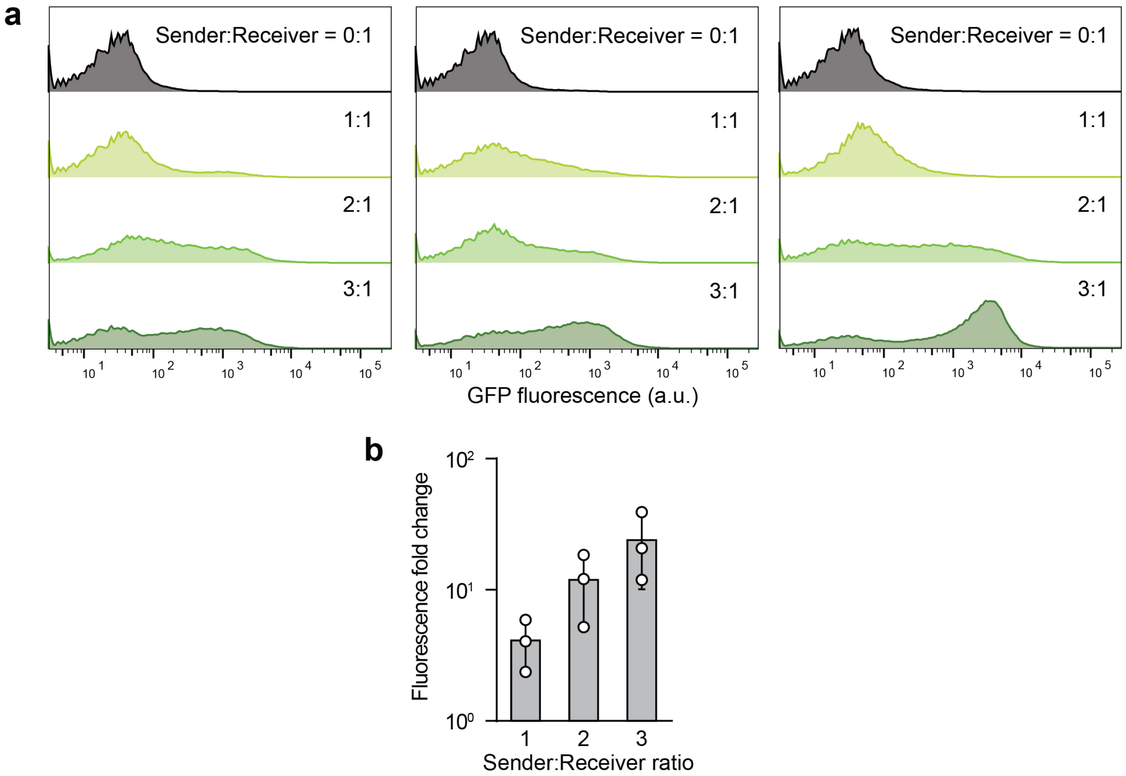

Figure 65 | **Induction of AHL receiver beads by AHL sender beads. (a)** Flow cytometry data of cells retrieved from receiver beads showed various levels of induction corresponding to different AHL sender bead to AHL receiver bead ratios (normalized to unit distribution, three biological replicates). **(b)** Fluorescence fold change of the receiver beads. Samples prepared in triplicate; data represent the mean ±1 SD.

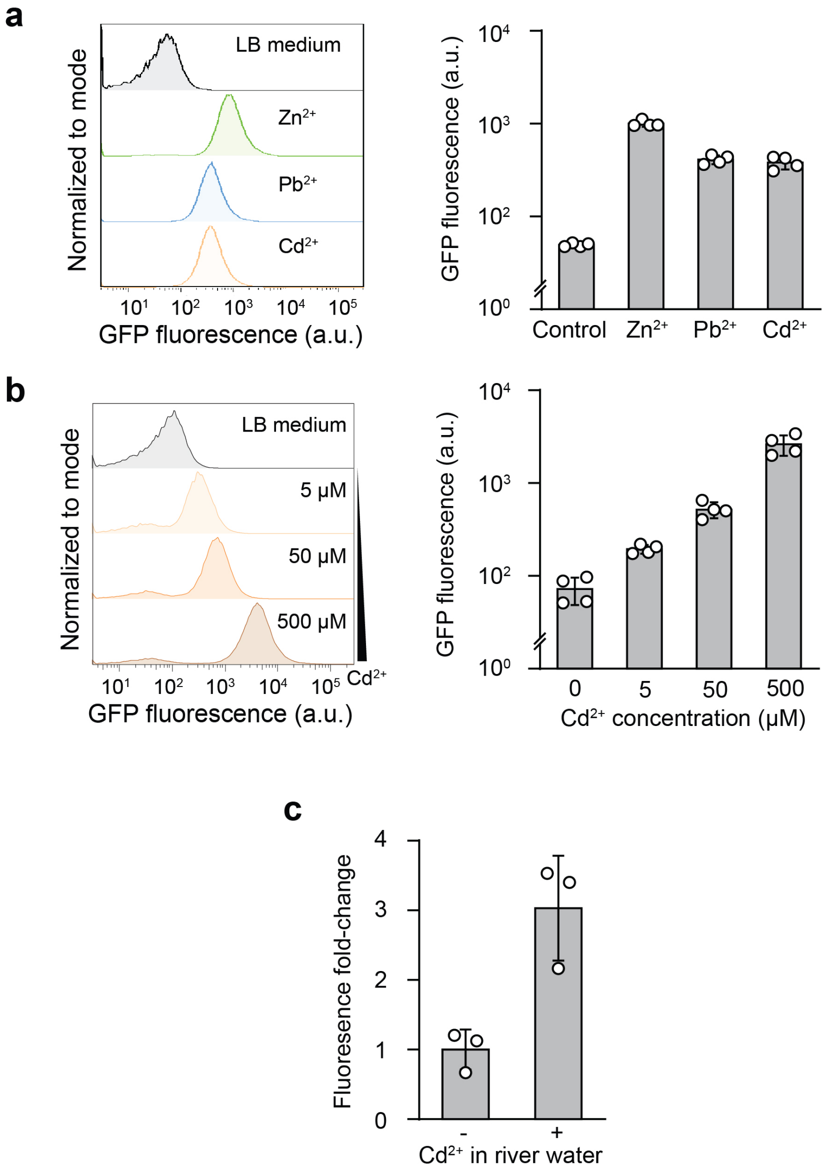

Figure 66 | **Heavy metal sensing in Charles River water samples. (a)** Left: Flow cytometry analysis of the heavy-metal-sensing strain. Bacteria in liquid were exposed for 3 hours to 300 μM $ZnCl_2$, 100 μM $Pb(NO_3)_2$, and 10 μM $CdCl_2$ in LB media, respectively. Right: Mean GFP fluorescence of the heavy-metal-sensing strain. Samples prepared in *n* = 4, data represent the mean ±1 SD. **(b)** Left: Response of the heavy-metal-sensing strain encapsulated in the tough hydrogel capsule to 0 μM, 5 μM, 50 μM, and 500 μM $CdCl_2$ after 3 hours of incubation. Right: Mean GFP fluorescence of the heavy-metal-sensing strain encapsulated in the tough hydrogel capsule. Samples prepared in *n* = 4, data represent the mean ±1 SD. **(c)** GFP fluorescence fold-change of encapsulated cells responding to cadmium ions in Charles River water. Samples prepared in triplicate; data represent the mean ±1 SD.

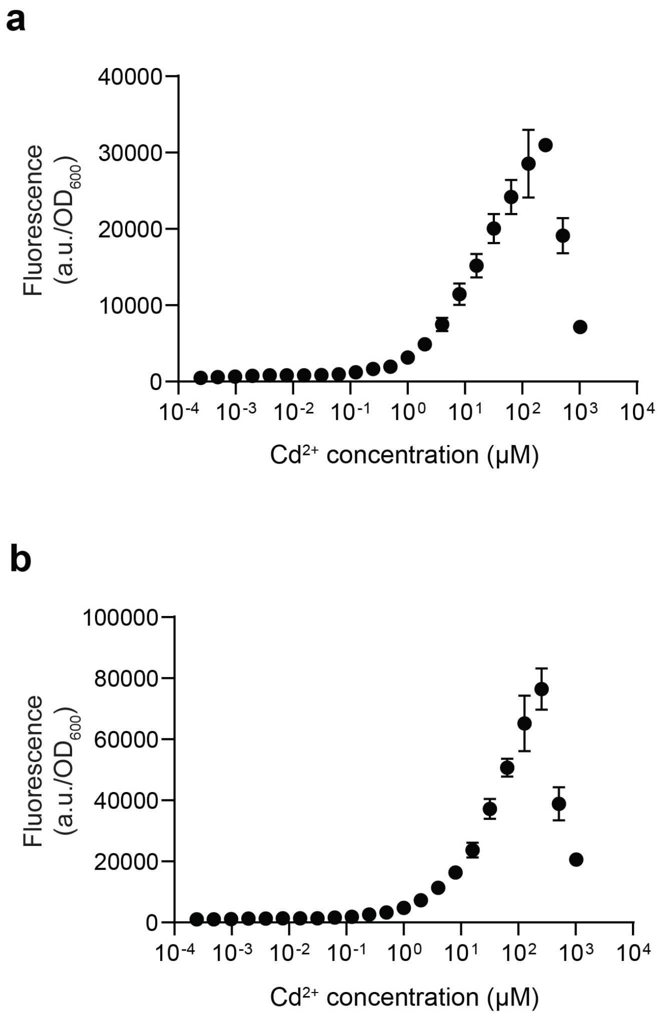

Figure 67 | **Dose-response curves of P*zntA*-GFP induced by Cd^{2+}.** The expression of GFP in cells harboring the plasmid pEZ074 after **(a)** 3 hours and **(b)** 6 hours of incubation with Cd^{2+}. Slow cell growth and reduced fluorescence were observed at [Cd^{2+}] > 256 μM.

Figure 68 | **Plasmid maps of pEZ055, pEZ058, and pEZ074.** ColE1 rep: ColE1 origin of replication; amp marker: resistance gene cassette for carbenicillin; gfp: green fluorescence protein.

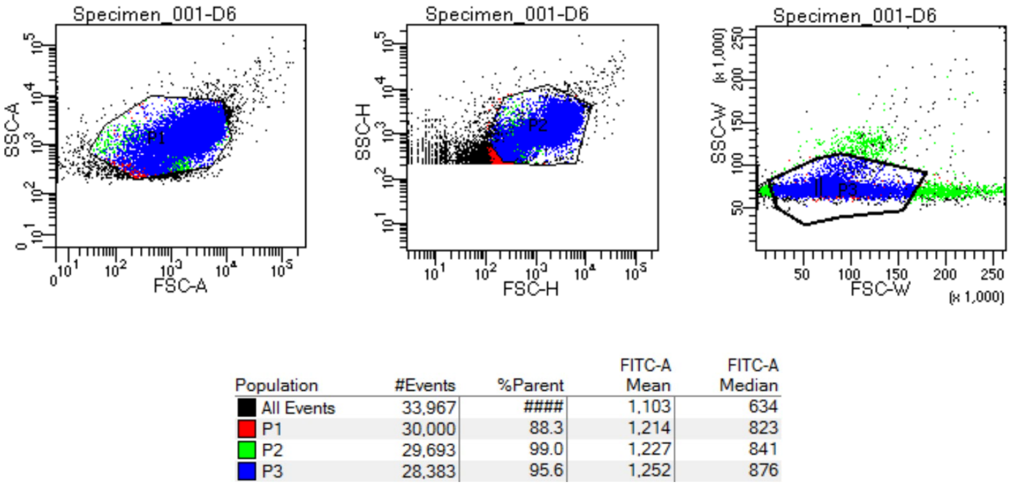

	Population	#Events	%Parent	FITC-A Mean	FITC-A Median
■	All Events	33,967	####	1,103	634
🟥	P1	30,000	88.3	1,214	823
🟩	P2	29,693	99.0	1,227	841
🟦	P3	28,383	95.6	1,252	876

Figure 69 | **Gating strategy for flow cytometry.** Top: Cells were gated using log forward scatter area (FSC-A) by log side scatter area (SSC-A), followed by gating on log forward scatter height (FSC-H) by log side scatter height (SSC-H), and subsequent gating on log forward scatter width (FSC-W) by log side scatter width (SSC-W). Bottom: Cell population abundance during each gating stage, in numbers and percentages.

B.2 Supplementary tables

Table 5 | List of bacterial strains used in this study

Name	Strain code	Construction method	Genotype
GRO, pIF auxotroph strain	rEc.β.dC.12'.ΔtY	Ref[258]	MG1655
GRO, pIF auxotroph strain	LspA.Y54β	Ref[258]	MG1655
aTc sensing strain	EZ055	DH5αPRO cells transformed with the pEZ055 plasmid	DH5αPRO
F' plasmid donor strain	CJ236	Acquired from NEB	K12
F' plasmid recipient strain	rcF453	Spontaneous resistant mutants generated from plating and re-streaking MG1655 on LB+Sm plate	MG1655
Zn/Pb/Cd sensing strain	EZ074	DH5αPRO cells transformed with the pEZ074 plasmid	DH5αPRO
SCRIBE $kanR_{OFF}$ reporter strain	F144	Ref[278]	DH5αPRO galK::$kanR_{W28TAA, A29TAG}$
AHL sender strain	AYC261	Ref[360]	DH5αPRO
AHL receiver strain	EZ058	DH5αPRO cells transformed with the pEZ058 plasmid	DH5αPRO
Heme sensing strain	mm1560	Ref[175]	Nissle 1917

Table 6 | List of plasmids used in this study

Name	Plasmid code	Construction method
$P_{\mathrm{LtetO\text{-}1}}$_*gfp*	pEZ055	See B.3 Methods and B.1 Figure 68
P_{lux}_*gfp*	pEZ058	See B.3 Methods and B.1 Figure 68
P_{zntA}_*gfp*	pEZ074	See B.3 Methods and B.1 Figure 68
P_{lacO}_SCRIBE(*kanR*)on	F944	Ref[278]
P_{TetO}_CRISPRi(*recJ*_gRNA & *xonA* gRNA)	F1156	Ref[361]
P_{TetO}_*LuxI*	AYC261	Ref[360]

B.3 Materials and methods

Bacterial strains and plasmids

A complete listing of bacterial strains and plasmids, including their sources, can be found in B.3 Table 5 and B.3 Table 6. Specifically, pEZ055, pEZ058, and pEZ074 (Supplementary Fig. 17) were constructed on a high copy number plasmid (pZE12) backbone carrying a green fluorescence protein (GFP) reporter gene and transformed into DH5αPRO cells. For the aTc-inducible plasmid (pEZ055), the original pZE12 $P_{LlacO\text{-}1}$ promoter was substituted by $P_{LtetO\text{-}1}$. For the AHL-sensing plasmid (pEZ058), the P_{lux} promoter was PCR amplified and cloned into pZE12 by substituting $P_{LlacO\text{-}1}$ promoter via Gibson Assembly. For the heavy-metal-sensing plasmid (pEZ074), the P_{zntA} promoter was PCR amplified from DH5αPRO *E. coli* genomic DNA and cloned into pZE12 by substituting $P_{LlacO\text{-}1}$ promoter via Gibson Assembly.

Manufacturing the alginate cores

5 wt % alginate solution was made by dissolving medium viscosity alginate (Sigma-Aldrich A2033) in MilliQ water followed by autoclaving at 120°C for 20 minutes to ensure sterility. A fresh bacterial culture (~10^9 cells/mL in LB plus antibiotics) was then mixed with the alginate solution in a one-to-one volume ratio to reach a final alginate concentration of 2.5 wt %. This bacteria-alginate premix was loaded into a syringe and disposed onto parafilm to form bead-like droplets. The droplets were solidified by immersing them in 5 wt % $CaCl_2$ (an ionic crosslinker, Sigma-Aldrich 223506) solution for 15 minutes.

Coating with tough hydrogel

A precursor solution composed of 2 wt % alginate, 30 wt % acrylamide (AAm; Sigma-Aldrich A8887), 0.046 wt % ammonium persulphate (APS; Sigma-Aldrich A3678), and 0.015 wt % *N*,*N*-

methylenebisacrylamide (MBAA; Sigma-Aldrich 146072) was thoroughly de-gassed. Before the coating process, the viscous precursor solution was mixed with an accelerator, *N*,*N*,*N'*,*N'*-tetramethylethylenediamine (TEMED; Sigma-Aldrich T9281; 0.1% times the volume of the precursor solution) to form a fast-curable pre-gel solution. Alginate cores from the previous section were dipped into the pre-gel solution to form a tunable thin shell layer of 100~1000 microns surrounding the core under a nitrogen atmosphere. To stabilize the shell layer, the hydrogel then was immersed in a MES buffer (0.1 M MES and 0.5 M NaCl, pH 6.0) together with cross-linkers and catalysts including 0.125 wt % 1-ethyl-3-(3-dimethylaminopropyl)carbodiimide (EDC), 0.0375 wt % N-hydroxysuccinimide (NHS), and 0.075 wt % adipic acid dihydrazide (AAD) to form the covalent bonding between the alginate and polyacrylamide network for 3 hours.

Retrieval of bacterial cells

After experiments described in the following sections, beads were retrieved from liquid and the tough shell around the alginate core was carefully removed with a razor blade and tweezers. The cores were then placed in tubes containing 1 mL phosphate-buffered solution (PBS; Research Products International) plus 55 mM sodium citrate (Sigma-Aldrich S4641) and homogenized with 5 mm stainless steel beads on a TissueLyzer II (Qiagen 85300) at 30 Hz for 30 minutes. To quantify cell density, homogenized samples were serially diluted (10x) and plated on LB plus antibiotics agar plates. Colony forming units (CFU) were counted after overnight incubation at 37°C.

Growth of bacteria in beads

All the beads containing *E. coli* cells underwent an outgrowth step after they were taken out of the crosslinking solution to replenish their CFU counts. Each bead was placed in a well on a 24-well plate and incubated in LB plus antibiotics and 20 mM of $CaCl_2$ at 37°C. Any beads that showed bacterial growth in the surrounding media were discarded. To quantify the bacterial growth kinetics inside the alginate core, at each time point (every 3 hours for a total duration of 24 hours, see B.1 Figure 55), cells were retrieved from beads and plated on LB plus antibiotics agar plates for CFU counting.

Comparison with alginate and agarose shell

Alginate cores containing EZ074 cells were prepared as described previously. For coating with alginate shell[280], alginate cores were dipped in 2.5 wt% alginate solution and crosslinked in 0.1 M $CaCl_2$ for 30 minutes. For coating with agarose shell[276], alginate cores were covered by 2 wt% agarose solution (~40°C) and let solidify for 30 minutes. Coated beads were then incubated in 1 mL LB plus antibiotics and shaken at 200 rpm for 12 hours at 37°C.

Swelling test

Hydrogel beads containing EZ074 cells were incubated in PBS plus 20 mM of $CaCl_2$ at 37°C for 14 days. At given time points, the beads were retrieved and weighted (normalized to D0) using an electronic scale. Day 0 was defined as 12 hours post manufacturing of the beads.

Compression test

The compression of hydrogel beads was carried out using a mechanical testing machine (Z2.5; Zwick/Roell) with a 20-N load cell. The samples were compressed in air or in PBS plus 20 mM of $CaCl_2$ by two rigid flat substrates at a loading speed of 2 mm min^{-1}. As the beads will be immersed in liquid in all practical applications, the mechanical properties (force and displacement) in air were determined in the swollen state. This was carried out by keeping the bead immersed in PBS plus 20 mM of $CaCl_2$ up until the measurement. The approximate engineering stress is defined as:

$$\frac{P}{\pi r_0^2}$$

where r_0, and P are the initial radius of the bead, and the magnitude of the compressive load, respectively[273,359]. After testing, beads were incubated in LB overnight and the surrounding media were plated to detect potential cell leakage from compression.

Controlling GRO life span

GROs (rEc.β.dC.12'.ΔtY and LspA.Y54β) were grown in LB plus 1 mM p-iodo-L-phenylalanine (pIF; Sigma-Aldrich I8757), 0.02% L-arabinose (L-ara), and carbenicillin at 30°C overnight[258], washed twice with PBS to remove pIF and L-ara, and encapsulated in hydrogel beads. GRO beads were then incubated in LB plus carbenicillin with or without 1 mM pIF at 4°C overnight to allow pIF infusion. At t = 0, beads were placed in 50 mL LB medium and incubated at 30°C for 12 h, 24 h, and 48 h. Cells were retrieved at given time points and plated on LB plus carbenicillin with 1 mM pIF and 0.02% L-ara agar plates for CFU counting. Survival rates were calculated by normalizing CFU counts to t = 0.

Detecting GRO escape

GROs (rEc.β.dC.12'.ΔtY and LspA.Y54β) were grown in LB plus 1 mM pIF, 0.02% L-ara, and carbenicillin at 30°C overnight, washed twice with PBS to remove pIF and L-ara, and encapsulated in alginate beads with or without the tough hydrogel coating. The beads were then incubated in 5 mL LB plus carbenicillin at 30°C with 200 rpm shaking for 3 days. Media from each tube was plated on LB plus carbenicillin plates for CFU counts.

Environmental insult experiments

For antibiotics and acidic condition treatments, beads containing EZ074 cells were incubated in 1 mL of LB plus carbenicillin at 37°C for 12 to bring cell densities in the different beads to a similar level (~10^9 per bead). At t = 0, culture media was switched to LB plus 30 μg/ml kanamycin and LB at pH 4, respectively. At the end of the experiments, beads were retrieved from liquid media, and cells were harvested for CFU counting.

Microscopy of hydrogel beads

Hydrogel beads containing EZ074 cells post-outgrowth were incubated in LB at pH 4 and shaken at 120 rpm at 37°C for 4 hours. At the end of treatment, the alginate cores of the beads were retrieved and washed in PBS twice. The cores were cut in half with a razor blade and stained using Live/dead™ BacLight™ Bacterial Viability Kit for microscopy & quantitative assays (Thermo Fisher Scientific L7012). Microscopy was performed using a confocal microscope (SP 8; Leica) with excitation wavelength at 495 nm and emission wavelength at 515 nm for living cells; and excitation wavelength at 495 nm and emission wavelength at 635 nm for dead cells. Z-stack was performed at a fixed step size of 17 μm.

Bacterial conjugation

The F' plasmid (containing chloramphenicol resistance) donor strain CJ236 was encapsulated in beads and underwent overnight outgrowth in LB without antibiotics. The donor beads were placed in 2 mL of LB and co-cultured with recipient strain rcF453 (with streptomycin resistance). After 24 hours of incubation at 37°C (shaking at 100 rpm), the surrounding media was plated on LB plus streptomycin (Sm, 25 μg/mL) and LB plus streptomycin (25 μg/mL) and chloramphenicol (Cm, 12.5 μg/mL). The conjugation efficiency was calculated as:

$$\frac{CFU\ on\ LB + Sm + Cm}{CFU\ on\ LB + Sm}$$

DNA escape test

A linear DNA fragment encoding a GFP transcriptional unit (~1k bp) was amplified using PCR and encapsulated in the hydrogel beads at 3e9 copy/μL. Soluble DNA in the surrounding media after 72-hr incubation was quantified using qPCR (Roche LightCycler 96) with an optimized amplicon (314 bp). A standard curve was constructed using a serial dilution (10x) of the same fragment.

Small molecule diffusion assay

Two fluorescent dyes, rhodamine B and fluorescein, were used as surrogates for small molecule diffusion assay. Coated beads were soaked in dye solutions for various time periods, weighted, and transferred into 2 mL of PBS and incubated in the dark for 24 hr. The fluorescence of the PBS at equilibrium was measured (494/521 nm and 540/625 nm with a Synergy H1 Hybrid Multi-Mode Reader, BioTek Instruments), calibrated by the total weight of PBS plus bead, and normalized to the saturated maximum incubation period in dyes (24 hours).

aTc induction in beads

Beads containing EZ055 were incubated in LB plus carbenicillin and 200 ng/mL aTc at 37°C for 8 hours. The bead was then retrieved and sliced with a sharp razor blade at a thickness of ~0.5 mm. The sliced sample was then imaged with a Zeiss LSM 700 confocal microscope with excitation wavelength at 488 nm and emission wavelength at 515 nm. To test inducibility after long-term storage, beads were kept at 4°C over the course of 30 days. At each time point, beads were retrieved and induced in LB plus carbenicillin and 200 ng/mL aTc at 37°C for 8 hours. Fluorescence profiles were characterized using a Synergy H1 Hybrid Multi-Mode Reader (488 nm excitation, 530/30 detection).

Heme sensing in beads

Defibrinated horse blood (Hemostat Laboratories DHB030) was used as the source of blood and was lysed by first diluting 1:10 in simulated gastric fluid (SGF) (0.2% NaCl, 0.32% pepsin, 84 mM HCl, pH 1.2) to release heme. This stock solution was diluted to 300 ppm in PBS right before experiments. Beads were placed in PBS or PBS + blood for 8 hours at 37°C. Cells were retrieved and measured for luminescence using a Synergy H1 plate reader. The relative luminescence units were normalized by CFU (measured through plating). Luminescence images of intact beads were acquired using a ChemiDoc Touch Imaging System (Bio-Rad).

Memory of chemical exposure (SCRIBE) in beads

A higher efficiency version of SCRIBE (Synthetic Cellular Recorders Integrating Biological Events) was used in this study[278,285]. The SCRIBE strain was encapsulated in tough hydrogel beads and incubated in LB media with carbenicillin (100 µg/mL), chloramphenicol (25 µg/mL), aTc (100 ng/ml), and IPTG (1 mM) at 37°C. A control group was incubated using the same conditions but without the inducers (aTc and IPTG). At given time points, cells were retrieved from the beads and plated on LB plus kanamycin (50 µg/mL) agar plates as well as LB plus carbenicillin and chloramphenicol agar plates. The recombinant frequency was calculated by dividing the colony count on the LB plus kanamycin plate (kan-resistant cells) by the colony count on the LB plus carbenicillin and chloramphenicol plate (total viable cells).

Quorum sensing between beads

Beads containing the AHL sender strain (AYC261) and AHL receiver strain (EZ058) were placed in 1 mL LB plus 250 ng/mL aTc in a 12-well plate at specific ratios (sender:receiver = 0:1, 1:1, 2:1, and 3:1). After 24 hours of incubation at 37°C, we retrieved and diluted AHL receiver cells 1:20 into phosphate-buffered solution (PBS, Research Products International) and ran them on a BD-FACS LSRFortessa-HTS cell analyzer (BD Biosciences). We measured at least 20,000 cells for each sample and consistently gated by forward scatter and side scatter for all cells in an experiment. GFP intensity was measured on the FITC channel (488-nm excitation laser, 530/30 detection filter). Data from flow cytometry is normalized to unit distribution (normalized to the area under the curve). Cells were gated using log forward scatter area (FSC-A) by log side scatter area (SSC-A), followed by gating on log forward scatter height (FSC-H) by log side scatter height (SSC-H), and subsequent gating on log forward scatter width (FSC-W) by log side scatter width (SSC-W), as exemplified in B.1 Figure 69.

Heavy metal sensing

To test inducibility of the Zn/Pb/Cd sensing strain (EZ074) in liquid, cells were grown overnight and diluted 200x in fresh LB plus 300 μM $ZnCl_2$, 100 μM $Pb(NO_3)_2$, and 10 μM $CdCl_2$, respectively on a 96-well plate. After 3 hours of incubation at 37°C, we retrieved bacterial cells and analyzed their GFP profile with flow cytometry. To build the dose-response curves for Cd^{2+} induction, an overnight culture of EZ074 was diluted 200x in fresh LB plus antibiotics and induced with different concentrations of $CdCl_2$. The GFP expression profiles were measured using a Synergy H1 Hybrid Multi-Mode Reader and normalized to their OD_{600} values. For testing inducibility in beads, EZ074 was encapsulated in tough hydrogel beads and incubated overnight in LB media with carbenicillin at 4°C. Before the experiment, beads were incubated at 37°C for 12 hours for bacterial cell outgrowth. Hydrogel beads were then placed in fresh LB medium with carbenicillin and corresponding metal ions at given concentrations and incubated at 37°C for 3 hours. Bacterial cells were retrieved and analyzed with flow cytometry. Data from flow cytometry is normalized to mode (normalized to peak value), which allows the visualization of differences in relative percentages of cell populations of interest.

Metal sensing in Charles River water

Beads containing EZ074 were incubated in 4x LB media at 4°C overnight to reach equilibrium. At t = 0, beads were placed in teabags and transferred to beakers containing 100 mL of fresh Charles River water with or without 5 mM $CdCl_2$. After 6 hours of incubation at room temperature, cells were retrieved and analyzed with flow cytometry. Data from flow cytometry is normalized to mode.

Appendix C

Additional Information and Protocols for Chapter 4

C.1 Supplementary figures

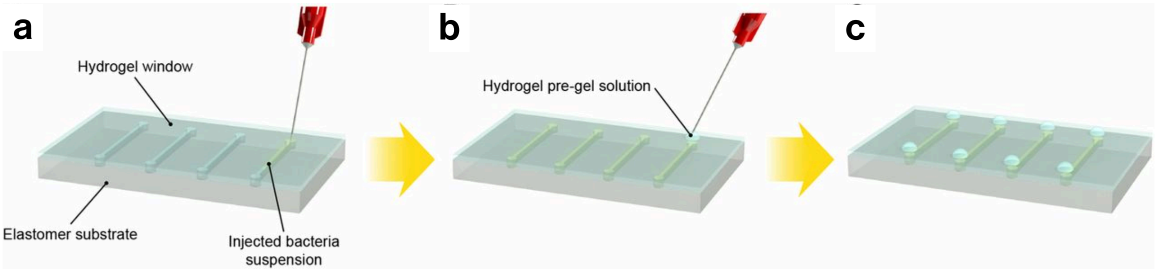

Figure 70 | **Schematic illustration of cell suspension injection and sealing of injection points. (a)** Bacteria were injected into the cavities at the hydrogel–elastomer interface with metallic needles from the hydrogel side. **(b)** Injection holes were sealed on the hydrogel–elastomer device with drops of fast-curable pregel solution. **(c)** We obtained the hydrogel–elastomer device with fully encapsulated bacteria.

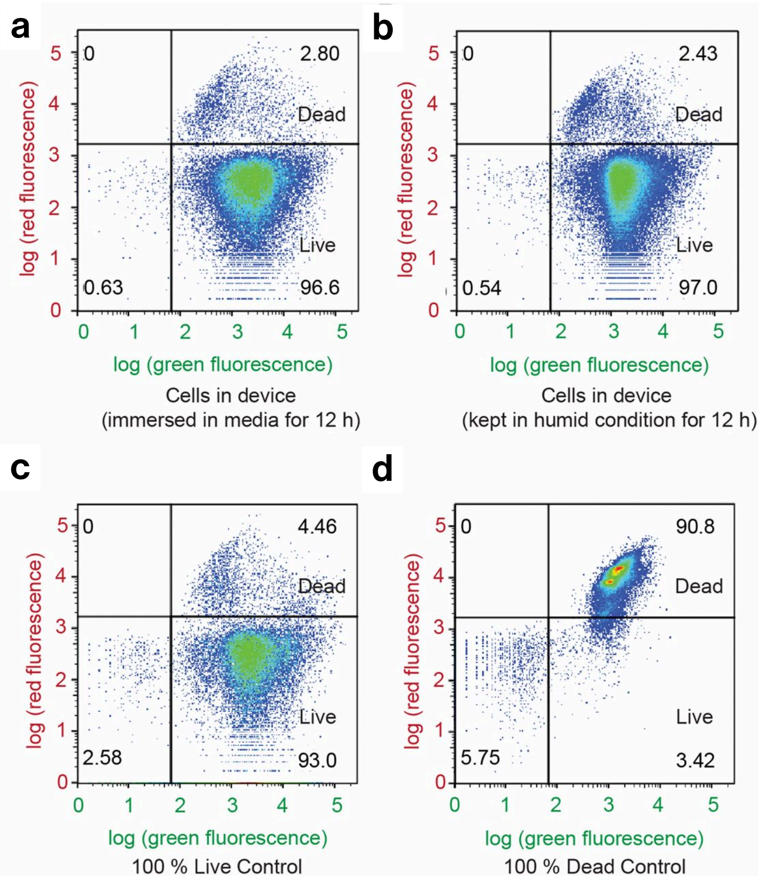

Figure 71 | **Flow cytometry analysis using live/dead stains** for **(a)** cells retrieved from the living device that has been immersed in media for 12 h, **(b)** cells retrieved from the living device that has been placed in a humid environment for 12 h, **(c)** live-cell controls, and **(d)** dead-cell controls. Green fluorescence denotes both live and dead bacteria, and red fluorescence denotes bacteria that have been damaged and leaky membranes. The distributions of the live and dead populations are illustrated in the plots, with thresholds determined by controls. Over 95% of cells in the hydrogel–elastomer devices immersed in media or placed in humid chamber remained viable after 12 h.

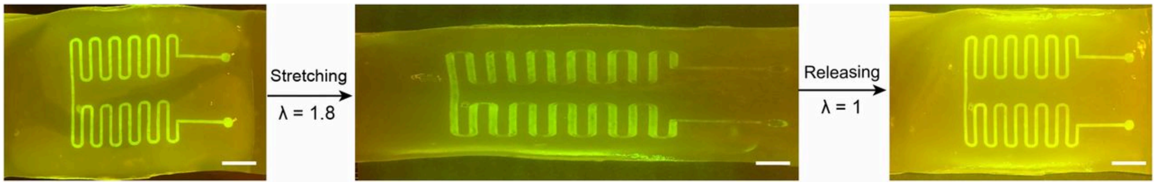

Figure 72 | **Functional living device under large uniaxial stretch.** After GFP was switched on in the wavy channels of Ecoflex–hydrogel hybrid matrix, the device was stretched to 1.8 times its original length and then released. The device, including cells encapsulated, can maintain functionality under large deformation without failure or leakage. (Scale bar: 5 mm.)

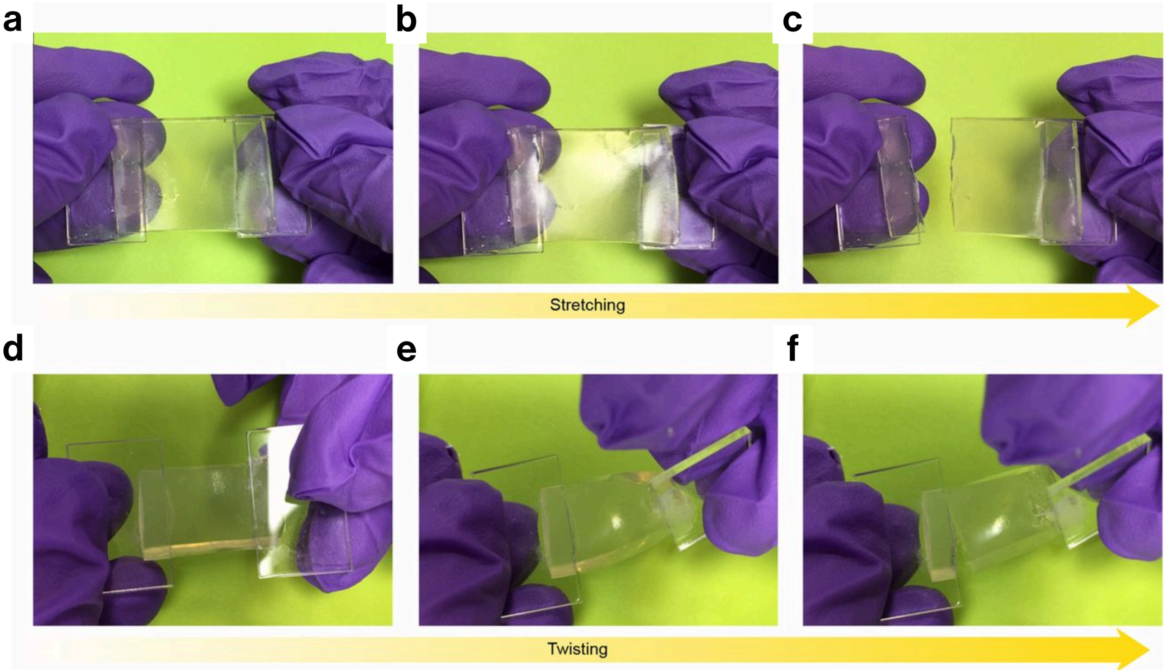

Figure 73 | **Deformation of agar-based living devices.** An agar-based control device that encapsulated Rham$_{RCV}$/GFP bacteria with the same dimensions as the hydrogel–elastomer hybrid was fabricated. The agar device fractured even under moderate deformation, including **(a-c)** a stretch of 1.1 or **(d-f)** a twist of 60°.

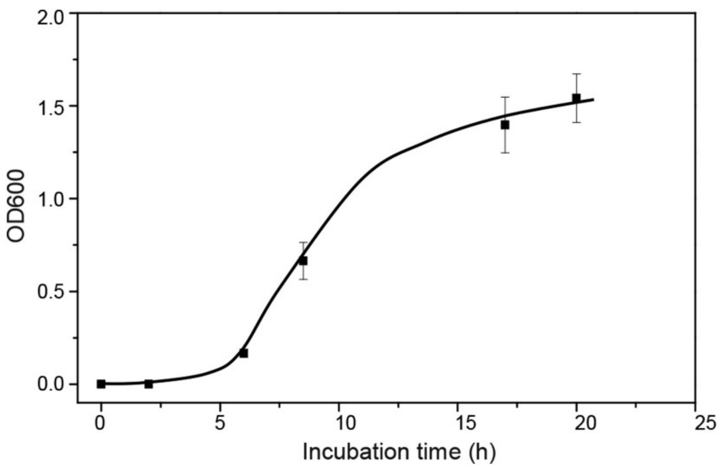

Figure 74 | **Cell leakage from the agar device.** The medium surrounding the agar device (without any deformation) was collected to measure OD_{600}. The high OD_{600} after 10 h indicates the large cell populations in the medium and cell leakage even without any deformation of agar gel.

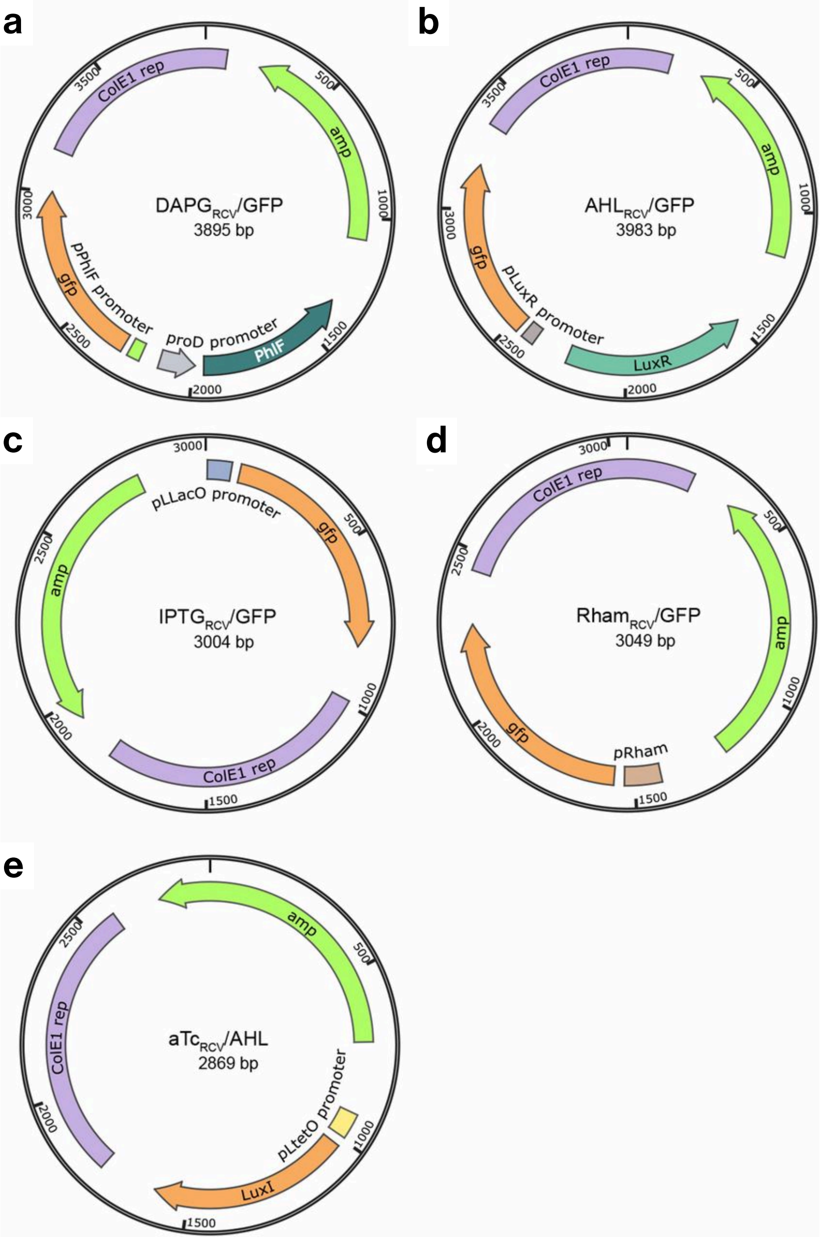

Figure 75 | **Plasmid maps of the plasmids constructed.** **(a)** DAPG$_{RCV}$/GFP, **(b)** AHL$_{RCV}$/GFP, **(c)** IPTG$_{RCV}$/GFP, **(d)** Rham$_{RCV}$/GFP, and **(e)** aTc$_{RCV}$/AHL. Plasmids were constructed as described in C.2 Materials and methods. amp, Ampicillin resistance gene; ColE1 rep, replication origin from ColE1 plasmid.

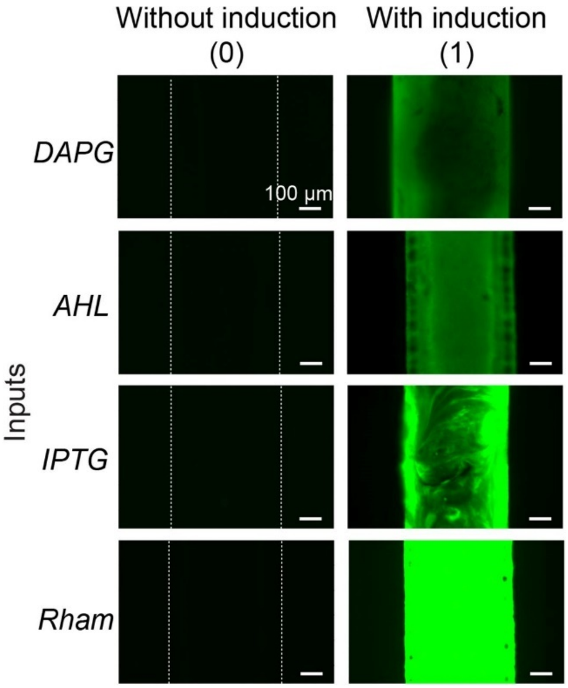

Figure 76 | **Microscopic images of different cell strains in the chamber encapsulated in the living device.** When a cell strain was induced, the channels showed fluorescence [denoted as (1)]. If not induced, the channel stayed dark [denoted as (0)]. Scale bars are shown in images.

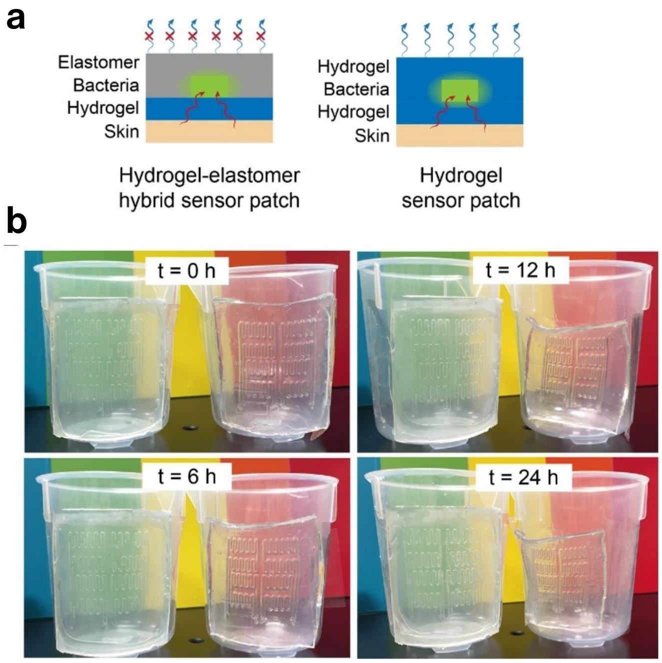

Figure 77 | **Anti-dehydration property of the sensor patch. (a)** Schematic illustration of the hydrogel–elastomer hybrid sensor patch, which has the anti-dehydration property over the pure hydrogel device. The silicone elastomer cover effectively prevents the evaporation of water from the hydrogel and dehydration of the living patch. **(b)** Time-lapse snapshots of hydrogel–elastomer hybrid sensor patch (Left) and pure hydrogel sensor patch (Right) mounted on a plastic beaker at room temperature with low humidity (25°C and 50% relative humidity) for 24 h. The elastomer outer layer of the hydrogel–elastomer hybrid device significantly slowed down the dehydration process of the hydrogel and provided a sustained humid environment for encapsulated cells for over 24 h. However, distorted channels became apparent on patches made of pure hydrogels when they were exposed to air for 6 h because of dehydration.

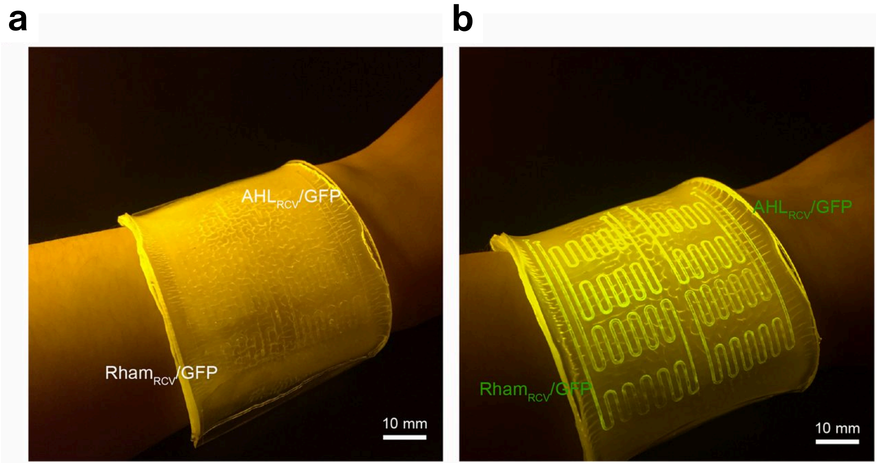

Figure 78 | **Living patch control experiments. (a)** When no inducer was smeared on the skin and the living sensor patch was adhered on skin conformably, the channels with Rham$_{RCV}$/GFP and AHL$_{RCV}$/GFP in the living patch did not show any differences. **(b)** When both inducers Rham and AHL were smeared on the skin and the living patch was applied, the channels with Rham$_{RCV}$/GFP and AHL$_{RCV}$/GFP in the living patch became fluorescent. Scale bars are shown in images.

C.2 Materials and methods

Materials

The hydrogel was composed of two types of cross-linked polymers: ionically cross-linked alginate and covalently cross-linked PAAm. For the stretchy PAAm network in hydrogel, acrylamide (AAm; A8887; Sigma-Aldrich) was used as the monomer, *N*,*N*-methylenebisacrylamide (MBAA; 146072; Sigma-Aldrich) was used as the cross-linker, and 2-hydroxy-4′-(2-hydroxyethoxy)-2-methylpropiophenone (Irgacure 2959; 410896; Sigma-Aldrich) was used as the photoinitiator. Calcium sulfate (C3771; Sigma-Aldrich) slurry acted as the ionic cross-linker with sodium alginate (A2033; Sigma-Aldrich) for the dissipative network. As for elastomers, Sylgard 184 [polydimethylsiloxane (PDMS; Dow Corning] or Ecoflex (Smooth-On) was molded and activated with benzophenone (B9300; Sigma-Aldrich). Purple Nitrile Examination Gloves (Kimberly-Clark) were also used as an elastomer substrate. Ammonium persulfate (APS; A3678; Sigma-Aldrich) as a thermoinitiator and *N*,*N*,*N*′,*N*′-tetramethylethylenediamine (TEMED; T9281; Sigma-Aldrich) as a cross-linking accelerator were used in the fast-curable pregel solution for sealing of injection points. For cell induction, DAPG (sc-206518; Santa Cruz Biotechnology), AHL (K3007; Sigma-Aldrich), IPTG (I5502; Sigma-Aldrich), Rham (W373011; Sigma-Aldrich), and aTc (37919; Sigma-Aldrich) were used as the signaling molecules. Carbenicillin (C1389; Sigma-Aldrich) was added as an antibiotic in the LB–Miller medium (L3522; Sigma-Aldrich) for cell culture. The LIVE/DEAD BacLight Bacterial Viability and Counting Kit (L34856; Sigma-Aldrich) was used for cell viability assay.

Fabrication of hydrogel and elastomer hybrid

Elastomers with microstructured cavities were prepared by soft lithography with a feature size of 500 μm in width and 200 μm in depth. Then, the prepared microstructured elastomer was assembled with hydrogel to form a robust hydrogel–elastomer hybrid as described in the previous report[306]. Briefly, the surface of the elastomer was treated with 10% (wt/vol) benzophenone solution in ethanol for 10 min, washed, and dried with nitrogen. The pregel solution [12.05% (wt/vol) AAm, 1.95% (wt/vol) sodium alginate, 0.2% Irgacure 2959, 0.012% MBAA] was carefully degassed and mixed with calcium sulfate slurry (2×10^{-2} M in pregel solution) to form physically cross-linked hydrogel. To introduce robust bonding between assembled hydrogel and elastomer, the physically cross-linked hydrogel was assembled with the surface treated elastomer followed by UV irradiation (365 nm; UVP CL-1000) for 30 min. The resultant hydrogel–elastomer hybrid was washed with PBS for three times, sterilized using germicidal UV irradiation thoroughly, and immersed in LB with antibiotics for 12 h before bacterial cell seeding. Fast-curable pregel solution [30.05% (wt/vol) AAm, 1.95% (wt/vol) sodium alginate, 0.012% MBAA, 0.142% APS, 0.10% TEMED], which could be cured at room temperature in 5 min, is used for sealing the holes after cell seeding.

Bacterial strains and plasmids

The plasmids used in this study were constructed with standard molecular cloning techniques. To create constructs for the expression of output genes under tight regulation by DAPG-, IPTG-, AHL-, or Rham-inducible promoters, pZE-AmpR-pL(lacO)-*gfp* (IPTG-inducible) was used as a starting point. All promoters were amplified using PCR and inserted in place of pL(LacO) by Gibson assembly. The corresponding repressors or activators, which can interact with small molecule inducers, were inserted into the *E. coli* genome or cloned onto the same plasmid that harbors the promoter-*gfp* output module. For example, the proteins PhlF and LacI repressed DAPG- and IPTG-inducible promoters, respectively. PhlF was inserted in a plasmid under the regulation of proD promoter, whereas the LacI repressor was already present in the genome of DH5αPRO. Similarly, the AHL-inducible transcriptional activator, LuxR, was constitutively expressed from a plasmid and can activate promoter pLuxR on binding to AHL. The regulatory components necessary for Rham induction were already present in the *E. coli* genome and did not require additional engineering. To construct the AHL sender plasmid, *LuxI* was put onto a plasmid under the regulation of aTc-inducible promoter PLtetO. Finally, all ligations for plasmid construction were transformed into *E. coli* strain DH5αPRO with standard protocols and are described in C.1 Figure 75.

Cell induction in the living device

The cell-contained device was immersed in LB broth with carbenicillin and inducer(s) at 25°C as mentioned in the text. Inducers could be added in LB at final concentrations of 100 μM DAPG, 100 nM AHL, 1 mM IPTG, 12 mM Rham, and/or 200 ng/mL aTc. Alternatively, a piece of sterilized tissue paper (Kimtech) was dipped in LB with inducer in it and put on top of the hydrogel layer. The device and the tissue paper were kept at 25°C and relative humidity of 90%. The latter method was not only applicable for the cell to receive inducers from the environment (e.g., induction of IPTG_{RCV}/GFP by IPTG) but also, more suitable for intercellular communication when dilution of signaling molecules by the environment was undesirable. Every induction/detection experiment was performed and repeated at least three times.

Cell viability assay

By using the LIVE/DEAD BacLight Bacterial Viability and Counting Kit in combination with flow cytometry, the cell viability assay was conducted for cells retrieved from devices and live/dead controls. The fluorescent LIVE/DEAD BacLight Bacterial Viability and Counting Kit consists of two stains: the green fluorescent nucleic acid stain SYTO 9, which stains the nucleic acids of both living and dead bacteria, and the red fluorescent nucleic acid stain propidium iodide, which only stains bacteria that have damaged and leaky membranes. Rham_{RCV}/GFP bacterial suspensions were retrieved from the device by poking a hole from the hydrogel using metal needles after 12, 24, 48, and 72 h of culture. Live-cell controls (untreated) and dead-cell controls (isopropyl alcohol-treated) were set as standards. A diluted bacterial suspension and the LIVE/DEAD BacLight solution were mixed together and incubated at room temperature protected from light for 15 min. The stained cell samples were then analyzed by an LSRFortessa Flow Cytometer (BD Biosciences). For each sample, at least 10^4 events were recorded using a flow rate of 0.5 μL/s. FlowJo (TreeStar) was used to analyze the data. All events were gated by forward scatter and side scatter. In C.1 Figure 71, green fluorescence denotes both live and dead bacteria, and the red fluorescence denotes bacteria that have been damaged and leaky membranes. The distributions of the live and dead populations were distinguished in the cytograms.

Cell escape test

An intact hydrogel–elastomer living device, and a defective living device (with weak hydrogel–elastomer bonding) were tested for comparison. Also, the agar hydrogel with the same dimensions as the hydrogel–elastomer hybrid and encapsulating $\mathrm{Rham}_{\mathrm{RCV}}$/GFP bacteria was used as a control. We first deformed the living materials, which contained $\mathrm{Rham}_{\mathrm{RCV}}$/GFP bacteria in different modes (i.e., twisting and stretching), and then immersed them in LB for 24 h. To test the bacteria leakage, LB solutions surrounding the device were collected for streaking on LB agar plates after 24 h, and OD_{600} measurements by UV-Visible Spectrophotometer (Thermo Scientific) were taken after 6, 12, 20, and 24 h.

In addition, we prepared agar hydrogel with bacteria encapsulated: 1.5% (wt/vol) agar was dissolved in water at 90°C. When the agar solution cooled down to ~40°C, the $\mathrm{Rham}_{\mathrm{RCV}}$/GFP bacteria was mixed with the solution. As it continued to cool down, the solution could solidify and become a gel.

GFP expression assay

For quantitative measurement of GFP expression, the bacteria were isolated from the device by 32-gauge needles and diluted to 10^7 cells per 1 mL. Single-cell fluorescence was measured using an LSRFortessa Flow Cytometer with a 488-nm laser for GFP. For each sample, at least 10^4 events were recorded using a flow rate of 0.5 μL/s. FlowJo was used to analyze the data. All events were gated by forward scatter and side scatter. Integration of cell numbers over fluorescence was calculated and normalized to the maximum fluorescence. For qualitative observation of GFP expression by the naked eye, the living devices were exposed to benchtop UltraSlim Blue Light Transilluminators (New England Biogroup; wavelength of 470 nm). We extracted the green channel from optical images and adjusted the exposure by setting gamma correction to 0.2 in Adobe Photoshop CS6 (Adobe). Microscopic observation was done by the aid of a fluorescent microscope (Nikon Eclipse LV100ND), and all imaging conditions, such as beam power and exposure time, were maintained the same across different samples.

Preparation and testing of sensor patch on the skin

The robust hybrid patches with wavy microchannels were fabricated by using hydrogel (PAAm-alginate) and silicone elastomer (Sylgard 184) following the previously described method. Bacterial suspension of Rham_{RCV}/GFP was infused to the upper two channels of the patch, and AHL_{RCV}/GFP was infused to the lower two channels of the patch. Before we adhered the living patch on the forearm, the skin was smeared with LB of 12 mM Rham and/or 100 nM AHL. Note that these two inducers are nontoxic and safe to be applied on the skin. The living patch was conformably mounted on the skin with the PDMS layer exposed to air and fixed on the skin by a clear Scotch tape. To show the anti-dehydration property of the wearable living patch, a pure hydrogel device without an elastomer layer was fabricated by assembling micropatterned hydrogel and flat hydrogel sheet. To compare dehydration of hydrogel–elastomer hybrids and the hydrogel device without the elastomer layer, these two types of devices were conformably attached to curved surfaces of plastic beakers. The dehydration tests were carried out at room temperature with low humidity (25°C and 50% relative humidity) for 24 h. To show the stretchability of the living patch, we also fabricated the living skin patch with Ecoflex instead of PDMS in the same design and dimension. As illustrated in C.1 Figure 72, the stretchable skin patch with induced bacteria can be stretched and relaxed to 1.8 times its original length without failure.

Preparation and testing of living chemical detectors on nitrile glove fingertips

To show the living chemical sensors at the nitrile glove fingertips, hydrogel–elastomeric glove hybrids with spiral microchannels were prepared. We first laminated thin hydrogel sheets with patterned cell chambers on the fingertips of nitrile gloves and then, encapsulated different inducible cell inside. Different strains of bacteria (IPTG_{RCV}/GFP, AHL_{RCV}/GFP, and Rham_{RCV}/GFP) were injected into spiral-shaped cell chambers at different fingertips. To test the functionality of the fingertip sensor array, we used a cluster of cotton balls soaked in LB with 1 mM IPTG and 12 mM Rham. The glove was worn to grab the wet cotton balls, and hydrogels at the fingertips contacted the inducer-containing cotton balls. The fluorescence at the fingertips was exampled after 4 h of contact with the cotton balls using the benchtop transilluminator.

References

1. Sanchez, C., Arribart, H. & Giraud Guille, M. M. Biomimetism and bioinspiration as tools for the design of innovative materials and systems. *Nat. Mater.* **4**, 277–288 (2005).
2. Liu, K. & Jiang, L. Bio-inspired design of multiscale structures for function integration. *Nano Today* **6**, 155–175 (2011).
3. Wegst, U. G. K. *et al.* Bioinspired structural materials. *Nat. Mater.* **14**, 23–36 (2014).
4. Lu, Y., Aimetti, A. A., Langer, R. & Gu, Z. Bioresponsive materials. *Nat. Rev. Mater.* **2**, (2016).
5. Palagi, S. & Fischer, P. Bioinspired microrobots. *Nat. Rev. Mater.* **3**, 113–124 (2018).
6. Barthelat, F., Yin, Z. & Buehler, M. J. Structure and mechanics of interfaces in biological materials. *Nat. Rev. Mater.* **1**, (2016).
7. Cameron, D. E., Bashor, C. J. & Collins, J. J. A brief history of synthetic biology. *Nat. Rev. Microbiol.* **12**, 381–390 (2014).
8. Gardner, T. S., Cantor, C. R. & Collins, J. J. Construction of a genetic toggle switch in Escherichia coli. *Nature* **403**, 339–342 (2000).
9. Elowitz, M. B. & Leibler, S. A synthetic oscillatory network of transcriptional regulators. *Nature* **403**, 335–338 (2000).
10. Del Vecchio, D., Dy, A. J. & Qian, Y. Control theory meets synthetic biology. *J. R. Soc. Interface* **13**, 20160380 (2016).
11. Seelig, G., Soloveichik, D., Zhang, D. Y. & Winfree, E. Enzyme-Free Nucleic Acid Logic Circuits. *Science (80-.).* **314**, 1585–1588 (2006).
12. Weber, E., Engler, C., Gruetzner, R., Werner, S. & Marillonnet, S. A modular cloning system for standardized assembly of multigene constructs. *PLoS One* **6**, e16765–e16765 (2011).
13. Brophy, J. A. N. & Voigt, C. A. Principles of genetic circuit design. *Nat. Methods* **11**, 508 (2014).
14. Sedlmayer, F., Aubel, D. & Fussenegger, M. Synthetic gene circuits for the detection, elimination and prevention of disease. *Nat. Biomed. Eng.* **2**, 399–415 (2018).
15. Benenson, Y. Biomolecular computing systems: principles, progress and potential. *Nat. Rev. Genet.* **13**, 455–468 (2012).
16. Farzadfard, F. & Lu, T. K. Emerging applications for DNA writers and molecular recorders. *Science* **361**, 870–875 (2018).
17. Ryu, M.-H. *et al.* Control of nitrogen fixation in bacteria that associate with cereals. *Nat. Microbiol.* **5**, 314–330 (2019).
18. Praveschotinunt, P. *et al.* Engineered E. coli Nissle 1917 for the delivery of matrix-tethered therapeutic domains to the gut. *Nat. Commun.* **10**, 5580 (2019).
19. Sun, G. L., Reynolds, E. E. & Belcher, A. M. Using yeast to sustainably remediate and extract heavy metals from waste waters. *Nat. Sustain.* **3**, 303–311 (2020).
20. Heveran, C. M. *et al.* Biomineralization and Successive Regeneration of Engineered Living Building Materials. *Matter* **2**, 481–494 (2020).
21. Smith, R. S. H. *et al.* Hybrid Living Materials: Digital Design and Fabrication of 3D Multimaterial Structures with Programmable Biohybrid Surfaces. *Adv. Funct. Mater.* **30**, 1907401 (2019).
22. Chen, A. Y., Zhong, C. & Lu, T. K. Engineering living functional materials. *ACS Synth. Biol.* **4**, 8–11 (2015).
23. Nguyen, P. Q., Courchesne, N. D., Duraj-thatte, A., Praveschotinunt, P. & Joshi, N. S. Engineered

Living Materials: Prospects and Challenges for Using Biological Systems to Direct the Assembly of Smart Materials. *Adv. Mater.* **1704847**, 1–34 (2018).
24. Basu, S., Gerchman, Y., Collins, C. H., Arnold, F. H. & Weiss, R. A synthetic multicellular system for programmed pattern formation. *Nature* **434**, 1130–1134 (2005).
25. Chen, A. Y. *et al.* Synthesis and patterning of tunable multiscale materials with engineered cells. *Nat. Mater.* **13**, 515–23 (2014).
26. Toda, S., Blauch, L. R., Tang, S. K. Y., Morsut, L. & Lim, W. A. Programming self-organizing multicellular structures with synthetic cell-cell signaling. *Science (80-.).* **361**, 156–162 (2018).
27. DiMarco, R. L. & Heilshorn, S. C. Multifunctional materials through modular protein engineering. *Adv. Mater.* **24**, 3923–3940 (2012).
28. Moradali, M. F. & Rehm, B. H. A. Bacterial biopolymers: from pathogenesis to advanced materials. *Nat. Rev. Microbiol.* **18**, 195–210 (2020).
29. Rehm, B. H. A. Bacterial polymers: biosynthesis, modifications and applications. *Nat. Rev. Microbiol.* **8**, 578–592 (2010).
30. Purnick, P. E. M. & Weiss, R. The second wave of synthetic biology: from modules to systems. *Nat. Rev. Mol. cell Biol.* **10**, 410–422 (2009).
31. Lee, S. Y. *et al.* A comprehensive metabolic map for production of bio-based chemicals. *Nat. Catal.* **2**, 18–33 (2019).
32. Lang, K. & Chin, J. W. Cellular Incorporation of Unnatural Amino Acids and Bioorthogonal Labeling of Proteins. *Chem. Rev.* **114**, 4764–4806 (2014).
33. Elbaz, J., Yin, P. & Voigt, C. A. Genetic encoding of DNA nanostructures and their self-assembly in living bacteria. *Nat. Commun.* **7**, 11179 (2016).
34. Wei, S.-P. *et al.* Formation and functionalization of membraneless compartments in Escherichia coli. *Nat. Chem. Biol.* **16**, 1143–1148 (2020).
35. Meyer, A. J., Segall-Shapiro, T. H., Glassey, E., Zhang, J. & Voigt, C. A. Escherichia coli "Marionette" strains with 12 highly optimized small-molecule sensors. *Nat. Chem. Biol.* **15**, 196–204 (2018).
36. Daniel, R., Rubens, J. R., Sarpeshkar, R. & Lu, T. K. Synthetic analog computation in living cells. *Nature* **497**, 619–623 (2013).
37. Farzadfard, F. & Lu, T. K. Genomically encoded analog memory with precise in vivo DNA writing in living cell populations. *Science (80-.).* **346**, 1256272 (2014).
38. Levskaya, A. *et al.* Engineering Escherichia coli to see light. *Nature* **438**, 441–442 (2005).
39. Piraner, D. I., Abedi, M. H., Moser, B. A., Lee-Gosselin, A. & Shapiro, M. G. Tunable thermal bioswitches for in vivo control of microbial therapeutics. *Nat. Chem. Biol.* **13**, 75–80 (2016).
40. Ellis, T., Wang, X. & Collins, J. J. Diversity-based, model-guided construction of synthetic gene networks with predicted functions. *Nat. Biotechnol.* **27**, 465–471 (2009).
41. Kelly, J. R. *et al.* Measuring the activity of BioBrick promoters using an in vivo reference standard. *J. Biol. Eng.* **3**, 4 (2009).
42. Chen, Y.-J. *et al.* Characterization of 582 natural and synthetic terminators and quantification of their design constraints. *Nat. Methods* **10**, 659–664 (2013).
43. Tamsir, A., Tabor, J. J. & Voigt, C. A. Robust multicellular computing using genetically encoded NOR gates and chemical/wires/'. *Nature* **469**, 212–215 (2011).
44. Wan, X. *et al.* Cascaded amplifying circuits enable ultrasensitive cellular sensors for toxic metals. *Nat. Chem. Biol.* **15**, 540–548 (2019).
45. Stricker, J. *et al.* A fast, robust and tunable synthetic gene oscillator. *Nature* **456**, 516–519 (2008).
46. Grindley, N. D. F., Whiteson, K. L. & Rice, P. A. Mechanisms of Site-Specific Recombination. *Annu. Rev. Biochem.* **75**, 567–605 (2006).
47. Bonnet, J., Subsoontorn, P. & Endy, D. Rewritable digital data storage in live cells via engineered control of recombination directionality. *Proc. Natl. Acad. Sci.* **109**, 8884–8889 (2012).

48. Siuti, P., Yazbek, J. & Lu, T. K. Synthetic circuits integrating logic and memory in living cells. *Nat. Biotechnol.* **31**, 448–452 (2013).
49. Kalyoncu, E., Ahan, R. E., Ozcelik, C. E. & Seker, U. O. S. Genetic Logic Gates Enable Patterning of Amyloid Nanofibers. *Adv. Mater.* **31**, 1902888 (2019).
50. Qi, L. S. *et al.* Repurposing CRISPR as an RNA-guided platform for sequence-specific control of gene expression. *Cell* **152**, 1173–1183 (2013).
51. McCarty, N. S., Graham, A. E., Studená, L. & Ledesma-Amaro, R. Multiplexed CRISPR technologies for gene editing and transcriptional regulation. *Nat. Commun.* **11**, 1281 (2020).
52. Gilbert, C. & Ellis, T. Biological engineered living materials: growing functional materials with genetically programmable properties. *ACS Synth. Biol.* **8**, 1–15 (2018).
53. Gao, X. J., Chong, L. S., Kim, M. S. & Elowitz, M. B. Programmable protein circuits in living cells. *Science* **361**, 1252–1258 (2018).
54. Olson, E. J. & Tabor, J. J. Post-translational tools expand the scope of synthetic biology. *Curr. Opin. Chem. Biol.* **16**, 300–306 (2012).
55. Green, A. A., Silver, P. A., Collins, J. J. & Yin, P. Toehold switches: de-novo-designed regulators of gene expression. *Cell* **159**, 925–939 (2014).
56. Xie, Z., Wroblewska, L., Prochazka, L., Weiss, R. & Benenson, Y. Multi-Input RNAi-Based Logic Circuit for Identification of Specific Cancer Cells. *Science (80-.).* **333**, 1307–1311 (2011).
57. Simon, A. J., d'Oelsnitz, S. & Ellington, A. D. Synthetic evolution. *Nat. Biotechnol.* **37**, 730–743 (2019).
58. Rodriguez, E. A. *et al.* The Growing and Glowing Toolbox of Fluorescent and Photoactive Proteins. *Trends Biochem. Sci.* **42**, 111–129 (2017).
59. Thorne, N., Inglese, J. & Auld, D. S. Illuminating insights into firefly luciferase and other bioluminescent reporters used in chemical biology. *Chem. Biol.* **17**, 646–657 (2010).
60. Liljeruhm, J. *et al.* Engineering a palette of eukaryotic chromoproteins for bacterial synthetic biology. *J. Biol. Eng.* **12**, 8 (2018).
61. Narsing Rao, M. P., Xiao, M. & Li, W.-J. Fungal and Bacterial Pigments: Secondary Metabolites with Wide Applications. *Front. Microbiol.* **8**, 1113 (2017).
62. Guo, Z., Richardson, J. J., Kong, B. & Liang, K. Nanobiohybrids: Materials approaches for bioaugmentation. *Sci. Adv.* **6**, eaaz0330–eaaz0330 (2020).
63. Omenetto, F. G. & Kaplan, D. L. New opportunities for an ancient material. *Science* **329**, 528–531 (2010).
64. Moon, T. S., Lou, C., Tamsir, A., Stanton, B. C. & Voigt, C. a. Genetic programs constructed from layered logic gates in single cells. *Nature* **491**, 249–53 (2012).
65. Liu, Y. *et al.* Directing cellular information flow via CRISPR signal conductors. *Nat. Methods* **13**, 938–944 (2016).
66. Roquet, N., Soleimany, A. P., Ferris, A. C., Aaronson, S. & Lu, T. K. Synthetic recombinase-based state machines in living cells. *Science (80-.).* **353**, aad8559 (2016).
67. Prindle, A. *et al.* A sensing array of radically coupled genetic 'biopixels'. *Nature* **481**, 39–44 (2011).
68. Billerbeck, S. *et al.* A scalable peptide-GPCR language for engineering multicellular communication. *Nat. Commun.* **9**, 5057 (2018).
69. Zeng, J. *et al.* A Synthetic Microbial Operational Amplifier. *ACS Synth. Biol.* **7**, 2007–2013 (2018).
70. Baig, H. *et al.* Synthetic biology open language visual (SBOL visual) version 2.2. *J. Integr. Bioinform.* **1**, (2020).
71. Lee, K.-Y. Y., Buldum, G., Mantalaris, A. & Bismarck, A. More Than Meets the Eye in Bacterial Cellulose: Biosynthesis, Bioprocessing, and Applications in Advanced Fiber Composites. *Macromol. Biosci.* **14**, 10–32 (2013).
72. Yadav, V. *et al.* Novel in vivo-degradable cellulose-chitin copolymer from metabolically engineered

gluconacetobacter xylinus. *Appl. Environ. Microbiol.* **76**, 6257–6265 (2010).
73. Florea, M. *et al.* Engineering control of bacterial cellulose production using a genetic toolkit and a new cellulose-producing strain. *Proc. Natl. Acad. Sci.* 201522985 (2016).
74. Abhijith, R., Ashok, A. & Rejeesh, C. R. Sustainable packaging applications from mycelium to substitute polystyrene: a review. *Mater. Today Proc.* **5**, 2139–2145 (2018).
75. Wang, P.-A., Xiao, H. & Zhong, J.-J. CRISPR-Cas9 assisted functional gene editing in the mushroom Ganoderma lucidum. *Appl. Microbiol. Biotechnol.* **104**, 1661–1671 (2019).
76. Gilbert, C. *et al.* Living materials with programmable functionalities grown from engineered microbial co-cultures. *bioRxiv* (2019) doi:10.1101/2019.12.20.882472.
77. Schaumberg, K. A. *et al.* Quantitative characterization of genetic parts and circuits for plant synthetic biology. *Nat. Methods* **13**, 94–100 (2015).
78. Lienert, F., Lohmueller, J. J., Garg, A. & Silver, P. A. Synthetic biology in mammalian cells: next generation research tools and therapeutics. *Nat. Rev. Mol. Cell Biol.* **15**, 95–107 (2014).
79. Mitiouchkina, T. *et al.* Plants with genetically encoded autoluminescence. *Nat. Biotechnol.* 1–3 (2020).
80. Bredenoord, A. L., Clevers, H. & Knoblich, J. A. Human tissues in a dish: The research and ethical implications of organoid technology. *Science (80-.).* **355**, eaaf9414 (2017).
81. Kriegman, S., Blackiston, D., Levin, M. & Bongard, J. A scalable pipeline for designing reconfigurable organisms. *Proc. Natl. Acad. Sci.* **117**, 1853–1859 (2020).
82. Kassaw, T. K., Donayre-Torres, A. J., Antunes, M. S., Morey, K. J. & Medford, J. I. Engineering synthetic regulatory circuits in plants. *Plant Sci.* **273**, 13–22 (2018).
83. Lew, T. T. S., Koman, V. B., Gordiichuk, P., Park, M. & Strano, M. S. The Emergence of Plant Nanobionics and Living Plants as Technology. *Adv. Mater. Technol.* **5**, 1900657 (2019).
84. Franke, R. & Schreiber, L. Suberin — a biopolyester forming apoplastic plant interfaces. *Curr. Opin. Plant Biol.* **10**, 252–259 (2007).
85. Li, F.-S., Phyo, P., Jacobowitz, J., Hong, M. & Weng, J.-K. The molecular structure of plant sporopollenin. *Nat. Plants* **5**, 41–46 (2018).
86. Zhong, C. *et al.* Strong underwater adhesives made by self-assembling multi-protein nanofibres. *Nat. Nanotechnol.* **9**, 858–66 (2014).
87. Nguyen, P. Q., Botyanszki, Z., Tay, P. K. R. & Joshi, N. S. Programmable biofilm-based materials from engineered curli nanofibres. *Nat. Commun.* **5**, 4945 (2014).
88. Huang, J. *et al.* Programmable and printable Bacillus subtilis biofilms as engineered living materials. *Nat. Chem. Biol.* **15**, 34–41 (2018).
89. Bourdeau, R. W. *et al.* Acoustic reporter genes for noninvasive imaging of microorganisms in mammalian hosts. *Nature* **553**, 86–90 (2018).
90. Tay, P. K. R., Nguyen, P. Q. & Joshi, N. S. A Synthetic Circuit for Mercury Bioremediation Using Self-Assembling Functional Amyloids. *ACS Synth. Biol.* **6**, 1841–1850 (2017).
91. Zhang, C. *et al.* Engineered Bacillus subtilis biofilms as living glues. *Mater. Today* **28**, 40–48 (2019).
92. Liu, X. *et al.* 3D Printing of Living Responsive Materials and Devices. *Adv. Mater.* **30**, 1704821 (2017).
93. Tang, T.-C. *et al.* Tough Hydrogel-Based Biocontainment of Engineered Organisms for Continuous, Self-Powered Sensing and Computation. *BioRxiv* (2020).
94. Whitesides, G. M. Self-Assembly at All Scales. *Science (80-.).* **295**, 2418–2421 (2002).
95. Seeman, N. C. & Sleiman, H. F. DNA nanotechnology. *Nat. Rev. Mater.* **3**, 1–23 (2017).
96. Dong, Y. *et al.* DNA Functional Materials Assembled from Branched DNA: Design, Synthesis, and Applications. *Chem. Rev.* **120**, 9420–9481 (2020).
97. Woolston, B. M., Edgar, S. & Stephanopoulos, G. Metabolic Engineering: Past and Future. *Annu. Rev. Chem. Biomol. Eng.* **4**, 259–288 (2013).
98. Wagner, H. J. *et al.* Synthetic biology-inspired design of signal-amplifying materials systems. *Mater.*

Today **22**, 25–34 (2019).

99. Pena-Francesch, A., Jung, H., Demirel, M. C. & Sitti, M. Biosynthetic self-healing materials for soft machines. *Nat. Mater.* **19**, 1230–1235 (2020).
100. English, M. A. *et al.* Programmable CRISPR-responsive smart materials. *Science (80-.).* **365**, 780–785 (2019).
101. Cui, M. *et al.* Exploiting mammalian low-complexity domains for liquid-liquid phase separation--driven underwater adhesive coatings. *Sci. Adv.* **5**, eaax3155 (2019).
102. Wallace, A. K., Chanut, N. & Voigt, C. A. Silica Nanostructures Produced Using Diatom Peptides with Designed Post-Translational Modifications. *Adv. Funct. Mater.* **n/a**, 2000849 (2020).
103. Amiram, M. *et al.* Evolution of translation machinery in recoded bacteria enables multi-site incorporation of nonstandard amino acids. *Nat. Biotechnol.* **33**, 1272–1279 (2015).
104. Qian, Z.-G., Pan, F. & Xia, X.-X. Synthetic biology for protein-based materials. *Curr. Opin. Biotechnol.* **65**, 197–204 (2020).
105. Keating, K. W. & Young, E. M. Synthetic biology for bio-derived structural materials. *Curr. Opin. Chem. Eng.* **24**, 107–114 (2019).
106. Meng, D.-C. *et al.* Production and characterization of poly(3-hydroxypropionate-co-4-hydroxybutyrate) with fully controllable structures by recombinant Escherichia coli containing an engineered pathway. *Metab. Eng.* **14**, 317–324 (2012).
107. Deepankumar, K. *et al.* Supramolecular β-Sheet Suckerin–Based Underwater Adhesives. *Adv. Funct. Mater.* **30**, 1907534 (2020).
108. Brangwynne, C. P. *et al.* Germline P Granules Are Liquid Droplets That Localize by Controlled Dissolution/Condensation. *Science (80-.).* **324**, 1729–1732 (2009).
109. Bracha, D., Walls, M. T. & Brangwynne, C. P. Probing and engineering liquid-phase organelles. *Nat. Biotechnol.* **37**, 1435–1445 (2019).
110. Nakamura, H. *et al.* Intracellular production of hydrogels and synthetic RNA granules by multivalent molecular interactions. *Nat. Mater.* **17**, 79–89 (2018).
111. Kolinko, I. *et al.* Biosynthesis of magnetic nanostructures in a foreign organism by transfer of bacterial magnetosome gene clusters. *Nat. Nanotechnol.* **9**, 193–197 (2014).
112. Chatterjee, A. *et al.* Cephalopod-inspired optical engineering of human cells. *Nat. Commun.* **11**, 2708 (2020).
113. Farhadi, A., Ho, G. H., Sawyer, D. P., Bourdeau, R. W. & Shapiro, M. G. Ultrasound imaging of gene expression in mammalian cells. *Science (80-.).* **365**, 1469–1475 (2019).
114. Flemming, H.-C. & Wingender, J. The biofilm matrix. *Nat. Rev. Microbiol.* **8**, 623–633 (2010).
115. Rumbaugh, K. P. & Sauer, K. Biofilm dispersion. *Nat. Rev. Microbiol.* **18**, 571–586 (2020).
116. Knowles, T. P. J. & Buehler, M. J. Nanomechanics of functional and pathological amyloid materials. *Nat. Nanotechnol.* **6**, 469–479 (2011).
117. Blanco, L. P., Evans, M. L., Smith, D. R., Badtke, M. P. & Chapman, M. R. Diversity, biogenesis and function of microbial amyloids. *Trends Microbiol.* **20**, 66–73 (2012).
118. Barnhart, M. M. & Chapman, M. R. Curli biogenesis and function. *Annu. Rev. Microbiol.* **60**, 131–147 (2006).
119. Wang, X. *et al.* Programming Cells for Dynamic Assembly of Inorganic Nano-Objects with Spatiotemporal Control. *Adv. Mater.* **30**, 1705968 (2018).
120. Kalyoncu, E., Ahan, R. E., Olmez, T. T. & Safak Seker, U. O. Genetically encoded conductive protein nanofibers secreted by engineered cells. *RSC Adv.* **7**, 32543–32551 (2017).
121. Dorval Courchesne, N.-M. *et al.* Biomimetic engineering of conductive curli protein films. *Nanotechnology* **29**, 454002 (2018).
122. Jiang, L. *et al.* Programming Integrative Extracellular and Intracellular Biocatalysis for Rapid, Robust, and Recyclable Synthesis of Trehalose. *ACS Catal.* **8**, 1837–1842 (2018).

123. Botyanszki, Z., Tay, P. K. R., Nguyen, P. Q., Nussbaumer, M. G. & Joshi, N. S. Engineered catalytic biofilms: Site-specific enzyme immobilization ontoE. colicurli nanofibers. *Biotechnol. Bioeng.* **112**, 2016–2024 (2015).
124. Pu, J. *et al.* Virus Disinfection from Environmental Water Sources Using Living Engineered Biofilm Materials. *Adv. Sci. (Weinheim, Baden-Wurttemberg, Ger.* **7**, 1903558 (2020).
125. Wang, X. *et al.* Immobilization of functional nano-objects in living engineered bacterial biofilms for catalytic applications. *Natl. Sci. Rev.* **6**, 929–943 (2019).
126. Seker, U. O. S., Chen, A. Y., Citorik, R. J. & Lu, T. K. Synthetic Biogenesis of Bacterial Amyloid Nanomaterials with Tunable Inorganic–Organic Interfaces and Electrical Conductivity. *ACS Synth. Biol.* **6**, 266–275 (2016).
127. Charrier, M. *et al.* Engineering the S-Layer of Caulobacter crescentus as a Foundation for Stable, High-Density, 2D Living Materials. *ACS Synth. Biol.* **8**, 181–190 (2019).
128. Fang, J., Kawano, S., Tajima, K. & Kondo, T. In Vivo Curdlan/Cellulose Bionanocomposite Synthesis by Genetically ModifiedGluconacetobacter xylinus. *Biomacromolecules* **16**, 3154–3160 (2015).
129. Walker, K. T., Goosens, V. J., Das, A., Graham, A. E. & Ellis, T. Engineered cell-to-cell signalling within growing bacterial cellulose pellicles. *Microb. Biotechnol.* **12**, 611–619 (2018).
130. Fan, G., Graham, A. J., Kolli, J., Lynd, N. A. & Keitz, B. K. Aerobic radical polymerization mediated by microbial metabolism. *Nat. Chem.* (2020) doi:10.1038/s41557-020-0460-1.
131. Fan, G., Dundas, C. M., Graham, A. J., Lynd, N. A. & Keitz, B. K. Shewanella oneidensis as a living electrode for controlled radical polymerization. *Proc. Natl. Acad. Sci.* **115**, 4559–4564 (2018).
132. Gao, M. *et al.* A natural in situ fabrication method of functional bacterial cellulose using a microorganism. *Nat. Commun.* **10**, 437 (2019).
133. Koch, A. J. & Meinhardt, H. Biological pattern formation: from basic mechanisms to complex structures. *Rev. Mod. Phys.* **66**, 1481–1507 (1994).
134. Salazar-Ciudad, I. Mechanisms of pattern formation in development and evolution. *Development* **130**, 2027–2037 (2003).
135. Kondo, S. & Miura, T. Reaction-Diffusion Model as a Framework for Understanding Biological Pattern Formation. *Science (80-.).* **329**, 1616–1620 (2010).
136. Luo, N., Wang, S. & You, L. Synthetic Pattern Formation. *Biochemistry* **58**, 1478–1483 (2019).
137. Kim, H., Jin, X., Glass, D. S. & Riedel-Kruse, I. H. Engineering and modeling of multicellular morphologies and patterns. *Curr. Opin. Genet. Dev.* **63**, 95–102 (2020).
138. Santos-Moreno, J. & Schaerli, Y. Using Synthetic Biology to Engineer Spatial Patterns. *Adv. Biosyst.* **3**, 1800280 (2018).
139. Fernandez-Rodriguez, J., Moser, F., Song, M. & Voigt, C. A. Engineering RGB color vision into Escherichia coli. *Nat. Chem. Biol.* (2017).
140. Jin, X. & Riedel-Kruse, I. H. Biofilm Lithography enables high-resolution cell patterning via optogenetic adhesin expression. *Proc. Natl. Acad. Sci.* **115**, 3698 LP – 3703 (2018).
141. Moser, F., Tham, E., González, L. M., Lu, T. K. & Voigt, C. A. Light-Controlled, High-Resolution Patterning of Living Engineered Bacteria Onto Textiles, Ceramics, and Plastic. *Adv. Funct. Mater.* **29**, 1901788 (2019).
142. Liu, C. *et al.* Sequential Establishment of Stripe Patterns in an Expanding Cell Population. *Science (80-.).* **334**, 238–241 (2011).
143. Tabor, J. J. *et al.* A synthetic genetic edge detection program. *Cell* **137**, 1272–1281 (2009).
144. TURING, A. The chemical basis of morphogenesis. *Bull. Math. Biol.* **52**, 153–197 (1990).
145. Karig, D. *et al.* Stochastic Turing patterns in a synthetic bacterial population. *Proc. Natl. Acad. Sci.* **115**, 6572–6577 (2018).
146. Potvin-Trottier, L., Lord, N. D., Vinnicombe, G. & Paulsson, J. Synchronous long-term oscillations in a synthetic gene circuit. *Nature* **538**, 514–517 (2016).

147. Mushnikov, N. V, Fomicheva, A., Gomelsky, M. & Bowman, G. R. Inducible asymmetric cell division and cell differentiation in a bacterium. *Nat. Chem. Biol.* **15**, 925–931 (2019).
148. Molinari, S. *et al.* A synthetic system for asymmetric cell division in Escherichia coli. *Nat. Chem. Biol.* **15**, 917–924 (2019).
149. Glass, D. S. & Riedel-Kruse, I. H. A Synthetic Bacterial Cell-Cell Adhesion Toolbox for Programming Multicellular Morphologies and Patterns. *Cell* **174**, 649-658.e16 (2018).
150. Perry, C. C. & Keeling-Tucker, T. Biosilicification: the role of the organic matrix in structure control. *JBIC J. Biol. Inorg. Chem.* **5**, 537–550 (2000).
151. van der Meer, J. R. & Belkin, S. Where microbiology meets microengineering: design and applications of reporter bacteria. *Nat. Rev. Microbiol.* **8**, 511–522 (2010).
152. Pardee, K. *et al.* Rapid, Low-Cost Detection of Zika Virus Using Programmable Biomolecular Components. *Cell* **165**, 1255–1266 (2016).
153. Li, S., Li, Y. & Smolke, C. D. Strategies for microbial synthesis of high-value phytochemicals. *Nat. Chem.* **10**, 395–404 (2018).
154. Bereza-Malcolm, L. T., Mann, G. lay & Franks, A. E. Environmental sensing of heavy metals through whole cell microbial biosensors: a synthetic biology approach. *ACS Synth. Biol.* **4**, 535–546 (2014).
155. Ostrov, N. *et al.* A modular yeast biosensor for low-cost point-of-care pathogen detection. *Sci. Adv.* **3**, e1603221 (2017).
156. Belkin, S. *et al.* Remote detection of buried landmines using a bacterial sensor. *Nat. Biotechnol.* **35**, 308 (2017).
157. Liu, X. *et al.* Stretchable living materials and devices with hydrogel--elastomer hybrids hosting programmed cells. *Proc. Natl. Acad. Sci.* **114**, 2200–2205 (2017).
158. Landry, B. P., Palanki, R., Dyulgyarov, N., Hartsough, L. A. & Tabor, J. J. Phosphatase activity tunes two-component system sensor detection threshold. *Nat. Commun.* **9**, 1433 (2018).
159. Chen, Y. *et al.* Tuning the dynamic range of bacterial promoters regulated by ligand-inducible transcription factors. *Nat. Commun.* **9**, 64 (2018).
160. Salis, H. M., Mirsky, E. A. & Voigt, C. A. Automated design of synthetic ribosome binding sites to control protein expression. *Nat. Biotechnol.* **27**, 946–950 (2009).
161. Shaw, W. M. *et al.* Engineering a Model Cell for Rational Tuning of GPCR Signaling. *Cell* **177**, 782-796.e27 (2019).
162. Maxmen, A. Living therapeutics: Scientists genetically modify bacteria to deliver drugs. *Nat. Med.* **23**, 5–7 (2017).
163. Bose, S. *et al.* A retrievable implant for the long-term encapsulation and survival of therapeutic xenogeneic cells. *Nat. Biomed. Eng.* **4**, 814–826 (2020).
164. Sankaran, S. & del Campo, A. Optoregulated Protein Release from an Engineered Living Material. *Adv. Biosyst.* 1800312 (2018) doi:10.1002/adbi.201800312.
165. Sankaran, S., Becker, J., Wittmann, C. & del Campo, A. Optoregulated Drug Release from an Engineered Living Material: Self-Replenishing Drug Depots for Long-Term, Light-Regulated Delivery. *Small* **15**, 1804717 (2018).
166. Dai, Z. *et al.* Versatile biomanufacturing through stimulus-responsive cell–material feedback. *Nat. Chem. Biol.* **15**, 1017–1024 (2019).
167. Gerber, L. C., Koehler, F. M., Grass, R. N. & Stark, W. J. Incorporation of Penicillin-Producing Fungi into Living Materials to Provide Chemically Active and Antibiotic-Releasing Surfaces. *Angew. Chemie* **124**, 11455–11458 (2012).
168. González, L. M., Mukhitov, N. & Voigt, C. A. Resilient living materials built by printing bacterial spores. *Nat. Chem. Biol.* **16**, 126–133 (2019).
169. Sankaran, S., Zhao, S., Muth, C., Paez, J. & Del Campo, A. Toward Light-Regulated Living Biomaterials. *Adv. Sci. (Weinheim, Baden-Wurttemberg, Ger.* **5**, 1800383 (2018).

170. Saadeddin, A. *et al.* Functional Living Biointerphases. *Adv. Healthc. Mater.* **2**, 1213–1218 (2013).
171. Hay, J. J. *et al.* Living biointerfaces based on non-pathogenic bacteria support stem cell differentiation. *Sci. Rep.* **6**, 21809 (2016).
172. Hay, J. J. *et al.* Bacteria-Based Materials for Stem Cell Engineering. *Adv. Mater.* **30**, 1804310 (2018).
173. Rodrigo-Navarro, A., Rico, P., Saadeddin, A., Garcia, A. J. & Salmeron-Sanchez, M. Living biointerfaces based on non-pathogenic bacteria to direct cell differentiation. *Sci. Rep.* **4**, 5849 (2014).
174. Lufton, M. *et al.* Living Bacteria in Thermoresponsive Gel for Treating Fungal Infections. *Adv. Funct. Mater.* **28**, 1801581 (2018).
175. Mimee, M. *et al.* An ingestible bacterial-electronic system to monitor gastrointestinal health. *Science (80-.).* **360**, 915–918 (2018).
176. Din, M. O., Martin, A., Razinkov, I., Csicsery, N. & Hasty, J. Interfacing gene circuits with microelectronics through engineered population dynamics. *Sci. Adv.* **6**, eaaz8344–eaaz8344 (2020).
177. Patel, S. R. & Lieber, C. M. Precision electronic medicine in the brain. *Nat. Biotechnol.* **37**, 1007–1012 (2019).
178. Webster, D. P. *et al.* An arsenic-specific biosensor with genetically engineered Shewanella oneidensis in a bioelectrochemical system. *Biosens. Bioelectron.* **62**, 320–324 (2014).
179. Shao, J. *et al.* Smartphone-controlled optogenetically engineered cells enable semiautomatic glucose homeostasis in diabetic mice. *Sci. Transl. Med.* **9**, eaal2298 (2017).
180. Tschirhart, T. *et al.* Electronic control of gene expression and cell behaviour in Escherichia coli through redox signalling. *Nat. Commun.* **8**, 14030 (2017).
181. Krawczyk, K. *et al.* Electrogenetic cellular insulin release for real-time glycemic control in type 1 diabetic mice. *Science (80-.).* **368**, 993–1001 (2020).
182. Slate, A. J., Whitehead, K. A., Brownson, D. A. C. & Banks, C. E. Microbial fuel cells: An overview of current technology. *Renew. Sustain. Energy Rev.* **101**, 60–81 (2019).
183. Bird, L. J. *et al.* Engineered living conductive biofilms as functional materials. *MRS Commun.* **9**, 505–517 (2019).
184. Li, F., Wang, L., Liu, C., Wu, D. & Song, H. Engineering exoelectrogens by synthetic biology strategies. *Curr. Opin. Electrochem.* **10**, 37–45 (2018).
185. Gadhamshetty, V. & Koratkar, N. Nano-engineered biocatalyst-electrode structures for next generation microbial fuel cells. *Nano Energy* **1**, 3–5 (2012).
186. Yong, Y.-C., Yu, Y.-Y., Zhang, X. & Song, H. Highly Active Bidirectional Electron Transfer by a Self-Assembled Electroactive Reduced-Graphene-Oxide-Hybridized Biofilm. *Angew. Chemie* **126**, 4569–4572 (2014).
187. McCormick, A. J. *et al.* Photosynthetic biofilms in pure culture harness solar energy in a mediatorless bio-photovoltaic cell (BPV) system. *Energy Environ. Sci.* **4**, 4699 (2011).
188. Joshi, S., Cook, E. & Mannoor, M. S. Bacterial Nanobionics via 3D Printing. *Nano Lett.* **18**, 7448–7456 (2018).
189. Melis, A. Solar energy conversion efficiencies in photosynthesis: Minimizing the chlorophyll antennae to maximize efficiency. *Plant Sci.* **177**, 272–280 (2009).
190. Kim, M. J. *et al.* A Broadband Multiplex Living Solar Cell. *Nano Lett.* **20**, 4286–4291 (2020).
191. Schuergers, N., Werlang, C., Ajo-Franklin, C. M. & Boghossian, A. A. A Synthetic Biology Approach to Engineering Living Photovoltaics. *Energy Environ. Sci.* **10**, 1102–1115 (2017).
192. Cestellos-Blanco, S., Zhang, H., Kim, J. M., Shen, Y. & Yang, P. Photosynthetic semiconductor biohybrids for solar-driven biocatalysis. *Nat. Catal.* **3**, 245–255 (2020).
193. Sakimoto, K. K., Wong, A. B. & Yang, P. Self-photosensitization of nonphotosynthetic bacteria for solar-to-chemical production. *Science (80-.).* **351**, 74–77 (2015).
194. Wei, W. *et al.* A surface-display biohybrid approach to light-driven hydrogen production in air. *Sci. Adv.* **4**, eaap9253–eaap9253 (2018).

195. Guo, J. *et al.* Light-driven fine chemical production in yeast biohybrids. *Science* **362**, 813–816 (2018).

196. Bernardi, D., DeJong, J. T., Montoya, B. M. & Martinez, B. C. Bio-bricks: Biologically cemented sandstone bricks. *Constr. Build. Mater.* **55**, 462–469 (2014).

197. Lee, Y. S. & Park, W. Current challenges and future directions for bacterial self-healing concrete. *Appl. Microbiol. Biotechnol.* **102**, 3059–3070 (2018).

198. Pungrasmi, W., Intarasoontron, J., Jongvivatsakul, P. & Likitlersuang, S. Evaluation of Microencapsulation Techniques for MICP Bacterial Spores Applied in Self-Healing Concrete. *Sci. Rep.* **9**, 12484 (2019).

199. Boothby, T. C. *et al.* Tardigrades Use Intrinsically Disordered Proteins to Survive Desiccation. *Mol. Cell* **65**, 975-984.e5 (2017).

200. Ferreiro, A., Crook, N., Gasparrini, A. J. & Dantas, G. Multiscale Evolutionary Dynamics of Host-Associated Microbiomes. *Cell* **172**, 1216–1227 (2018).

201. Jones, M., Huynh, T., Dekiwadia, C., Daver, F. & John, S. Mycelium Composites: A Review of Engineering Characteristics and Growth Kinetics. *J. Bionanoscience* **11**, 241–257 (2017).

202. Chang, J. *et al.* Modified recipe to inhibit fruiting body formation for living fungal biomaterial manufacture. *PLoS One* **14**, e0209812 (2019).

203. Islam, M. R., Tudryn, G., Bucinell, R., Schadler, L. & Picu, R. C. Mechanical behavior of mycelium-based particulate composites. *J. Mater. Sci.* **53**, 16371–16382 (2018).

204. Jiang, B. *et al.* Lignin as a Wood-Inspired Binder Enabled Strong, Water Stable, and Biodegradable Paper for Plastic Replacement. *Adv. Funct. Mater.* **30**, 1906307 (2019).

205. Nguyen, P. Q. Synthetic biology engineering of biofilms as nanomaterials factories. *Biochem. Soc. Trans.* **45**, 585–597 (2017).

206. Nussbaumer, M. G. *et al.* Bootstrapped Biocatalysis: Biofilm-Derived Materials as Reversibly Functionalizable Multienzyme Surfaces. *ChemCatChem* **9**, 4328–4333 (2017).

207. Duraj-Thatte, A. M. *et al.* Genetically Programmable Self-Regenerating Bacterial Hydrogels. *Adv. Mater.* **31**, 1901826 (2019).

208. Dorval Courchesne, N.-M., Duraj-Thatte, A., Tay, P. K. R., Nguyen, P. Q. & Joshi, N. S. Scalable Production of Genetically Engineered Nanofibrous Macroscopic Materials via Filtration. *ACS Biomater. Sci. Eng.* acsbiomaterials.6b00437 (2016) doi:10.1021/acsbiomaterials.6b00437.

209. Park, S.-J. *et al.* Phototactic guidance of a tissue-engineered soft-robotic ray. *Science (80-.).* **353**, 158–162 (2016).

210. Van Tittelboom, K., De Belie, N., De Muynck, W. & Verstraete, W. Use of bacteria to repair cracks in concrete. *Cem. Concr. Res.* **40**, 157–166 (2010).

211. Wang, J., Van Tittelboom, K., De Belie, N. & Verstraete, W. Use of silica gel or polyurethane immobilized bacteria for self-healing concrete. *Constr. Build. Mater.* **26**, 532–540 (2012).

212. Gerber, L. C., Koehler, F. M., Grass, R. N. & Stark, W. J. Incorporating microorganisms into polymer layers provides bioinspired functional living materials. *Proc. Natl. Acad. Sci.* **109**, 90–94 (2011).

213. Chawla, P. R., Bajaj, I. B., Survase, S. A. & Singhal, R. S. Microbial cellulose: fermentative production and applications. *Food Technol. Biotechnol.* **47**, 107–124 (2009).

214. Huang, Y. *et al.* Recent advances in bacterial cellulose. *Cellulose* **21**, 1–30 (2013).

215. Hsieh, Y.-C., Yano, H., Nogi, M. & Eichhorn, S. J. An estimation of the Young's modulus of bacterial cellulose filaments. *Cellulose* **15**, 507–513 (2008).

216. Kondo, T., Rytczak, P. & Bielecki, S. Bacterial NanoCellulose Characterization. *Bacterial Nanocellulose* 59–71 (2016) doi:10.1016/b978-0-444-63458-0.00004-4.

217. Wang, J., Tavakoli, J. & Tang, Y. Bacterial cellulose production, properties and applications with different culture methods – A review. *Carbohydr. Polym.* **219**, 63–76 (2019).

218. Ludwicka, K. *et al.* Medical and Cosmetic Applications of Bacterial NanoCellulose. *Bacterial Nanocellulose* 145–165 (2016) doi:10.1016/b978-0-444-63458-0.00009-3.

219. Gwon, H. *et al.* A safe and sustainable bacterial cellulose nanofiber separator for lithium rechargeable batteries. *Proc. Natl. Acad. Sci.* **116**, 19288–19293 (2019).
220. Teh, M. Y. *et al.* An Expanded Synthetic Biology Toolkit for Gene Expression Control in Acetobacteraceae. *ACS Synth. Biol.* **8**, 708–723 (2019).
221. Jacek, P., Ryngajłło, M. & Bielecki, S. Structural changes of bacterial nanocellulose pellicles induced by genetic modification of Komagataeibacter hansenii ATCC 23769. *Appl. Microbiol. Biotechnol.* **103**, 5339–5353 (2019).
222. Jayabalan, R., Malini, K., Sathishkumar, M., Swaminathan, K. & Yun, S. E. Biochemical characteristics of tea fungus produced during kombucha fermentation. *Food Sci. Biotechnol.* **19**, 843–847 (2010).
223. Lee, M. E., DeLoache, W. C., Cervantes, B. & Dueber, J. E. A Highly Characterized Yeast Toolkit for Modular, Multipart Assembly. *ACS Synth. Biol.* **4**, 975–986 (2015).
224. Ong, E., Gilkes, N. R., Miller, R. C., Warren, R. A. J. & Kilburn, D. G. The cellulose-binding domain (CBDCex) of an exoglucanase fromCellulomonas fimi: Production inEscherichia coli and characterization of the polypeptide. *Biotechnol. Bioeng.* **42**, 401–409 (1993).
225. Antošová, Z., Herkommerová, K., Pichová, I. & Sychrová, H. Efficient secretion of three fungal laccases fromSaccharomyces cerevisiaeand their potential for decolorization of textile industry effluent-A comparative study. *Biotechnol. Prog.* **34**, 69–80 (2017).
226. Villares, A. *et al.* Lytic polysaccharide monooxygenases disrupt the cellulose fibers structure. *Sci. Rep.* **7**, (2017).
227. Lee, C.-R. *et al.* Co-fermentation using Recombinant Saccharomyces cerevisiae Yeast Strains Hyper-secreting Different Cellulases for the Production of Cellulosic Bioethanol. *Sci. Rep.* **7**, (2017).
228. Bhagia, S., Dhir, R., Kumar, R. & Wyman, C. E. Deactivation of Cellulase at the Air-Liquid Interface Is the Main Cause of Incomplete Cellulose Conversion at Low Enzyme Loadings. *Sci. Rep.* **8**, (2018).
229. Yamanaka, S. *et al.* The structure and mechanical properties of sheets prepared from bacterial cellulose. *J. Mater. Sci.* **24**, 3141–3145 (1989).
230. Soykeabkaew, N., Sian, C., Gea, S., Nishino, T. & Peijs, T. All-cellulose nanocomposites by surface selective dissolution of bacterial cellulose. *Cellulose* **16**, 435–444 (2009).
231. Shi, X., Zheng, F., Pan, R., Wang, J. & Ding, S. Engineering and Comparative Characteristics of Double Carbohydrate Binding Modules as a Strength Additive for Papermaking Applications. *BioResources* **9**, (2014).
232. Butchosa, N., Leijon, F., Bulone, V. & Zhou, Q. Stronger cellulose microfibril network structure through the expression of cellulose-binding modules in plant primary cell walls. *Cellulose* **26**, 3083–3094 (2019).
233. McIsaac, R. S., Gibney, P. A., Chandran, S. S., Benjamin, K. R. & Botstein, D. Synthetic biology tools for programming gene expression without nutritional perturbations in Saccharomyces cerevisiae. *Nucleic Acids Res.* **42**, 1–8 (2014).
234. McIsaac, R. S. *et al.* Fast-acting and nearly gratuitous induction of gene expression and protein depletion inSaccharomyces cerevisiae. *Mol. Biol. Cell* **22**, 4447–4459 (2011).
235. Pothoulakis, G. & Ellis, T. Synthetic gene regulation for independent external induction of the Saccharomyces cerevisiae pseudohyphal growth phenotype. *Commun. Biol.* **1**, (2018).
236. Cardinal-Watkins, C. & Nicell, J. A. Enzyme-Catalyzed Oxidation of 17β-Estradiol Using Immobilized Laccase from Trametes versicolor. *Enzyme Res.* **2011**, 725172 (2011).
237. Adeel, M., Song, X., Wang, Y., Francis, D. & Yang, Y. Environmental impact of estrogens on human, animal and plant life: A critical review. *Environ. Int.* **99**, 107–119 (2017).
238. Avar, P. *et al.* β-Estradiol and ethinyl-estradiol contamination in the rivers of the Carpathian Basin. *Environ. Sci. Pollut. Res.* **23**, 11630–11638 (2016).
239. Pathak, G. P., Strickland, D., Vrana, J. D. & Tucker, C. L. Benchmarking of optical dimerizer

systems. *ACS Synth. Biol.* **3**, 832–838 (2014).
240. Jarque, S., Bittner, M., Blaha, L. & Hilscherova, K. Yeast Biosensors for Detection of Environmental Pollutants: Current State and Limitations. *Trends Biotechnol.* **34**, 408–419 (2016).
241. Adeniran, A., Stainbrook, S., Bostick, J. & Tyo, K. Detection of a peptide biomarker by engineered yeast receptors. *ACS Synth. Biol.* acssynbio.7b00410 (2018) doi:10.1021/acssynbio.7b00410.
242. Singh, J., Abhilash, P., Singh, H., Singh, R. & Singh, D. Genetically engineered bacteria: an emerging tool for environmental remediation and future research perspectives. *Gene* **480**, 1–9 (2011).
243. Farrar, K., Bryant, D. & Cope-Selby, N. Understanding and engineering beneficial plant--microbe interactions: plant growth promotion in energy crops. *Plant Biotechnol. J.* **12**, 1193–1206 (2014).
244. Peralta-Yahya, P. P., Zhang, F., del Cardayre, S. B. & Keasling, J. D. Microbial engineering for the production of advanced biofuels. *Nature* **488**, 320–328 (2012).
245. Way, J., Collins, J., Keasling, J. & Silver, P. Integrating Biological Redesign: Where Synthetic Biology Came From and Where It Needs to Go. *Cell* **157**, 151–161 (2014).
246. Dana, G. V., Kuiken, T., Rejeski, D. & Snow, A. a. Synthetic biology: Four steps to avoid a synthetic-biology disaster. *Nature* **483**, 29–29 (2012).
247. Epstein, M. M. & Vermeire, T. Scientific Opinion on Risk Assessment of Synthetic Biology. *Trends Biotechnol.* **34**, 601–603 (2016).
248. Hagen, K. Science Policy and Concomitant Research in Synthetic Biology—Some Critical Thoughts. *Nanoethics* **10**, 201–213 (2016).
249. Torres, L., Krüger, A., Csibra, E., Gianni, E. & Pinheiro, V. B. Synthetic biology approaches to biological containment: pre-emptively tackling potential risks. *Essays Biochem.* **60**, 393–410 (2016).
250. Wright, O., Stan, G. B. & Ellis, T. Building-in biosafety for synthetic biology. *Microbiol. (United Kingdom)* **159**, 1221–1235 (2013).
251. Mandell, D. J. *et al.* Biocontainment of genetically modified organisms by synthetic protein design. *Nature* **518**, (2014).
252. Lee, J. W., Chan, C. T. Y., Slomovic, S. & Collins, J. J. Next-generation biocontainment systems for engineered organisms. *Nat. Chem. Biol.* **14**, 530 (2018).
253. Schmidt, M. & de Lorenzo, V. Synthetic bugs on the loose: containment options for deeply engineered (micro) organisms. *Curr. Opin. Biotechnol.* **38**, 90–96 (2016).
254. Clement T Y Chan, Jeong Wook Lee, D Ewen Cameron, Caleb J Bashor, J. J. C. 'Deadman'and 'passcode'microbial kill switches for bacterial containment. *Nat. Chem. Biol.* **12**, 82–85 (2015).
255. Wright, O., Delmans, M., Stan, G.-B. & Ellis, T. GeneGuard: a modular plasmid system designed for biosafety. *ACS Synth. Biol.* **4**, 307–316 (2014).
256. Gallagher, R. R., Patel, J. R., Interiano, A. L., Rovner, A. J. & Isaacs, F. J. Multilayered genetic safeguards limit growth of microorganisms to defined environments. *Nucleic Acids Res.* **43**, 1945–1954 (2015).
257. Lajoie, M. J. *et al.* Probing the limits of genetic recoding in essential genes. *Science (80-.).* **342**, 361–363 (2013).
258. Rovner, A. *et al.* Recoded organisms engineered to depend on synthetic amino acids. *Nature* **518**, 89–93 (2015).
259. Nicodemus, G. D. & Bryant, S. J. Cell encapsulation in biodegradable hydrogels for tissue engineering applications. *Tissue Eng. Part B Rev.* **14**, 149–165 (2008).
260. Seliktar, D. Designing cell-compatible hydrogels for biomedical applications. *Science (80-.).* **336**, 1124–1128 (2012).
261. Choi, M. *et al.* Light-guiding hydrogels for cell-based sensing and optogenetic synthesis in vivo. *Nat. Photonics* **7**, 987–994 (2013).
262. Anselmo, A. C., McHugh, K. J., Webster, J., Langer, R. & Jaklenec, A. Layer-by-Layer Encapsulation

of Probiotics for Delivery to the Microbiome. *Adv. Mater.* (2016) doi:10.1002/adma.201603270.

263. Lee, K. Y. & Mooney, D. J. Alginate: properties and biomedical applications. *Prog. Polym. Sci.* **37**, 106–126 (2012).
264. Dong, Q.-Y. *et al.* Alginate-based and protein-based materials for probiotics encapsulation: a review. *Int. J. Food Sci. Technol.* **48**, 1339–1351 (2013).
265. Kearney, C. & Mooney, D. Macroscale delivery systems for molecular and cellular payloads. *Nat Mater* **12**, 1004–1017 (2013).
266. Billiet, T., Vandenhaute, M., Schelfhout, J., Van Vlierberghe, S. & Dubruel, P. A review of trends and limitations in hydrogel-rapid prototyping for tissue engineering. *Biomaterials* **33**, 6020–6041 (2012).
267. Kim, B. J. *et al.* Cytoprotective alginate/polydopamine core/shell microcapsules in microbial encapsulation. *Angew. Chemie Int. Ed.* **53**, 14443–14446 (2014).
268. Li, P., Müller, M., Chang, M. W., Frettlöh, M. & Schönherr, H. Encapsulation of autoinducer sensing reporter bacteria in reinforced alginate-based microbeads. *ACS Appl. Mater. Interfaces* **9**, 22321–22331 (2017).
269. Zhang, B.-B., Wang, L., Charles, V., Rooke, J. C. & Su, B.-L. Robust and biocompatible hybrid matrix with controllable permeability for microalgae encapsulation. *ACS Appl. Mater. Interfaces* **8**, 8939–8946 (2016).
270. Sun, J.-Y. *et al.* Highly stretchable and tough hydrogels. *Nature* **489**, 133–136 (2012).
271. Valade, D., Wong, L. K., Jeon, Y., Jia, Z. & Monteiro, M. J. Polyacrylamide hydrogel membranes with controlled pore sizes. *J. Polym. Sci. Part A Polym. Chem.* **51**, 129–138 (2013).
272. Atkinson, J. *The mechanics of soils and foundations*. (CRC Press, 2017).
273. Liu, X. *et al.* Ingestible hydrogel device. *Nat. Commun.* **10**, 1–10 (2019).
274. Houghton, L. A. *et al.* Motor activity of the gastric antrum, pylorus, and duodenum under fasted conditions and after a liquid meal. *Gastroenterology* **94**, 1276–1284 (1988).
275. Zarket, B. C. & Raghavan, S. R. Onion-like multilayered polymer capsules synthesized by a bioinspired inside-out technique. *Nat. Commun.* **8**, (2017).
276. Eun, Y.-J., Utada, A. S., Copeland, M. F., Takeuchi, S. & Weibel, D. B. Encapsulating Bacteria in Agarose Microparticles Using Microfluidics for High-Throughput Cell Analysis and Isolation. *ACS Chem. Biol.* **6**, 260–266 (2011).
277. Kong, H. J., Kim, E. S., Huang, Y.-C. & Mooney, D. J. Design of biodegradable hydrogel for the local and sustained delivery of angiogenic plasmid DNA. *Pharm. Res.* **25**, 1230–1238 (2008).
278. Farzadfard, F. & Lu, T. K. Genomically encoded analog memory with precise in vivo DNA writing in living cell populations. *Science (80-.).* **346**, 1256272–1256272 (2014).
279. Golmohamadi, M. & Wilkinson, K. J. Diffusion of ions in a calcium alginate hydrogel-structure is the primary factor controlling diffusion. *Carbohydr. Polym.* **94**, 82–87 (2013).
280. Li, Z. *et al.* Biofilm-Inspired Encapsulation of Probiotics for the Treatment of Complex Infections. *Adv. Mater.* **30**, 1803925 (2018).
281. Bjerketorp, J., Håkansson, S., Belkin, S. & Jansson, J. K. Advances in preservation methods: keeping biosensor microorganisms alive and active. *Curr. Opin. Biotechnol.* **17**, 43–49 (2006).
282. Roggo, C. & van der Meer, J. R. Miniaturized and integrated whole cell living bacterial sensors in field applicable autonomous devices. *Curr. Opin. Biotechnol.* **45**, 24–33 (2017).
283. Kim, B. C. & Gu, M. B. A bioluminescent sensor for high throughput toxicity classification. *Biosens. Bioelectron.* **18**, 1015–1021 (2003).
284. Cevenini, L., Calabretta, M. M., Tarantino, G., Michelini, E. & Roda, A. Smartphone-interfaced 3D printed toxicity biosensor integrating bioluminescent “sentinel cells”. *Sensors Actuators B Chem.* **225**, 249–257 (2016).
285. Farzadfard, F., Gharaei, N., Citorik, R. J. & Lu, T. K. Efficient Retroelement-Mediated DNA Writing in Bacteria. *bioRxiv* 2020.02.21.958983 (2020) doi:10.1101/2020.02.21.958983.

286. Pedersen, M. W. *et al.* Ancient and modern environmental DNA. *Philos. Trans. R. Soc. B Biol. Sci.* **370**, 20130383 (2015).

287. Sheth, R. U. & Wang, H. H. DNA-based memory devices for recording cellular events. *Nat. Rev. Genet.* 1 (2018).

288. Weiss, R., Knight, T. & Sussman, G. Cellular computation and communication using engineered genetic regulatory networks. *Cell. Comput.* 120–121 (2001).

289. Chen, M.-T. & Weiss, R. Artificial cell-cell communication in yeast Saccharomyces cerevisiae using signaling elements from Arabidopsis thaliana. *Nat. Biotechnol.* **23**, 1551–1555 (2005).

290. Järup, L. & Åkesson, A. Current status of cadmium as an environmental health problem. *Toxicol. Appl. Pharmacol.* **238**, 201–208 (2009).

291. Brocklehurst, K. R. *et al.* ZntR is a Zn (II)-responsive MerR-like transcriptional regulator of zntA in Escherichia coli. *Mol. Microbiol.* **31**, 893–902 (1999).

292. *310 CMR 30.000*. (2015).

293. Mayall, R. M., Hicks, E. C., Renaud-Young, M. M. F., Lloyd, D. C., Oberding, L. K., & George, I. F. S. System and methods for the detection of multiple chemical compounds. (2017).

294. Knierim, C., Greenblatt, C. L., Agarwal, S. & Greiner, A. Blocked bacteria escape by ATRP grafting of a PMMA shell on PVA microparticles. *Macromol. Biosci.* **14**, 537–545 (2014).

295. De Las Heras, A., Carreño, C. A. & De Lorenzo, V. Stable implantation of orthogonal sensor circuits in Gram-negative bacteria for environmental release. *Environ. Microbiol.* **10**, 3305–3316 (2008).

296. Pardee, K. *et al.* Paper-Based Synthetic Gene Networks. *Cell* **159**, 940–954 (2014).

297. Mimee, M., Tucker, A. C., Voigt, C. A. & Lu, T. K. Programming a human commensal bacterium, Bacteroides thetaiotaomicron, to sense and respond to stimuli in the murine gut microbiota. *Cell Syst.* **1**, 62–71 (2015).

298. Friedland, A. E. *et al.* Synthetic Gene Networks That Count. *Science (80-.).* **324**, 1199–1202 (2009).

299. Siuti, P., Yazbek, J. & Lu, T. K. Engineering genetic circuits that compute and remember. *Nat. Protoc.* **9**, 1292–1300 (2014).

300. Cheng, A. A. & Lu, T. K. Synthetic Biology : An Emerging Engineering Discipline. *Annu. Rev. Biomed. Eng.* **14**, 155–178 (2012).

301. Feinberg, A. W. *et al.* Muscular Thin Films for Building Actuators and Powering Devices. *Science (80-.).* **317**, 1366–1370 (2007).

302. Nawroth, J. C. *et al.* A tissue-engineered jellyfish with biomimetic propulsion. *Nat. Biotechnol.* **30**, 792–797 (2012).

303. Lee, K. Y. & Mooney, D. J. Hydrogels for Tissue Engineering. *Chem. Rev.* **101**, 1869–1880 (2001).

304. Zhao, X. *et al.* Active scaffolds for on-demand drug and cell delivery. *Proc. Natl. Acad. Sci.* **108**, 67–72 (2010).

305. Zhao, X. Multi-scale multi-mechanism design of tough hydrogels: building dissipation into stretchy networks. *Soft Matter* **10**, 672–687 (2014).

306. Yuk, H., Zhang, T., Parada, G. A., Liu, X. & Zhao, X. Skin-inspired hydrogel-elastomer hybrids with robust interfaces and functional microstructures. *Nat. Commun.* **7**, (2016).

307. Gong, J. P., Katsuyama, Y., Kurokawa, T. & Osada, Y. Double-Network Hydrogels with Extremely High Mechanical Strength. *Adv. Mater.* **15**, 1155–1158 (2003).

308. Sun, J.-Y. *et al.* Highly stretchable and tough hydrogels. *Nature* **489**, 133–136 (2012).

309. Yuk, H., Zhang, T., Lin, S., Parada, G. A. & Zhao, X. Tough bonding of hydrogels to diverse non-porous surfaces. *Nat. Mater.* **15**, 190–196 (2015).

310. Lin, S. *et al.* Design of stiff, tough and stretchy hydrogel composites via nanoscale hybrid crosslinking and macroscale fiber reinforcement. *Soft Matter* **10**, 7519–7527 (2014).

311. Lee, J. N., Jiang, X., Ryan, D. & Whitesides, G. M. Compatibility of mammalian cells on surfaces of poly (dimethylsiloxane). *Langmuir* **20**, 11684–11691 (2004).

312. Darnell, M. C. *et al.* Performance and biocompatibility of extremely tough alginate/polyacrylamide hydrogels. *Biomaterials* **34**, 8042–8048 (2013).
313. Robb, W. L. Thin Silicone Membranes-Their Permeation Properties and Ssome Applications. *Ann. N. Y. Acad. Sci.* **146**, 119–137 (1968).
314. Huh, D. *et al.* Reconstituting Organ-Level Lung Functions on a Chip. *Science (80-.).* **328**, 1662–1668 (2010).
315. Halldorsson, S., Lucumi, E., Gómez-Sjöberg, R. & Fleming, R. M. T. Advantages and challenges of microfluidic cell culture in polydimethylsiloxane devices. *Biosens. Bioelectron.* **63**, 218–231 (2015).
316. Jang, K.-I. *et al.* Rugged and breathable forms of stretchable electronics with adherent composite substrates for transcutaneous monitoring. *Nat. Commun.* **5**, (2014).
317. Yuk, H. *et al.* Hydraulic hydrogel actuators and robots optically and sonically camouflaged in water. *Nat. Commun.* **8**, (2017).
318. Liao, I.-C., Moutos, F. T., Estes, B. T., Zhao, X. & Guilak, F. Composite Three-Dimensional Woven Scaffolds with Interpenetrating Network Hydrogels to Create Functional Synthetic Articular Cartilage. *Adv. Funct. Mater.* **23**, 5833–5839 (2013).
319. Belkin, S. Microbial whole-cell sensing systems of environmental pollutants. *Curr. Opin. Microbiol.* **6**, 206–212 (2003).
320. Teulé, F. *et al.* Silkworms transformed with chimeric silkworm/spider silk genes spin composite silk fibers with improved mechanical properties. *Proc. Natl. Acad. Sci.* **109**, 923 LP – 928 (2012).
321. Tero, A. *et al.* Rules for Biologically Inspired Adaptive Network Design. *Science (80-.).* **327**, 439–442 (2010).
322. Inda, M. E. & Lu, T. K. Microbes as Biosensors. *Annu. Rev. Microbiol.* **74**, 337–359 (2020).
323. Packer, M. S. & Liu, D. R. Methods for the directed evolution of proteins. *Nat. Rev. Genet.* **16**, 379–394 (2015).
324. Morrison, M. S., Podracky, C. J. & Liu, D. R. The developing toolkit of continuous directed evolution. *Nat. Chem. Biol.* **16**, 610–619 (2020).
325. Gleizer, S. *et al.* Conversion of Escherichia coli to Generate All Biomass Carbon from CO(2). *Cell* **179**, 1255-1263.e12 (2019).
326. Hossain, A. *et al.* Automated design of thousands of nonrepetitive parts for engineering stable genetic systems. *Nat. Biotechnol.* (2020) doi:10.1038/s41587-020-0584-2.
327. Nielsen, A. A. K. *et al.* Genetic circuit design automation. *Science (80-.).* **352**, (2016).
328. Casini, A., Storch, M., Baldwin, G. S. & Ellis, T. Bricks and blueprints: methods and standards for DNA assembly. *Nat. Rev. Mol. Cell Biol.* **16**, 568–576 (2015).
329. Zhang, W., Mitchell, L. A., Bader, J. S. & Boeke, J. D. Synthetic Genomes. *Annu. Rev. Biochem.* **89**, 77–101 (2020).
330. Adamala, K. P., Martin-Alarcon, D. A., Guthrie-Honea, K. R. & Boyden, E. S. Engineering genetic circuit interactions within and between synthetic minimal cells. *Nat. Chem.* **9**, 431–439 (2017).
331. Ceroni, F. *et al.* Burden-driven feedback control of gene expression. *Nat. Methods* **15**, 387–393 (2018).
332. Segall-Shapiro, T. H., Meyer, A. J., Ellington, A. D., Sontag, E. D. & Voigt, C. A. A 'resource allocator' for transcription based on a highly fragmented T7 RNA polymerase. *Mol. Syst. Biol.* **10**, 742 (2014).
333. Burger, B. *et al.* A mobile robotic chemist. *Nature* **583**, 237–241 (2020).
334. Butler, K. T., Davies, D. W., Cartwright, H., Isayev, O. & Walsh, A. Machine learning for molecular and materials science. *Nature* **559**, 547–555 (2018).
335. Stokes, J. M. *et al.* A Deep Learning Approach to Antibiotic Discovery. *Cell* **180**, 688-702.e13 (2020).
336. Camacho, D. M., Collins, K. M., Powers, R. K., Costello, J. C. & Collins, J. J. Next-Generation Machine Learning for Biological Networks. *Cell* **173**, 1581–1592 (2018).
337. Qin, Z. *et al.* Artificial intelligence method to design and fold alpha-helical structural proteins from the

primary amino acid sequence. *Extrem. Mech. Lett.* **36**, 100652 (2020).
338. Wong, B. G., Mancuso, C. P., Kiriakov, S., Bashor, C. J. & Khalil, A. S. Precise, automated control of conditions for high-throughput growth of yeast and bacteria with eVOLVER. *Nat. Biotechnol.* **36**, 614–623 (2018).
339. Rovner, A. J. *et al.* Recoded organisms engineered to depend on synthetic amino acids. *Nature* **518**, 89–93 (2015).
340. McLeod, C. & Nerlich, B. Synthetic biology, metaphors and responsibility. *Life Sci. Soc. policy* **13**, 13 (2017).
341. Trump, B. D. *et al.* Co-evolution of physical and social sciences in synthetic biology. *Crit. Rev. Biotechnol.* **39**, 351–365 (2019).
342. Levin, M., Bongard, J. & Lunshof, J. E. Applications and ethics of computer-designed organisms. *Nat. Rev. Mol. Cell Biol.* **21**, 655–656 (2020).
343. Chen, C. & Liu, B. Y. Changes in major components of tea fungus metabolites during prolonged fermentation. *J. Appl. Microbiol.* **89**, 834–839 (2000).
344. DiCosimo, R., McAuliffe, J., Poulose, A. J. & Bohlmann, G. Industrial use of immobilized enzymes. *Chem. Soc. Rev.* **42**, 6437 (2013).
345. Shah, N., Ul-Islam, M., Khattak, W. A. & Park, J. K. Overview of bacterial cellulose composites: A multipurpose advanced material. *Carbohydr. Polym.* **98**, 1585–1598 (2013).
346. Wu, S.-C. & Lia, Y.-K. Application of bacterial cellulose pellets in enzyme immobilization. *J. Mol. Catal. B Enzym.* **54**, 103–108 (2008).
347. Wu, S.-C., Wu, S.-M. & Su, F.-M. Novel process for immobilizing an enzyme on a bacterial cellulose membrane through repeated absorption. *J. Chem. Technol. Biotechnol.* **92**, 109–114 (2017).
348. Chen, L., Zou, M. & Hong, F. F. Evaluation of Fungal Laccase Immobilized on Natural Nanostructured Bacterial Cellulose. *Front. Microbiol.* **6**, 1245 (2015).
349. Viswanath, B., Rajesh, B., Janardhan, A., Kumar, A. P. & Narasimha, G. Fungal laccases and their applications in bioremediation. *Enzyme Res.* **2014**, (2014).
350. Allen, H. K. *et al.* Call of the wild: antibiotic resistance genes in natural environments. *Nat. Rev. Microbiol.* **8**, 251–259 (2010).
351. Crofts, T. S. *et al.* Shared strategies for β-lactam catabolism in the soil microbiome. *Nat. Chem. Biol.* **14**, 556–564 (2018).
352. Baldwin, W. & Kubitschek, H. E. Buoyant Density Variation During the Cell Cycle of Saccharomyces cerevisiae. *J. Bacteriol.* **158**, 701–704 (1984).
353. Clasen, C., Sultanova, B., Wilhelms, T., Heisig, P. & Kulicke, W.-M. Effects of Different Drying Processes on the Material Properties of Bacterial Cellulose Membranes. *Macromol. Symp.* **244**, 48–58 (2006).
354. Shaw, W. M. *et al.* Engineering a Model Cell for Rational Tuning of GPCR Signaling. *Cell* **177**, 782-796.e27 (2019).
355. Adeniran, A., Sherer, M. & Tyo, K. E. J. Yeast-based biosensors: Design and applications. *FEMS Yeast Res.* **15**, 1–15 (2015).
356. Bamba, T., Inokuma, K., Hasunuma, T. & Kondo, A. Enhanced cell-surface display of a heterologous protein using SED1 anchoring system in SED1-disrupted Saccharomyces cerevisiae strain. *J. Biosci. Bioeng.* **125**, 306–310 (2018).
357. Shinohara, N. *et al.* The plant cell-wall enzyme AtXTH3 catalyses covalent cross-linking between cellulose and cello-oligosaccharide. *Sci. Rep.* **7**, 46099 (2017).
358. Lee, M. E., DeLoache, W. C., Cervantes, B. & Dueber, J. E. A Highly-characterized Yeast Toolkit for Modular, Multi-part Assembly. *ACS Synth. Biol.* **4**, 975–986 (2015).
359. Tomović, N. S., Trifković, K. T., Rakin, M. P., Rakin, M. B. & Bugarski, B. M. Influence of compression speed and deformation percentage on mechanical properties of calcium alginate particles.

Chem. Ind. Chem. Eng. Q. **21**, 411–417 (2015).

360. Chen, A. Y. *et al.* Synthesis and patterning of tunable multiscale materials with engineered cells. *Nat. Mater.* **13**, 515–523 (2014).

361. Farzadfard, F. *et al.* Single-nucleotide-resolution computing and memory in living cells. *Mol. Cell* **75**, 769–780 (2019).